A CORRELATION POLARIMETER FOR DEEP SPACE POLARIZATION TRACKING

Heinz Rudolf Paul Prunsch

NAVAL POSTGRADUATE SCHOOL
Monterey, California

THESIS

A CORRELATION POLARIMETER
FOR DEEP SPACE POLARIZATION TRACKING

by

Heinz Rudolf Paul Prunsch

June 1975

Thesis Advisor: J.E. Ohlson

REPORT DOCUMENTATION PAGE		READ INSTRUCTIONS BEFORE COMPLETING FORM
1. REPORT NUMBER	2. GOVT ACCESSION NO.	3. RECIPIENT'S CATALOG NUMBER
4. TITLE (and Subtitle) A Correlation Polarimeter for Deep Space Polarization Tracking		5. TYPE OF REPORT & PERIOD COVERED Ph.D. Thesis; June 1975 6. PERFORMING ORG. REPORT NUMBER
7. AUTHOR(s) Heinz Rudolf Paul Prunsch		8. CONTRACT OR GRANT NUMBER(s)
9. PERFORMING ORGANIZATION NAME AND ADDRESS Naval Postgraduate School Monterey, California 93940		10. PROGRAM ELEMENT, PROJECT, TASK AREA & WORK UNIT NUMBERS
11. CONTROLLING OFFICE NAME AND ADDRESS Naval Postgraduate School Monterey, California 93940		12. REPORT DATE June 1975 13. NUMBER OF PAGES 244
14. MONITORING AGENCY NAME & ADDRESS(if different from Controlling Office)		15. SECURITY CLASS. (of this report) Unclassified 15a. DECLASSIFICATION/DOWNGRADING SCHEDULE

16. DISTRIBUTION STATEMENT (of this Report)

Approved for public release; distribution unlimited.

17. DISTRIBUTION STATEMENT (of the abstract entered in Block 20, if different from Report)

18. SUPPLEMENTARY NOTES

19. KEY WORDS (Continue on reverse side if necessary and identify by block number)

Deep space polarization tracking
Faraday rotation in the solar corona
Correlation polarimeter

20. ABSTRACT (Continue on reverse side if necessary and identify by block number)

A correlation polarimeter for the National Aeronautics and Space Administration/Jet Propulsion Laboratory (NASA/JPL) Deep Space Network Mars Station (64 m parabolic antenna) at Goldstone, California has been developed. For polarization tracking a waveguide half-wave plate is used to allow synthesis of a rotating cross polarized feed system. The coherent polarimeter existing at the tracking station since 1968 uses a

(20. ABSTRACT Continued)

phase locked loop (PLL) to coherently detect an error signal, which then drives the feed system. Because the PLL has the normal "loss of lock" problem at low signal-to-noise-ratios, making polarization tracking impossible, a correlation polarimeter which overcomes this limitation has been developed. The active correlation of the signal components in the reference and error channels accomplishes a detection of the error signal. The theory of the correlation polarimeter and its performance are presented. The installation at the NASA/JPL Deep Space Network Mars Station (DSS 14) is described. In addition a Faraday rotation measurement in the solar corona using the German-American spacecraft Helios 1 was done between April 18 and May 1, 1975. Data were taken to a sun-earth-probe angle of about 0.6 degrees. At smaller angles a possible fast varying random linear polarization or depolarization of the signal was observed. The data obtained will aid in a better understanding of the characteristics of the solar corona.

A Correlation Polarimeter for Deep Space Polarization Tracking

by

Heinz Rudolf Paul Prunsch
Kapitänleutnant (Lieutenant Commander), Federal German Navy
M.S., Naval Postgraduate School, 1973

Submitted in partial fulfillment of the
requirements for the degree of

DOCTOR OF PHILOSOPHY

from the

NAVAL POSTGRADUATE SCHOOL

ABSTRACT

A correlation polarimeter for the National Aeronautics and Space Administration/Jet Propulsion Laboratory (NASA/JPL) Deep Space Network Mars Station (64 m parabolic antenna) at Goldstone, California has been developed. For polarization tracking a waveguide half-wave plate is used to allow synthesis of a rotating cross polarized feed system. The coherent polarimeter existing at the tracking station since 1968 uses a phase locked loop (PLL) to coherently detect an error signal, which then drives the feed system. Because the PLL has the normal "loss of lock" problem at low signal-to-noise-ratios, making polarization tracking impossible, a correlation polarimeter which overcomes this limitation has been developed. The active correlation of the signal components in the reference and error channels accomplishes a detection of the error signal. The theory of the correlation polarimeter and its performance are presented. The installation at the NASA/JPL Deep Space Network Mars Station (DSS 14) is described. In addition a Faraday rotation measurement in the solar corona using the German-American spacecraft Helios 1 was done between April 18 and May 1, 1975. Data were taken to a sun-earth-probe angle of about 0.6 degrees. At smaller angles a possible fast varying random linear polarization or depolarization of the signal was observed. The data obtained will aid in a better understanding of the characteristics of the solar corona.

TABLE OF CONTENTS

LIST OF TABLES

Table

LIST OF FIGURES

Figure

Figure

Figure

Figure

ACKNOWLEDGMENT

The author is indebted to J.E. Ohlson who provided continuous advice and guidance as well as encouragement during the last two years.

I also thank G.S. Levy and W.H. Pickering of the Jet Propulsion Laboratory for their efforts to make my appointment as research affiliate with the Jet Propulsion Laboratory for this particular project possible. In addition I feel indebted to C.T. Stelzried, B. Seidel, R. Goldstein, K.B. Wallace all of the Jet Propulsion Laboratory for their support and cooperation.

I also thank the station personnel of the NASA/JPL Deep Space Mars Station for their cooperation during the actual experiment. I also feel an obligation to thank Cdr. W.R. Zimmermann (FGN) for his initial work on the correlation polarimeter chassis which provided a good starting point for the research and development described in this dissertation.

I. INTRODUCTION

In many applications it is of interest to measure the plane of polarization of a received signal. This is particularly useful for the exploration of space. For example, astrophysicists are interested in the polarization and its rate of change for radio sources emitting polarized signals. Another application is the measurement of Faraday rotation in the earth's ionosphere and in the solar corona. The latter is the main area of application of the correlation polarimeter described in this dissertation.

Faraday rotation in the solar corona is caused by the solar magnetic field in conjunction with the plasma surrounding the sun. For the Faraday rotation measurement a linearly polarized signal with known orientation of the plane of polarization must be used. The transmission path passing through the solar corona will result in a rotation of the polarization plane of the transmitted signal. The amount of rotation depends on the electron density and magnetic field along the ray path [1].

By knowing or measuring the solar magnetic field (e.g., magnetometer data) one is able to calculate the electron density of the solar corona.

Transient effects in the corona Faraday rotation measurements have been observed but attempts to correlate these with solar activities have not yet been conclusive [1,2,3,4,6].

As shown by Stelzried and others [1,3] the minor axis of the polarization ellipse is buried in the noise due to the low signal-to-noise-ratio (SNR) in Faraday rotation measurements in the near region of the solar corona.

The first Faraday rotation measurements of the solar corona were made in November 1968 using the 64 m paraboloid of the NASA/JPL Deep Space Network Mars Station (DSS-14) at Goldstone, California in conjunction with the Pioneer VI spacecraft, which transmitted a linearly polarized 2292 Mhz continuous wave (CW) signal through this magnetized plasma [1,2].

The equipment used for this and later polarization measurements was the coherent polarimeter [1,5] which allowed measurements to a ray path offset from the sun as close as 4 solar radii. The coherent polarimeter employs a phase-locked-loop (PLL) which provides a reference signal for polarization angle error detection. The PLL could not keep lock at the high noise temperature and low SNR at about 4 solar radii ray path offset from the sun. The high noise temperature was caused by the antenna side-lobes "seeing" the sun. Another contribution was the effect of spectral broadening of the CW signal in the denser regions of the solar corona [6].

To overcome these limitations of the present coherent polarimeter the correlation polarimeter described in this dissertation was developed and incorporated into the NASA/JPL

Deep Space Network Mars Station receiver system at Goldstone, California. See Figure 1.

The correlation polarimeter does not employ a phase-locked-loop and therefore does not suffer the loss of lock problem of the coherent polarimeter scheme. Tests under high noise conditions at the NASA/JPL Deep Space Network Mars Station indicated that the correlation polarimeter is able to track at better than 10 dB smaller SNR than the coherent polarimeter.

It is anticipated that the correlation polarimeter will replace the coherent polarimeter for Faraday rotation measurements in low SNR applications.

The basic operation of the correlation polarimeter is described in Chapter III. In Chapter IV the system analysis is given as well as a theoretical performance comparison to the coherent polarimeter. The actual system as installed at the NASA/JPL Mars Station and test results are given in Chapter V. The Faraday rotation measurements of the solar corona are discussed in Chapter VI. In Chapter VII the conclusions resulting from tests as well as from the Faraday rotation measurements are given. Suggestions for future work are contained in Chapter VIII.

The operational correlation polarimeter as described extends the present polarization tracking capability of the NASA/JPL Mars Station to weaker signals and higher noise environments.

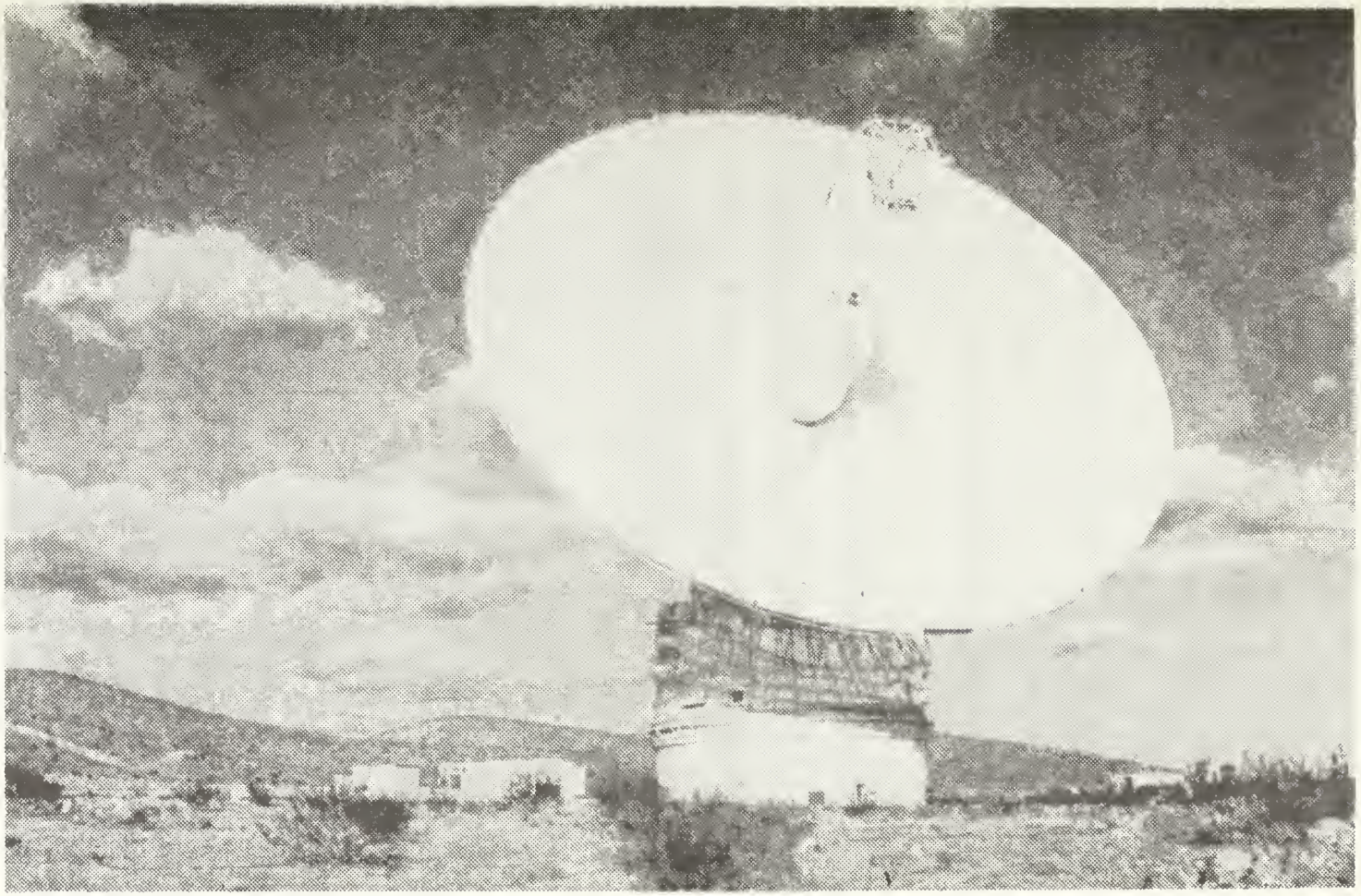

Figure 1 NASA/JPL DEEP SPACE NETWORK MARS STATION IN GOLDSTONE, CALIFORNIA

The Faraday rotation measurements of the solar corona during the first occultation of the Helios 1 spacecraft yielded results to much smaller ray path offsets from the sun than previously obtainable. In addition a possible fast varying random linear polarization or possible depolarization of the received signal at a sun earth probe angle of 0.6 degrees was observed. This effect had been suspected during previous Faraday rotation measurements but could not be confirmed then.

The development of the correlation polarimeter and the extended range of Faraday rotation measurements of the solar corona is a contribution towards a better understanding of the characteristics of the solar corona.

II. THE COHERENT POLARIMETER

The coherent polarimeter in use since 1968 at the NASA/JPL Mars Station has been described by Ohlson et. al. [5] and Stelzried [1]. The major points will be repeated here, incorporating the latest modifications in the polarizer operation.

A. THE POLARIZER

The key feature of the polarization tracking scheme for both the coherent and correlation polarimeter is the rotatable feed system in the Cassegrain antenna S-band feed cone.

This rotatable feed system is realized by the use of two interlocked quarter wave plates in line with the feed cone, forming a "half-wave plate" for linear polarization tracking. A simplified block diagram of the SPD (S-Band Polarization Diverse) cone is shown in Figure 2 [7]. Here the two quarter wave plates are identified as polarizers.

The half-wave plate rotates the plane of polarization of an incoming linearly polarized electromagnetic wave. The half-wave plate has the ability to rotate the plane of polarization by providing two characteristic propagation modes which have different phase velocities. The phase difference between the two modes at the output is 180° versus 0° at the input. This phase change brings about a flipping of the plane of polarization symmetrically about

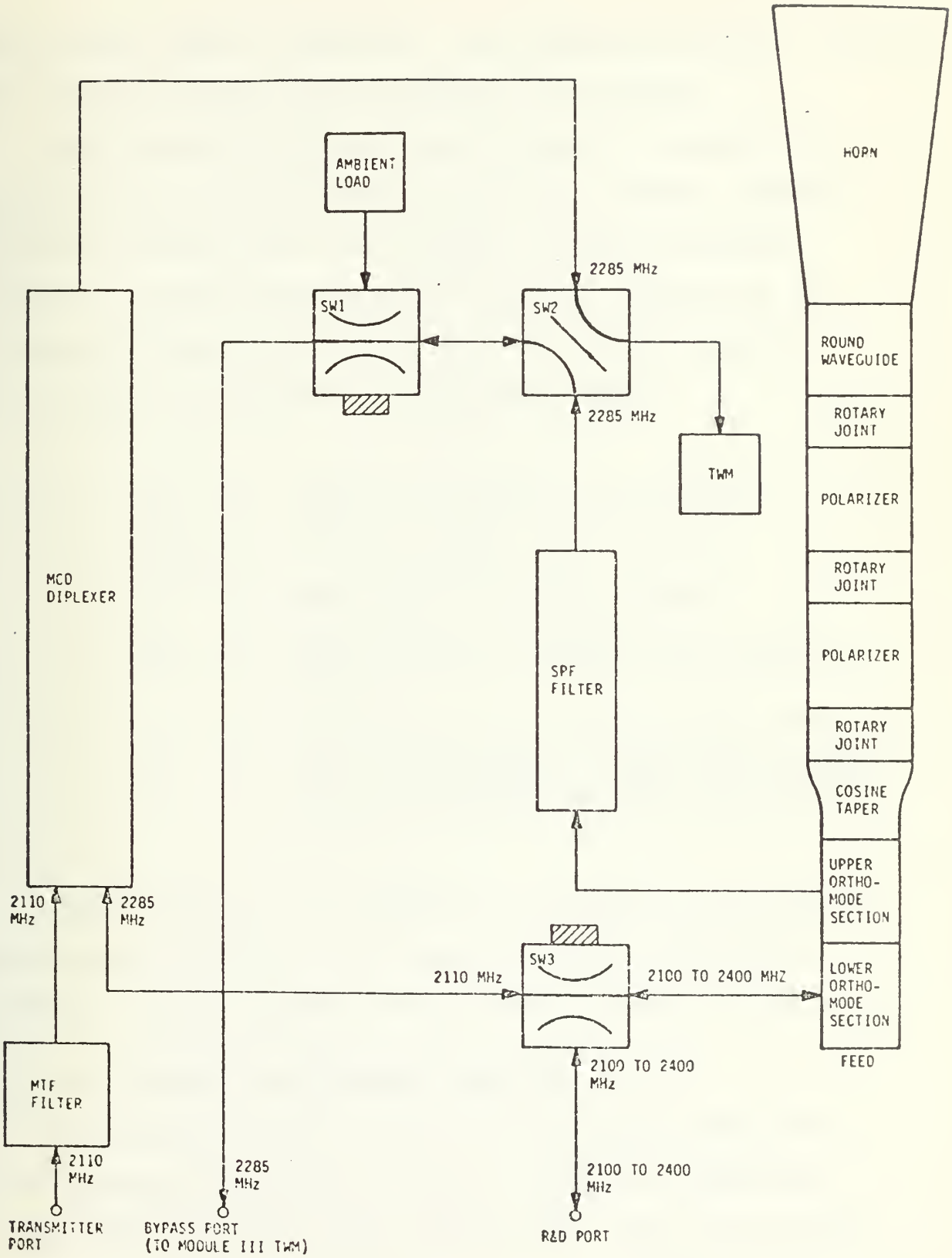

Figure 2 SIMPLIFIED BLOCK DIAGRAM OF THE SPD FEED CONE

the plates' axes of symmetry. By rotating the plate Δ radians, the plane of polarization rotates by 2Δ radians.

The rotatable half-wave plate used in a closed loop polarization tracking system aligns the incoming linearly polarized signal with the reference channel orthomode receiver. Misalignment causes a signal component to be received in the error channel of the orthomode receiver. See Figure 3 for geometric relations, where

S_{IN}	=	Plane of incoming polarization
S_{OUT}	=	Plane of output polarization
A	=	Amplitude of incoming signal
θ_{PL}	=	Angle between polarizer and reference channel
β	=	Angle between S_{IN} and reference channel
Δ	=	Angle between plat Y axis and incoming as well as output plane of polarization.

The half-wave plate polarizer is used for the coherent polarimeter as well as for the correlation polarimeter scheme. Figure 4 shows the polarizer in the SPD feed cone.

B. THE COHERENT POLARIMETER OPERATION

The present optimum system for moderately high SNR is the coherent polarimeter, which is similar to amplitude comparison monopulse angle tracking [8]. The key feature is the use of a rotatable feed, described in Section II.A.

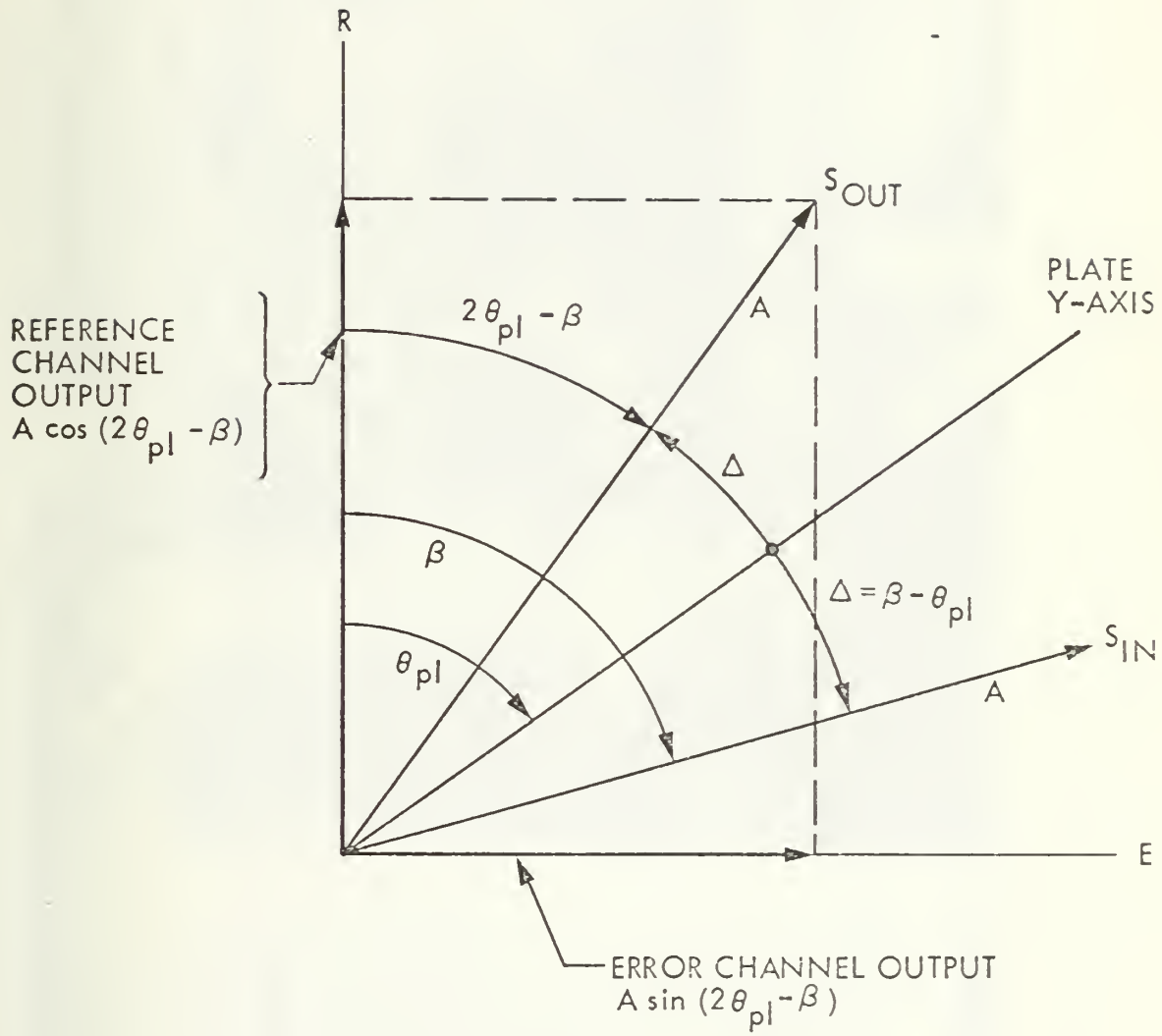

Figure 3 GEOMETRIC RELATIONS FOR THE HALF-WAVE PLATE POLARIZER

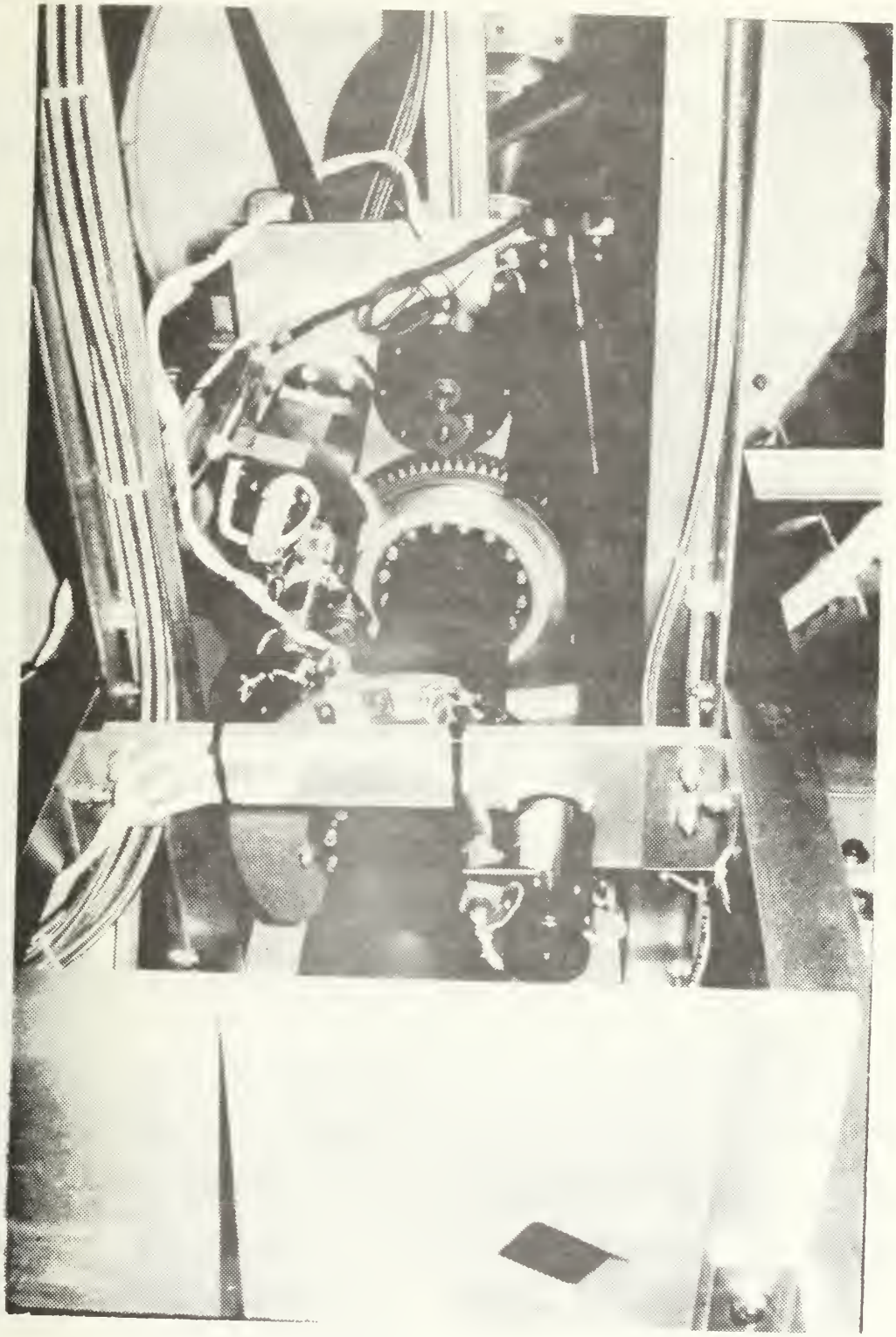

Figure 4 VIEW INTO THE SPD FEED CONE SHOWING THE POLARIZER

The presently used coherent polarimeter employs a PLL. A simplified block diagram of the coherent polarimeter is shown in Figure 5 [9].

The operation of the coherent polarimeter is easily understook [1,5]. The reference and error channel signals are the projections of the received electric field vector upon the reference and error axes, respectively. For the case of perfect alignment of the reference axis with the plane of polarization of the received signal, the reference channel will have all the power and the PLL [10] is locked to the signal. The error channel has no signal power, so the servo motor is driven by the system noise only. When the reference channel is slightly misaligned the error channel receives a signal component and by means of the coherent detector an error signal proportional to the angle error is generated which will drive the rotatable feed system back, so that the reference axis is again aligned with the signal axis.

Since the incorporated PLL is not able to stay in lock for low SNR, resulting from a weak signal, a high noise environment or doppler spreading of the signal, the performance of the system will deteriorate as the SNR in the PLL approaches unity [10].

The correlation polarimeter scheme proposed by Ohlson [11] and tested by Zimmermann [9] eliminates the "loss of lock" problem inherent for low SNR.

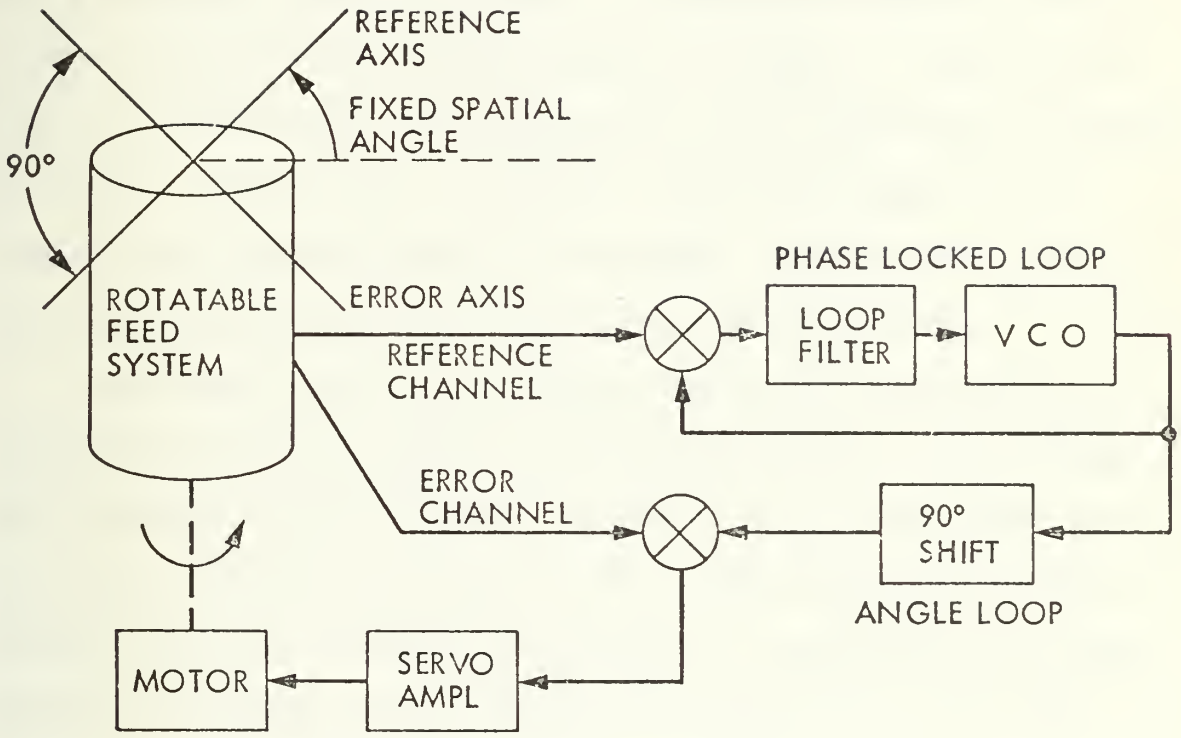

Figure 5 SIMPLIFIED BLOCK DIAGRAM OF THE COHERENT POLARIMETER

III. BASIC OPERATION OF THE CORRELATION POLARIMETER

It has been shown by Ohlson [11] that the basic correlation polarimeter is optimal when the signal can be modeled as a Gaussian random process. A simplified model of the correlation polarimeter is shown in Figure 6, where $H_r(f)$ and $H_e(f)$ represent all filtering in the reference and error channels respectively. Figure 7 shows the system with additional circuits such as automatic gain control (AGC), and a second multiplier with wide band inputs [9].

Reference and error channel signals are developed by the use of the previously mentioned rotatable feed system. The correlation polarimeter is based on the idea that for low SNR when the PLL can not give a good estimate of the signal phase for coherent detection, a correlation of the signal component in the reference channel r(t) with the signal component in the error channel e(t) will also accomplish a detection of the error channel signal. The signals r(t) and e(t) must have the same phase, since they are just different projections of the signal vector [9,11].

Again as for the coherent polarimeter the error signal is used to align the polarizer in such a fashion that all signal power is received in the reference channel of the orthomode transducer.

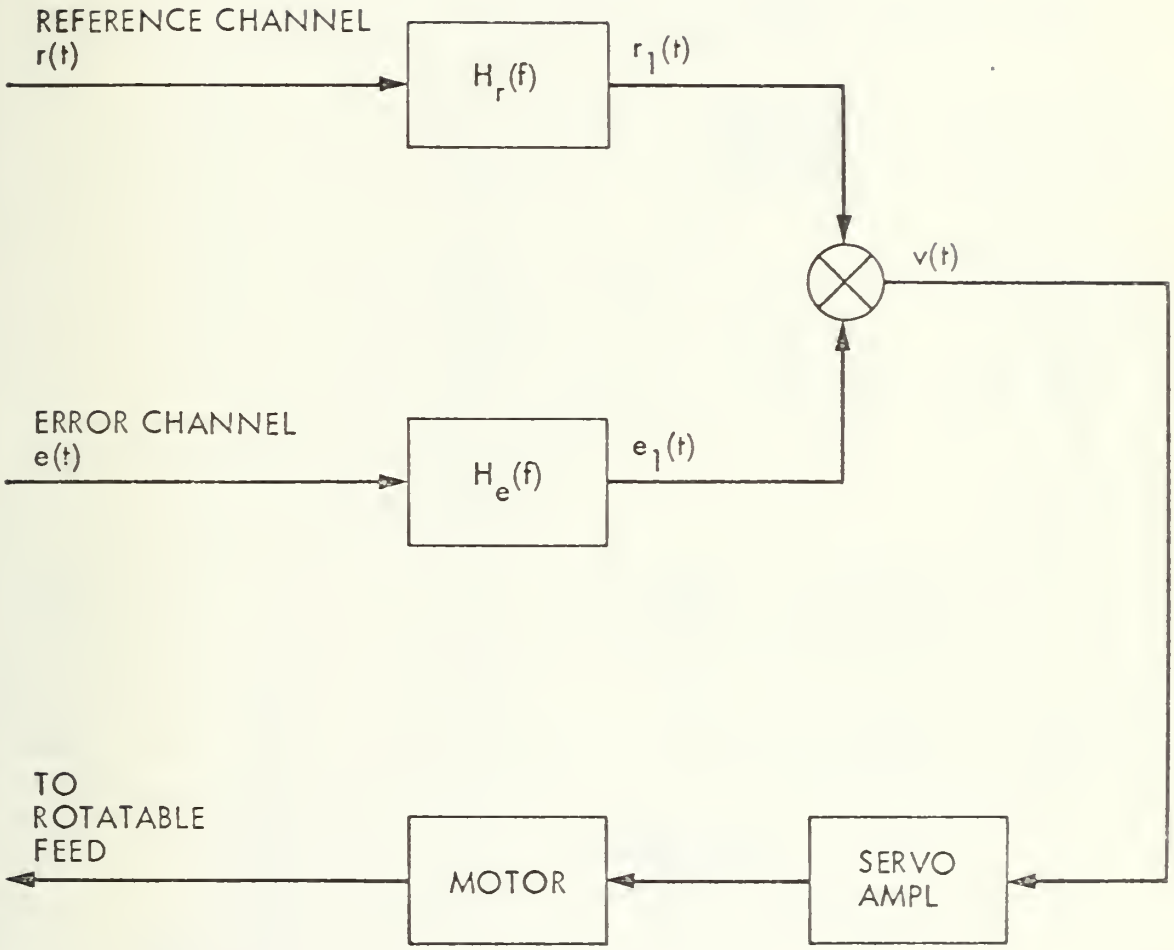

Figure 6 SIMPLIFIED MODEL OF THE CORRELATION POLARIMETER

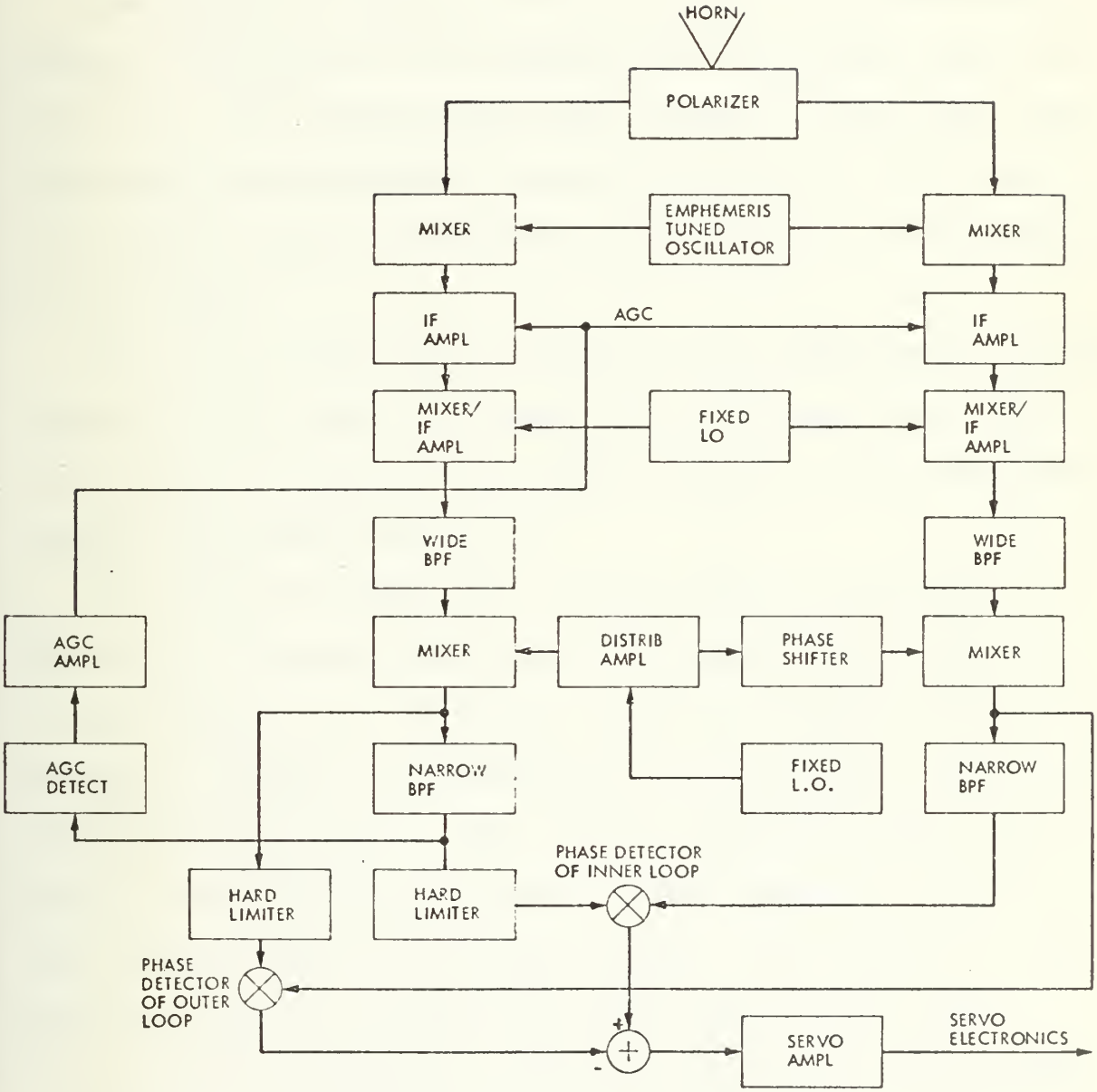

Figure 7 PRACTICAL CORRELATION POLARIMETER

IV. SYSTEM ANALYSIS

A. CORRELATOR OUTPUT

The correlator output v(t) is derived in the following section. The basis is the correlation polarimeter model in Figure 7. The reference and error channel in the inner and outer loop are considered perfectly phased up by the use of the indicated phase shifter and application of a test signal to the inputs.

The use of identical filtering in the reference and error channels in the inner and outer loop guarantees that phase shifts due to frequency variation are equal in the channels, leaving the system phased up.

The received signal s(t) as seen with the antenna's aperture is linearly polarized at an angle θ with respect to the reference x-y coordinate system of the polarizer. The y axis is assumed to be parallel to the reference channel of the orthomode receiver. The linearly polarized wide band noise is polarized at an angle $\theta+\phi$ with respect to the y axis of the same x-y coordinate system. See Figure 8. In addition there is a large portion of unpolarized noise received in the reference and error channels. The analysis is done with the hard limiters in the reference channels, as necessary to obtain a high drive for the phase detectors.

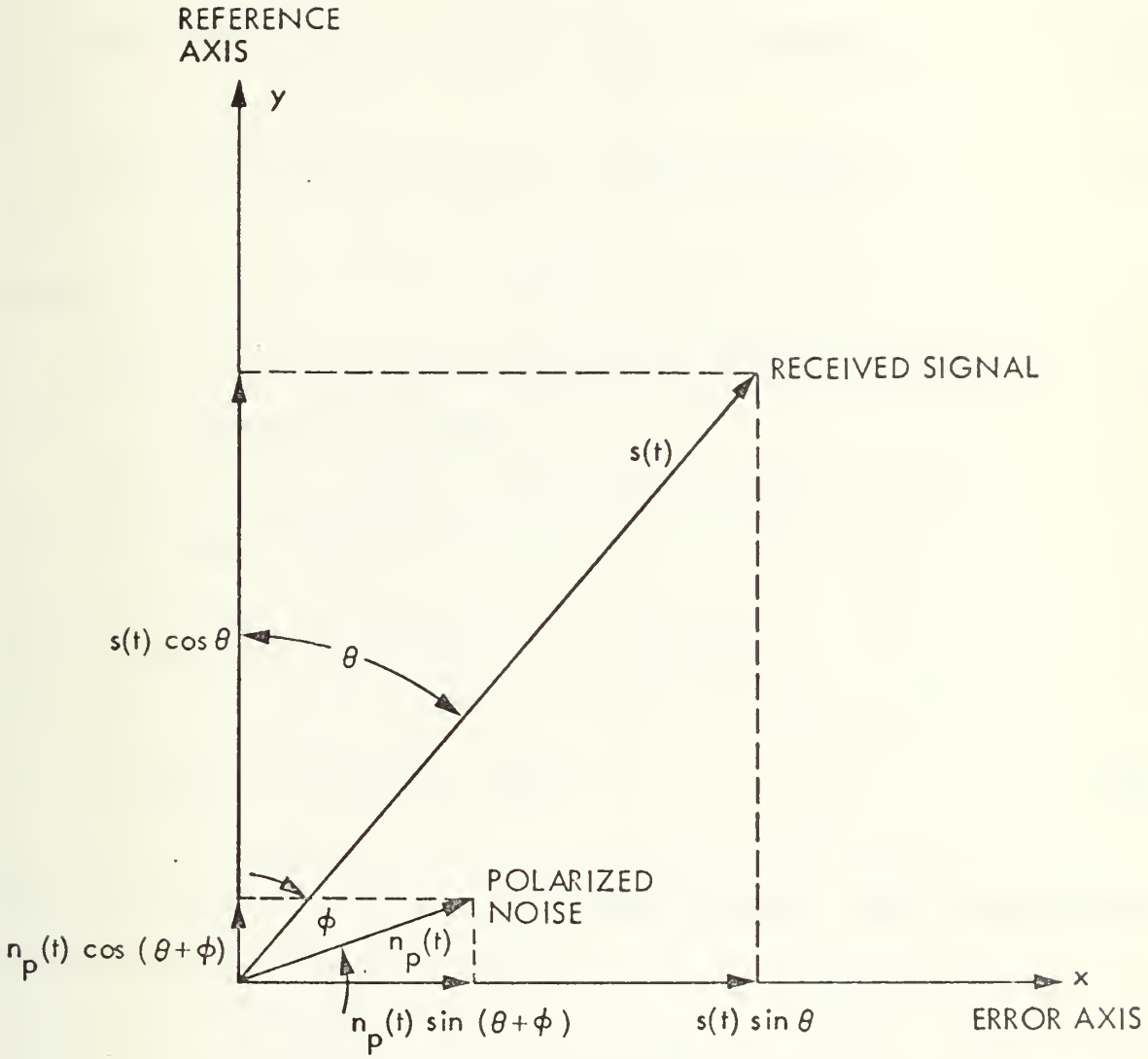

Figure 8 GEOMETRIC RELATIONS OF SIGNAL AND POLARIZED NOISE

We can define the reference and error channel signals as the projections of the received signal and polarized noise upon the coordinate axes as

$$r(t) = s(t) \cos \theta + n_r(t) + n_p(t) \cos(\theta+\phi) \quad (1)$$

$$e(t) = s(t) \sin \theta + n_e(t) + n_p(t) \sin(\theta+\phi) \quad (2)$$

where

r(t) is the received signal plus noise in the reference channel

e(t) is the received signal plus noise in the error channel.

The autocorrelation function of s(t) is

$$R_s(\tau) = E[s(t+\tau)\ s(t)] \quad (3)$$

where E[·] denotes statistical expectation. The corresponding power spectral density is

$$S_s(f) = \int_{\infty}^{\infty} R_s(\tau) \exp(-2j\pi f\tau)\, d\tau \quad (4)$$

The other autocorrelation functions and power spectral densities are defined similarly.

The noises $n_r(t)$, $n_e(t)$, and $n_p(t)$ are assumed to be independent, white, zero mean Gaussian random processes with double-sided power spectral densities

$$S_{n_r}(f) = \frac{N_r}{2} = \frac{kT_r}{2} \tag{5}$$

$$S_{n_e}(f) = \frac{N_e}{2} = \frac{kT_e}{2} \tag{6}$$

$$S_{n_p}(f) = \frac{N_p}{2} \tag{7}$$

where k = Boltzmann's constant

T_r = System noise temperature in reference channel

T_e = System noise temperature in error channel

and N_r, N_e and N_p are in units of W/Hz .

The corresponding autocorrelation functions are

$$R_{n_r}(\tau) = N_r\delta(\tau) \tag{8}$$

$$R_{n_e}(\tau) = N_e\delta(\tau) \tag{9}$$

$$R_{n_p}(\tau) = N_p\delta(\tau). \tag{10}$$

For ease of calculations all voltages are assumed to be on 1 ohm impedances so that the units in (4), (5), (6), and (7) are Watts/Hz and the average signal power is given by

$$P_s = E[s^2(t)] = R_s(0) . \tag{11}$$

Considering the inner loop first we want to find the statistics of the correlator output $v_i(t)$ given θ and ϕ. The mean of $v_i(t)$ and the spectrum of $v_i(t)$ given θ and ϕ are sufficient for determination of the system rms error $\sigma^2_{\theta_i}$.

From Figure 9 which models the basic loop and correlator we can write

$$r_1(t) = \int_{-\infty}^{\infty} r(\tau)\, h_r(t-\tau)\, d\tau \tag{12}$$

$$e_1(t) = \int_{-\infty}^{\infty} e(\tau)\, h_e(t-\tau)\, d\tau \tag{13}$$

where $h_r(t)$ and $h_e(t)$ are the impulse responses of the filtering done in the reference and error channel respectively. $H_r(f)$ and $H_e(f)$ are the corresponding Fourier transforms.

The filters $h_r(t)$ and $h_e(t)$ are assumed to be linear. In our case

$$h_r(t) = h_e(t). \tag{14}$$

The output of the filters can be written in the following form

$$r_1(t) = s_1(t) \cos\theta + n_{p_1}(t) \cos(\theta+\phi) + n_{r_1}(t) \tag{15}$$

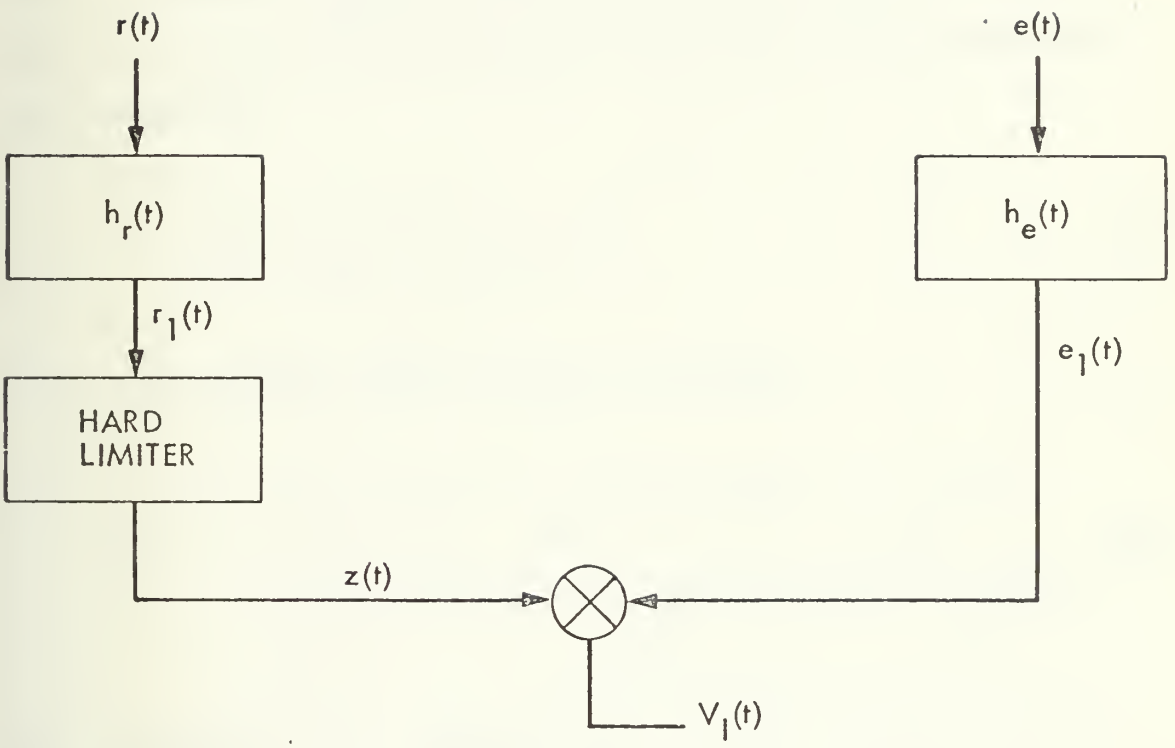

Figure 9 BASIC CORRELATOR LOOP MODEL

and

$$e_1(t) = s_1(t) \sin\theta + n_{p_1}(t) \sin(\theta+\phi) + n_{e_1}(t) \quad (16)$$

where $s_1(t)$, $n_{p_1}(t)$, $n_{r_1}(t)$, and $n_{e_1}(t)$ are the filtered versions of $s(t)$, $n_p(t)$, $n_r(t)$, and $n_e(t)$ respectively. Due to linear filtering the means of the processes will still be zero and the processes will still be independent and Gaussian.

Since

$$v_i(t) = e_1(t) \operatorname{sgn} r_1(t) \quad (17)$$

and substituting (15) and (16) we obtain

$$\begin{aligned} v_i(t) = {} & (s_1(t)\sin\theta + n_{p_1}(t)\sin(\theta+\phi) + n_{e_1}(t)) \\ & \cdot \operatorname{sgn}[s_1(t)\cos\theta + n_{p_1}(t)\cos(\theta+\phi) + n_{r_1}(t)] \end{aligned} \quad (18)$$

and calculating the expectation of $v_i(t)$, conditioned on θ and ϕ, the system S-curve for the inner loop can be obtained.

$$\begin{aligned} S(\theta,\phi) &= E[v_i(t)/\theta,\phi] \\ &= E[e_1(t)\operatorname{sgn}\{r_1(t)\}/\theta,\phi]. \end{aligned} \quad (19)$$

Under the assumption of s(t) being Gaussian and zero mean, [9,11] we also know that $r_1(t)$ and $e_1(t)$ are Gaussian with zero mean. Now the corresponding variances have to be determined to be able to specify the probability density functions. Since we deal with zero mean processes we can write

$$\sigma_{r_1}^2 = E[r_1^2(t)] \tag{20}$$

$$= E[(s_1(t)\cos\theta + n_{p_1}(t)\cos(\theta+\phi) + n_{r_1}(t))^2] \tag{21}$$

Since $s_1(t)$, $n_{p_1}(t)$, $n_{r_1}(t)$ are uncorrelated and zero mean, we obtain

$$\sigma_{r_1}^2 = \sigma_{s_1}^2 \cos^2\theta + \sigma_{n_{p_1}}^2 \cos^2(\theta+\phi) + \sigma_{n_{r_1}}^2 \tag{22}$$

where

$\sigma_{s_1}^2$ = average power in filtered version of s(t)

$\sigma_{n_{p_1}}^2$ = average power in filtered version of $n_p(t)$

$\sigma_{n_{r_1}}^2$ = average power in filtered version of $n_r(t)$.

In addition we define the one-sided filter noise bandwidths of $H_r(f)$ and $H_e(f)$ to be

$$B = \frac{\int_0^\infty |H_r(f)|^2 \, df}{|H_r(f_o)|^2} \tag{23}$$

where f_o is the center frequency of the filter. Since $H_r(f)$ and $H_e(f)$ are identical (23) applies for the reference as well as the error channel filters.

Calling B_I the equivalent noise bandwidth for the filtering in the inner loop channels we can write

$$\sigma_{n_{p_1}}^2 = N_p B_I \tag{25}$$

$$\sigma_{n_{r_1}}^2 = N_r B_I \quad . \tag{26}$$

Similar calculations and reasoning give us

$$\sigma_{e_1}^2 = \sigma_{s_1}^2 \sin^2\theta + \sigma_{n_{p_1}}^2 \sin^2(\theta+\phi) + \sigma_{n_{e_1}}^2 \tag{27}$$

where

$\sigma_{s_1}^2$ = average signal power in filtered version of s(t)

$\sigma_{n_{p_1}}^2$ = as defined in (25)

$\sigma_{n_{e_1}}^2$ = average power in filtered version of $n_e(t)$

and

$$\sigma_{n_{e_1}}^2 = B_I N_e \tag{28}$$

by the same reasoning as used to obtain (25) and (26).

As a result we have the normal density parameters

$$r_1(t) \sim N(0,\sigma_{r_1})$$

$$e_1(t) \sim N(0,\sigma_{e_1})$$

To find the joint normal probability density of $r_1(t)$ and $e_1(t)$, we in addition need to determine the correlation coefficient of $r_1(t)$ and $e_1(t)$. The derivation is done as follows.

$$\rho = \frac{E[r_1(t)e_1(t)]}{\sigma_{r_1}\sigma_{e_1}} \tag{29}$$

$\sigma_{r_1}^2$, $\sigma_{e_1}^2$ are as calculated in (22) and (27) and

$$E[r_1(t)e_1(t)] = E[(s_1(t)\cos\theta + n_{p_1}(t)\cos(\theta+\phi) + n_{r_1}(t))$$
$$(s_1(t)\sin\theta + n_{p_1}(t)\sin(\theta+\phi) + n_{e_1}(t))]. \tag{30}$$

Due to independence of the processes $s_1(t)$ $n_{p_1}(t)$, $n_{r_1}(t)$ and $n_{e_1}(t)$ and due to the zero mean property of the above processes the expression reduces to

$$E[r_1(t)e_1(t)] = E[s_1^2(t)\cos\theta\sin\theta + n_{p_1}^2(t)\cos(\theta+\phi)\sin(\theta+\phi)]$$
$$= \sigma_{s_1}^2\cos\theta\sin\theta + \sigma_{n_{p_1}}^2\cos(\theta+\phi)\sin(\theta+\phi). \tag{31}$$

Using (22), (27) and (31) we obtain

$$\rho = \frac{\sigma_{s_1}^2 \cos\theta\sin\theta + \sigma_{n_{p_1}}^2 \cos(\theta+\phi)\sin(\theta+\phi)}{\{(\sigma_{s_1}^2\cos^2\theta + \sigma_{n_{p_1}}^2\cos^2(\theta+\phi) + \sigma_{n_{r_1}}^2)(\sigma_{s_1}^2\sin^2\theta + \sigma_{n_{p_1}}^2\sin(\theta+\phi) + \sigma_{n_{e_1}}^2)\}^{1/2}} \tag{32}$$

Knowing $\sigma_{r_1}^2$, $\sigma_{e_1}^2$ and ρ allows us to calculate

$$E[v_i(t)/\theta,\phi] = \int_{-\infty}^{\infty}\int_{-\infty}^{\infty} e_1(t)\,\mathrm{sgn}(r_1(t))\,f_{R,E}(r_1(t),e_1(t))\,dr_1 de_1 \tag{33}$$

where $f_{R,E}(r_1,e_1)$ is the joint Gaussian probability density function of $r_1(t)$ and $e_1(t)$.

For simplicity substitute

$$\begin{aligned} r_1(t) &= y \\ e_1(t) &= x \\ \sigma_{r_1}^2 &= \sigma_y^2 \\ \sigma_{e_1}^2 &= \sigma_x^2 \end{aligned} \tag{34}$$

Using (34), (33) becomes

$$E[v_i(t)/\theta,\phi] = \int_{-\infty}^{\infty}\int_{-\infty}^{\infty} \frac{x \operatorname{sgn} y}{2\pi\rho\sigma_x\sigma_y(1-\rho^2)^{1/2}}$$

$$\cdot \exp\{\frac{-1}{2(1-\rho^2)}\left(\frac{x^2}{\sigma_x^2} - \frac{2\rho xy}{\sigma_x\sigma_y} + \frac{y^2}{\sigma_y^2}\right)\} \; dxdy. \quad (35)$$

This can be solved by standard quadratic expansion techniques

$$E[v_i(t)/\theta,\phi] = \int_{-\infty}^{\infty} \frac{\operatorname{sgn} y}{2\pi\sigma_x\sigma_y(1-\rho^2)^{1/2}} \exp\{\frac{-1}{2(1-\rho)^2}\frac{y^2}{\sigma_y^2}\}$$

$$\cdot \int_{-\infty}^{\infty} x \exp\{\frac{-1}{2(1-\rho^2)}\left(\frac{x^2}{\sigma_x^2} - \frac{2\rho xy}{\sigma_x\sigma_y} + \frac{\rho^2y^2}{\sigma_y^2} - \frac{\rho^2y^2}{\sigma_y^2}\right)\} \; dxdy \quad (36)$$

$$E[v_i(t)/\theta,\phi] = \int_{-\infty}^{\infty} \frac{\operatorname{sgn} y}{2\pi\rho\sigma_x\sigma_y(1-\rho^2)^{1/2}} \exp\{\frac{-1}{2(1-\rho)^2}\left(\frac{y^2}{\sigma_y^2} - \frac{\rho^2y^2}{\sigma_y^2}\right)\}$$

$$\cdot \int_{-\infty}^{\infty} x \exp\{\frac{-1}{2(1-\rho^2)\sigma_x^2}\left(x - \frac{\rho y\sigma_x}{\sigma_y}\right)^2\} \; dxdy \quad (37)$$

The second integral (over x) is easily solved, bringing it into the form of the expectation of a Gaussian random variable and we obtain after some calculations

$$E[v_i(t)/\theta,\phi] = \int_{-\infty}^{\infty} \frac{(sgn)\, y \sigma_x \rho}{\sqrt{2\pi}\ \sigma_y^2} \exp\{\frac{-y^2}{2\sigma_y^2}\}\ dy \tag{38}$$

which can be written as

$$E[v_i(t)/\theta,\phi] = \frac{\sigma_x \rho\, 2}{\sqrt{2\pi}\ \sigma_y^2} \int_{-\infty}^{\infty} y \exp\{\frac{-y^2}{2\sigma_y^2}\}\ dy = \sqrt{\frac{2}{\pi}}\ \sigma_x \rho\ . \tag{39}$$

From (29) and (34)

$$\rho = \frac{E[x\,y]}{\sigma_x \sigma_y} \tag{40}$$

and thus

$$E[v_i(t)/\theta,\phi] = \sqrt{\frac{2}{\pi}}\ \frac{E[x\,y]}{\sigma_y}\ . \tag{41}$$

Substituting the expressions for $E[x\,y]$ and σ_y from (31) and (22) using (34) into (41) yields

$$S_i(\theta,\phi) = E[v_i(t)/\theta,\phi] = \sqrt{\frac{2}{\pi}}\ \frac{\sigma_{s_1}^2 \cos\theta\sin\theta + \sigma_{n_{p_1}}^2 \cos(\theta+\phi)\sin(\theta+\phi)}{(\sigma_{s_1}^2 \cos^2\theta + \sigma_{n_{p_1}}^2 \cos^2(\theta+\phi) + \sigma_{n_{r_1}}^2)^{1/2}} \tag{42}$$

which is the system S-curve for given θ and ϕ in the inner loop. Exactly the same kind of calculations yield an expression of equal form for the outer loop correlator output expected value conditioned on θ and ϕ. The only difference to be realized is the different filtering in the outer loop, especially the wider bandwidth in the outer loop.

The expected value of the output of the outer loop $v_o(t)$, conditions on θ and ϕ is

$$S_o(\theta,\phi) = E[v_o(t)/\theta,\phi] = \sqrt{\frac{2}{\pi}} \frac{\sigma_{s_2}^2 \cos\theta\sin\theta + \sigma_{n_{p_2}}^2 \cos(\theta+\phi)\sin(\theta+\phi)}{(\sigma_{s_2}^2\cos^2\theta - \sigma_{n_{p_2}}^2\cos^2(\theta+\phi) + \sigma_{n_{r_2}}^2)^{1/2}} . \quad (43)$$

We again realize $h_{r_o}(t)$, the impulse response of all filtering in the reference channel of the outer loop to be equal to $h_{e_o}(t)$, the impulse response of all filtering in the error channel of the outer loop.

Also

$\sigma_{s_2}^2$ = average signal power in filtered version of s(t) in outer loop

$\sigma_{n_{p_2}}^2$ = average linearly polarized noise power in outer loop

$\sigma_{n_{r_2}}^2$ = average noise power of unpolarized noise in the reference channel of outer loop.

Also

$$\sigma_{n_{p_2}}^2 = N_p B_o$$

$$\sigma_{n_{r_2}}^2 = N_r B_o \qquad (44)$$

where

B_o = equivalent noise bandwidth of filtering in each, reference and error channel, of the outer loop (defined similar to (23)).

B. THE EFFECT OF LINEARLY POLARIZED NOISE ON THE DC TRACKING ERROR

1. Polarized Noise Received from the Sun

It is known that the quiet sun emits very little linearly polarized noise at S-band. Only during decimeter bursts is there the possibility of emission of linearly polarized noise at S-band. The duration of these bursts usually is less than ten minutes with some extending to several hours [12,13,14,15]. But generally these burst have circular polarization and quite often the emissions are unpolarized. Therefore we can assume that the received polarized noise component is in general much smaller (much less than 10%) of the total unpolarized noise.

Most noise in the system in the measurement of Faraday rotation in the solar corona is caused by sidelobes of the antenna seeing the sun. Due to the quadripod legs (Figure 10)

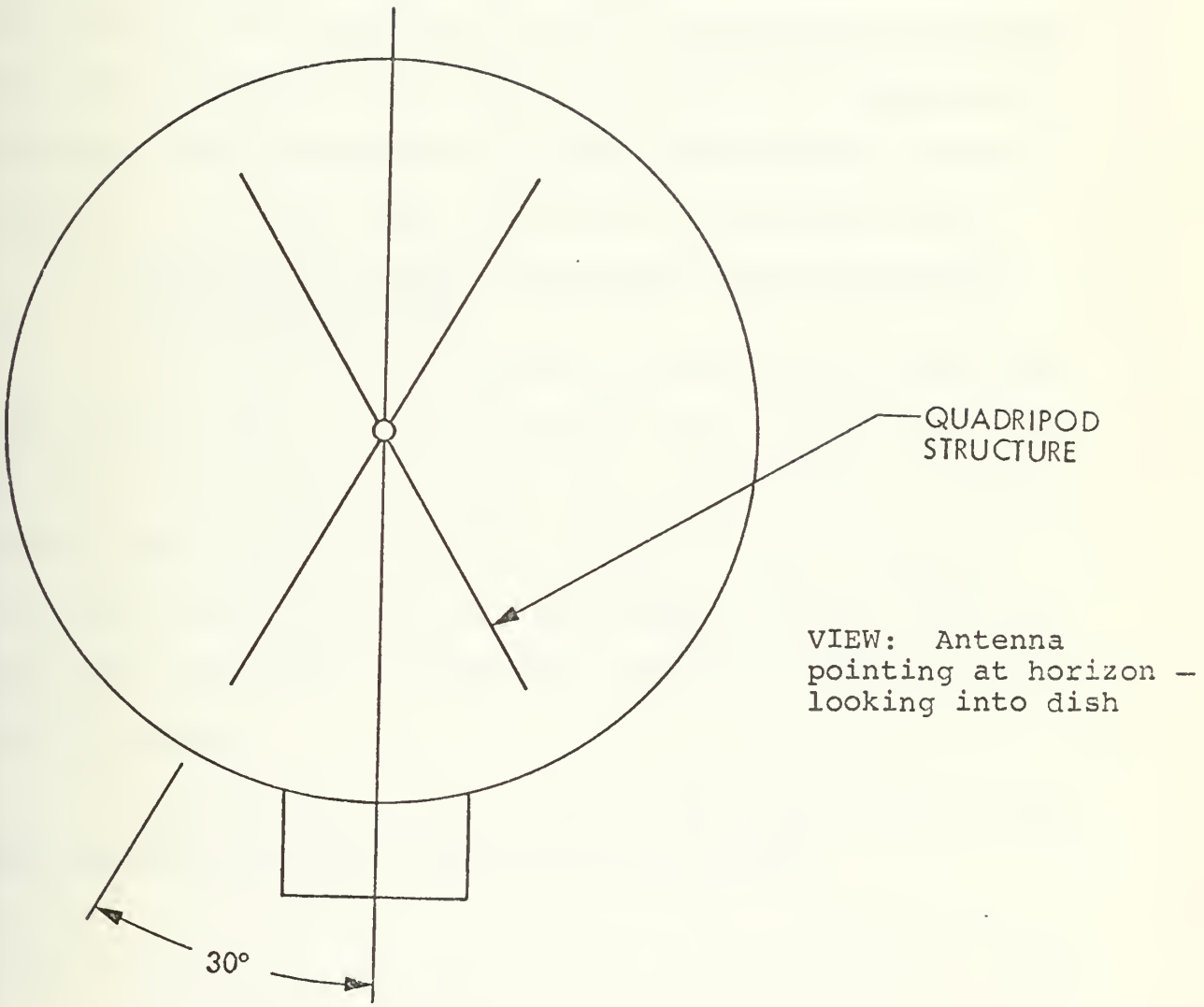

Figure 10 ANTENNA QUADRIPOD STRUCTURE

supporting the subreflector of the antenna, the sidelobes are not circularly distributed around the main lobe of the antenna. There are distinct sidelobes in angular orientation. If one of these sidelobes passes during the tracking period over burst regions on the sun emitting S-band linearly polarized noise, a polarization tracking bias will result. To eliminate this possible bias the correlation polarimeter was constructed with the outer loop, which is dominated by noise and will generate a dc signal compensating the bias signal in the inner loop output due to polarized noise.

2. Effects of Linearly Polarized Noise-Utilization of the Outer Loop

As long as we are tracking relatively far from the sun we can expect to receive hardly any linearly polarized noise and the signal-to-noise ratio will be high (> 0 dB). Under these considerations the effects of the linearly polarized noise regarding a polarization tracking bias in the inner loop will be negligible and the outer loop will not be needed.

In the high signal-to-noise ratio case with hardly any linearly polarized noise received clearly

$$\sigma_{s_1}^2 > \sigma_{n_{r_1}}^2 >> \sigma_{n_{p_1}}^2 \tag{45}$$

and the system S-curve, conditioned on θ (42), becomes

$$S_i(\theta) \simeq \sqrt{\frac{2}{\pi}} \frac{\sigma_{s_1}^2 \cos\theta \sin\theta}{(\sigma_{s_1}^2 \cos^2\theta + \sigma_{n_{r_1}}^2)^{1/2}} \tag{46}$$

and for very high signal-to-noise ratios it is possible to write

$$S_i(\theta) \simeq \sqrt{\frac{2}{\pi}} \quad \sigma_{s_1} \sin\theta \quad . \tag{47}$$

The latter case would only occur while tracking a spacecraft very far from the sun resulting in a measurement of only ionospheric Faraday rotation. These measurements are performed continuously with less involved schemes using geostationary satellites [1]. Under the circumstances of low signal-to-noise ratios, or at least the signal power received being comparable to the received noise power, but still

$$\sigma_{n_{p_1}}^2 << \sigma_{n_{r_1}}^2 \tag{48}$$

(46) would hold and there is no need for the outer loop to be used.

Now consider the linearly polarized noise being strong enough to make a contribution to the output of the inner loop. Clearly the bias would be from (42)

$$S_{I_B}(\theta,\phi) = \sqrt{\frac{2}{\pi}} \frac{\sigma_{n_{p_1}} \cos(\theta+\phi)\sin(\theta+\phi)}{(\sigma_{s_1}^2\cos^2\theta + \sigma_{n_{p_1}}^2\cos^2(\theta+\phi) + \sigma_{n_{r_1}}^2)^{1/2}} \tag{49}$$

To cancel this bias we employ the outer loop which has a much wider bandwidth than the inner loop. The output of the outer loop will be dominated by the linearly polarized noise and its dc output will be subtracted with a proper gain factor to cancel out the bias of the output of the inner loop (49).

The general output of the outer loop is given by (43). Due to the increased bandwidth of the filtering in the outer loop we have an even lower SNR in the outer loop than in the inner loop. Under these conditions

$$\sigma_{n_{p_2}}^2 \geq \sigma_{s_2}^2$$

and the main contribution to the output of the outer loop is a function of $\sigma_{n_{p_2}}^2$ and ϕ.

In addition when tracking well on the signal

$$\begin{aligned} \theta &\simeq 0 \\ \cos\theta &\simeq 1 \\ \sin\theta &\simeq \theta \end{aligned} \tag{50}$$

and the contribution due to the signal in the outer loop output since

$$\sigma_{n_{r_2}}^2 > \sigma_{n_{p_2}}^2 \geq \sigma_{s_2}^2$$

will be totally negligible. So we can write under these circumstances (tracking well, SNR in outer loop << 0 dB) for the output of the outer loop

$$S_o(\phi) = \sqrt{\frac{2}{\pi}} \frac{\sigma_{n_{p_2}}^2 \cos\phi \sin\phi}{(\sigma_{s_2}^2 + \sigma_{n_{p_2}}^2 \cos^2\phi + \sigma_{n_{r_2}}^2)^{1/2}} . \qquad (51)$$

We now subtract (51) with proper gain from (42) to obtain the system S-curve without an additional polarization tracking bias due to the received polarized noise.

$$S_s(\theta,\phi) = \sqrt{\frac{2}{\pi}} \frac{\sigma_{s_1}^2 \theta}{(\sigma_{s_1}^2 + \sigma_{n_{p_1}}^2 \cos^2\phi + \sigma_{n_{r_1}}^2)^{1/2}} \qquad (52)$$

To obtain (52) we have the condition from (49) and (51)

$$S_{I_B}(\theta,\phi) = G\, S_o(\theta,\phi)$$

$$G = \frac{S_{I_B}(\theta,\phi)}{S_o(\theta,\phi)} \qquad (53)$$

which is the gain ratio of outer loop to inner loop output yielding, when tracking well

$$G = \frac{\dfrac{\sigma_{n_{p_1}}^2}{(\sigma_{s_1}^2 + \sigma_{n_{p_1}}^2 \cos^2\phi + \sigma_{n_{r_1}}^2)^{1/2}}}{\dfrac{\sigma_{n_{p_2}}^2}{(\sigma_{s_2}^2 + \sigma_{n_{p_2}}^2 \cos^2\phi + \sigma_{n_{r_2}}^2)^{1/2}}} \quad . \tag{54}$$

Now recalling (25), (26), (44)

$$\sigma_{n_{p_1}}^2 = N_p B_I$$

$$\sigma_{n_{p_2}}^2 = N_p B_o$$

$$\sigma_{n_{r_1}}^2 = N_r B_I$$

$$\sigma_{n_{r_2}}^2 = N_r B_o$$

and assuming that the signal is well within the passband of inner and outer loop filtering, under the assumption that we are tracking well on the signal we can write (54) as

$$G = \frac{B_I(\sigma_{s_2}^2 + N_p B_o \cos^2\phi + N_r B_o)^{1/2}}{B_o(\sigma_{s_1}^2 + N_p B_I \cos^2\phi + N_r B_I)^{1/2}} \qquad (55)$$

Under the assumption that the SNR is well below 0 dB in the inner loop and $N_p << N_r$ we can approximate (55) by

$$G \tilde{-} \frac{B_I}{B_o}\sqrt{\frac{N_r B_o}{N_r B_I}} = \sqrt{\frac{B_I}{B_o}} \qquad (56)$$

We see that the gain ratio of the outer loop to the inner loop has to be adjusted according to the equivalent noise bandwidth used in the inner and outer loop respectively. The outer loop BW is unchangeable but the inner loop BW's are subject to selection by the operator and the outer loop gain has to be adjusted accordingly.

The outer loop gain settings for the different bandwidth settings in the inner loop are given in Appendix D.2.

C. THE AUTOMATIC GAIN CONTROL (AGC) LOOP AND ITS EFFECT ON THE SYSTEM S-CURVE

To avoid saturation of the IF amplifier stages in the reference and error channels and to be able to operate at constant total power in the receiver an AGC loop has been implemented.

Since we desire to receive all signal power in the reference channel the AGC detector has been built to act

on the reference channel total power only. The AGC loop controls both reference and error channel gain. A model of the AGC loop is shown in Figure 11, and its operation on reference and error channel is shown in principle in Figure 12.

Due to the high voltage levels at the input to the amplitude detector, realized by a simple diode followed by a lowpass filter, we are operating in the linear mode of the diode detector.

The output of the amplitude detector will be compared to a bias voltage b and the difference of the two voltages will be passed through the AGC amplifier/filter in the standard receiver system. The output of the AGC amplifier/filter is used to control the gain of the 50 MC mixer/amplifier in the receiver reference and error channel.

Consider the AGC loop as in Figure 11. Here F(s) is basically an imperfect integrator (AGC Amplifier/Filter) [16]. The input to the linear detector is Gaussian (signal and noise are assumed Gaussian). Davenport and Root [17, p. 269] show that for a zero mean Gaussian input process to a linear detector the dc output (expected value of the output) is

$$E[w(t)] = \frac{k\,\sigma_{r_1}}{\sqrt{2\pi}} \tag{57}$$

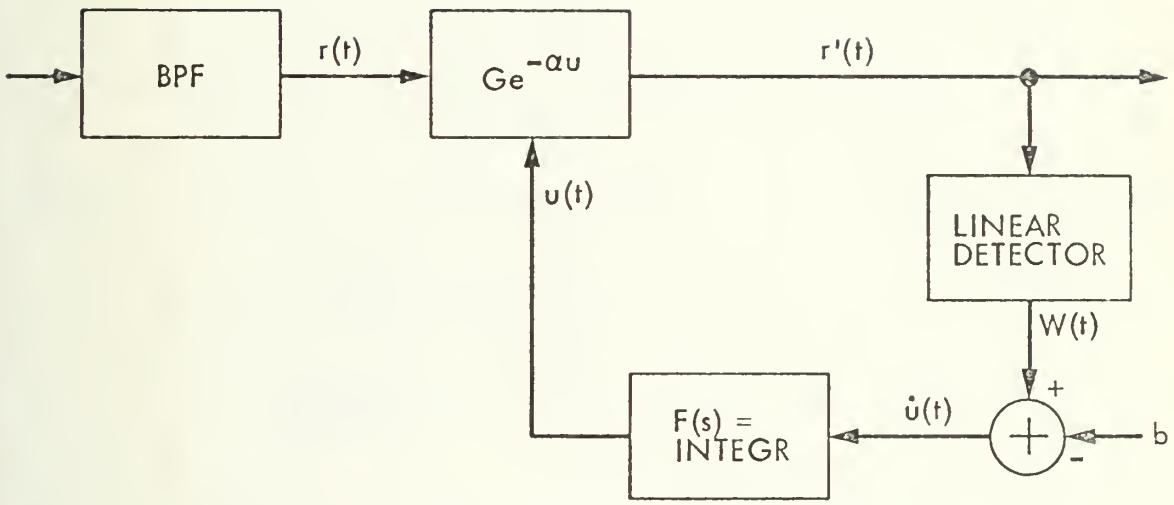

Figure 11 MODEL OF AGC LOOP

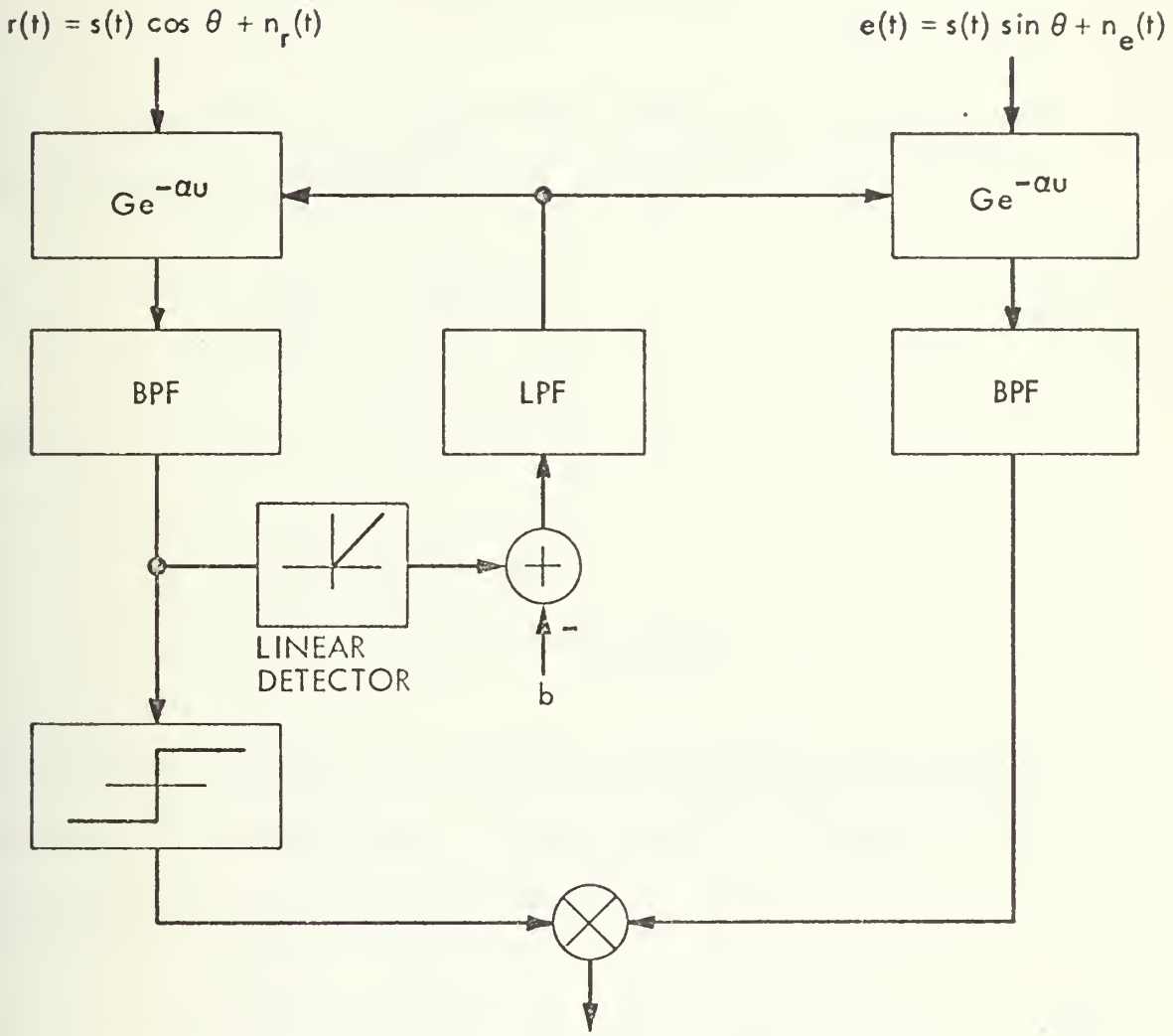

Figure 12 THE AGC LOOP FOR THE CORRELATION POLARIMETER (SIMPLIFIED)

where

$\sigma_{r_1}^2$ = variance of input process (assumed zero mean Gaussian)

k = gain of linear detector.

The voltage controlled amplifier characteristic is well approximated by [16,18]

$$g(u) = G\, e^{-\alpha u} \tag{58}$$

where

u = control voltage

G, α = parameters of amplifier.

Considering steady state (initial transients have died down) we can assume that u stabilized at a steady state value u_o and we are able to write

$$g(u_o) = G\, e^{-\alpha u_o} = G_o. \tag{59}$$

Therefore G_o is just a linear gain and we can express the output of the linear detector using (57) as

$$E[w(t)] = \frac{k\, G_o\, \sigma_r}{\sqrt{2\pi}}. \tag{60}$$

Realizing that

$$\sigma_{r_1}^2 = G_o^2 \sigma_r^2$$

$$= G_o^2(\sigma_s^2 \cos^2\theta + \sigma_{n_r}^2) \tag{61}$$

(neglecting any plarized noise) gives

$$E[w(t)] = \frac{k G_o \sqrt{\sigma_s^2 \cos^2\theta + \sigma_{n_r}^2}}{\sqrt{2\pi}} . \tag{62}$$

In steady state obviously

$$\dot{u}(t) = \frac{\partial u(t)}{\partial t} = 0 \tag{63}$$

which requires

$$b = E[w(t)]$$

$$= \frac{k G_o \sqrt{\sigma_s^2 \cos^2\theta + \sigma_{n_r}^2}}{\sqrt{2\pi}} \tag{64}$$

yielding

$$G_o = \frac{b\sqrt{2\pi}}{k\sqrt{\sigma_s^2 \cos^2\theta + \sigma_{n_r}^2}} \tag{65}$$

which is the steady state gain of the gain controlled amplifiers as shown in Figure 12 affecting the reference and error channels.

From Section IV.A. we know that the output of the correlator not considering the AGC loop is from (41)

$$E[v_i(t)/\theta] = \sqrt{\frac{2}{\pi}} \frac{E[x,y]}{\sigma_y} \tag{66}$$

where $E[x,y]$ and σ_y are as defined in equations (31) and (22) respectively. Neglecting the polarized noise we obtain

$$E[v_i(t)/\theta] = \sqrt{\frac{2}{\pi}} \frac{\sigma_{s_1}^2 \cos\theta \sin\theta}{(\sigma_{s_1}^2 \cos^2\theta + \sigma_{n_{r_1}}^2)^{1/2}} . \tag{67}$$

Realizing again that the AGC voltage controls the error channel gain in the same manner as in the reference channel but being derived from the reference channel signal and noise one can rewrite (66) in the following manner

$$E[v_{AGC}(t)/\theta] = \sqrt{\frac{2}{\pi}} \frac{E[x_{AGC}\, y_{AGC}]}{\sigma_{y_{AGC}}} \tag{68}$$

Where x_{AGC} and y_{AGC} are equivalent to x and y as defined in (34) respectively, but considering AGC mode operation. $v_{AGC}(t)$ is the output of the inner loop phase detector in AGC mode operation.

From (61) and (65) we have

$$\sigma_{y\ AGC}^2 = G_o^2\ \sigma_y^2$$

$$\sigma_{y\ AGC} = \frac{b\sqrt{2\pi}}{k} \cdot \tag{69}$$

Now calculate $E[x_{AGC}\ y_{AGC}]$. Obviously x_{AGC} is given by

$$x_{AGC} = G_o(s(t)\sin\theta + n_e(t))$$

$$= \frac{b\sqrt{2\pi}\ (s(t)\sin\theta + n_e(t))}{k\ (\sigma_s^2\ \cos^2\theta + \sigma_{n_r}^2)^{1/2}} \tag{70}$$

and similarly

$$y_{AGC} = \frac{b\sqrt{2\pi}\ (s(t)\cos\theta + n_r(t))}{k\ (\sigma_s^2\ \cos^2\theta + \sigma_{n_r}^2)^{1/2}} \cdot \tag{71}$$

Forming $E[x_{AGC}\ y_{AGC}]$ yields

$$E[x_{AGC}\ y_{AGC}] = \frac{b^2\ 2\pi\ \sigma_s^2\ \cos\theta\ \sin\theta}{k^2(\sigma_s^2\ \cos^2\theta + \sigma_{n_r}^2)} \cdot \tag{72}$$

Using (69) and (72) we obtain

$$E[v_{AGC}(t)/\theta] = \frac{2\ b}{k}\ \frac{\sigma_s^2\ \sin\theta\ \cos\theta}{\sigma_s^2\ \cos^2\theta + \sigma_{n_r}^2} \cdot \tag{73}$$

Rewriting we obtain

$$E[v_{AGC}(t)/\theta] = \frac{2\ b}{k}\ \frac{\tan\ \theta}{1 + \frac{1}{SNR_{REF}}} \tag{74}$$

where

SNR_{REF} = Signal-to-noise ratio of the reference channel at the input to the hard limiter and AGC detector.

For comparison the result obtained without considering the AGC loop ((67) rewritten) is given by

$$E[v(t)/\theta] = \sqrt{\frac{2}{\pi}}\ \frac{\sigma_s\ \sin\ \theta}{\sqrt{1 + \frac{1}{SNR_{REF}}}}\ . \tag{75}$$

During calibration of the system at $\theta = 45°$ the servo gain is set up to yield +3 volt error voltage at infinite SNR_{REF}. During the actual tracks the SNR will be decreasing as the signal ray path approaches the sun, resulting in a decrease in the system servo gain. This decrease is as seen from (74) and (75) stronger for the case using the AGC loop. In Figure 13 the SNR dependent gain factor for the correlator output

$$K = \frac{1}{1 + \frac{1}{SNR}} \tag{76}$$

is shown.

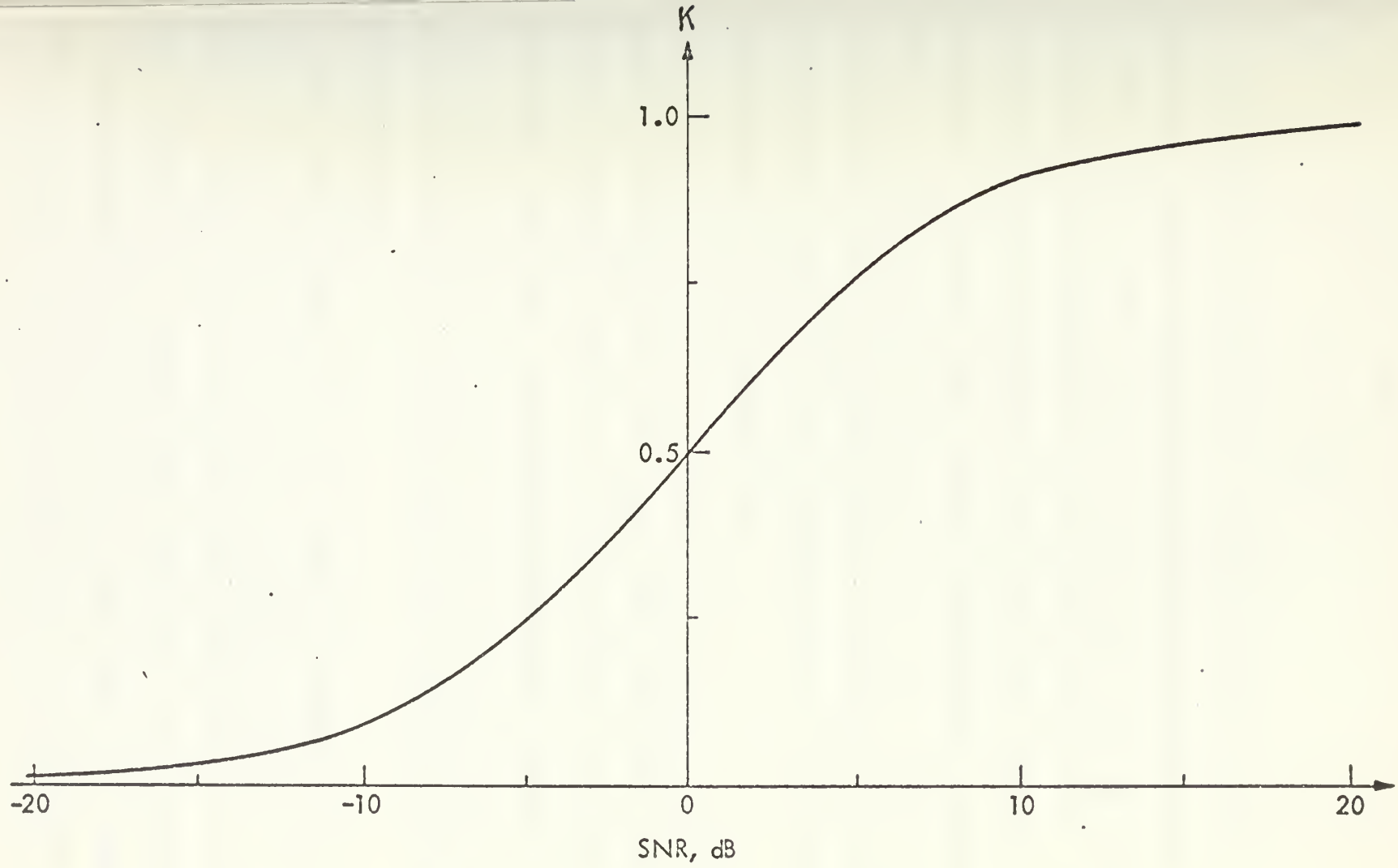

Figure 13 PLOT OF SNR DEPENDENT ERROR VOLTAGE GAIN FACTOR K

For low SNR (76) approaches

$$K \rightarrow SNR.$$

It should be noted that the gain decrease of the correlator output with decreasing SNR is equivalent to increasing the time constant in the servo loop and thereby increasing the integration time for the servo loop. This increase of the integration time will partly offset the increase of the rms angle tracking error which normally would be caused by the decrease of the SNR. The AGC loop is therefore not only advantageous in preventing saturation of amplifier stages but also offsets part of the performance degradation with decreasing SNR.

The effect of the AGC circuit on the outer loop is exactly the same as for the inner loop, since the gain controlled amplifier affects the signal before it is split into the inner and outer loop reference and error channel components. Also the gain ratio between the inner and outer loop output for cancelling the tracking offset due to polarized noise is unaffected.

The above assumed that the control voltage to the 50 MHz IF mixer amplifiers can be considered constant in steady state, allowing the gain of the mixer amplifier to be modeled as a constant G_o. Ohlson [18] showed that this assumption is valid when the inverse of the closed loop time constant of the AGC loop $1/\tau$ is much smaller than the bandwidth of

the fast varying component of the controlled wave form.

In our case the bandwidth of the reference channel signal plus noise is determined by the BPF's at 250 Hz center frequency, with 3 dB bandwidths selectable in 5 steps from 5 to 125 Hz. The closed loop time constant is determined by the AGC loop filter in the receiver, the 50 MHz mixer amplifier gain control characteristic, the gain of the linear detector and by the bias voltage [16,18].

The time constant of the AGC loop filter is adjustable to three different values of 340, 34 and 4 seconds. In conjunction with the correlation polarimeter the time constant of 340 or 34 sec. will be used. In addition the gain of the linear detector will be adjusted to be of the same value or less than the gain of the coherent AGC detector used in the receiver. Under these operating conditions the AGC loop time constant will not be less then 1.93 sec. [16] and the requirement for the assumption that we operate in steady state and can linearize the gain of the voltage controlled mixer amplifier

$$1/\tau \ll \text{BW of fast varying components in ref. channel}$$

is satisfied.

The AGC loop prevents saturation in the system and affects the gain of the correlators.

With decreasing SNR in the reference channel the gain of the correlator will also decrease, yielding a longer integration time in the servo loop and thereby offsetting some of the performance degradation due to the decreased SNR. It should also be noted that the decrease in the gain of the correlators at very low SNR is of such magnitude (see Figure 25) that for proper operation the servo gain has to be increased and thereby offsetting the advantage of automatically increasing the servo loop time constant.

D. THE RMS ANGLE TRACKING ERROR DUE TO NOISE

The general expression for the RMS angle tracking error for the correlation polarimeter due to noise considering the inner loop only using no hardlimiter in the reference channel has been derived by Ohlson and Zimmermann [11,9] and is given by

$$\sigma_\theta^2 = \frac{2 N_e W_s}{K^2} (2 N_r W_n + I) \tag{77}$$

where

N_e = one-sided noise spectral density in error channel

$$W_s = \frac{\int_0^\infty |F(f)|^2 \, df}{|F(0)|^2} \tag{78}$$

= single sided noise bandwidth of servo system

$F(f)$ = closed loop transfer function of servo loop

$$K = \int_{-\infty}^{\infty} H(f) \cdot S_s(f)\, df \tag{79}$$

$$H(f) = H_r(f)\, H_e^*(f)$$

where * indicates complex conjugate

$S_s(f)$ = signal power spectral density

N_r = noise spectral power density in reference channel

W_n = single sided noise BW of systems bandpass filters defined as

$$W_n = \frac{\int_0^{\infty} |H(f)|^2\, df}{|H(f_o)|^2} . \tag{80}$$

Assume $|H(f_o)|^2 = 1$, then

$$W_n = \int_0^{\infty} |H(f)|^2 df \tag{81}$$

$$I = \int_{-\infty}^{\infty} |H(f)|^2\, S_s(f)\, df. \tag{82}$$

1. RMS Angle Tracking Error Degradation due to Use of the Hard Limiter in the Reference Channel in the Inner Loop.

The servo loop is actually a third order system, but is very closely approximated by a second order system with the transfer function

$$F(s) = \frac{1}{1 + 2\xi s/\omega_o + s^2/\omega_o} \tag{83}$$

where

ξ = damping ratio

ω_o = natural frequency

and its low pass-single-sided noise bandwidth w_s is defined as in (78).

Following similar arguments as in the derivation of the system rms tracking error for the coherent polarimeter by Ohlson et. al. [5] we determined the system SNR at the output of the phase detector of the inner loop.

Elliptic and misalignment errors have little effect on the system rms tracking error and will be ignored [5]. The output of the phase detector, v(t) is representable in the form [5,9,11]

$$v(t) = S(\theta) + n'(t) \tag{84}$$

where

$$S(\theta) = E[v_i(t)/\theta].$$

Under the assumption that we track well we can approximate $S(\theta)$ by the slope of the error curve at $\theta = 0$ multiplied by the angle error θ

$$S(\theta)\Big|_{\theta \sim 0} \simeq \left.\frac{\partial E[v_i(t)/\theta]}{\partial \theta}\right|_{\theta=0} \cdot \theta \tag{85}$$

which can be written

$$S(\theta)\Big|_{\theta \to 0} = g_o\, \theta \tag{86}$$

so that

$$v(t)\Big|_{\substack{\text{Low}\\\text{Pass}}} = g_o\, \theta + n'(t)\ . \tag{87}$$

We now construct a similar model for the system noise as done by Ohlson et. al. [5]. The system noise model used is represented in Figure 14. The diagram represents (87) with an additional open loop gain G.

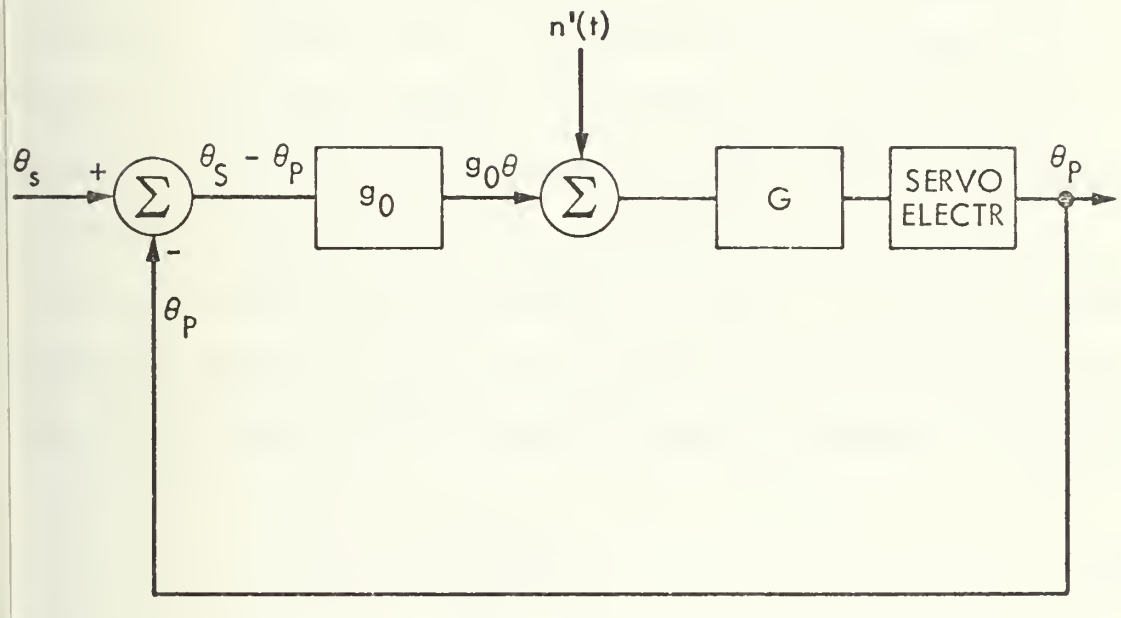

Figure 14 SYSTEM NOISE MODEL

θ_p is the polarizer angle

θ_s is the angle of polarization of the received signal.

The assumption $\sin\theta \simeq \theta$ is needed to make a linearized analysis possible.

To find the rms angle error we assume that θ_s = constant. We see that we can move the entry point of n'(t) back to the first summing node where the power spectral density of n'(t) is attenuated by $1/g_o^2$. The attenuated noise then is seen by a system with noise bandwidth W_s. Since the servo noise bandwidth is small, the noise power spectral density seen by the system is well expressed by the zero frequency noise power spectral density yielding

$$\sigma_\theta^2 = \frac{S_v(0)\ W_s}{g_o^2} \tag{88}$$

where

$S_v(0)$ = zero frequency input noise power spectral density to servo amplifier.

(88) is an equivalent form of σ_θ^2 as derived by Ohlson [11] and Zimmermann [9].

To calculate the effect on the rms error due to the addition of the hard limiter in the reference channel we only need to find the following ratio

$$\frac{\sigma_{\theta_M}^2}{\sigma_{\theta_{HL}}^2} = \frac{\dfrac{S_{V_M}(0)}{g_{o_M}^2}}{\dfrac{S_{V_{HL}}(0)}{g_{o_{HL}}^2}} \tag{89}$$

where

$\sigma_{\theta_M}^2$ = RMS angle error using no hard limiter

$\sigma_{\theta_{HL}}^2$ = RMS angle error using hard limiter in reference channel

$S_{V_H}(0)$ = zero frequency noise spectral density at input to servo loop using no hard limiter in the reference channel

$S_{V_{HL}}(0)$ = as above, but using hard limiter in reference channel

g_{o_H} = as defined in (86) using no hard limiter in reference channel

$g_{o_{HL}}$ = as defined in (86) using hard limiter in reference channel.

As seen from (89) we only need to find the zero frequency noise power spectral density at the output of the phase detector and the slope of the system S-curve at $\theta = 0$ for the determination of the performance degradation due to the use of the hard limiter.

The inner loop models used for the calculations are shown in Figures 15 and 16. The calculation is based on the assumption that the system is tracking well assuming $\theta \simeq 0$ and therefore $\cos\theta \simeq 1$, $\sin\theta \simeq \theta$. The effect of the linearly polarized noise on the rms angle error is assumed negligible due to the generally small amount of linearly polarized noise received.

$$\begin{aligned} r(t) &= s(t) + n_1(t) \\ e(t) &= n_2(t). \end{aligned} \tag{90}$$

$s(t)$, $n_1(t)$ and $n_2(t)$ are independent zero mean Gaussian processes, being the filtered versions of the received processes at the input to the hard limiter in the reference channel and to the phase detector in the error channel respectively. The autocorrelation functions are denoted $R_s(\tau)$, $R_{n_1}(\tau)$ and $R_{n_2}(\tau)$ respectively.

Due to the processes being uncorrelated we have

$$\begin{aligned} R_r(\tau) &= R_s(\tau) + R_{n_1}(\tau) \\ R_e(\tau) &= R_{n_2}(\tau) \end{aligned} \tag{91}$$

Now consider the version with the hard limiter in the reference channel. From Thomas [19 p. 284] we know that the

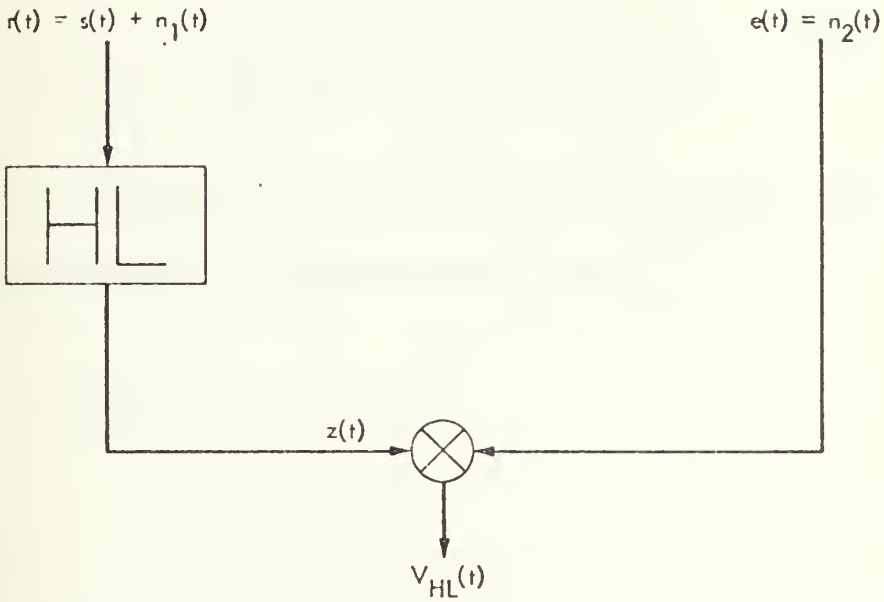

Figure 15 INNER LOOP MODEL WITH HARD LIMITER IN REFERENCE CHANNEL

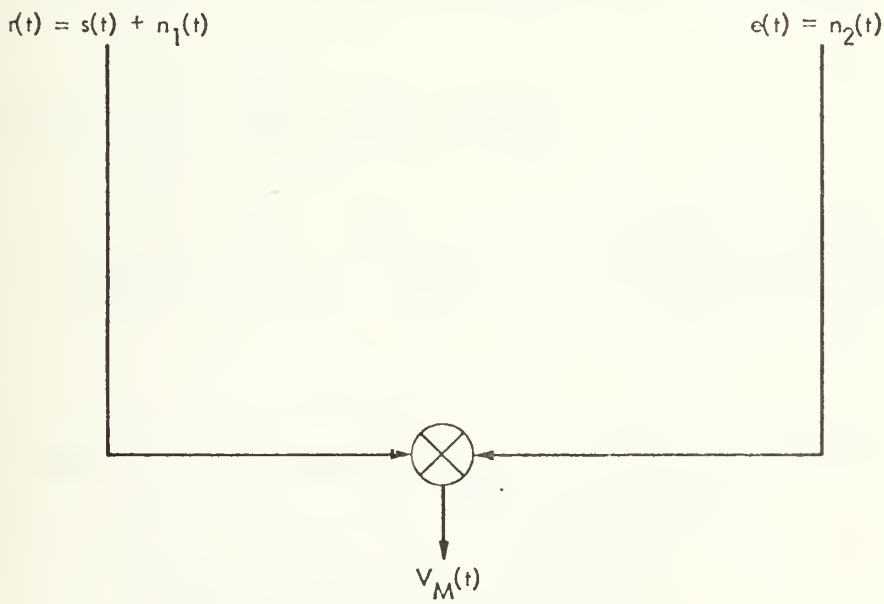

Figure 16 INNER LOOP MODEL WITHOUT HARD LIMITER

output autocorrelation function of the hard limiter is given by

$$R_z(\tau) = \frac{2}{\pi} \sin^{-1}\left\{\frac{R_s(\tau) + R_{n_1}(\tau)}{R_s(0) + R_{n_1}(0)}\right\} . \tag{92}$$

Since the processes are uncorrelated the output autocorrelation function of the correlator is

$$R_v(\tau) = R_{n_2}(\tau)\ R_z(\tau) \tag{93}$$

and

$$S_{V_{HL}}(0) = \int_{-\infty}^{\infty} R_v(\tau)d\tau = \int_{-\infty}^{\infty} R_{n_2}(\tau)\ R_z(\tau)d\tau \tag{94}$$

substituting $R_z(\tau)$ from (92) yields

$$S_{V_{HL}}(0) = \frac{2}{\pi} \int_{-\infty}^{\infty} R_{n_2}(\tau) \sin^{-1}\left\{\frac{R_s(\tau) + R_{n_1}(\tau)}{R_s(0) + R_{n_1}(0)}\right\}d\tau . \tag{95}$$

The next step is to evaluate $g_{o_{HL}}$. Here we need to consider

$$\begin{aligned} r(t) &= s(t) \cos\theta + n_1(t) \\ e(t) &= s(t) \sin\theta + n_2(t) \end{aligned} \tag{96}$$

where $s(t)$, $n_1(t)$, $n_2(t)$ are as defined above. Now

$$v_{HL}(t) = e(t) \text{ sgn } r(t) \tag{97}$$

and therefore

$$E[v_{HL}(t)/\theta] = \int_{-\infty}^{\infty}\int x(\text{sgn}y)\ f_{e,r}(x,y,\rho)\ dx\ dy \tag{98}$$

where

$f_{e,r}(x,y,\rho)$ = joint probability density function of $r(t)$ and $e(t)$.

Since $s(t)$, $n_1(t)$, $n_2(t)$ are independent zero mean Gaussian processes we can write

$$\begin{aligned} E[e(t)] &= 0 \\ \sigma_s^2 &= R_s(0) \\ \sigma_r^2 &= \sigma_s^2 \cos^2\theta + \sigma_1^2 \\ \sigma_e^2 &= \sigma_s^2 \sin\theta + \sigma_2^2 \end{aligned} \tag{99}$$

where

$$\begin{aligned} \sigma_1^2 &= E[n_1^2(t)] \\ \sigma_2^2 &= E[n_2^2(t)] \end{aligned} \tag{100}$$

$$\sigma_s^2 = E[s^2(t)].$$

We now go through calculations analogous to the derivation of the system S-curve for the inner loop but leaving out the polarized noise which is considered to be lumped into the noise $n_1(t)$ in the reference and $n_2(t)$ in the error channel respectively.

In addition we neglect the influence of the AGC loop, since it will have the same effect when using a hard limiter in the reference channel as when just using a pure multiplication scheme. We are only interested in the ratio of $\frac{J_{\theta_M}^2}{J_{\theta_{HL}}^2}$ so the effect of AGC cancels out. Keeping in mind that the process are zero mean Gaussian and calculating the joint Gaussian probability density function $f_{re}(x,y,\rho)$ one finds following the derivation in Section IV.A.

$$E[v_{HL}(t)/\theta] = \sqrt{\frac{2}{\pi}}\ \sigma_s \frac{\cos\theta \sin\theta}{\sqrt{\cos^2\theta + \frac{\sigma_1^2}{\sigma_s^2}}} \qquad (101)$$

and for tracking well we can linearize to

$$E[v_{HL}(t)/\theta]\Big|_{\theta\approx 0} = \sqrt{\frac{2}{\pi}} \frac{\sigma_s}{\sqrt{1 + \frac{\sigma_1^2}{\sigma_s^2}}}\ \theta\ . \qquad (102)$$

From (102) we easily obtain

$$g_{o_{HL}} = \left.\frac{\partial E[v_{HL}(t)/\theta]}{\partial \theta}\right|_{\theta=0} \tag{103}$$

$$= \sqrt{\frac{2}{\pi}} \frac{\sigma_s}{\sqrt{1 + \frac{\sigma_1^2}{\sigma_s^2}}} .$$

Now let us consider the case for the pure multiplier where r(t) and e(t) are directly fed to the correlator (Figure 14).

The system S-curve $S_M(\theta)$ is easily obtained

$$v_M(t) = [s(t) \cos \theta + n_1(t)][s(t) \sin \theta + n_2(t)]. \tag{104}$$

Keeping in mind that s(t), $n_1(t)$ and $n_2(t)$ are independent and therefore uncorrelated zero mean Gaussian random processes we obtain

$$E[v_M(t)/\theta] = R_s(0) \cos \theta \sin \theta. \tag{105}$$

When tracking well

$$\begin{aligned} &\theta \simeq 0 \\ &\cos \theta \simeq 1 \\ &\sin \theta \simeq \theta \\ &R_s(0) = \sigma_s^2 \end{aligned} \tag{106}$$

and we obtain

$$E[v_M(t)/\theta]\Big|_{\theta\to 0} = \sigma_s^2\,\theta \tag{107}$$

and

$$g_{o_M} = \left.\frac{\partial E[v_M(t)/\theta]}{\partial\theta}\right|_{\theta=0} = \sigma_s^2 \,. \tag{108}$$

Now calculate $S_{v_M}(0)$. First recall

$$S_{v_M}(0) = \int_{-\infty}^{\infty} R_{v_M}(\tau)\, d\tau \,. \tag{109}$$

Assuming that θ is small gives as for the case using the hard limiter in the reference channel

$$\begin{aligned} r(t) &= s(t) + n_1(t) \\ e(t) &= n_2(t) \end{aligned} \tag{90}$$

and

$$\begin{aligned} R_r(\tau) &= R_s(\tau) + R_{n_1}(\tau) \\ R_e(\tau) &= R_{n_2}(\tau) \end{aligned} \tag{91}$$

yielding

$$R_{v_M}(\tau) = R_r(\tau)\ R_e(\tau)$$

$$= (R_s(\tau) + R_{n_1}(\tau))\ R_{n_2}(\tau). \qquad (110)$$

Analogous to (93) we obtain

$$S_{v_M}(0) = \int_{-\infty}^{\infty} (R_s(\tau) + R_{n_1}(\tau))\ R_{n_2}(\tau)\ d\tau\ . \qquad (111)$$

Substituting (95), (103), (108) and (111) into (89) we obtain

$$\frac{\sigma_{\theta_M}^2}{\sigma_{\theta_{HL}}^2} = \frac{\frac{1}{\sigma_s^2}\int_{-\infty}^{\infty} R_{n_2}(\tau)[R_s(\tau) + R_{n_1}(\tau)]\ d\tau}{(1 + \frac{\sigma_1^2}{\sigma_s^2})\int_{-\infty}^{\infty} R_{n_2}(\tau)\ \sin^{-1}\{\frac{R_s(\tau) + R_{n_1}(\tau)}{R_s(0) + R_{n_1}(0)}\}\ d\tau} \qquad (112)$$

which simplifies to

$$\frac{\sigma_{\theta_M}^2}{\sigma_{\theta_{HL}}^2} = \frac{\int_{-\infty}^{\infty} R_{n_2}(\tau)\{\frac{R_s(\tau) + R_{n_1}(\tau)}{R_s(0) + R_{n_1}(0)}\}d\tau}{\int_{-\infty}^{\infty} R_{n_2}(\tau)\ \sin^{-1}\{\frac{R_s(\tau) + R_{n_1}(\tau)}{R_s(0) + R_{n_1}(0)}\}}\ . \qquad (113)$$

It is unfortunate that (113) is in general not solvable algebraically and numerical evaluation is necessary.

Under the assumption of high Q filtering preceeding the input to the hard limiter and correlator the auto-correlation functions are [10,17,19]

$$R_{n_2}(\tau) = r_2(\tau) \cos \omega_o \tau$$

and

$$\frac{R_s(\tau) + R_{n_1}(\tau)}{R_s(0) + R_{n_1}(0)} = r_1(\tau) \cos \omega_o \tau \qquad (114)$$

where

$$|r_1(\tau)| \leq 1.$$

The above requires symmetrical spectra about ω_o which is reasonable in most applications.

The difficult part is the evaluation of the term

$$\sin^{-1} \{r_1(\tau) \cos \omega_o \tau\}.$$

We are only interested in the output of the hard limiter at ω_o, the so called first zonal output for the active correlation in the phase detector.

Going through calculations similar to those of Springett and Simon [21] and finding a closed form we

obtain, analogous to Davenport and Root's (8-132)[17], for the first zonal output of the hard limiter

$$R_1(\tau) = \frac{8}{\pi^2}\left[\frac{E(r_1(\tau)) - (1 - r_1^2(\tau))\, K(r_1(\tau))}{r_1(\tau)}\right] \cos \omega_o \tau \quad (115)$$

where

$E(x)$ = complete elliptic integral of the second kind

$K(x)$ = complete elliptic integral of the first kind.

From (115) we also have

$$\sin^{-1}\{r_1(\tau)\cos\omega_o\tau\}\Big|_{\text{1st zone}} = \frac{4}{\pi}\left[\frac{E(r_1(\tau)) - (1-r_1^2(\tau))K(r_1(\tau))}{r_1(\tau)}\right]\cos\omega_o\tau. \quad (116)$$

Substituting (114) and (116) into (113), using only the first zone autocorrelation function we obtain

$$\frac{\sigma_{\theta_M}^2}{\sigma_{\theta_{HL}}^2} = \frac{\int_{-\infty}^{\infty} r_2(\tau)\, \cos^2(\omega_o\tau)\, r_1(\tau)\, d\tau}{\frac{4}{\pi}\int_{-\infty}^{\infty} r_2(\tau)\, \cos^2(\omega_o\tau)\left[\frac{E(r_1(\tau)) - (1-r_1^2(\tau))K(r_1(\tau))}{r_1(\tau)}\right] d\tau} \quad (117)$$

Since

$$\cos^2 x = \frac{1}{2} + \frac{1}{2}\cos 2x$$

and since we are only interested in the dc terms we can write

$$\frac{\sigma_{\theta_M}^2}{\sigma_{\theta_{HL}}^2} = \frac{\int_{-\infty}^{\infty} r_2(\tau)\, r_1(\tau)\, d\tau}{\frac{4}{\pi}\int_{-\infty}^{\infty} r_2(\tau)\left[\frac{E(r_1(\tau)) - (1 - r_1^2(\tau))K(r_1(\tau))}{r_1(\tau)}\right] d\tau} . \tag{118}$$

This represents the general expression for the performance degradation of the system due to the use of the hard limiter in the reference channel.

a. Algebraic Solution - Special Case 1

To get an algebraic answer to (118) we assume the following: The system is tracking well, only the reference channel receives a signal component ($\theta = 0$). The received linearly polarized noise is small and considered lumped into the respective total noise in the channels. Both channels are dominated by unpolarized noise and the spacecraft signal undergoes spectral broadening in the solar corona [6]. In addition we assume that the signal spectrum is approximately white over the BW of the filters preceeding the hard limiter and correlator.

Since the filtering in the correlation polarimeter is well approximated by a single tuned RC filter the autocorrelation functions at the output of these filters under the previously stated assumptions are well approximated by

$$R_o(\tau) = R_o(0)\ e^{-\alpha|\tau|}\cos\ \omega_o\tau \tag{119}$$

and therefore $r_2(\tau)$ and $r_1(\tau)$ become

$$\begin{aligned} r_2(\tau) &= R_o(0)\ e^{-\alpha|\tau|} \\ r_1(\tau) &= e^{-\alpha|\tau|} \end{aligned} \tag{120}$$

where $r_1(\tau)$ is the normalized input autocorrelation function to the hard limiter.

Substituting (120) into (118) we obtain, after simplification

$$\frac{\sigma_{\theta_M}^2}{\sigma_{\theta_{HL}}^2} = \frac{\pi}{4}\ \frac{\int_0^\infty e^{-\alpha\tau}\ d\tau}{\int_0^\infty \{E(e^{-\alpha\tau}) - (1 - e^{-2\alpha\tau})\ K(e^{-\alpha\tau})\}d\tau} \tag{121}$$

The integral in the numerator is readily evaluated to yield $1/2\alpha$. Call the integral in the denominator I and let $e^{-\alpha\tau} = x$, then I is

$$I = \frac{1}{\alpha}\int_0^1 \frac{E(x) - (1 - x^2)\ K(x)}{x}\ dx \tag{122}$$

which is readily found in Gradsteyn and Ryzhik [22, p. 627]

$$\begin{aligned} I &= \frac{1}{\alpha}\ [2E(1) - 2E(0) + K(0)] \\ &= (2 - \pi/2)\ \frac{1}{\alpha}\ . \end{aligned} \tag{123}$$

Substituting the above results into (121) we obtain

$$\frac{\sigma_{\theta_M}^2}{\sigma_{\theta_{HL}}^2} = \frac{\pi}{8(2 - \pi/2)} = -0.384 \text{ dB}. \tag{124}$$

b. Algebraic Solution - Special Case 2

Another algebraic solution for (113) is possible. Assume $n_2(t)$, $n_1(t)$ and $s(t)$ to be Gaussian sinusoids with autocorrelation functions

$$\begin{aligned} R_{n_2}(\tau) &= \sigma_{n_2}^2 \cos \omega_o \tau \\ R_{n_1}(\tau) &= \sigma_{n_1}^2 \cos \omega_o \tau \\ R_s(\tau) &= \sigma_s^2 \cos \omega_o \tau \end{aligned} \tag{125}$$

respectively.

From (113) substituting (125) one obtains after simplification

$$\frac{\sigma_{\theta_M}^2}{\sigma_{\theta_{HL}}^2} = \frac{\int_{-\infty}^{\infty} \cos^2 \omega_o \tau \, d\tau}{\int_{-\infty}^{\infty} \cos \omega_o \tau \sin^{-1}\{\cos \omega_o \tau\} \, d\tau} . \tag{126}$$

One immediately realizes that (126) is indeterminate. Therefore we have to write

$$\frac{\sigma_{\theta_M}^2}{\sigma_{\theta_{HL}}^2} = \frac{\lim_{T\to\infty} \int_{-T}^{T} \cos^2 \omega_o \tau \, d\tau}{\lim_{T\to\infty} \int_{-T}^{T} \cos \omega_o \tau \sin^{-1}\{\cos \omega_o \tau\} \, d\tau} . \qquad (127)$$

Considering the term $\sin^{-1}\{\cos \omega_o \tau\}$ in the integral of the denominator we find that

$$\sin^{-1}\{\cos \omega_o \tau\} = f(x) \qquad (128)$$

which describes a triangular wave with an amplitude of $\pi/2$. This triangular wave can be expressed by a Fourier series [20]

$$f(x) = \frac{4}{\pi} \sum_{n=1,3,5}^{\infty} \frac{(-1)^{(n-1)/2}}{n^2} \cos \omega_o n\tau. \qquad (129)$$

Since $R_{n_2}(\tau)$ is narrowband and we follow the output of the correlator by a low pass filter only the first harmonic affects the result and we can write

$$f(x)_{LP} = \frac{4}{\pi} \cos \omega_o \tau. \qquad (130)$$

This yields

$$\frac{\sigma_{\theta_M}^2}{\sigma_{\theta_{HL}}^2} = \frac{\lim_{T\to\infty} \int_{-T}^{T} \cos^2 \omega_o \tau \, d\tau}{\lim_{T\to\infty} \int_{-T}^{T} \cos \omega_o \tau \{\frac{4}{\pi} \cos \omega_o \tau\} d\tau} \qquad (131)$$

$$= \frac{\pi}{4} = -1.05 \text{ dB}. \qquad (132)$$

The results (132) and (124) for these special cases indicate that the performance degradation due to the use of the hard limiter in the reference channel is on the order of and likely below 1.05 dB. The degradation in performance can well be considered compensated for by the replacement of the pure multipliers with phase detectors having much smaller drift problems. The use of the phase detectors reduces the dc tracking offset drift considerably compared to the previously used multipliers as correlators [9].

2. The Influence of the Outer Loop on the RMS Angle Error

All calculations done for the inner loop apply with some additional considerations for the outer loop. The inner and the outer loop are only different in their pre-detection bandwidth. In addition the gain of the outer loop is different to the one in the inner loop. The gain factor is

$$G = (B_I/B_O)^{1/2}.$$

Since the phase detectors are followed by the same low pass filter beeing narrower in bandwidth than their pre-detection bandwidth the contribution of the outer loop is approximately

$$\sigma_{\theta_o}^2 = G^2 \sigma_\theta^2$$

where σ_θ^2 = rms angle tracking error due to the inner loop only.

For the present correlation polarimeter

$$G \leq 0.2$$

From the above discussion it is clear that the contribution of the outer loop on the rms angle tracking error is small and can be neglected for all practical purposes. In addition the outer loop will only be used when there is evidence of polarized noise being received, which will cause a tracking offset.

3. The AGC Loop and Its Effect on the RMS Angle Error

The system rms angle tracking error is basically a function of the signal to noise ratio. Under the assumption that the AGC loop does nothing else but keep the total power input to the correlation polarimeter constant, the AGC loop can be modeled as a linear gain in front of the correlation polarimeter. A linear gain does not change the SNR and therefore the influence on the system rms angle error is negligible, provided that the inverse time constant of the AGC loop is much smaller than the bandwidth of the fast varying signal component (see Ohlson [18]). In our case this condition is fulfilled as explained in Section IV.C.

E. THEORETICAL PERFORMANCE COMPARISON OF THE CORRELATION POLARIMETER AND THE COHERENT POLARIMETER

A comparison of the theoretical performance of the correlation polarimeter with the coherent polarimeter has been made by Ohlson [11] and Zimmerman [9].

A special case assuming real filter response and a filter gain of unity allows a comparison of the system rms angle tracking error, when neglecting the effect of the hard limiter in the reference channel. Zimmerman [9] and Ohlson [11] obtained for the correlation polarimeter

$$\sigma_\theta^2 = \frac{kT_e}{4P_s\tau} F_D \tag{133}$$

and for the coherent polarimeter

$$\sigma_\theta^2 = \frac{kT_e}{4P_s\tau} F_D' \tag{134}$$

where

$$F_D = 1 + \frac{k T_R W_n}{P_s} \tag{135}$$

= reference channel degradation factor of correlation polarimeter

$$F_D' = \left\{ \frac{I_o\left(\frac{2P_s}{k\,T_R\,W_n}\right)}{I_1\left(\frac{2P_s}{k\,T_R\,W_n}\right)} \right\}^{-2} \tag{136}$$

= reference channel degradation factor of coherent polarimeter

and in both cases a first order servo loop was assumed with a single-sided system noise bandwidth of

$$W_s = \int_0^\infty \frac{1}{1 + \omega^2\tau^2} \frac{d\omega}{2\pi} = \frac{1}{4\tau} \cdot \tag{137}$$

Also

k = Boltzmann's constant

T_e = error channel operating temperature

T_R = reference channel operating temperature

τ = time constant of servo loop

W_n = IF bandwidth of correlation polarimeter and loop bandwidth of coherent polarimeter at RF (i.e., twice lowpass noise bandwidth)

P_s = signal power

I_o, I_1 = Bessel functions of imaginary arguments.

In Figure 17, F_D and F_D' are plotted vs SNR in the reference channel. It has to be pointed out that the PLL of the coherent polarimeter does not stay in lock for SNR's below 0 dB. The curve for F_D' is therefore very optimistic at SNR's below 0 dB.

The performance degradation factor for the correlation polarimeter using the hard limiter in the reference channel has been estimated in Section IV.D.1 to be about 1 dB and is indicated by the dashed curve.

It should be noted that the theoretical correlation polarimeter performance at low SNR's is superior to the coherent polarimeter, even neglecting the loss of lock problem for the coherent polarimeter.

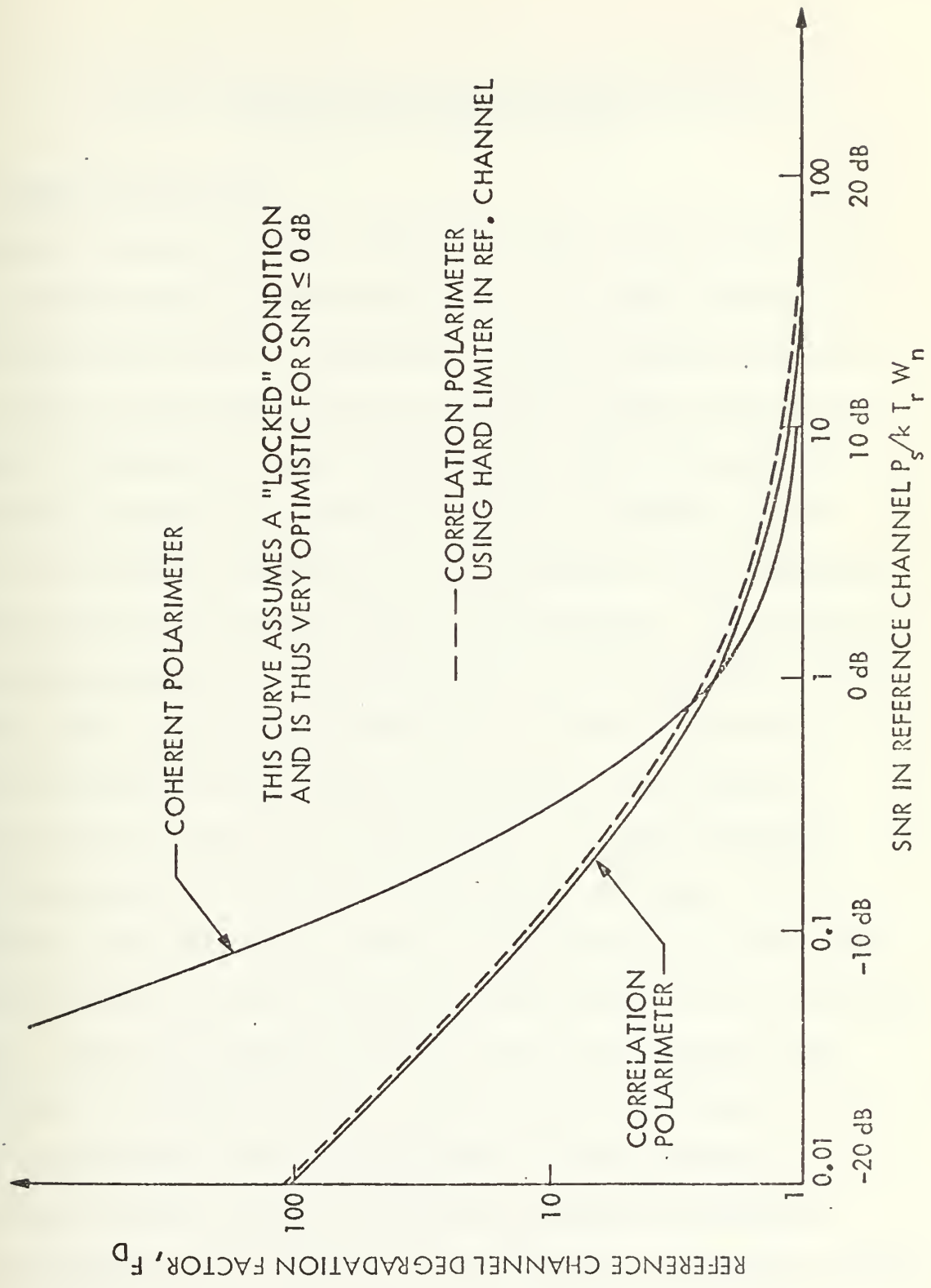

Figure 17 THE REFERENCE CHANNEL DEGRADATION FACTOR FOR THE CORRELATION AND COHERENT POLARIMETER

V. CORRELATION POLARIMETER FOR THE NASA/JPL - DEEP SPACE MARS STATION

A. SYSTEM DEVELOPMENT

After the idea of the system had been tested by the use of a working model by Zimmermann [9], the first version of the chassis was built. Zimmermann did some initial testing. Very soon it was found that the original design exhibited a number of problems. The main problems were an excessive crosstalk between the reference and error channels (less than 30 dB channel separation) and excessive drift problems in the analog multipliers used as correlators. To track out the varying doppler of the spacecraft an automatic frequency control (AFC) loop was implemented. It was impossible to obtain the desired performance of the AFC loop using an offset single tuned filter followed by a linear detector and bias circuit to derive the AFC error voltage. Due to the use of the selectable BPF's at the fourth I.F. the slope of the AFC curve changed with the switching of the selectable BPF's. The rest frequency for the loop also changed with selection of different BPF's. Due to these problems at low SNR's no frequency lock was possible. These problems resulted in major changes of the correlation polarimeter.

To eliminate the crosstalk the reference and error channel BPF's at the third IF were separated (previously on one circuit board). This did not result in satisfactory

reduction of the crosstalk levels. It was found that most of the crosstalk resulted from poor isolation of the power supplies between reference and error channel.

Phase detectors driven by hard limiters in the reference channel were used in place of the multipliers to overcome the dc drift problems. Even though the dc drift problems could be eliminated an increase in the reference to error channel crosstalk was observed.

The final solution to the crosstalk problem was a total separation (by filtering with pi networks) of the power supplies for the error and reference channel as well as for the hard limiters. The final crosstalk was measured to be -60 dB from error to reference channel and -54 dB from reference to error channel.

A solution for the problem with the AFC circuit was beyond practical limits. Due to the possibility of using a computer tuned synthesizer which could be programmed to follow the doppler characteristic of the spacecraft exactly, the AFC circuit was no longer needed. The doppler predictions for spacecrafts are accurate within less than 1 Hz at 2.3 GHz except for a possible offset and the slow spacecraft oscillator drift. With this change, the requirements for the installation of the correlation polarimeter in the NASA/JPL Deep Space Mars Station (DSS-14) also changed. The final installation is described in the following section.

B. SYSTEM DESCRIPTION

1. The Correlation Polarimeter Chassis

a. The Inner Loop

A functional block diagram of the correlation polarimeter is shown in Figure 18. The 9.995 MC L.O. as well as the -3 dB power splitter and the phase shifter on top of the page are external to the correlation polarimeter main chassis. The phase shifter is needed to phase up the reference and error channel signals at the IF frequency of 250 Hz.

The reference and error channel signals at 10 MC are mixed with the external L.O. to give an IF of 5 KC. The indicated lowpass filters at the output of mixers 2 and 3 are needed to block feedthrough of 10 MC and L.O. components and to properly terminate the mixer outputs for high frequency components. The signals at 5 KC are then amplified and passed through 250 Hz wide stagger tuned bandpass filters. In the following mixers A and B with the 4750 Hz L.O. the last IF of 250 Hz is generated. The signals are amplified and then passed through selectable bandpass filters. The bandwidth is selected fitting the spectral width of the signals as recorded with a spectrum analyzer. The output of the BPF's is fed through additional amplifier stages and a hard limiter in the reference channel to the phase detector of the inner loop which fulfills the function of the correlator. The output of the phase detector is low-pass filtered and fed to the servo amplifier in the correlation polarimeter.

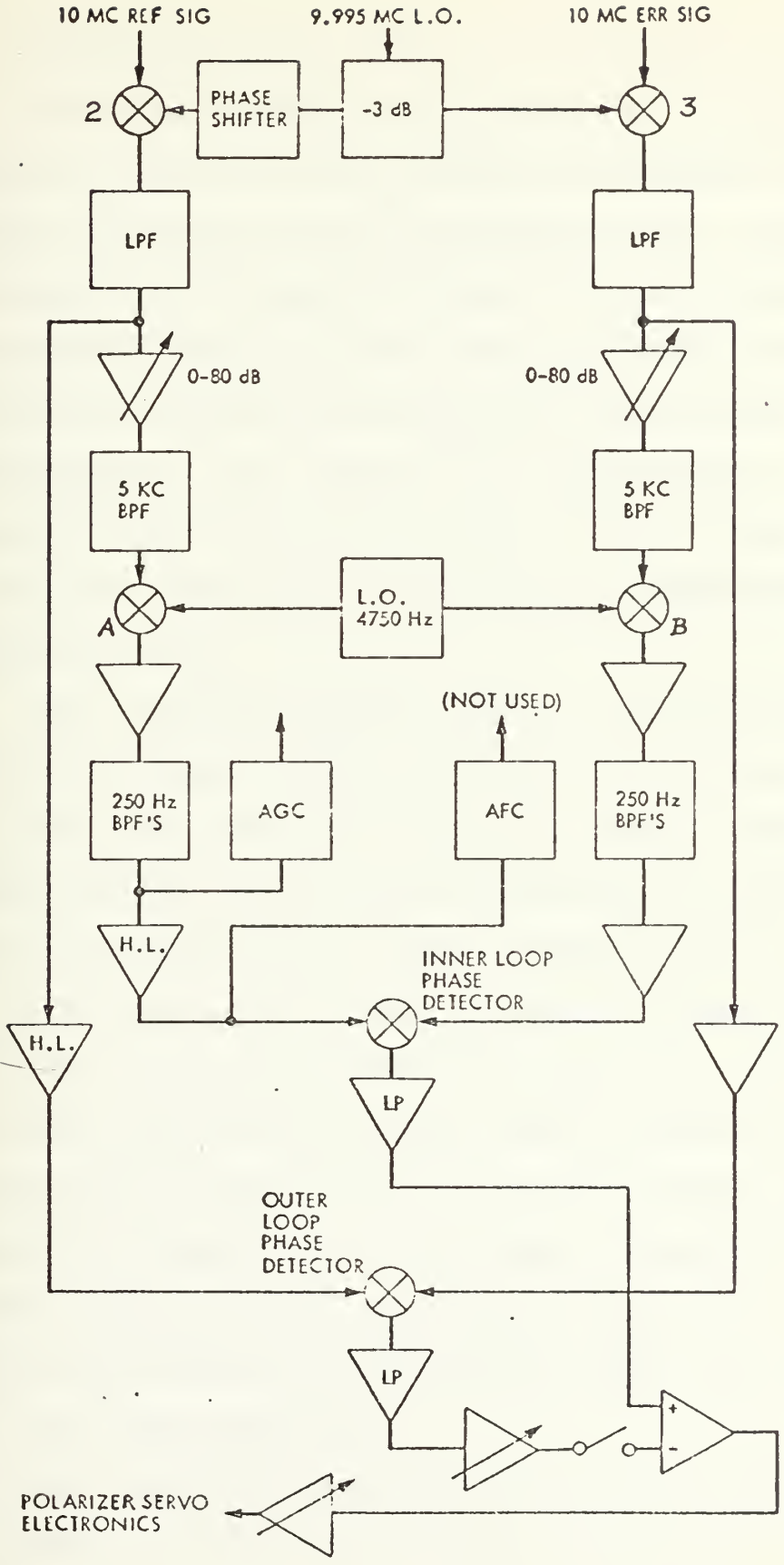

Figure 18 FUNCTIONAL BLOCK DIAGRAM OF THE CORRELATION POLARIMETER

b. The Outer Loop

The outer loop is, as described in Section IV.B.2, a wideband loop which is used to cancel out tracking bias effects due to received linearly polarized noise. Since there are basically no bandpass filters in the correlation polarimeter chassis for the outer loop, the bandwidth is determined by the bandwidth preceding the correlation polarimeter chassis. The reference and error signal of the outer loop are taken off from the output of the lowpass filters after the first mixers. The center frequency of these signals is 5 KC.

The reference channel signal is amplified and passed through the hard limiter, driving the reference for the outer loop phase detector. The error channel signal is amplified and then in the phase detector of the outer loop correlated against the reference channel signal. The output of the phase detector after lowpass filtering and adjustable gain is subtracted from the inner loop output if needed to cancel polarization offsets due to polarized noise. On the front panel a switch is located which connects the outer loop to the subtractor. To be able to counteract any dc drift problems in the outer loop dc amplifiers a dc zero offset potentiometer was installed on the front panel.

c. The Servo Amplifier

The output of the subtractor is fed to the servo amplifier where the servo error voltage is amplified to be equivalent to the servo error voltage of the coherent

polarimeter phase detector. This voltage is for an equivalent polarizer angle of 45° with respect to a test signal +3 volts. In addition, remaining dc offsets in the amplifiers can be balanced out by the use of a dc offset potentiometer on the front panel. The outer loop and the servo zero offsets are zeroed during the precalibration before each day's spacecraft track. The gain of the amplifiers is also set during precalibration.

d. The AGC Circuit

The AGC circuit has been designed to replace the normal AGC detector of the coherent polarimeter. The AGC circuit in the correlation polarimeter is only a part of the AGC loop of the receiver. The difference is in the fact that the correlation polarimeter AGC detector is working on the total power received and passed through the BPF's at the 250 Hz IF. The detector is realized by a simple diode detector followed by a lowpass filter. An amplifier with variable gain follows, allowing the adjustment of the correlation polarimeter dynamic AGC corresponding to dynamic AGC of the coherent phase detector used for the phase locked loop receivers at the Deep Space Network Mars Station.

e. The Automatic Frequency Control Circuit (AFC)

As already mentioned in Section V.A. the AFC circuit is no longer needed and is presently disabled. The problems encountered by using a single lowpass filter on its cutoff characteristic with a diode detector following have also been mentioned.

The combination of the different BPF characteristics at the 250 Hz IF and the lowpass characteristic of the AFC filter changes the rest point of the AFC output voltage and the slope of the AFC voltage curve resulting in frequency drift at low SNR's. This drift caused the fourth IF to drift out of the passband of the filters, and therefore making the correlation polarimeter inoperative. All these problems resulted in the decision to utilize an existing computer driven emphemeris tuned oscillator (ETO) [6] to generate a stable IF frequency.

2. The Correlation Polarimeter System at NASA/JPL Mars Station

The correlation polarimeter has been installed at the NASA/JPL Mars Station. It was desirable to use as many components of the existing receiver system as possible. In addition normal station operation could not be affected by the installed system. These requirements were met and the installation of the correlation polarimeter was done in April 1975.

In addition the two open loop receivers existing at the tracking station were modified and their 10 MC IF outputs connected to the computer software spectrum analyzer to allow determination of frequency offsets and observation of the spacecraft carrier spectrum. The ETO was connected to receiver 1 and the two open loop receivers to function as tuned local oscillator, tracking out the spacecraft doppler and thereby generating a frequency stable 50 MC first IF.

A simplified system configuration for the correlation polarimeter is shown in Figure 19. The reference and error channel signals as derived in the SPD cone polarizer assembly (see Section II.A) are amplified in the two S-band kryogenic masers in the antenna. The first IF of 50 MC is also generated in the structure beneath the cones in the antenna. The local oscillator utilized in the coherent mode is the receiver VCO incorporated in the receiver PLL. The VCO frequency is passed through a frequency multiplier chain (X 96) and then used in the S-band mixer to generate the first IF of 50 MC. The 50 MC IF is amplified and from the antenna through coaxial hardlines connected to the nearby control building. Here the remaining components of the receiver are located. For the correlation polarimeter the VCO is replaced by the emphemeris tuned oscillator (also called PLO for programmed local oscillator).

The 50 MC IF then is amplified by the gain controlled IF amplifier combined with the second mixer. The local oscillator frequency for the second mixer is 60 MC, derived from the station reference frequency of 10 MC. For the correlation polarimeter system these reference and error channel 10 MC IF's are split off the normal receiver IF amplifier chain, bandpass filtered and amplified and fed to the input of the correlation polarimeter. In the correlation polarimeter the 10 MC IF's are converted to the third IF of 5 KC center frequency.

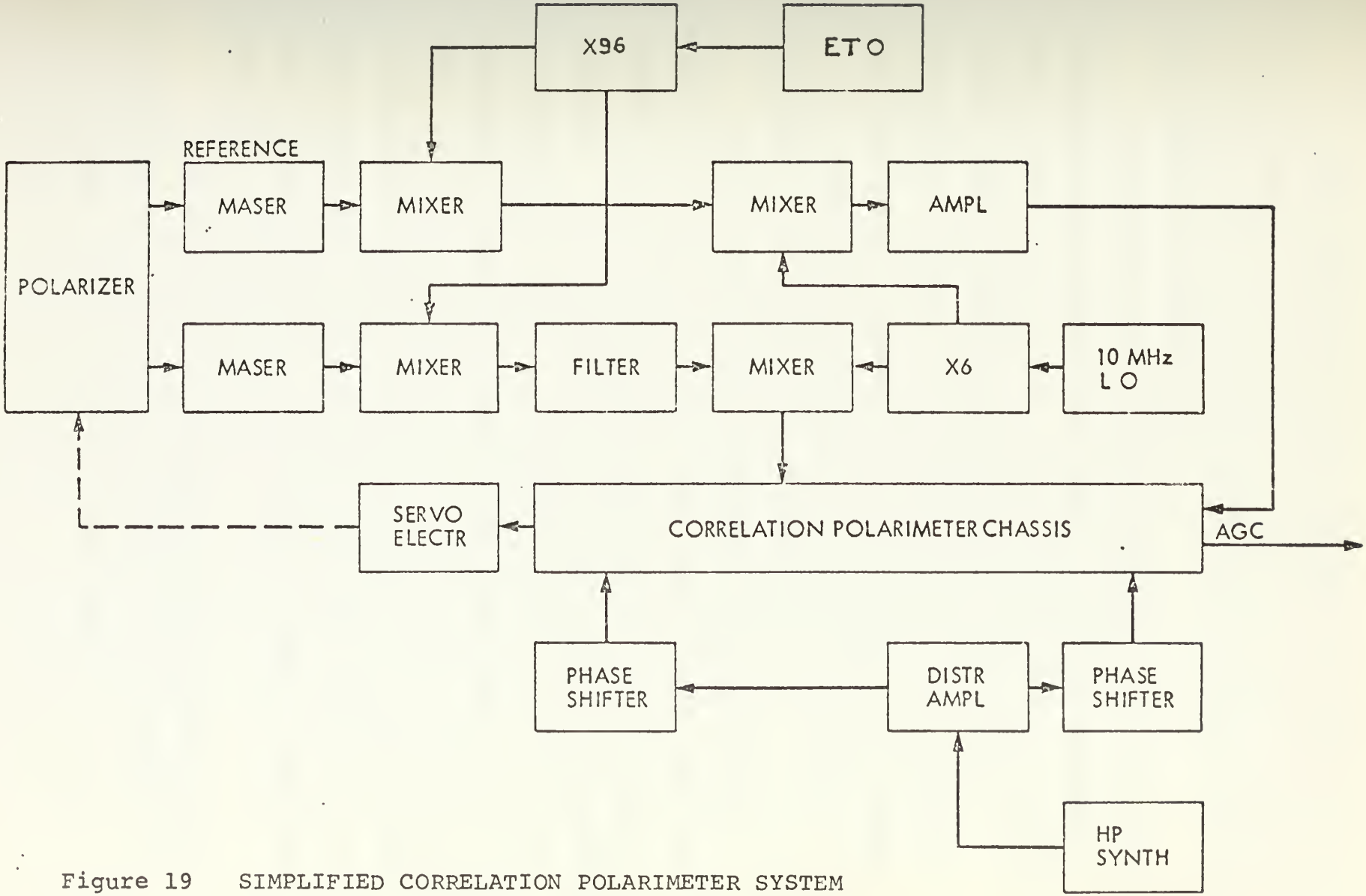

Figure 19 SIMPLIFIED CORRELATION POLARIMETER SYSTEM

After amplification and bandpass filtering the third IF is converted to the fourth IF of 250 Hz center frequency and finally the polarization servo error voltage is derived. (For details see Section V.A.)

The dynamic AGC voltage derived at the fourth IF in the correlation polarimeter chassis replaces the coherent dynamic AGC voltage and is fed to the receiver AGC amplifier filter, finally controlling the gain of the 50 MC IF amplifiers in front of the second mixers in the reference and error channel, respectively. The dynamic AGC voltage of the correlation polarimeter is adjusted to result in equivalent AGC voltage to the coherent AGC.

The external local oscillator set at 9.995 MC nominally for the correlation polarimeter mixes with the incoming 10 MC IF to generate the third IF of 5 KC center frequency. It is realized by a HP 5100 B frequency synthesizer. The synthesizer output is amplified, split and fed to the correlation polarimeter chassis, providing the L.O. for the reference channel mixer directly and through a phase shifter for the error channel. The phase shifter is used to obtain phase coherence of the reference and error channel to allow proper derivation of the servo error voltage at the inner and outer loop phase detectors.

The correlation polarimeter error voltage is fed to the polarizer electronics controlling the position of the half wave plate in the SPD cone assembly.

Figure 20 shows a block diagram of the system as it is installed in the staion control room. The implementation with the use of switch boxes, switching of normal receiver AGC to correlation polarimeter AGC operation, coherent to correlation polarimeter servo error voltage and selection of either VCO or ETO drive for the local oscillator multiplier chain resulted in the possibility of nearly instantaneous change between the coherent and correlation polarimeter configurations. In addition, by selecting different switch combinations the possibility of hybrid mode operation exists. For example, the servo error voltage or the dynamic AGC voltage can be derived from the correlation polarimeter while the receiver still uses the VCO and operates in a phase locked mode.

As soon as the ETO is selected the dynamic AGC and the servo error voltage must be derived in the correlation polarimeter since the normal receiver does not have the needed phased reference for the receiver AGC and servo detector.

The hybrid mode described above is therefore only of interest for testing purposes. During precalibration the correlation polarimeter AGC voltage is used and set to be equal to the normal receiver AGC voltage for equal input signal levels.

In addition to the equipment indicated in Figure 20, a low frequency spectrum analyzer HP 3580 A and a frequency counter HP 5302 A were installed in the control room near the correlation polarimeter chassis. See Figure 21.

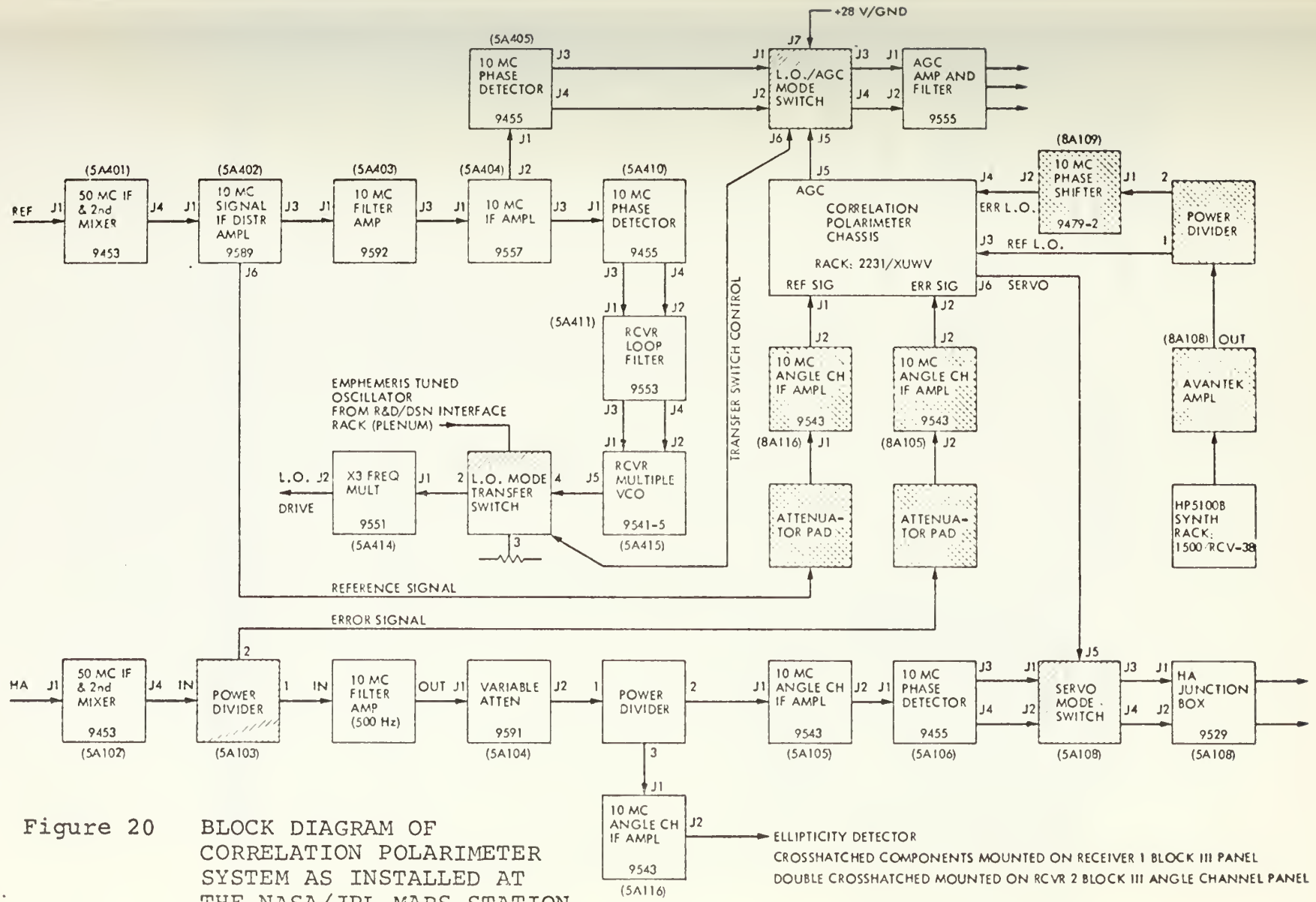

Figure 20 BLOCK DIAGRAM OF CORRELATION POLARIMETER SYSTEM AS INSTALLED AT THE NASA/JPL MARS STATION

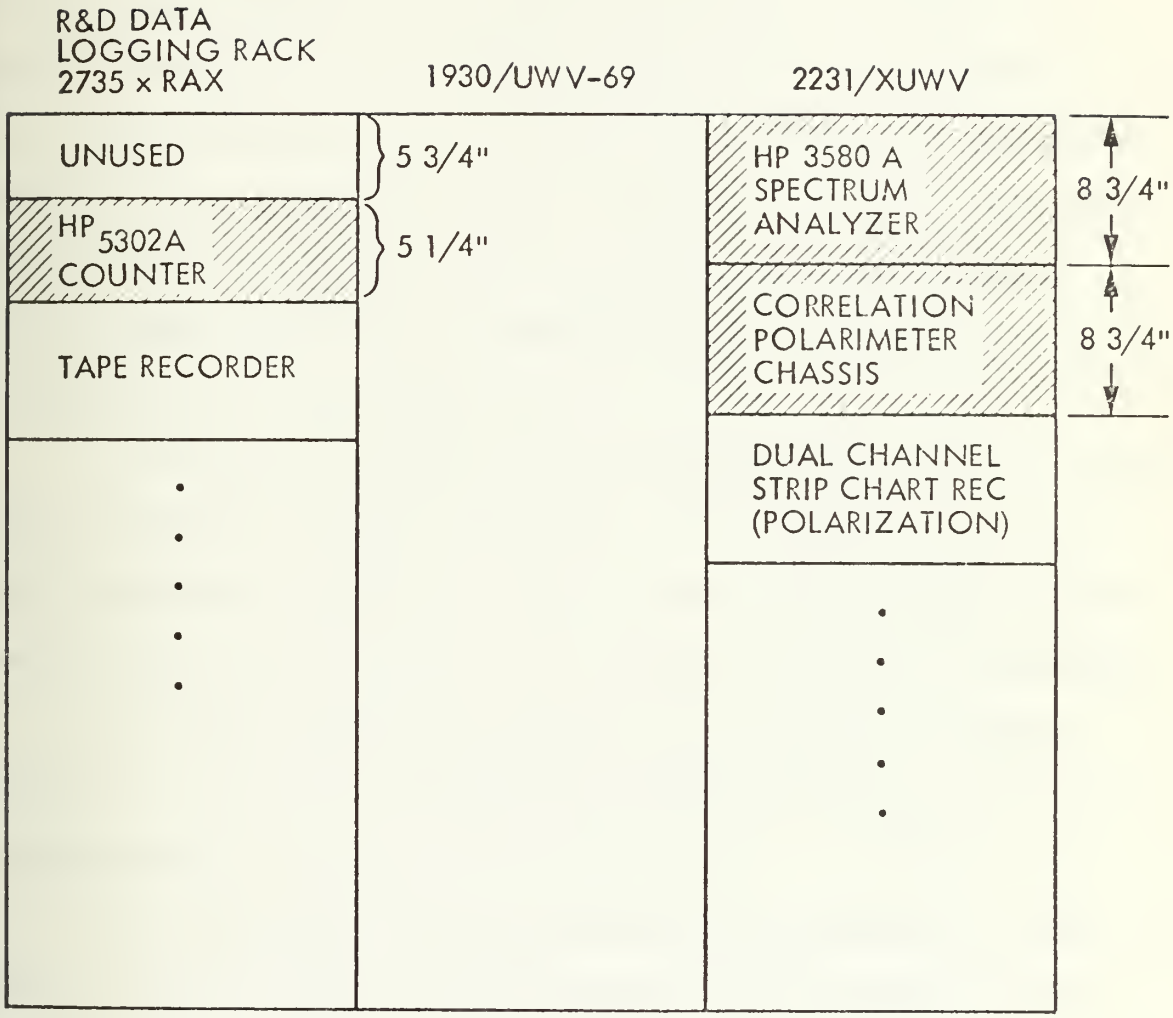

Figure 21 RACK LOCATION OF CORRELATION POLARIMETER CHASSIS AND ADDITIONAL INSTRUMENTATION

Figure 22 shows the correlation polarimeter and the spectrum analyzer as installed at NASA/JPL Mars Station.

The spectrum analyzer is used to insure that the reference and error channel signals at the inputs to the BPF's at the 250 Hz IF are actually centered at the 250 Hz IF. Small offsets can be corrected by selecting a slightly different L.O. frequency at the third L.O. driving the input mixers in the correlation polarimeter. Larger frequency offsets (over about 50 Hz) should be corrected by offsetting the emphemeris tuned oscillator.

The counter is only used to check the accuracy of the above described spectrum analyzer. It is connected to the sweep oscillator output of the spectrum analyzer and allows constant monitoring of the instantaneous frequency displayed.

For more detailed information on the correlation polarimeter including wiring and circuit diagrams refer to the appendices.

For frequency acquisition and determination of the spectral width of the received signal and to confirm that the polarizer is properly tracking the open loop receivers in conjunction with a two channel computer controlled spectrum analyzer were used. The basic description of this instrumentation follows.

3. The Open Loop Receivers and the Computer Software Spectrum Analyzer as Used in Connection with the Correlation Polarimeter

To determine the spacecraft frequency for proper ETO operation and to determine the spacecraft's spectral

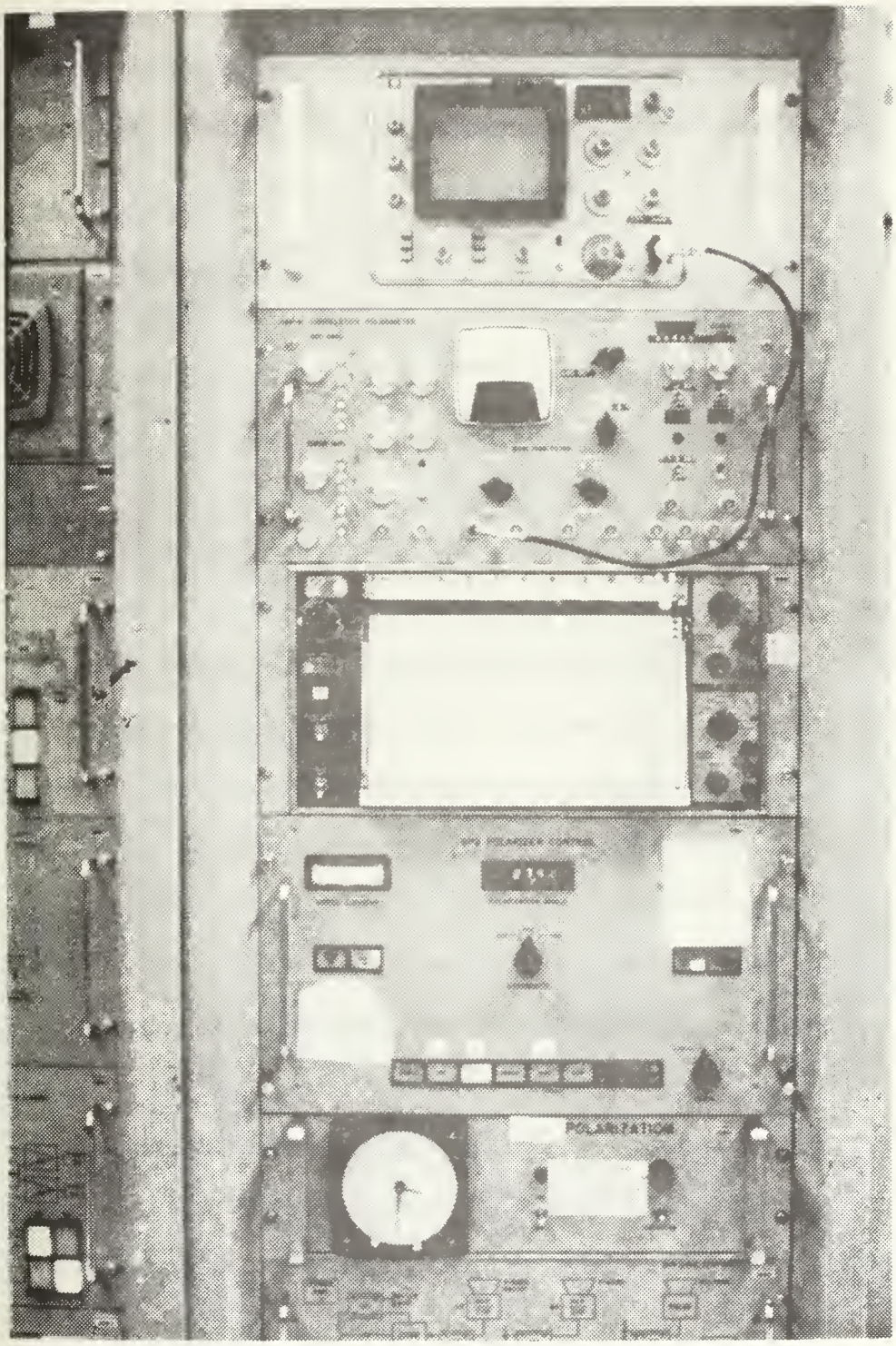

Figure 22 THE CORRELATION POLARIMETER AS INSTALLED AT THE NASA/JPL MARS STATION

characteristic for optimum operation of the correlation polarimeter the already existing open loop receivers and the computer software spectrum analyzer at the Mars Tracking Station were utilized. The correct frequency determination of the spacecraft signal is necessary to obtain an IF frequency within the pass band of the narrowest bandwidth used in the system. Even though there exist predicts which are based on doppler characteristics, a drift of the spacecraft oscillator, in particular of the Helios 1 spacecraft of about +16 Hz/day was observed. In the coherent mode of operation, meaning the spacecraft oscillator is locked to the uplink frequency, total offsets of less than ±10 Hz were observed. The determination of the signal spectrum is of importance too, since the selection of the proper bandwidth in the correlation polarimeter determines the performance characteristic. If a bandwidth wider than the signal spectrum is selected the SNR will be less than optimum. A selection of a bandwidth which does not pass all the signal power also results in less than optimum performance [11].

In addition by monitoring the spectrum of the reference and error channel simultaneously the proper operation of the polarizer can be checked. When the polarizer tracks well no signal component should be found in the error channel, provided no ellipticity component is generated in the solar corona. So far [1,6] including the first occultation of the Helios spacecraft no evidence of an ellipticity component has been found.

The open loop receivers are connected to the reference and error channel masers. The S-band inputs are mixed with the L.O. frequency provided by the ETO and the X 96 multiplier chains in the same way as for the regular receivers (block III).

The 50 MC IF is then amplified and amplitude adjusted in a manual gain control (MGC) mode and mixed with 60 MC to provide the 10 MC second IF. The 10 MC IF then is amplified and passes through coaxial hard lines connected to the input of the computer software spectrum analyzer, located in the pedestal control room of the antenna, here the spectrum is measured, averaged and displayed.

Due to the low SNR encountered during solar occultations and the spectral broadening effects in the solar corona an averaging of 1 to 2 minutes per displayed set of spectra (reference and error channel) had to be used. Even during the periods of high SNR's the spectra have to be taken using the open loop receivers with the ETO providing the L.O. drive since the phase-locked-loop receivers would track out most of the phase modulation, causing part of the spectral broadening.

Also an AGC mode operation would result in partially tracking out of the varying amplitude components in the spectrum.

The additional work needed to modify and set up this equipment contributed significantly to the successful

operation of the correlation polarimeter at the NASA/JPL Mars Station. A block diagram of the open loop receiver configuration is shown in Figure 23. For simplicity only one frequency multiplier chain is shown, but each channel has its own frequency multiplier chain driven by the same emphemeris tuned oscillator.

C. SYSTEM PERFORMANCE TESTS

The correlation polarimeter chassis has been laboratory tested and after the installation at the NASA/JPL Deep Space Network Mars Station (DSS-14) high noise tests were performed. In particular, polarization acquisition and tracking test comparisons were made to the regular coherent polarimeter. All tests were successful and indicated a clear polarization tracking improvement. More detailed information will be given in the next subsections.

1. Laboratory Test Results

The laboratory tests mainly were performed to test every single circuit with respect to its performance, to determine saturation levels, and test the overall performance of the correlation polarimeter chassis in open loop fashion. The noise bandwidth of the BPF needed for calculation of the gain factor for the outer loop were determined. The change of the slope of the system S-curve with decreasing SNR was measured and agreement with the theory was found.

During testing no Gaussian signal was available. The use of a sinusoidal signal with added noise generated by noise diodes had to be used.

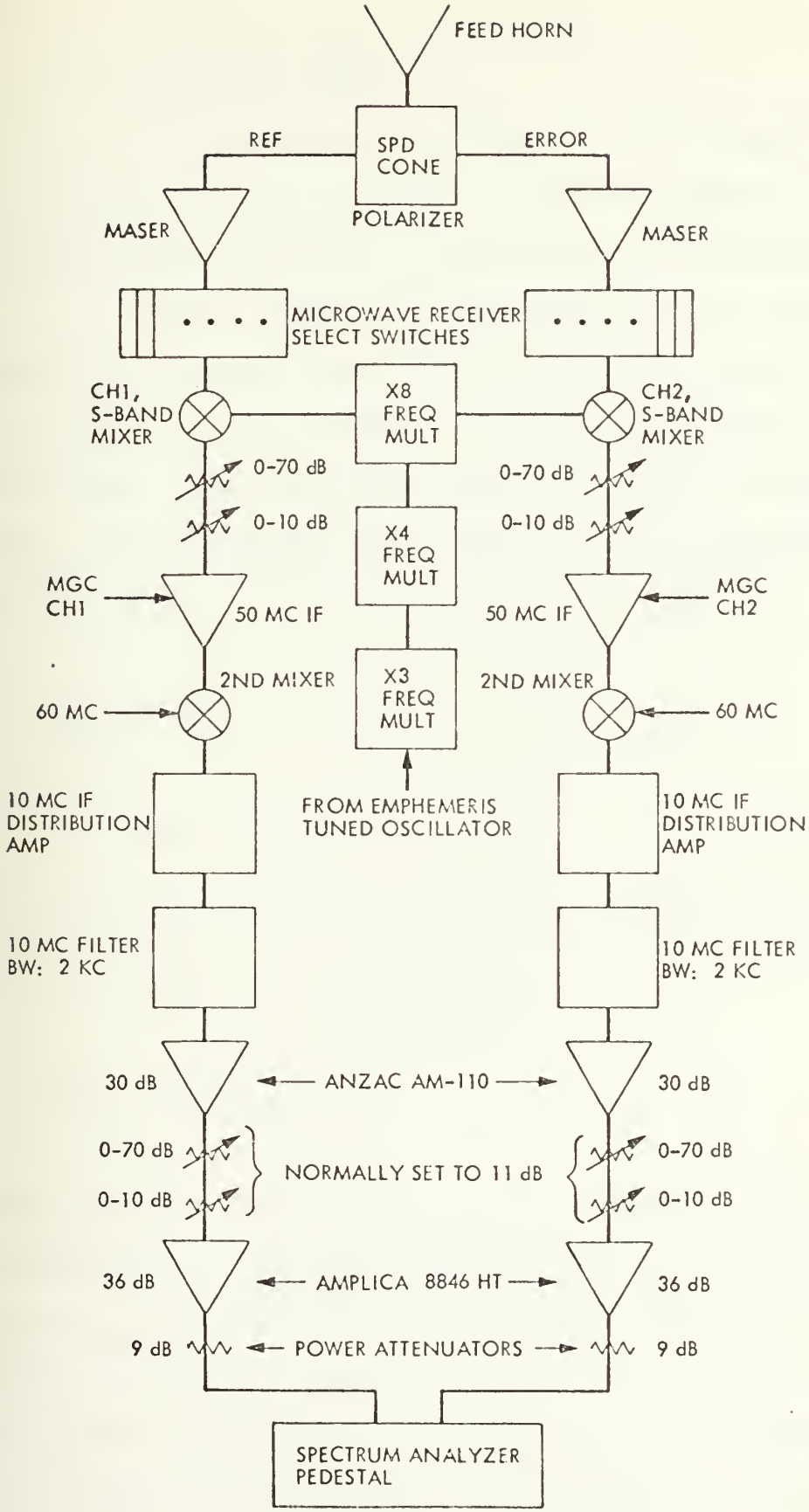

Figure 23 BLOCK DIAGRAM OF OPEN LOOP RECEIVER CONFIGURATION

a. Sinusoidal Test Signal Plus Noise in the AGC Loop

Let us explore the effect of the sinusoidal signal on the AGC circuit first. Figure 24 shows a model of the AGC loop as used for the following calculations.

The AGC circuit is operating with a linear detector and therefore the statement that it keeps the total power constant is not correct if a sinusoidal signal plus noise is used. The linear detector will keep the envelope constant. In particular the output of a linear detector driven by a constant envelope sinusoidal signal is

$$V_{AV_S} = k\sqrt{2}\quad \sigma_s \tag{138}$$

where k = gain of linear detector

and if driven by noise alone as given by Davenport and Root [17, p. 269]

$$V_{AV_N} = k\sqrt{\frac{\pi}{2}}\quad \sigma_n \quad . \tag{139}$$

Assuming that the AGC loop was calibrated with a strong sinusoidal signal (essentially infinite SNR) to give a power level of P_{cal} at the input to the linear detector, then at low SNR's we obtain a different power level because the statistics of the input are different. The AGC loop will keep the value of the average envelope constant and therefore

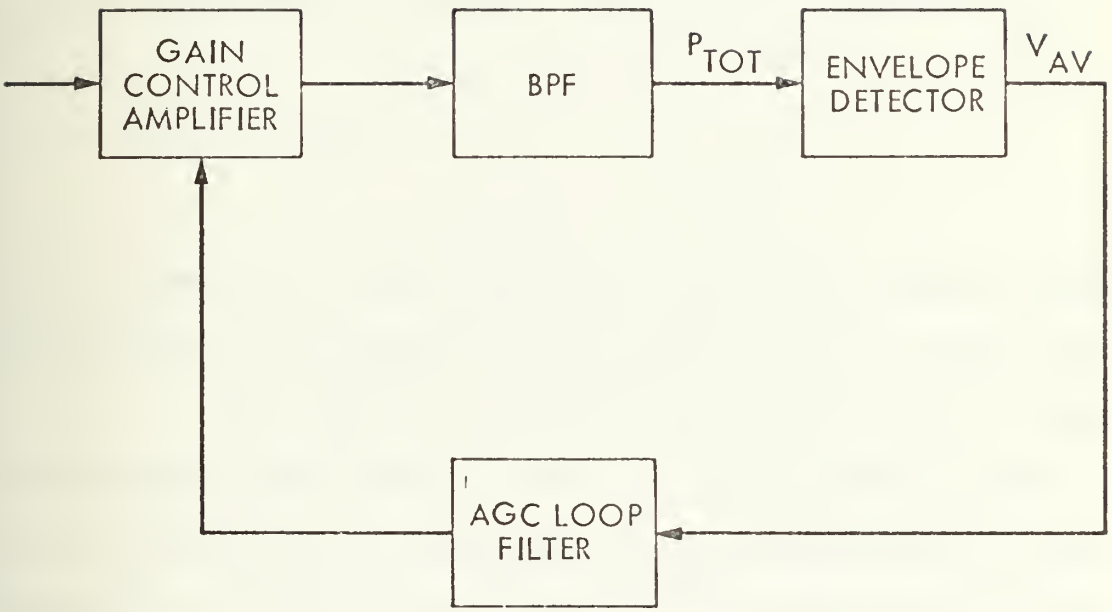

Figure 24 AGC LOOP MODEL FOR CALCULATION OF SINUSOIDAL SIGNAL PLUS NOISE INPUTS FOR TEST PURPOSES

using (138) and (139) we obtain for the limit of very low SNR operation

$$2\,P_{cal} = \frac{\pi}{2}\,\sigma_n^{\,2}$$

$$\sigma_n^{\,2} = \frac{4}{\pi}\,P_{cal} = P_{TOT} \tag{140}$$

This indicates that in the low SNR condition the total power P_{TOT} at the input to the AGC detector is increased by

$$\frac{4}{\pi} = 1.05 \text{ dB}$$

This increase has been observed during tests and has been considered in the signal level calculations for high noise.

The derived change of the total power in the correlation polarimeter of about 1 dB depending on the input SNR has been disregarded in the measurement of the dependence of the system S-curve on the input SNR to the phase detector board of the inner loop.

b. The System S-Curve Dependence on the SNR

The change of the system S-curve with varying SNR was explored. Again a sinusoidal test signal with added noise was used. The AGC action was simulated by keeping the AGC detector voltage constant while changing the SNR at the output of the BPF's at the 250 Hz IF.

The system calibration normally takes place at an equivalent polarizer angle of 45° with respect to the incoming

test signal, yielding a servo error voltage of +3 volts. For this reason the test was conducted injecting equal signals into error and reference channel and adding independent noise. Polarized noise could not be realistically simulated in the laboratory and its effect on the system S-curve could not be laboratory tested.

Neglecting the 1 dB increase in total power due to the AGC action on sinusoidal signal plus noise, and assuming that the AGC keeps the total power constant we have the following signals components in the reference and error channel, respectively

$$r(t) = k' \frac{s(t) \cos \theta}{\sqrt{\sigma_s^2 \cos^2 \theta + \sigma_{n_r}^2}} \tag{141}$$

$$e(t) = k' \frac{s(t) \sin \theta}{\sqrt{\sigma_s^2 \cos^2 \theta + \sigma_{n_r}^2}}$$

where

$$\frac{k'}{\sqrt{\sigma_s^2 \cos^2 \theta + \sigma_{n_r}^2}}$$

is the term resulting from the AGC action.

Due to the hard limiter the amplitude information in the reference channel is lost. Using the result for the output of a hard limiter from Viterbi [10, pp. 40-42], we obtain at the output of the hard limiter

$$z(t) = \frac{s(t)}{\sqrt{1 + 1/\mu \, SNR_{IN} \cos^2\theta}} \tag{142}$$

with $\frac{\pi}{4} < \mu < 2$ and $\mu = \frac{\pi}{4}$ for low SNR

$\mu = 2$ for high SNR

and $SNR_{REF} = SNR_{IN}\cos^2\theta$ is the SNR in the reference channel at the equivalent polarizer angle. SNR_{IN} is defined as the SNR in the reference channel at $\theta = 0°$.

The servo dc output voltage is calculated to be

$$E[v(t)/\theta] = \frac{k' \, \sigma_s^2 \sin\theta}{\sqrt{1 + 1/\mu \, SNR \cos^2\theta}\sqrt{\sigma_s^2\cos^2\theta + \sigma_{n_r}^2}}$$

$$= \frac{K \tan\theta}{\sqrt{1 + 1/\mu \, SNR \cos^2\theta}\sqrt{1 + \frac{1}{SNR \cos^2\theta}}} \tag{143}$$

where $K = k'\sigma_s$ and during precalibration it is set to

$$K = +3 \text{ V at } \theta = 45°$$

for very high SNR (test signal).

The theoretical curve for different SNR's for this point ($\theta = 45°$, $K = +3$ V in (143)) was calculated using (143). With the aid of an Kronhite low pass filter the servo error voltage was taken for different SNR's using the 125 Hz and the 5 Hz wide BPF's. Essential agreement with the theoretical curve was found. The result is plotted in Figure 25.

Since $\dfrac{1}{SNR_{IN}\cos^2\theta}$ at $\theta = 45°$ is 3 dB larger than at $\theta = 0°$, we have the following approximate relation between the value of the error curve at $\theta = 45°$ and the slope at $\theta = 0°$ neglecting the factor μ.

$$S(45°) = \frac{K}{1 + \dfrac{2}{SNR_{IN}}} \tag{144}$$

and

$$\left.\frac{\partial S(\theta)}{\partial \theta}\right|_{\theta=0} \approx \left.\frac{K}{(1 + \dfrac{1}{SNR_{IN}})\cos^2\theta}\right|_{\theta=0} = \frac{K}{1 + \dfrac{1}{SNR_{IN}}} . \tag{145}$$

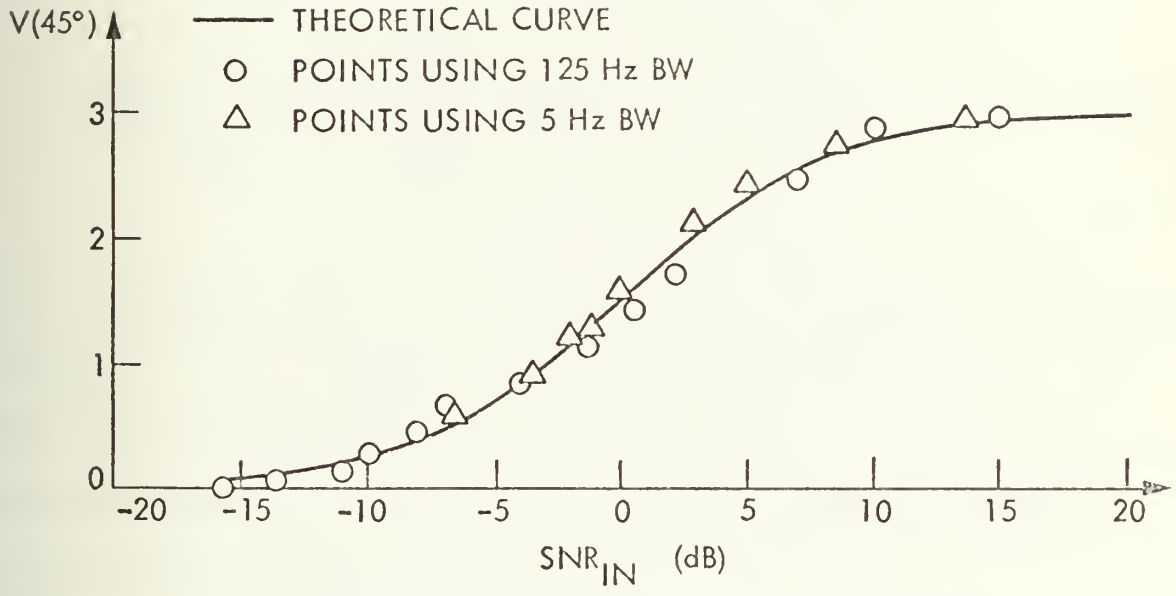

Figure 25 PLOT OF SERVO ERROR VOLTAGE AT $\theta = 45°$ VS SNR_{IN}

And we can form

$$\frac{\left.\frac{\partial S(\theta)}{\partial \theta}\right|_{\theta=0}}{S(45°)} \approx \frac{1 + \frac{2}{SNR_{IN}}}{1 + \frac{1}{SNR_{IN}}}$$

yielding

$$\left.\frac{\partial S(\theta)}{\partial \theta}\right|_{\theta=0} \approx \frac{1 + \frac{2}{SNR}}{1 + \frac{1}{SNR}} S(45°) . \qquad (146)$$

This indicates that for very low SNR's the slope of the error curve at $\theta = 0°$ is about 3 dB larger than at $\theta = 45°$. We are mainly interested in the slope of the error curve for polarization error angles near 0° (the trackpoint should be at an error angle of 0°).

As a result of the decrease in the error voltage with decreasing SNR the servo gain was set to have a gain margin of about 9. In addition additional R-C filtering was provided (switches on front panel) to insure that at high servo gain setting no saturation due to noise would occur.

c. Additional Laboratory Test Results

Besides the test described in the previous section other measurements on the correlation polarimeter were made. The 3 dB as well as the equivalent noise

bandwidth as needed for the calculation of the gain factor

$$G = (B_I/B_o)^{1/2}$$

were made. The results are given in Table 5 (Appendix B.1.).

The cross talk levels at the input to the phase detector board of the inner loop were measured.

The channel separation was found to be -54 dB from reference to error channel and -60 dB from error to reference channel respectively.

Tests over long periods of time and transients in the power supply revealed an instability of the outer loop phase detector, leading to the use of a different phase detector circuit, which eliminated the instability.

First laboratory tests with added noise indicated a dc offset at the output of the inner loop phase detector. The problem was traced to overloading of the hard limiter circuit by the phase detector. As a result a transistor driver after the hard limiter was introduced and its bias resistors were adjusted to give no dc offsets under any noise condition.

The saturation levels in the stages of the reference and error channels in the correlation polarimeter were determined and as a result the final calculation of the levels was performed for test signal and high noise operation. The final level settings as well as the saturation levels and other laboratory test results are given in Appendix B.

The gains were set up according to the test signal level calculation and then the high noise case was simulated. The measurement of the levels under high noise conditions agreed within ±10% of the calculated levels.

The bandwidths of all amplifiers were determined to be much wider than the filter BW's used. Therefore the filtering in the correlation polarimeter is solely determined by the bandpass filters.

2. High Noise Test Results at the NASA/JPL Deep Space Network Mars Station

The correlation polarimeter was installed at the NASA/JPL Mars Station on April 6 and 7, 1975. The signal levels were adjusted according to the calculations based on the saturation levels and bandwidths of the components used. The open loop receivers were connected to the computer software spectrum analyzer in the pedestal and the signal levels were set accordingly.

After the installation of the above system tests were done to verify the predicted operational advantage of the correlation polarimeter over the coherent polarimeter. After verification of proper operation of the correlation polarimeter a servo error voltage curve without noise (servo voltage vs polarization error angle) of the correlation polarimeter and of the coherent polarimeter was taken. These curves are given in Figure 26. It will be noted that the curve for both polarimeters is the same for the region of 45° to 150°.

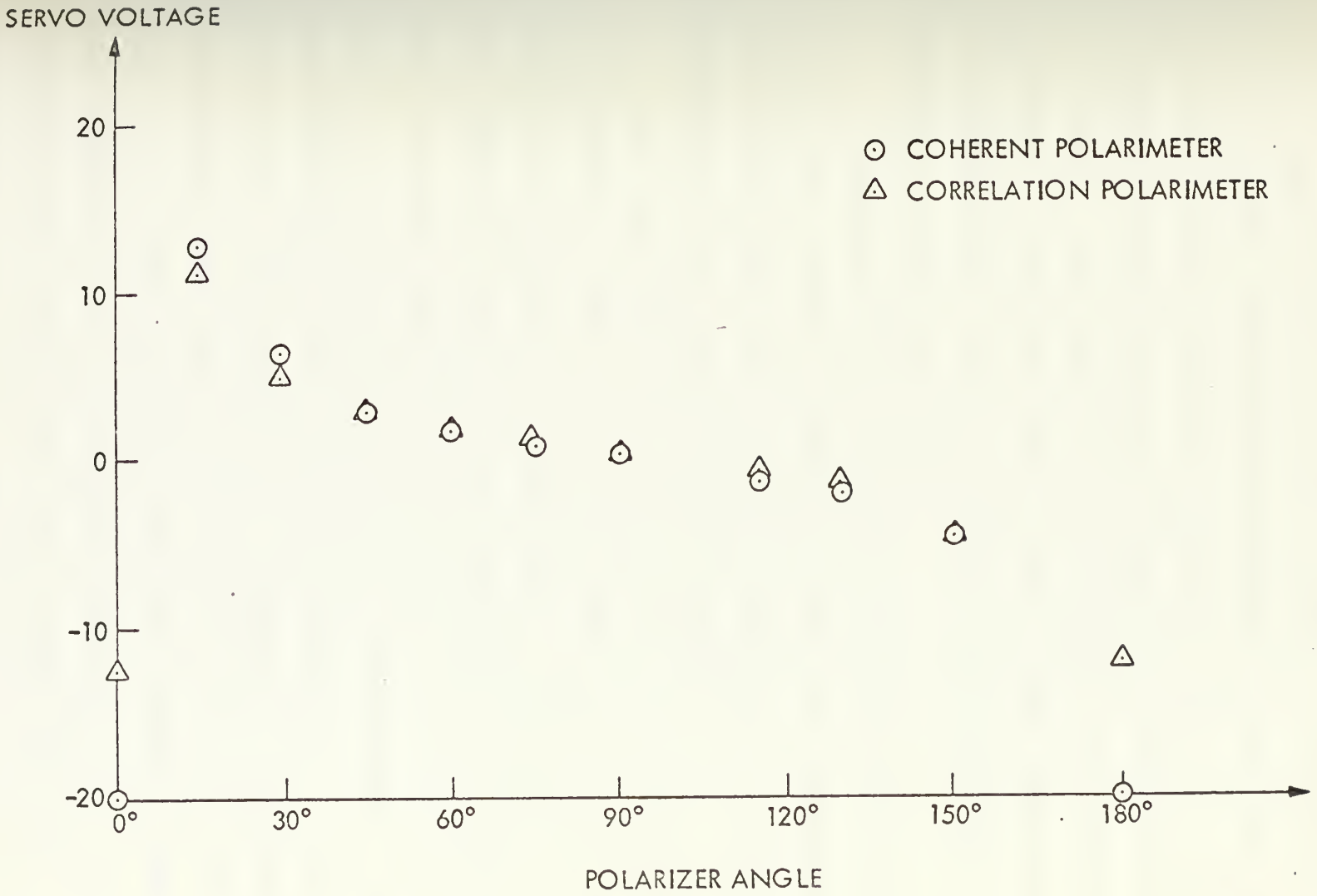

Figure 26 SERVO ERROR VOLTAGE CURVE FOR COHERENT AND CORRELATION POLARIMETER AT NASA/JPL MARS STATION

The probes injecting a test signal are mounted to give a linearly polarized signal corresponding to a 90° polarizer angle. In addition on Figure 26 it will be noted that at 0° and 180° polarizer angle the correlation polarimeter is unable to reach the error voltage of the coherent polarimeter of -20 volts. The correlation polarimeter uses operational amplifiers to obtain the servo error voltage levels desired. The maximum output voltage obtainable from these operational amplifiers is about ±12 volts.

Tracking should take place around the zero error voltage point and the difference in the two curves at large polarization angle errors does not degrade the tracking performance of the correlation polarimeter.

As next step tests using Cygnus A as a noise source were performed. The antenna was pointed at Cygnus A resulting in a system noise temperature of up to 590° K. A test signal was injected at the probes and its amplitude was set to give different signal-to-noise-ratios at the input to the correlation polarimeter and therefore to the phase detectors in the correlation polarimeter. A spot check of the value of the error voltage at an equivalent polarization angle error of 45° at a SNR of 0 dB at the input to the inner loop phase detector revealed a servo error voltage of 1.07 volts which agrees well with the laboratory test giving 1 volt for the same equivalent polarization angle error. The next test consisted of snap-on

tests at high system noise temperatures injecting a test signal into the probes and using Cygnus A as a noise source.

It was found that the coherent polarimeter, even using a narrow loop bandwidth, could not lock on to a test signal of -162 dBm while the system noise temperature was 590° K. The correlation polarimeter did clearly track, using a 50 Hz predetection bandwidth at the 250 Hz IF, and was able to snap-on from 45° off the normal polarizer position with respect to the test signal. The coherent polarimeter did barely track at a signal level of about -158 dBm at the same system noise temperature of 590° K.

Considering in addition that the narrow loop BW (12 Hz) used with the coherent polarimeter has to be compared to about 50 Hz with the correlation polarimeter a clear improvement of about 10 dB by the use of the correlation polarimeter results. At that time no further tests could be made since the antenna was scheduled for other users.

During the Faraday rotation measurement two other tests of the correlation polarimeter using the sun as noise source were made. The test signal used in the first tests was set to be -148 dBm and the system-noise temperature was varied by pointing the antenna off and on the sun. The medium polarizer servo bandwidth was selected. The polarizer was slewed off 20° from its normal position of 90° and then the polarization tracking loop was closed for the measurement. The receiver AGC BW selected was medium, the BW in the

correlation polarimeter was set at 25 Hz. The results are given in Table 1.

The time constant as given is measured to 63% of the final value. Values for the overshoot are not given since the large tracking jitter in these high noise tests makes a determination of the overshoot impossible. The peak to peak fluctuations around the track point $6\sigma_\theta$ were estimated and are given in the table also.

These tests even though not very extensive, indicate a clear advantage of the correlation polarimeter over the coherent polarimeter.

On April 26 1975 another opportunity for testing of the correlation polarimeter was obtained. Again the sun was used as a noise source. At this time the antenna was pointed directly onto the face of the sun, resulting in a system noise temperature of 10 300°K. The test signal injected into the probes had an equivalent strength of the power level predicted for the Helios space craft at this time, of -144 dBm. Snap-on tests from 45° off normal polarizer alignment with the probe signal were performed. The correlation polarimeter was able to perform well under the above conditions. The normal PLL receivers were not able to lock on the signal and coherent polarization tracking was not possible. The outer loop of the correlation polarimeter was switched in and out and no tracking offsets with or without its use could be determined. This indicated that the sun at

TABLE 1

Correlation Polarimeter Tests on April 19, 1975

Test signal level = -148 dBm
Correlation Polarimeter BW = 25 Hz
Receiver AGC BW = Medium
Polarizer BW = Medium
Polarizer slewed off by 20°

Test 1

System Temperature = 1000° K
τ = 10 sec Track point = 88.5°
$6\sigma_\theta$ = 2°
Duration of the test 1.2 minutes

Test 2

System Temperature = 4000° K
τ = 13 sec Track point = 88°
$6\sigma_\theta$ could not be determined. (Fluctuation around track point could not be observed long enough.)
Coherent receiver could not lock onto signal
Coherent polarimeter would not work
Duration of test ca. 1.5 minutes

Test 3

System Temperature = 8000° K
τ = 23 sec Track point = 91°
$6\sigma_\theta$ = 10°
Duration of test ca. 2.5 minutes

that time did not emit any polarized noise at S-band. The results of the tests on April 26, 1975 are given in Table 2.

The test results of April 19 and April 26 have been used in connection with the equation for the rms tracking error for the correlation polarimeter to compare the experimentally obtained rms tracking error with the theoretical values. Using equation (133) with (135) neglecting that the test signal is not Gaussian and neglecting the effect of the hard limiter the calculated rms tracking error for the tests is tabulated in Table 3. The overshoot needed for determination of the second order servo loop bandwidth could not be determined. Therefore the servo loop was approximated by a first order system. This approximation is already incorporated in equation (133).

The results show reasonable agreement between the observed and the calculated rms tracking error. The observed rms error especially on April 26, 1975, are in general considered too optimistic since not enough time could be spent to observe the fluctuations of the polarization angle around the track point. The observations showed general agreement with the theory, however.

It would have been desirable to perform more tests and to be able to observe the rms tracking error in closed loop fashion for longer periods of time but it is felt that the above described test results show an agreement of the general performance with the basic theory of the correlation polarimeter. Also a clear advantage of the correlation

TABLE 2

Correlation Polarimeter Tests on April 26, 1975

System Temperature = 10 300° K
Test signal = -144 dBm
AGC BW = narrow

Test 1

Polarization servo BW = high, duration of Test 1.7 minutes
Correlation polarimeter BW = 25 Hz
snap on from 45°
τ = 9 sec
Trackpoint = 92°
$6\sigma_\theta$ = 18°

Test 2

Polarization servo BW = high, duration of test 1.1 minutes
Correlation polarimeter BW = 25 Hz
snap on from 135°
τ = 17 sec
Trackpoint = 92°
$6\sigma_\theta$ = 18°

Test 3

Polarization servo BW = Medium, duration of test 5.7 minutes
Correlation polarimeter BW = 25 Hz
snap on from 45°
τ = 32 sec
Trackpoint = 91°
$6\sigma_\theta$ = 5°

TABLE 2 (Continued)

Correlation Polarimeter Tests on April 26, 1975

Test 4

Polarization servo BW = High, duration of test 3.3 minutes

Correlation polarimeter BW = 125 Hz

Snap on from 45°

τ = 10 sec

Trackpoint = 90°

$6\sigma_\theta$ = 35°

TABLE 3

Comparison of Observed and Calculated Tracking RMS Error for Tests on April 19 and 26, 1975

Tests on April 19, 1975

Test No.	Observed	Calculated first order loop approximation
1	0.4°	1.0°
2	not observed	2.1°
3	1.6°	2.4°

Tests on April 26, 1975

Test No.	Observed	Calculated first order loop approximation
1	3.0°	2.6°
2	3.0°	1.9°
3	0.8°	1.0°
4	5.8°	3.5°

polarimeter over the coherent polarimeter is apparent. Especially it was shown that the correlation polarimeter could track when the PLL had lost lock and made coherent polarization tracking impossible. The correlation polarimeter can track to at least 10 dB smaller SNR than the coherent polarimeter.

VI. FARADAY ROTATION MEASUREMENTS OF THE SOLAR CORONA

The installation of the correlation polarimeter at the NASA/JPL Deep Space Network Mars Station (DSS-14) in the early part of April 1975 made it available for the Faraday rotation measurement for the Helios 1 solar occultations. In particular the correlation polarimeter was used during the entry portion of the solar occultation of Helios 1.

In the next subsections the equations explaining Faraday rotation in the solar corona and information regarding the Helios 1 spacecraft are given. In the last section the actual measurement is described and the results obtained are presented.

A. BASIC RELATIONS GOVERNING FARADAY ROTATION IN THE SOLAR CORONA

The basic characteristics of the solar corona are described in the literature [1,3,4,12,13,14,15]. The solar corona consists of the region of the solar atmosphere which extends beyond the chromosphere. This region stretches out into the interplanetary region. The region of interest for Faraday rotation experiments reaches out to about 12 solar radii from the center of the sun. Electrons and protons with thermal energies on the order of 10^6 deg K, approximating a pure plasma are found in this region. Even though the density varies with respect to time and location, a static density for the "quiet" sun can be represented by an Allen-Baumbach

model with radial dependence [1]. This model is based on photometry observations of the brightness of the K corona during an eclipse. The equatorial electron density radial distribution was given (in electrons/m^3) by

$$N = 10^{14}\left(\frac{2.99}{R^{16}} + \frac{1.55}{R^{6}}\right) \tag{147}$$

where R is in solar radii. This electron density in connection with the solar magnetic field forms a magnetized plasma. Linearly polarized electromagnetic waves, as for example the signal emitted from the Helios 1 spacecraft, undergo a rotation of the polarization plane (Faraday rotation).

In Figure 27 the spacecraft signal as it traverses the solar corona and typical magnetic field lines of the sun are indicated. The magnetic field emanating from the sun is basically radial to distances of about two solar radii from the center of the sun. A spiral effect dominates at larger distances. The Archimedes spiral of the magnetic field lines is caused by the solar wind emanating from the rotating sun, dragging along the magnetic lines of flux [1]. The solar magnetic field is approximated by the Parker model [1] with

$$B_r = \frac{B_o}{R^2}$$

$$B_A = \frac{B_o}{R} \times \frac{\omega r}{v} \tag{148}$$

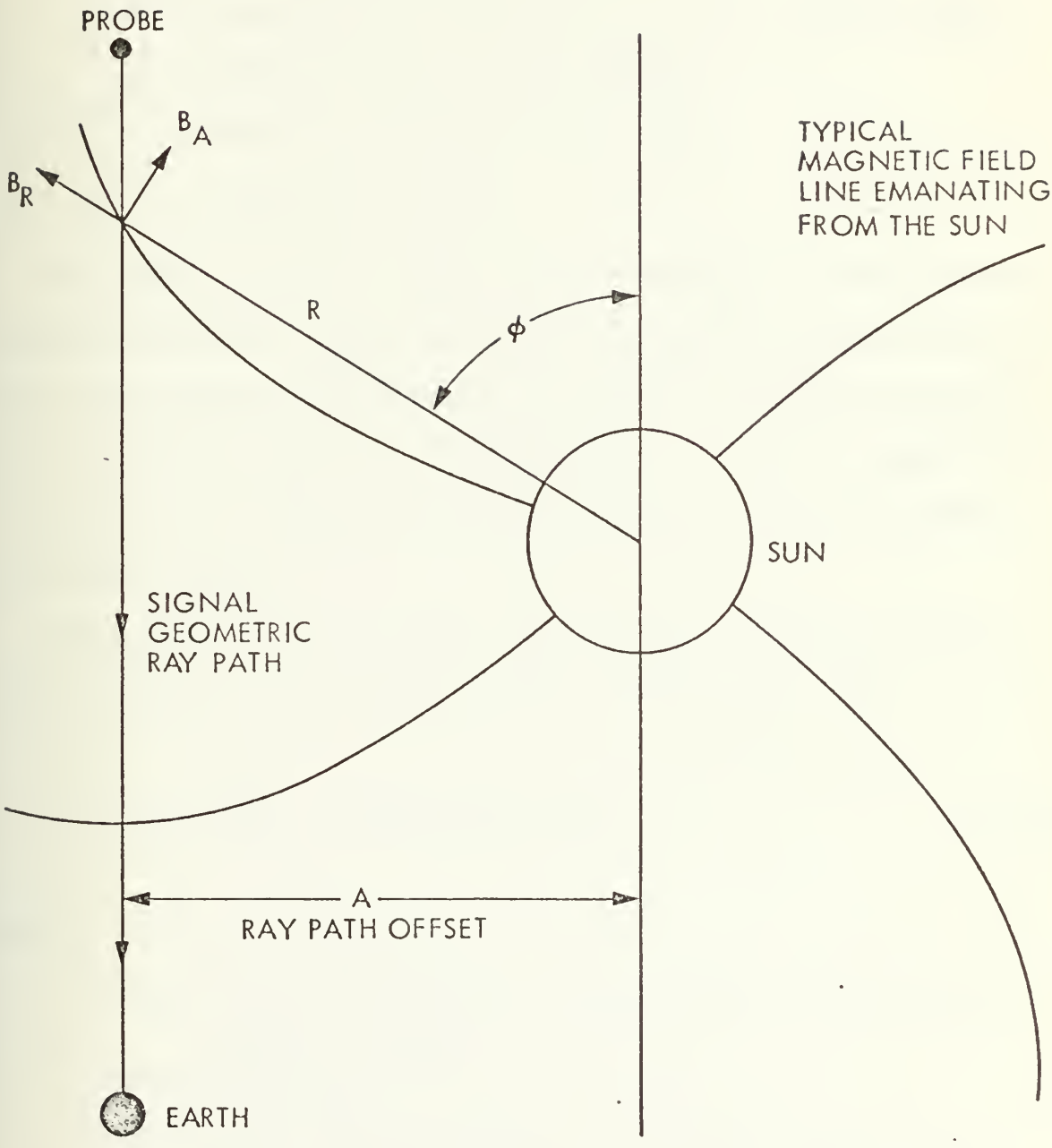

Figure 27 SIGNAL GEOMETRIC RAY PATH
IN THE SOLAR CORONA

where B_r = radial component of solar magnetic field, G.

B_A = azimuthal component of solar magnetic field, G.

B_o = magnetic field on sun surface, G.

R = distance from center of the sun, solar radii.

ω = rotation rate of sun rad/sec.

v = velocity of solar wind, m/sec.

r = radius of sun, m

The solar magnetic field in connection with the electron density along the signal ray path cause the Faraday rotation. The basic equation governing the effect of Faraday rotation has been well treated in the literature [24,25]. Stelzried [1] applied the theory to the solar corona and his results are stated below.

The contribution of the longitudinal component of the solar magnetic field (longitudinal to ray path) is

$$\Omega_L = \frac{Q_L L}{f^2} \int_s N(s)\, B_L(s)\, ds \qquad (149)$$

where

Ω_L = Faraday rotation in degrees due to longitudinal magnetic field

Q_L = 135.4816

L = unit scaling factor ($L = 6.9598 \times 10^8$ if R in solar radii)

f = signal frequency in Hz

N = electron density in electrons/m^3

B_L = longitudinal component of the magnetic field in G

ds = increment of ray path in the corona.

The contribution of the transverse component of the magnetic field in degrees is

$$\Omega_T = \frac{Q_T L}{f^3} \int_s N(s)\, B_T(s)\, ds \qquad (150)$$

where

$Q_T = 1.896205 \times 10^8$

B_T = transverse magnetic field component in G

Ω_T = Faraday rotation in degrees due to transverse component of magnetic field

Stelzried [1] did a Faraday rotation experiment using the linearly polarized signal of the Pioneer 6 spacecraft in 1968. Applying the Parker model for the solar magnetic field in conjunction with magnetometer data supplied by the Mt. Palomar observatory and measurement data obtained for the solar magnetic field from the Explorer 33 spacecraft to these Faraday rotation data resulted in a modified Allen-Baumbach electron density for the solar corona [1,3]. This modified density is given by

$$N = 10^{14} \left(\frac{1.55}{R^6} + \frac{0.01}{R^2}\right) \qquad (151)$$

where

N in electrons/m^3

R in solar radii.

He was only able to measure to a signal ray path offset of about four solar radii. Further data tracking was not possible since the coherent polarimeter could not stay in lock at a system noise temperature of about 300° K and a received spacecraft signal strength of about -163 dBm.

The Faraday rotation measurement using the Helios 1 spacecraft yielded results to much smaller ray path offsets. The reasons are twofold. The received power was about 19 dB higher than during the previous experiments. This higher power resulted from the use of the high power transmitter in connection with the high gain antenna on the spacecraft. In addition the sun's cycle is presently at its minimum and thereby effectively reducing the system noise temperature at equivalent ray path offsets.

In the next section the spacecraft Helios 1 used for the present Faraday rotation measurement is described.

B. THE HELIOS 1 SPACECRAFT

1. Helios 1 - Mission Description

The "Helios" program consisting of two spacecraft missions Helios 1 and Helios 2 is the largest joint space venture for the United States and the Federal Republic of Germany.

The Federal Republic of Germany was responsible for the development and construction of the spacecraft and for seven of the onboard experiments. The United States supplies three more onboard experiments, provides the launch vehicle and launches the vehicle into the solar orbit. The United States will also use the Deep Space Network stations 26 and 64 m antennas at Goldstone, California for telemetry reception and command links to the spacecrafts. The 100 meter radiotelescope in Effelsberg, Germany, will also be used for telemetry reception from the spacecraft. A further important contribution of the United States toward a successful space mission is the technical advice and training given to German personnel.

The main mission goal is to further scientific knowledge of the interplanetary region between sun and earth, especially between the sun and the planet Venus. The main experiments will explore the acceleration mechanism of the solar wind, and make magnetic and electric field, and cosmic ray and cosmic particle measurements in that region. In addition to these onboard experiments there will be several ground-based experiments. One of these is concerned with celestial mechanics using range and doppler data to further refine the knowledge of the properties and constants of the solar system and to provide another test of Einstein's theory of relativity. The other main ground-based experiment is the Faraday rotation measurement. This experiment besides

some others (i.e., transmission delay through solar corona) will provide additional data about the characteristics of the solar corona.

The launch of "Helios 1", the first mission, was originally set for June 1974 but then due to technical difficulties and modifications of the spacecraft delayed to December 10, 1974.

2. Description of the Spacecraft

The spacecraft Helios has the appearance of a large spool. The conical sections of the spacecraft body are 50% covered with solar cells and the remainder with second surface (i.e., front surface) mirrors. These mirrors reflect excess solar energy from the conical surfaces. The conical sections reflect unwanted solar energy and at the same time provide a reasonable angle of incidence between the sun rays and the solar cells.

The cylindrical section of the spacecraft contains most of the experiment packages and electronics. The magnetometer experiments are located on foldable transverse booms which are mounted on the central body as are the long experiment antennas. Only the openings for the experiments break through the insulating shell of the central body. The spacecraft is shown in Figure 28 [26]. The spacecraft is spin stabilized at a spacecraft body spin rate of 60 rpm. The spin axis is oriented normally to the plane of the ecliptic. The spacecraft trajectory lies in the plane of

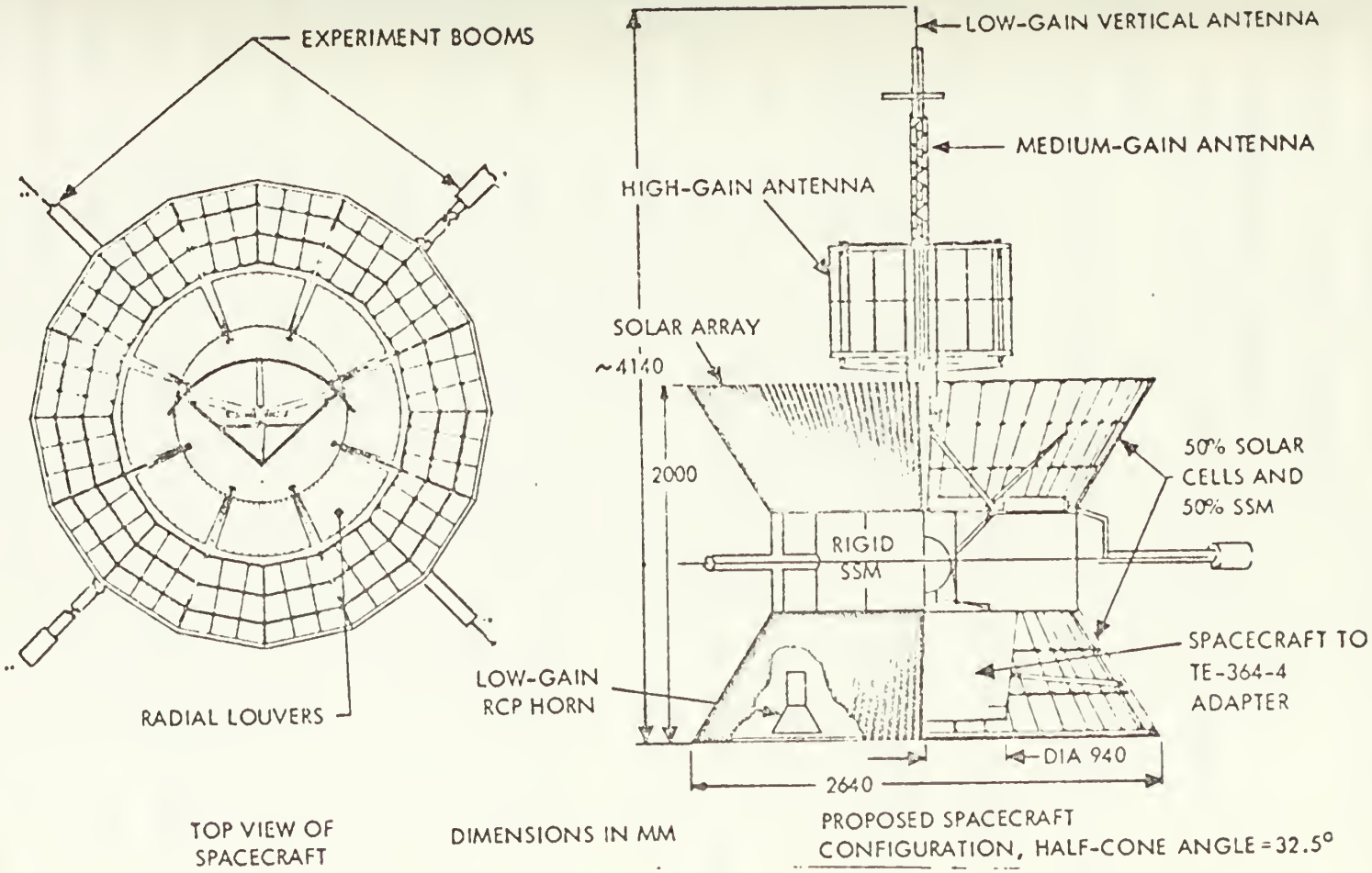

Figure 28 THE HELIOS SPACECRAFT

the ecliptic. This orientation provides illumination of the solar cells and positions the spacecraft's antennas such that their patterns will intercept the earth throughout the trajectory of the spacecraft.

3. Spacecraft Antennas

There are three antenna systems mounted on the spacecraft.

1. A two-antenna quasi-omnidirectional system ("low gain" antenna).
2. A "medium gain" antenna system whose "pancake" pattern lies in the plane of the ecliptic.
3. A "high gain" or "spot beam" antenna that is mechanically pointed at the earth throughout the spacecraft's heliocentric orbit.

The omnidirectional antenna is used during the period from shroud ejection following launch up through the orientation maneuver that positions the spin axis normal to the plane of the ecliptic.

The "medium gain" antenna is located above the high gain antenna but below the low gain antenna on the antenna mast. It consists of a single longitudinal helix antenna which will direct its maximum radiation in all directions within the plane of the ecliptic after the orientation of the spin axis normal to the plane of the ecliptic. The pattern is about 15° wide in the direction perpendicular to the ecliptic and has a downlink gain of 8 dB. The prior knowledge of this pattern enables the final positioning of the spacecraft spin axis toward the pole of the ecliptic. The "medium gain" antenna is connected through a diplexer

to the second transponder aboard the spacecraft. The second transponder is shared by the "medium" and the "high" gain antenna. The medium gain antenna will mainly be used as the receiving antenna during the heliocentric orbit.

The Helios spacecraft "high gain" or "spot beam" antenna is the main transmitting antenna during the heliocentric orbit. Its cylindrical, parabolically shaped reflector is mechanically despun to counter the spacecraft's body spin rate of 60 rpm. The spin angular velocity and phase angle with respect to the sun are constantly monitored and so adjusted by ground control that the antenna beam points toward the earth. The high gain antenna beam is linearly polarized (vertical to plane of ecliptic) with a beamwidth of 5 1/2 degrees within the plane of the ecliptic and 14 degrees normal to the plane of the ecliptic. The downlink gain of this antenna is 23 dB. This antenna is mainly used for the transmission of high rate telemetry from the spacecraft to the earth. The linearly polarized carrier signal from the high gain antenna is also used to carry out the Faraday rotation measurement in the solar corona. During the main phase of the mission the two 20 watt traveling wave tube amplifiers will be used for the transmission of the signals. The carrier frequency is 2297.592593 MHz [27]. The Helios radio system is shown in Figure 29.

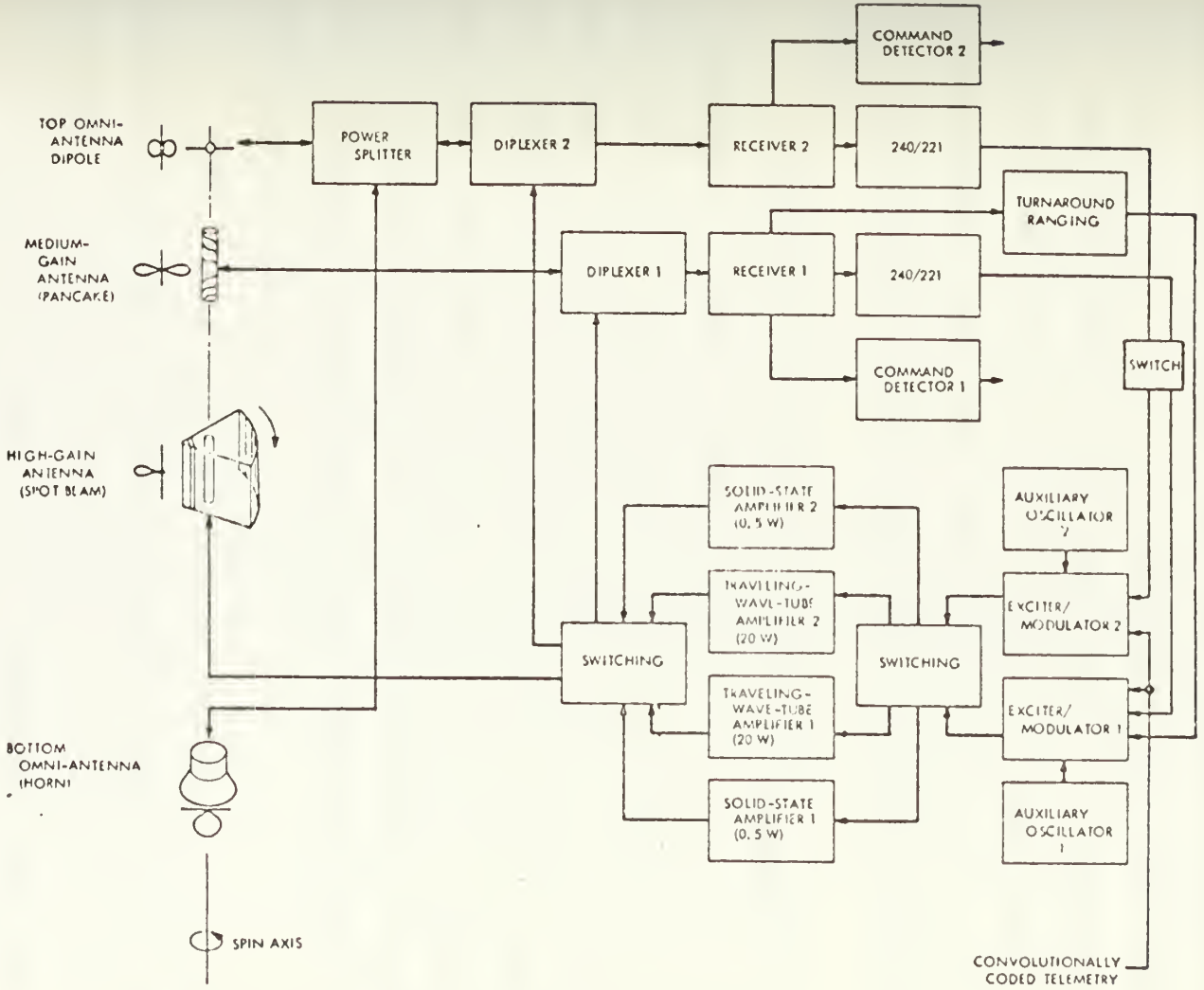

Figure 29 HELIOS RADIO SYSTEM

4. Helios 1 - Orbit

The Helios 1 spacecraft has an orbit which is within the plane of the ecliptic. In Figure 30 the projection of the orbit in the plane of the ecliptic relative to a fixed earth sun line is given. The orbit is heliocentric and its first perihelion of 0.3 AU constituted the closest approach of a man made object to the sun so far. As can be seen the period of revolution is about 190 days. The orbit of the spacecraft as needed for calculations of the ray path offset for the Faraday rotation experiment is fairly accurately known.

Pointing and doppler information obtained by the DSN (Deep Space Network) tracking stations are used for orbit determination. Right ascension and declinition are computed from the JPL SPACE computer program [29]. A correction to the calculated right ascension and declination is periodically obtained from antenna boresight and spacecraft doppler data. The JPL SPACE program also is used to provide the parameters for the doppler predictions as used with the emphemeris tuned oscillator.

The ray path offset during the first occultation entry is calculated from data obtained from the JPL SPACE program. A plot of the sun-earth-probe-angle for this period is given in Figure 31. It should be noted that Helios 1 is not occulted by the chromosphere during the first occultation. Also the first occultation is very suitable for a Faraday rotation measurement since the entry and exit rates

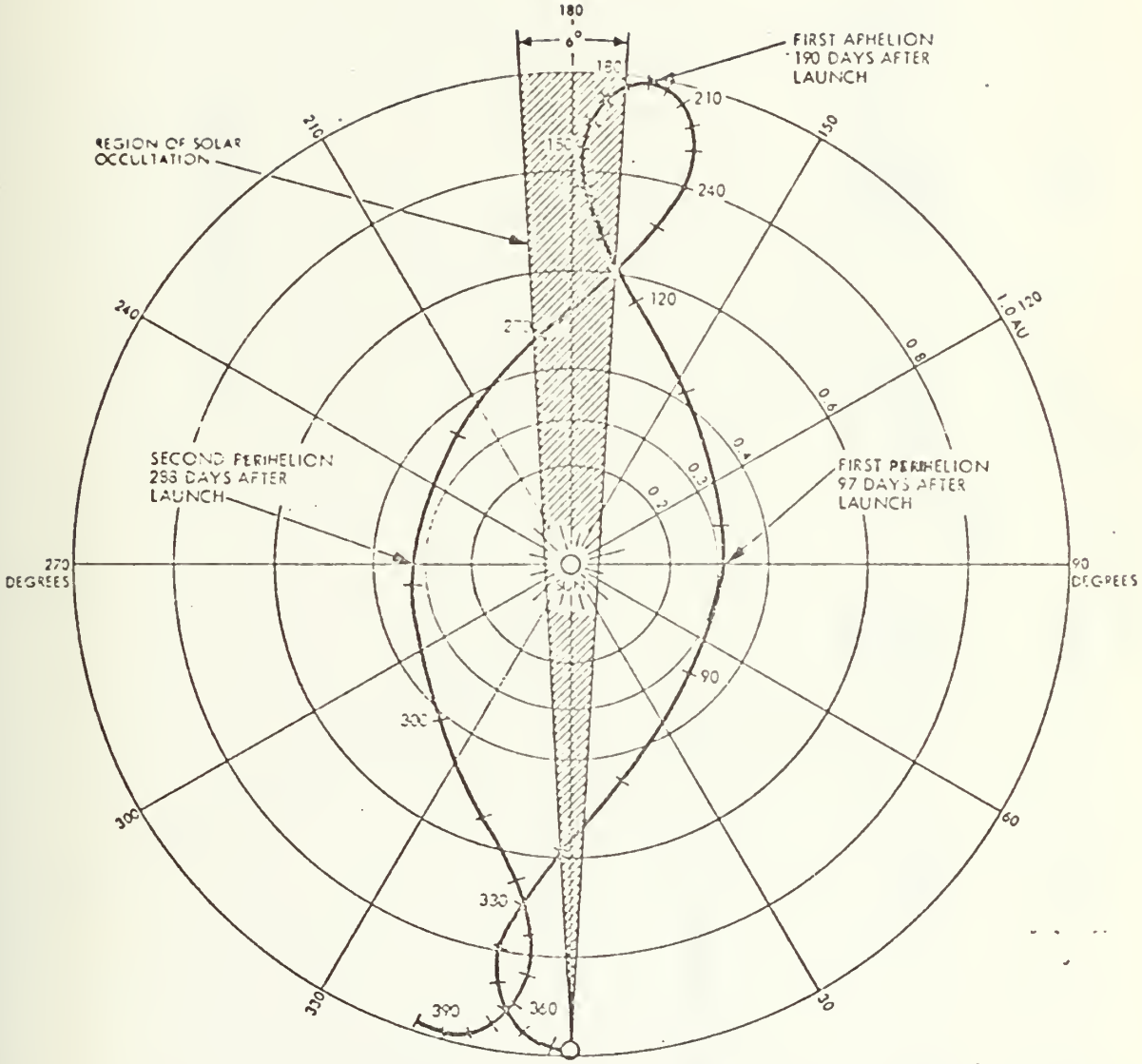

Figure 30 HELIOS ORBIT IN PLANE OF ECLIPTIC

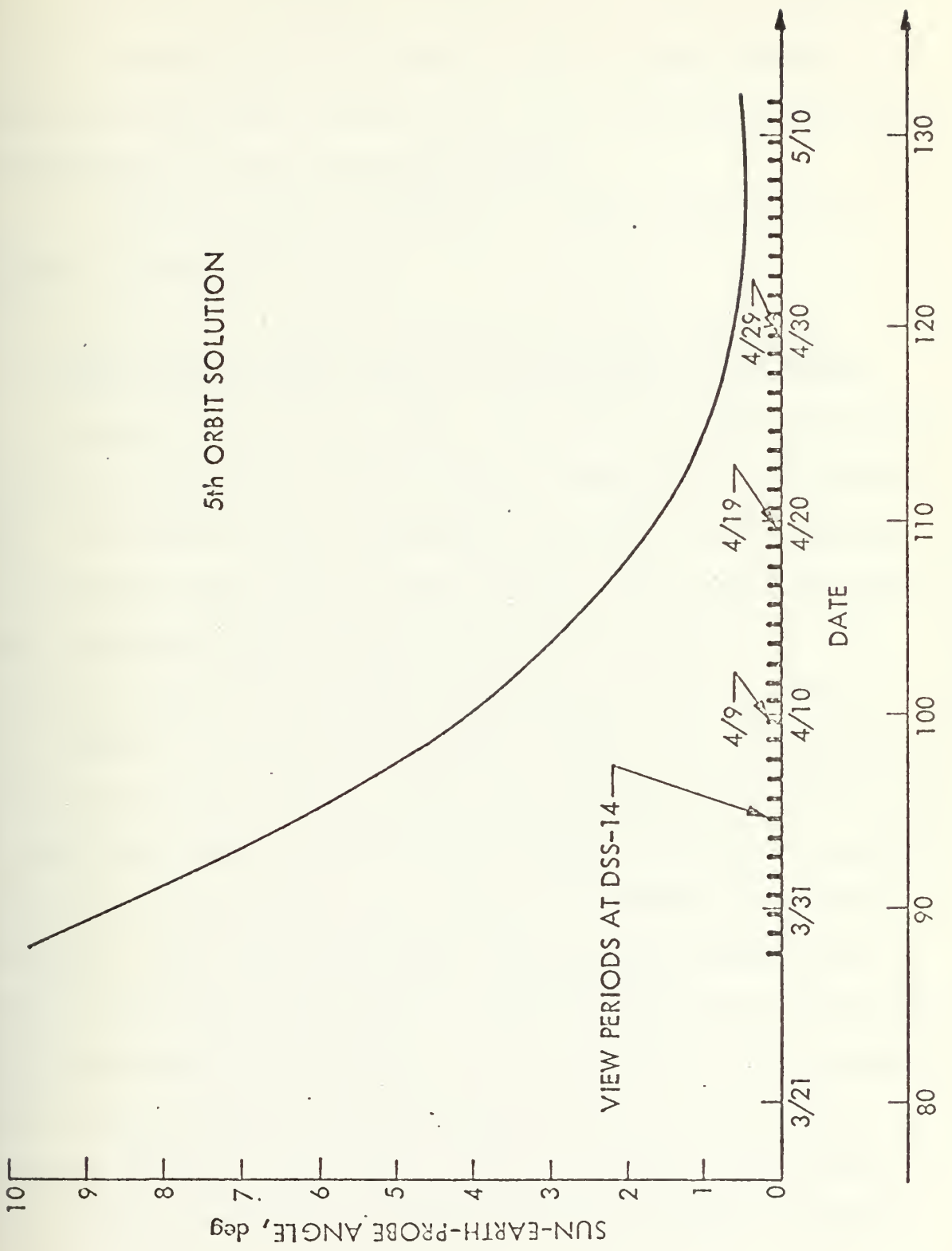

Figure 31 HELIOS FIRST ENTRY INTO SOLAR CORONA

are rather slow compared to Pioneer 6 in 1968 or compared to the second Helios occultation. The actual Faraday rotation measurement during the first occultation (entry) is described in the following section.

Table 4 gives a summary of facts regarding the Helios 1 spacecraft.

C. THE FARADAY ROTATION MEASUREMENT DURING THE FIRST SOLAR OCCULTATION (ENTRY) OF THE HELIOS 1 SPACECRAFT

During the period of April 18 to May 1, 1975 the Faraday rotation measurement on the Helios 1 spacecraft was carried out. The correlation polarimeter as well as the coherent polarimeter were used for data taking. The data taken with the two polarimeters showed remarkable agreement up to including April 29 at a sun earth probe angle of about 0.6 degrees. No tracking offsets between the two polarimeter schemes could be found. Also the tracking jitter of the two schemes was observed to be about equal, although it appeared that tracking with the correlation polarimeter resulted in slightly less jitter at higher system noise temperatures. Exact evaluation will only be possible after the polarization data as taken by a digital recording unit will be processed. It is anticipated that final data will not be available for several months. Up to April 29 no evidence of polarized noise being received or generated by the antenna could be found.

Table 4

Helios 1 Facts

Experiments flown on board Helios 1

a) Supplied by United States
- Fluxgate magnetometer (3)
- Plasma and radiowaves experiment (5)
- Cosmic ray experiment (7)

b) Supplied by Germany
- Plasma experiment (1)
- Fluxgate magnetometer (2)
- Search coil magnetometer (4)
- Cosmic ray experiment (6)
- Electron detector (8)
- Zodiac light photometer (9)
- Micrometeorid analyzer (10)
- Celestial mechanics experiment (11)

Numbers in parentheses give official experiment number.

Technical data of spacecraft Helios 1 [29]

Probe mass	340	kg
Max. diameter	2.773	meters
Height including antenna	4.208	meters
Magnetometer boom	3.20	meters
Deployable antenna (exp. 5)	16.00	meters
Orbit		
perihelion	0.30	AU
aphelion	1.0	AU
period of revolution	190	days
required lifetime	18	months

On April 20, 1975 it was observed that the polarization tracking system phasing had changed just before the track of Helios 1. A recalibration was not possible. The post-calibration revealed a phasing error of about 56° between the reference and error channel, resulting in a measurement offset of -5°. The data were corrected by adding +5° to the measured rotation angle. The problem of this phasing error had occurred previously and could not be traced. Additional antenna time was obtained for the night following the track on April 20. The problem was traced to be caused by a defective coaxial hardline leading from the antenna-dish to the receiver in the control building. The movement of the antenna apparently changed by stretching or bending the dielectric characteristics of the cable. The cable was replaced with a spare cable already existing and no further problems of this nature were observed.

During April 26 and 27 a gain instability of the reference channel maser was observed. Checks of the system before and after track revealed no phasing errors and it is assumed that the maser gain instability did not affect the quality of the polarization data.

On April 29, 1975 the system noise temperature had increased to about 210° K and the spacecraft carrier spectrum had broadened due to the effect of the solar corona to about 50 Hz in noncoherent mode, (noncoherent mode -spacecraft oscillator free running) and about 65 Hz in the coherent mode (coherent mode - spacecraft oscillator locked to uplink

frequency). It should be noted that at the beginning of the entry the spectral width was about 1 Hz. See Figure 32.

Under these conditions the PLL in the coherent polarimeter started to lose lock, but only for short durations. Tracking was still possible and switching between the coherent and the correlation polarimeter resulted in no tracking offsets. No evidence of polarized noise entering the receivers was found.

On April 30 it was found that both polarimeters were unable to track the spacecraft. The system noise temperature reached about 590° K and the signal spectrum had widened again to about 80 Hz. The noncoherent doppler rate showed a sudden change from about +16 Hz/day to more than about -50 Hz/day. In addition it was determined that the major antenna side lobes at the sun-earth-probe angle of less than 0.6 degree were sweeping over the surface of the sun, causing the high system noise temperature and in addition polarizing over 10% of the received noise.

The coherent polarimeter PLL could not lock up to the signal at all and tracking therefore was impossible. Attempts with the correlation polarimeter revealed that it tracked the major axis of the polarized noise. Even the use of the outer loop did not result in the ability to track the signal. Using the outer loop to cancel out the effect due to the polarized noise resulted in random drift of the polarizer. Observation of the spectra of the reference and error

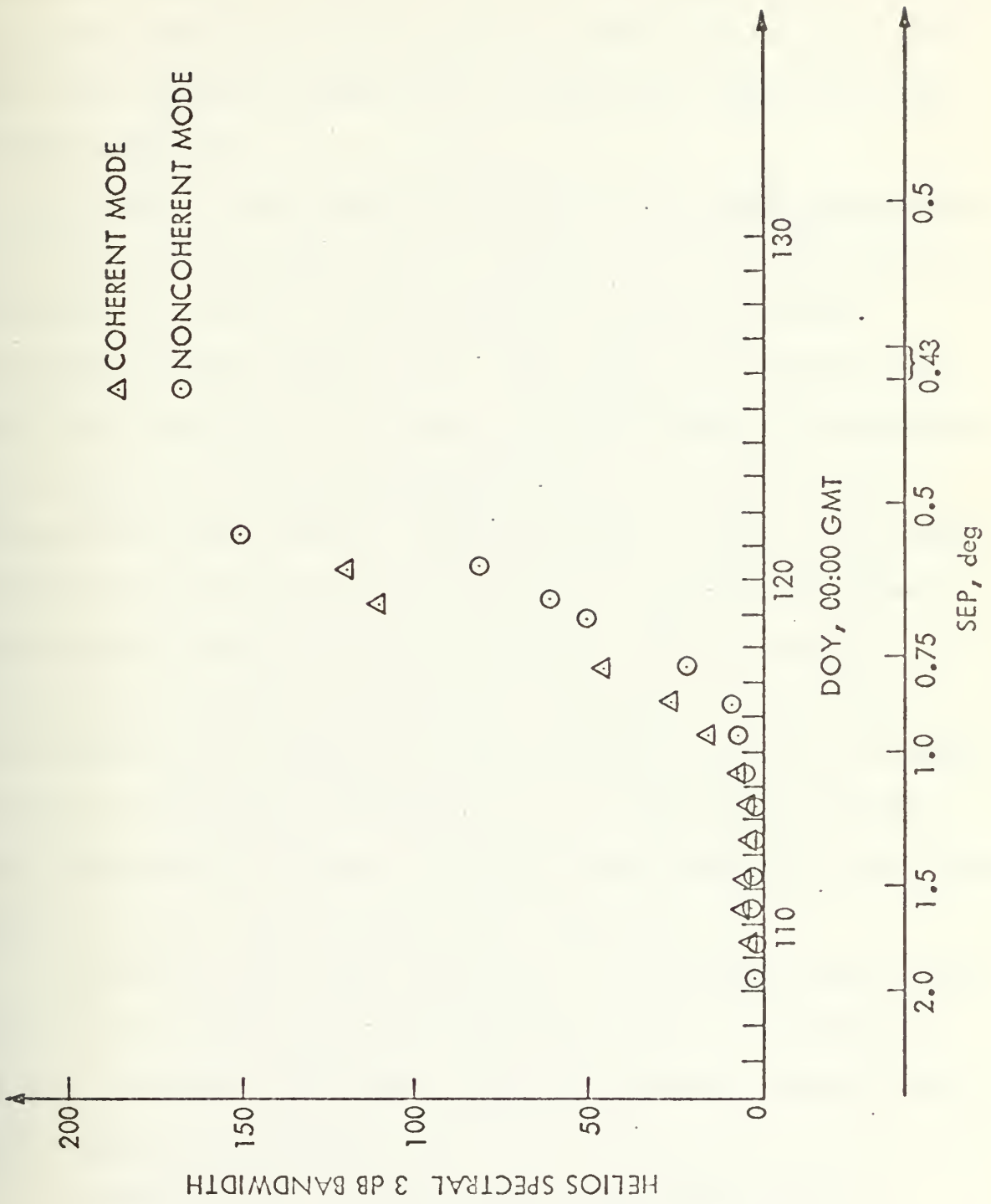

Figure 32 3 dB SPECTRAL BANDWIDTH OF HELIOS CARRIER SIGNAL VS DOY

channels indicated in addition an independence of the signal spectrum amplitude on the polarizer position. It appeared that both channels showed for any polarizer angle the same signal spectrum.

On May 1 a new attempt was made to track the polarization of Helios 1 now even closer to the sun. The results were as on April 30, 1975. Now the amount of polarized noise generated by the antenna major side lobes "seeing" the sun was more than 20% of the total received noise, as determined by rotation of the polarizer while monitoring the noise temperature strip chart. The noncoherent doppler shift had dropped by another 60 to 80 Hz and the noncoherent signal spectrum was about 150 to 160 Hz wide, showing another significant increase in spectral broadening. Again the amplitudes of the spectra in the reference and error channel showed no detectable dependence on the polarizer position. The coherent polarimeter as well as the correlation polarimeter again were not able to track the spacecraft.

Preliminary data were obtained by continuous observation and manual recording of the polarizer angle. In addition analog recorders were used. Only the manually recorded data are presently available.

The preliminary Faraday rotation data are given in Figure 33. The polarity change of the Faraday rotation is believed to have been caused by a change of the magnetic field polarity during the measurement period. It is possible

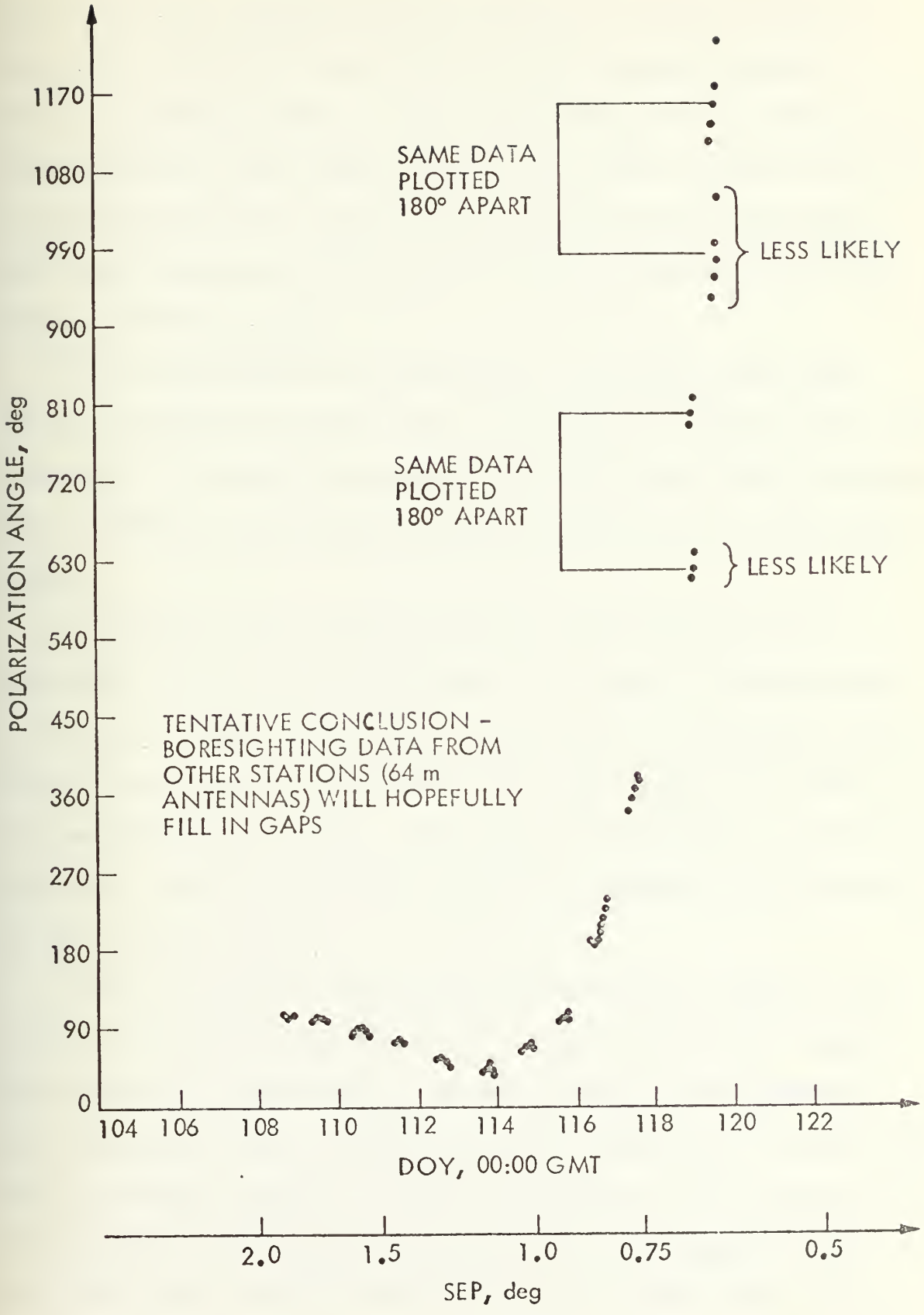

Figure 33 POLARIZATION ANGLE WITH RESPECT TO PLANE OF ECLIPTIC VS DOY (Prepublication data provided by California Institute of Technology)

that different magnetic field sectors of the sun due to the sun's rotation were affecting the Faraday rotation during the data taking. Later data evaluation in connection with magnetic field data for the sun in this period may give a final explanation for this previously unobserved effect. The steep increase in the curve leaves an ambiguity in the actual rotation angle.

It is anticipated that polarizer boresight data from other DSN stations might fill in the gaps, resolving the 180° ambiguity. The data is presented in the most likely estimated form, based on the slope of the obtained points during each track.

In Figure 34 the maximum system noise temperature as observed in the period from April 18 to May 1 (DOY 108-121) is plotted. The system noise temperature is measured with a square law detector monitoring the total power in 50 MHz IF of the reference channel. The 50 Mc IF bandwidth is several megaherz and therefore the square law detector is dominated by the system noise.

Figure 35 shows a plot of the noncoherent doppler error of the received spacecraft signal. The noncoherent doppler was measured by observation of the receiver VCO frequency and comparison with the predicted VCO frequency. In addition the ETO offset needed to obtain the center of the spacecraft spectrum at 10 MC gave an indication of the doppler error. The data until DOY 119 are given without error bars, since

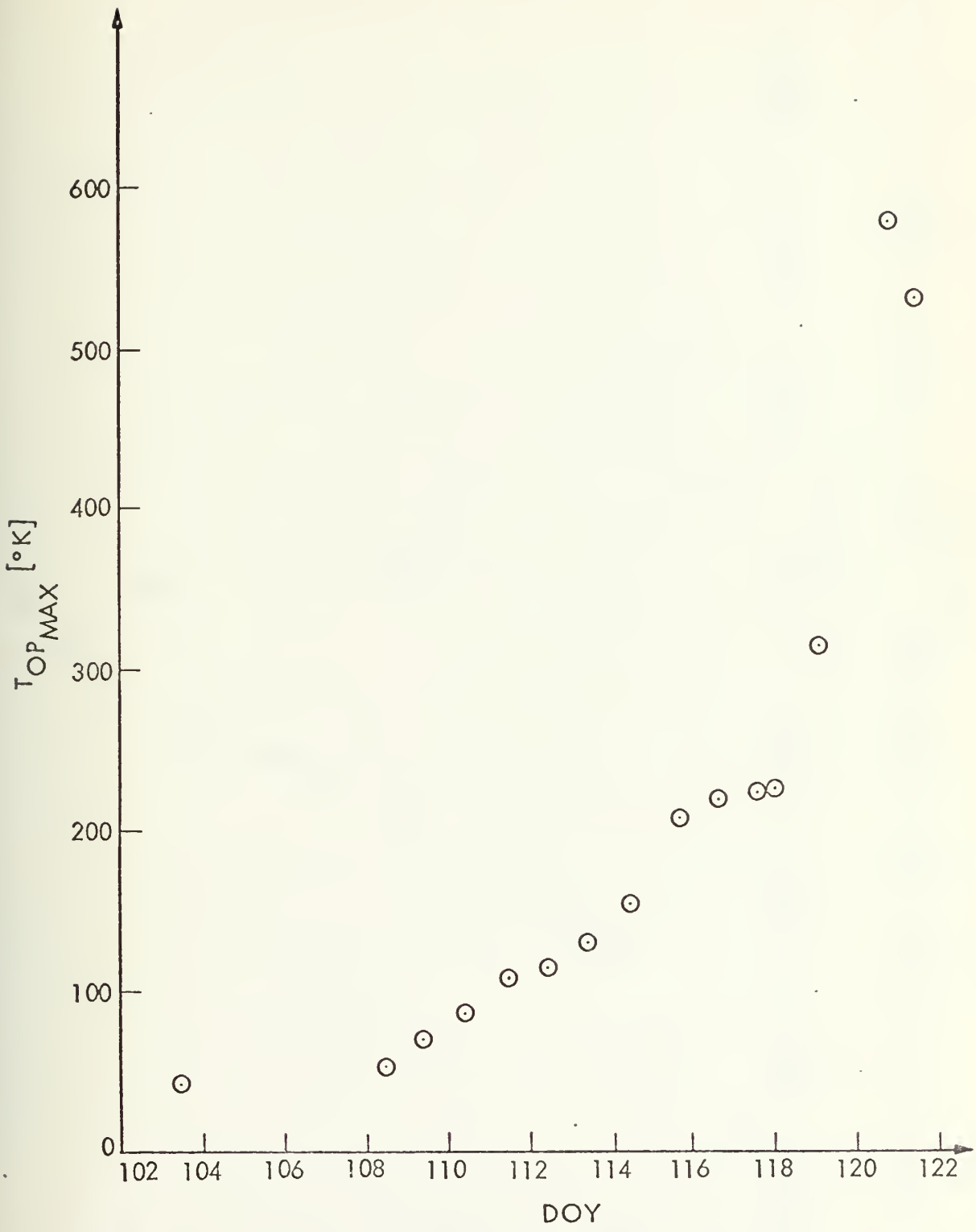

Figure 34 MAXIMUM OBSERVED SYSTEM OPERATING NOISE TEMPERATURE VS DOY

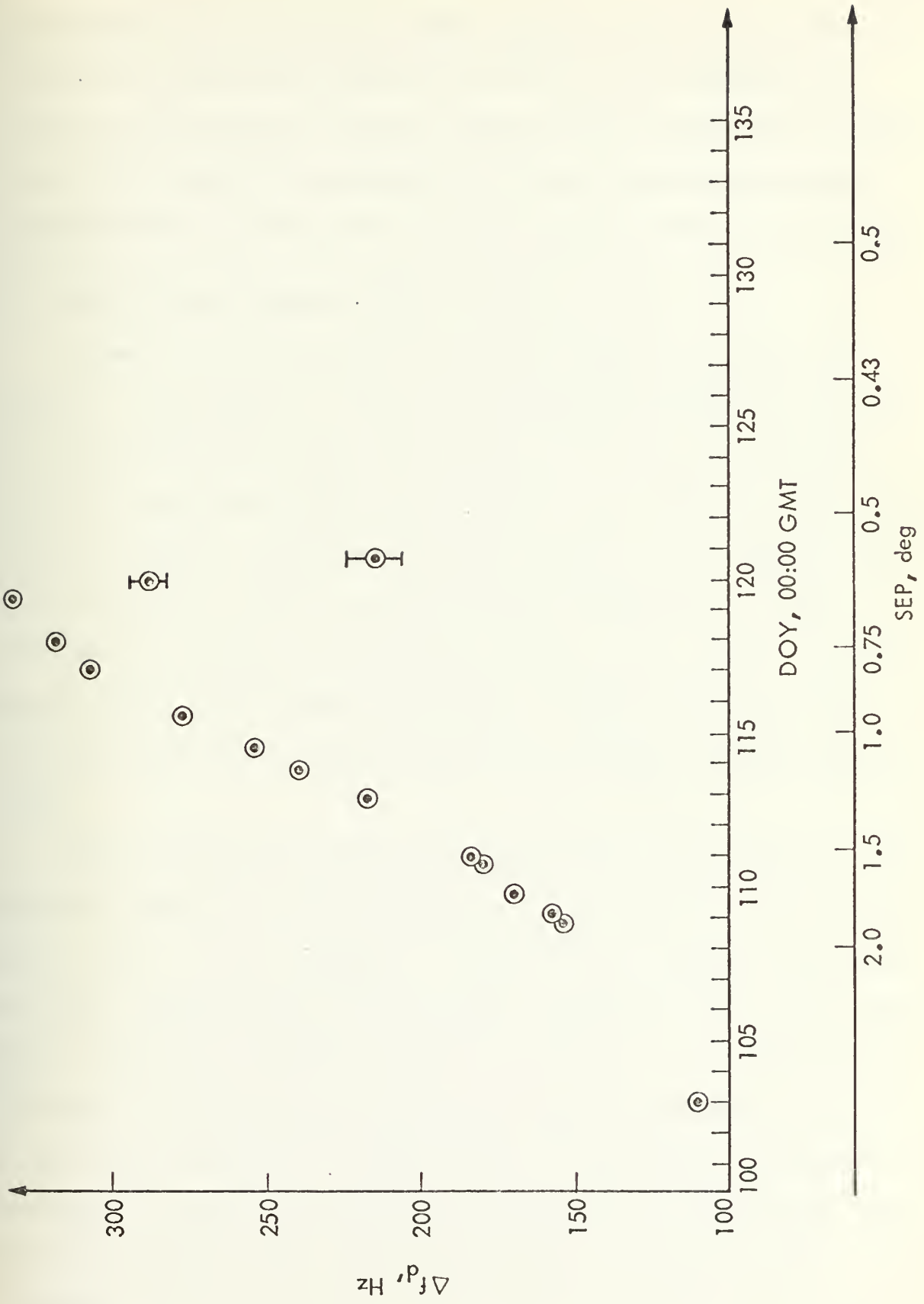

Figure 35 NONCOHERENT SPACECRAFT DOPPLER ERROR VS DOY

both observations gave the same doppler error. On DOY 120 and 121 the receiver could not lock on to the signal and only the information from the spectrum analyzer was available. Due to the spectral broadening as given in Figure 32 exact determination of the center of the spectrum was not possible.

D. SOLAR CORONA MEASUREMENTS ON MAY 13, 1975

On May 13, 1975 during the first occultation exit of Helios 1 an attempt to start polarization tracking was made. The sun-earth-probe angle was about 0.6°. It was observed that the receivers maintained solid lock. Still, polarization tracking was not possible, even at system noise temperatures as low as 220° K and a received signal strength of about -160 dBm. The spacecraft signal spectrum was observed to be about 100 to 120 Hz wide. To find an explanation for the observed facts the reference and error channel spectra were taken.

Prior to the data taking the open loop receivers and the spectrum analyzer were calibrated to give equal spectra for equal power in the channels. The software computer spectrum analyzer automatically scales both channels by the same scale factor after calculating a set of spectra. If no additional command is entered by the operator the error channel has a larger gain of about 8 (right shift 3) above the reference spectrum. During pre-calibration additional attenuation in the error channel of 8 dB yielded equal spectra in both channels.

Spectra in both channels were taken at fixed polarizer angles in steps of 30° from 0° to 180°. No difference (resolution ±1 dB) in the amplitude of the reference and error channel spectra could be found at any polarizer angle. The receiver in lock indication also was the same for all polarizer positions. A recording with the polarizer in right and left circular polarizer mode showed again equal power for both modes. In addition no ellipticity component on the ellipticity strip chart recorder could be found at any time. After these tests the polarizer was put into the autotrack mode. It was observed that tracking for short intermittent periods of up to about 10 minutes/hour was possible.

The polarizer was periodically slewed off its apparent trackpoint and in most instances no snap-on to the previous angle occurred. In many instances even slewing the polarizer off by 90° resulted in no return to the original value. The polarizer just jittered around the new position. During all this time the receivers were in solid lock and polarization tracking should have been possible. The polarized noise as generated by the antenna was observed to be about 17% of the total noise.

These results explain why the correlation polarimeter as well as the coherent polarimeter could not track on April 30 and May 1. The tests indicate that at least a large portion of the received signal was not polarized in one plane of

polarization. The equal power in the spectra for both circular polarization modes and the missing indication of any ellipticity indicate that the received signal is neither circularly nor elliptically polarized. The partial tracking ability indicates that at least a portion of the received signal is linearly polarized at definite angles for short durations. The major portion of the signal might be depolarized or linearly polarized with fast varying random orientation. Without further evaluation of the digitally recorded data no firmer conclusions can be reached on the effects of the solar corona on the signal during the tracking period of May 13, 1975.

VII. CONCLUSIONS

The development of the correlation polarimeter for the NASA/JPL Deep Space Mars Station provides the station with extended polarization tracking capability to at least 10 dB lower SNR's than previously possible. Actual tests on April 7, 19 and 26, 1975 as described in Section V.C.2 show a clear advantage over the coherent polarimeter. All tests done on the correlation polarimeter in the laboratory as well as in the actual system showed general agreement with the theory. The correlation polarimeter in addition provided an alternative way for the data taking during the Faraday rotation measurement described in Section VI.C thereby improving the confidence in the obtained data.

The impossibility of extending the tracking capability for the first Helios 1 occultation is seen in an apparent fast varying random orientation of the plane of polarization or depolarization of the signal. This effect has never been explored prior to the track on May 13, 1975. It is also possible that the Faraday rotation rate increased beyond the capabilities of the tracking system being even large enough not to be detectable on the spectrum analyzer. In addition the sudden change of the noncoherent spacecraft doppler error rate may indicate strong, so far unexplainable, effects. At this time it is not assumed likely that the drift of the spacecraft oscillator underwent such an abrupt change. A

better indication for solar effects would have been a sudden change in the coherent doppler error of the spacecraft. However, the coherent doppler error could not be observed on April 30 and May 1.

Future measurements will hopefully resolve the phenomena encountered at signal ray path offsets at sun-earth-probe-angles of less than 0.6° for the low activity portion of the 11 year solar cycle as presently encountered.

In addition, the observation of large amounts of polarized noise apparently generated by the antenna side lobes seeing the sun has not been observed previously and its magnitude (over 20%) exceeded all expectations.

The polarizing effect of the antenna is believed to be occurring when the antenna main lobe is still away from the sun, but the major side lobes which are less than 30 dB smaller are "seeing" the sun. Further tests would have to be performed to give a definite answer.

It is felt that for a weaker spacecraft signal the correlation polarimeter would have replaced the coherent polarimeter much before the encountered cutoff point in this experiment. The correlation polarimeter in particular was designed for spacecraft signals at least 15 to 16 dB weaker than encountered with Helios 1. Even up to the last few weeks before the experiment it was expected that about a 15 dB weaker signal would be received from Helios 1. The high gain antenna showed surface breakdown phenomena affecting

some of the onboard experiments. The use of the medium gain antenna would have resulted in about 15 dB less received signal power.

VIII. SUGGESTIONS FOR FUTURE WORK

The suggestions regarding a possible building of a second correlation polarimeter are as follows. To reduce the possibility of the encountered crosstalk problems the error and reference channels should be built entirely separately in two different sections of the chassis. Each channel as well as the dc amplifiers and additional components should have separate power supplies. Great care should be taken in shielding and ground point selection. Available standard power supplies should be used to insure better reliability and regulation. A sixth BPF of about 250 Hz BW at the 250 Hz IF spare position in the reference and error channel should be added to enable tracking at large spectral broadening effects as encountered with Helios 1. To counteract the effects of the polarized noise better, a wider predetection BW (now 2.2 KC) in front of the correlation polarimeter for the outer loop should be used. It is expected that a BW of about 6 KC might be sufficient. Due to the decision to use the correlation polarimeter in the AGC mode the need for the use of the hard limiters and phase detectors is no longer necessary. The AGC operation will always provide a high drive for the inner and outer loops. The use of standard multipliers in place of the phase detectors with hard limiters might be feasible once more. The elimination of the hard limiters would als decrease the

dependence of the system S-curve on the SNR, resulting in an increased error curve slope at lower SNR's than now exists. The AFC circuit should be omitted or a much more costly and complicated AFC circuit should be built. The present circuit is not operational and is not used as explained in Section V.B.1.d.

At the present time no suggestion for further instrumentation at the NASA/JPL Mars Station is given. It is felt that the effects observed on April 30, May 1 and May 13 need further exploration. The later evaluation of the digitally recorded, more extensive data might suggest additional tests necessitating more elaborate instrumentation for the second solar occultation of Helios 1.

APPENDIX A

THE CORRELATION POLARIMETER CHASSIS

The correlation polarimeter chassis is documented in this appendix. The function and location of all adjustable components as well as the circuit and wiring diagrams are given. The front panel components and the rear panel connectors are listed.

No referral to Zimmermann [9] for diagrams should be made. Nearly all of the circuits have been changed. All documentation of the correlation polarimeter is presented here.

1. LISTING - FRONT PANEL COMPONENTS AND REAR PANEL CONNECTORS

Figure 36 shows a picture of the front panel of the correlation polarimeter. The components are from top to bottom and left to right

- Power switch
- the switches and potentiometers for gain adjustment and the selection of amplifier stages in both channels
- the potentiometers to set the gain of the outer loop amplifier, the AGC amplifier and of the servo amplifier
- the control potentiometer for AFC gain and AFC reference voltage and the switch to reset the integrator of the AFC circuit (AFC circuit is not used and not operational at this time).

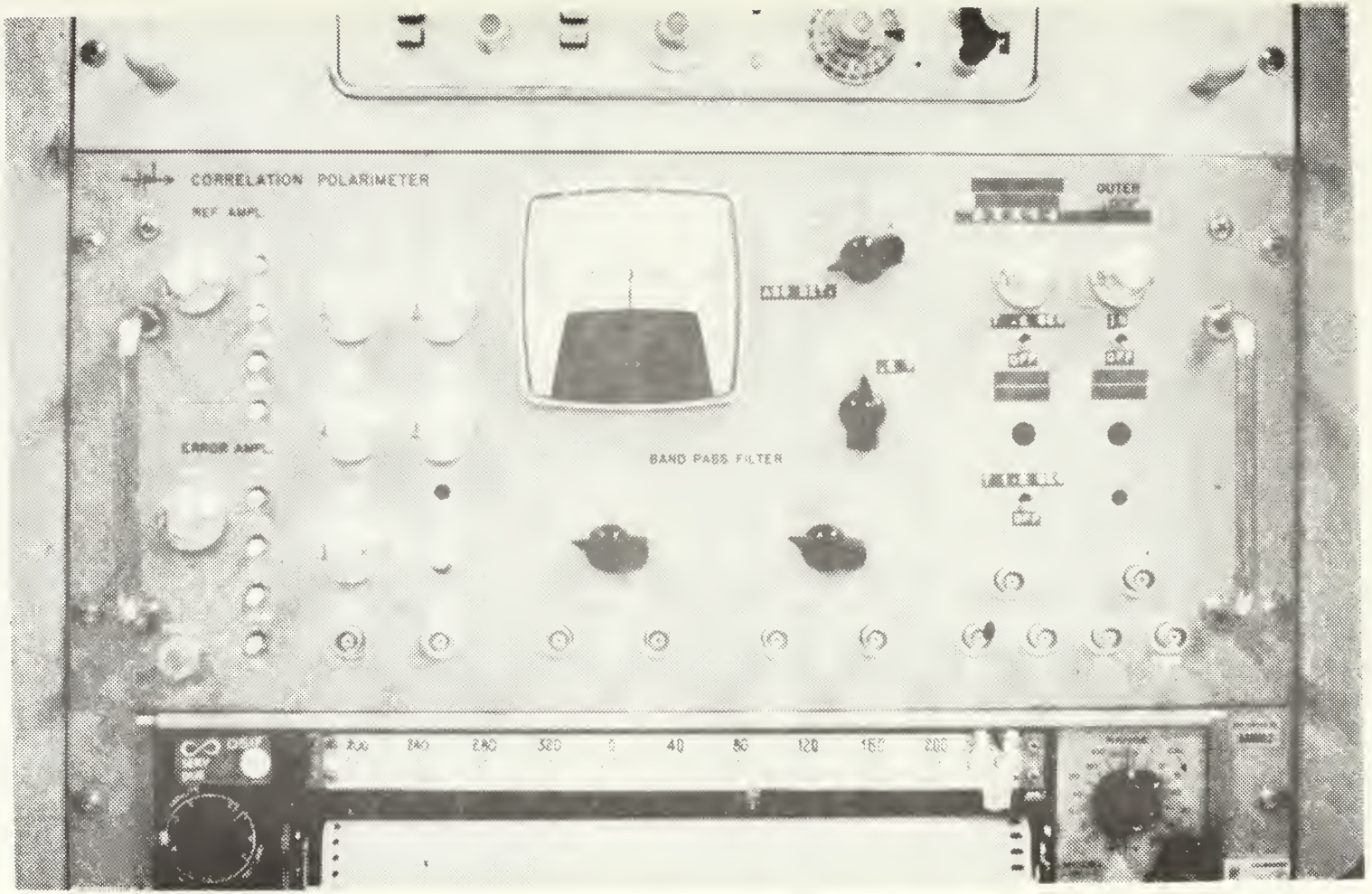

Figure 36 FRONT PANEL OF CORRELATION POLARIMETER CHASSIS

- the panel meter
- the selector switches for the band pass filter in reference and error channel
- the switch to connect different subsystems to the panel meter
- the range select switch for the panel meter
- the potentiometer to zero the servo amplifier and two switches to select additional RC filtering for the servo amplifier
- the potentiometer to zero the outer loop amplifier and the switch to enable or disable the outer loop
- and all the BNC connectors for monitoring purposes.

The rear panel connectors are given from left to right (rear view)

- J 1 Reference channel input (TNC)
- J 2 error channel input (TNC)
- J 3 reference channel local oscillator input (TNC)
- J 4 error channel local oscillator input (TNC)
- AFC output (TNC)
- J 5 AGC out (Bendix-PT 00A-8-45)
- J 6 servo out (Bendix - PT 02 E-8-45)

2. LOCATION AND FUNCTION OF CIRCUIT BOARDS, TRIMPOTENTIOMETERS AND TESTPOINTS

Figure 37 shows a top view into the correlation polarimeter, clearly identifying the location of the circuit boards. Figure 38 gives a bottom view showing the internal wiring of the correlation polarimeter. In the listings in connection with Figure 39 all adjustable components, testpoints and switches are specified by location and function.

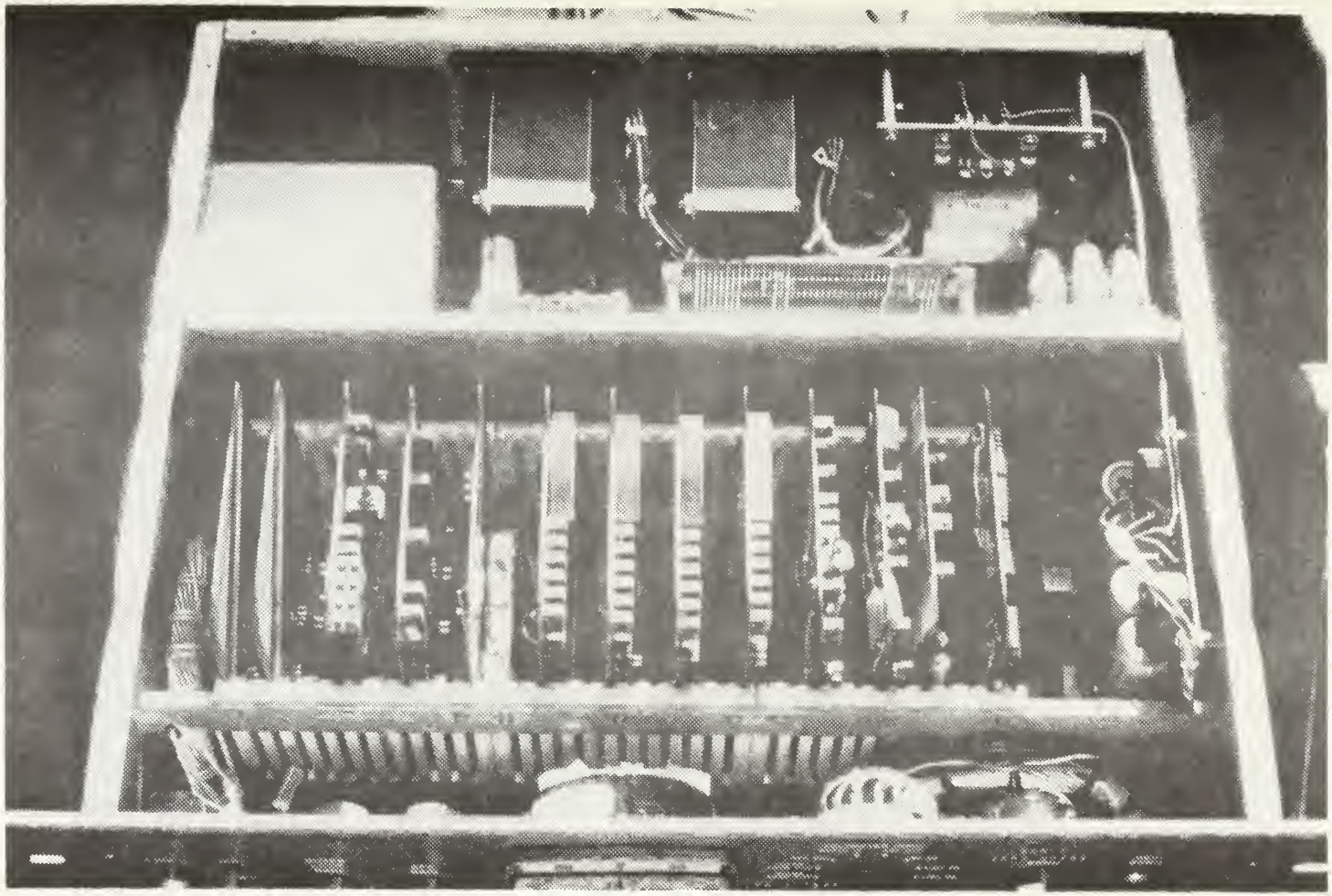

Figure 37 TOP VIEW OF CORRELATION POLARIMETER CHASSIS

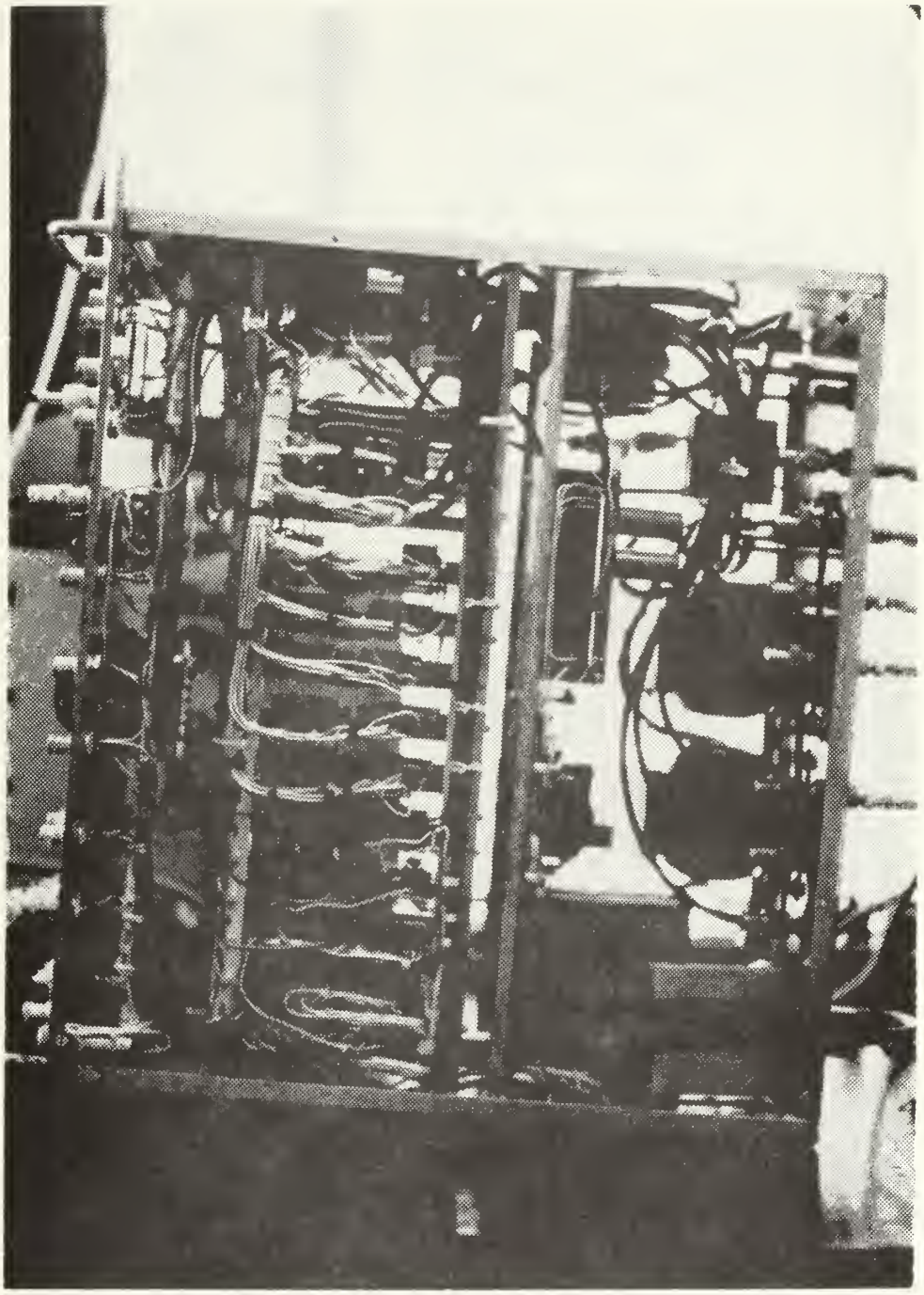

Figure 38 BOTTOM VIEW OF CORRELATION POLARIMETER CHASSIS

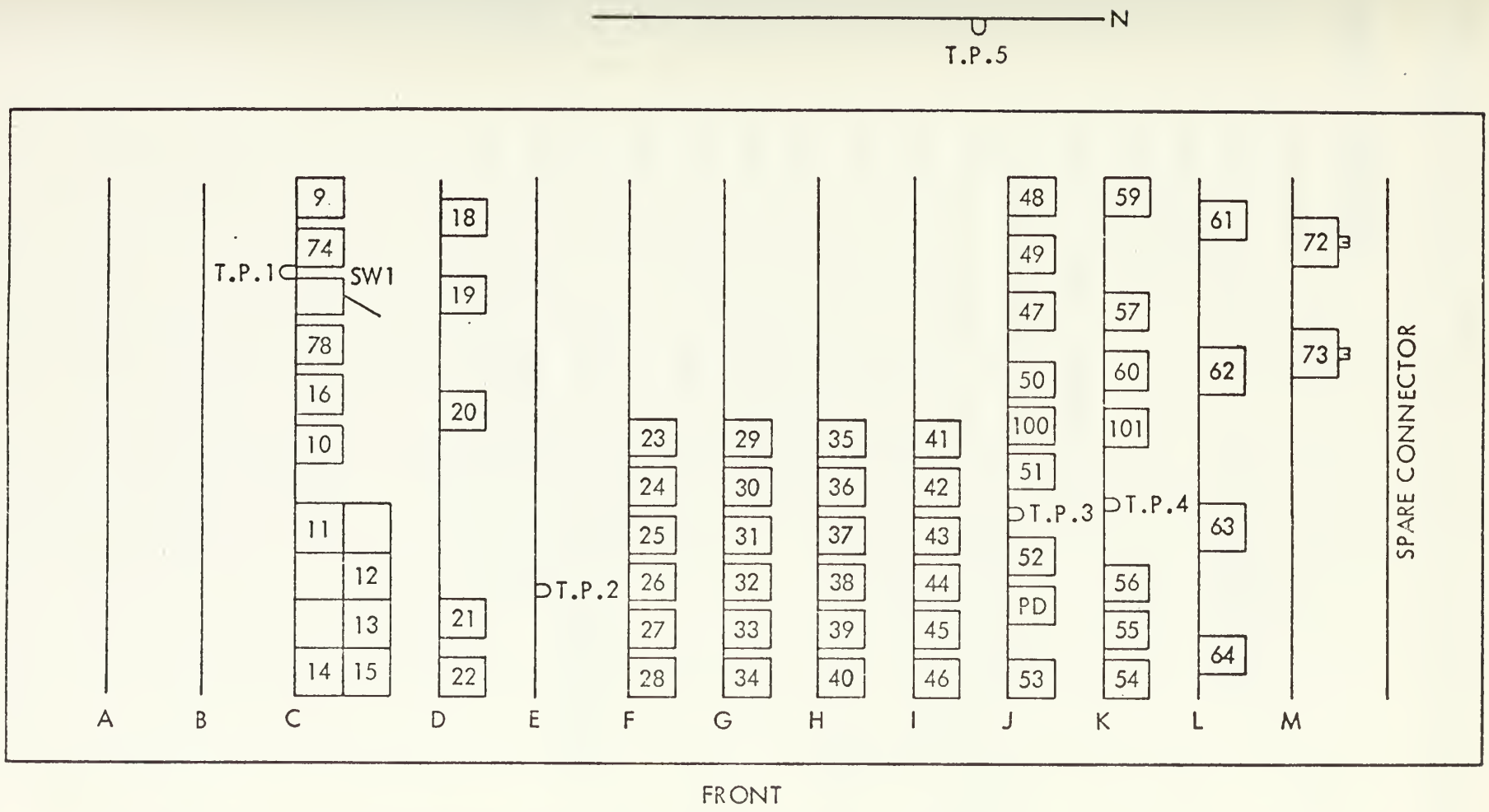

Figure 39 CORRELATION POLARIMETER CIRCUIT BOARD LOCATION

Listing of Circuit Boards in the Correlation Polarimeter

Board	Function
A	Reference Channel 5 KC IF Amplifiers
B	Error Channel 5 KC IF Amplifiers
C	AFC Circuit
D	AGC Circuit
E	5 KC IF Error Channel BPF
F	250 Hz Reference BPF's, BW = 5, 12.5, 25 Hz
G	250 Hz Reference BPF's, BW = 50, 125 Hz, Spare
H	250 Hz Error BPF's, BW = 5, 12.5, 25 Hz
I	250 Hz Error BPF's, BW = 50, 125 Hz, Spare
J	Inner Loop Phasedetector
K	Outer Loop Phasedetector
L	Servo Output Amplifier, Outer Loop Output Amplifier, 250 Hz IF Reference and Error Amplifiers
M	4750 Hz Local Oscillator Board
N	5 KC IF Reference Channel BPF

Listing of Potentiometers, Testpoints, and Switch On Circuit Boards

Board	Component No.	Value	Function
C	9	10 K	DC offset adjust of low pass filter in AFC circuit
	74	10 K	Adjsut of AFC threshold voltage
	SW 1		Polarity switch of AFC voltage
	TP 1		Output integrator No. 16 (AFC)
	78	10 K	not used
	16	10 K	DC offset adjust for integrator stage, operational amplifier 740, No. 16
	10	10 K	DC offset adjust for summing amplifier No. 10
	11	10 K	DC offset adjust for amplifier No. 11
	12	10 K	DC offset adjust for amplifier No. 12
	13	10 K	not used
	14	10 K	not used
	15	10 K	gain adjust for AFC input
D	18	10 K	DC offset adjust last stage AGC amplifier No. 18
	19	10 K	DC offset adjust amplifier No. 19
	20	10 K	DC offset adjust amplifier No. 20
	21	10 K	DC offset adjust amplifier No. 21
	22	10 K	AGC ac gain adjust

Board	Component No.	Value	Function
E	TP 2		Output 5 KC Error channel BPF
F	23	20 K	Frequency adjust for reference channel BPF BW = 5 Hz
	24	500 Ω	Input level adjust for reference BPF BW = 5 Hz
	25	20 K	Frequency adjust for reference channel BPF BW = 12.5 Hz
	26	500 Ω	Input level adjust for reference BPF BW = 12.5 Hz
	27	20 K	Frequency adjust of reference BPF BW = 25 Hz
	28	500 Ω	Input level adjust of reference BPF BW = 25 Hz
G	29	20 K	Frequency adjust of reference BPF BW = 50 Hz
	30	500 Ω	input level adjust of reference BPF BW = 50 Hz
	31	20 K	Frequency adjust of reference BPF BW = 125 Hz
	32	500 Ω	input level adjust of reference BPF BW = 125 Hz
	33	20 K	Frequency adjust of reference BPF spare
	34	500 Ω	Input level adjust of reference BPF spare

Board	Component No.	Value	Function
H	35	20 K	Frequency adjust of error BPF BW = 5 Hz
	36	500 Ω	Input level adjust of error BPF BW = 5 Hz
	37	20 K	Frequency adjust of error BPF BW = 12.5 Hz
	38	500 Ω	Input level adjust of error BPF BW = 12.5 Hz
	39	20 K	Frequency adjust of error BPF BW = 25 Hz
	40	500 Ω	Input level adjust of error BPF BW = 25 Hz
I	41	20 K	Frequency adjust of error BPF BW = 50 Hz
	42	500 Ω	Input level adjust of error BPF BW = 50 Hz
	43	20 K	Frequency adjust of error BPF BW = 125 Hz
	44	500 Ω	Input level adjust of error BPF BW = 125 Hz
	45	20 K	Frequency adjust of error BPF spare
	46	500 Ω	Input level adjust of error BPF spare

Board	Component No.	Value	Function
J	48	10 K	DC offset for summing amplifier No. 48
	49	50 K	Input level adjust of error signal to input amplifier No. 47 of inner loop phase detector
	47	10 K	DC offset for error channel input amplifier to phase detector No. 47
	50	10 K	DC offset for error channel monitor amplifier No. 50
	100	10 K	DC offset for RC filter amplifier No. 100
	51	10 K	DC offset for reference channel monitor amplifier No. 51
	TP 3		Output of phase detector before RC filtering
	52	50 K	Input level adjust for reference channel input to hard limiter of inner loop
	PD	1 K	Balance setting for phase detector
	53	10 K	DC offset adjust of hard limiter No. 53
K	59	10 K	DC offset adjust for outer loop hard limiter No. 59
	57	10 K	DC offset adjust for reference monitor amplifier No. 57
	60	10 K	DC offset adjust for input reference channel amplifier No. 60

Board	Component No.	Value	Function
K	101	10 K	DC offset adjust of RC filter amplifier No. 101
	TP 4		Output of phase detector before RC filtering
	56	10 K	DC offset adjust for error channel monitor amplifier No. 56
	55	50 K	error channel input level adjust
	54	10 K	DC offset adjust for error channel input amplifier No. 54
L	61	10 K	DC offset adjust for outer loop amplifier No. 61
	62	1 K	input level adjust to 250 Hz reference IF amplifier
	63	1 K	Input level adjust to 250 Hz error IF amplifier
	64	10 K	DC offset to servo output amplifier No. 64
M	72	100	Adjust of center frequency of BPF in the 4750 L.O. output
	73	50 K	Gain adjust of the BPF in the 4750 Hz L.O. output
N	TP 5		Output of 5 KC reference channel BPF

3. CORRELATION POLARIMETER - CIRCUIT DIAGRAMS

In this section all circuit diagrams as of May 1975 are given. The operational amplifiers are numbered on the boards and for easy locating these numbers are given on the circuit diagrams also.

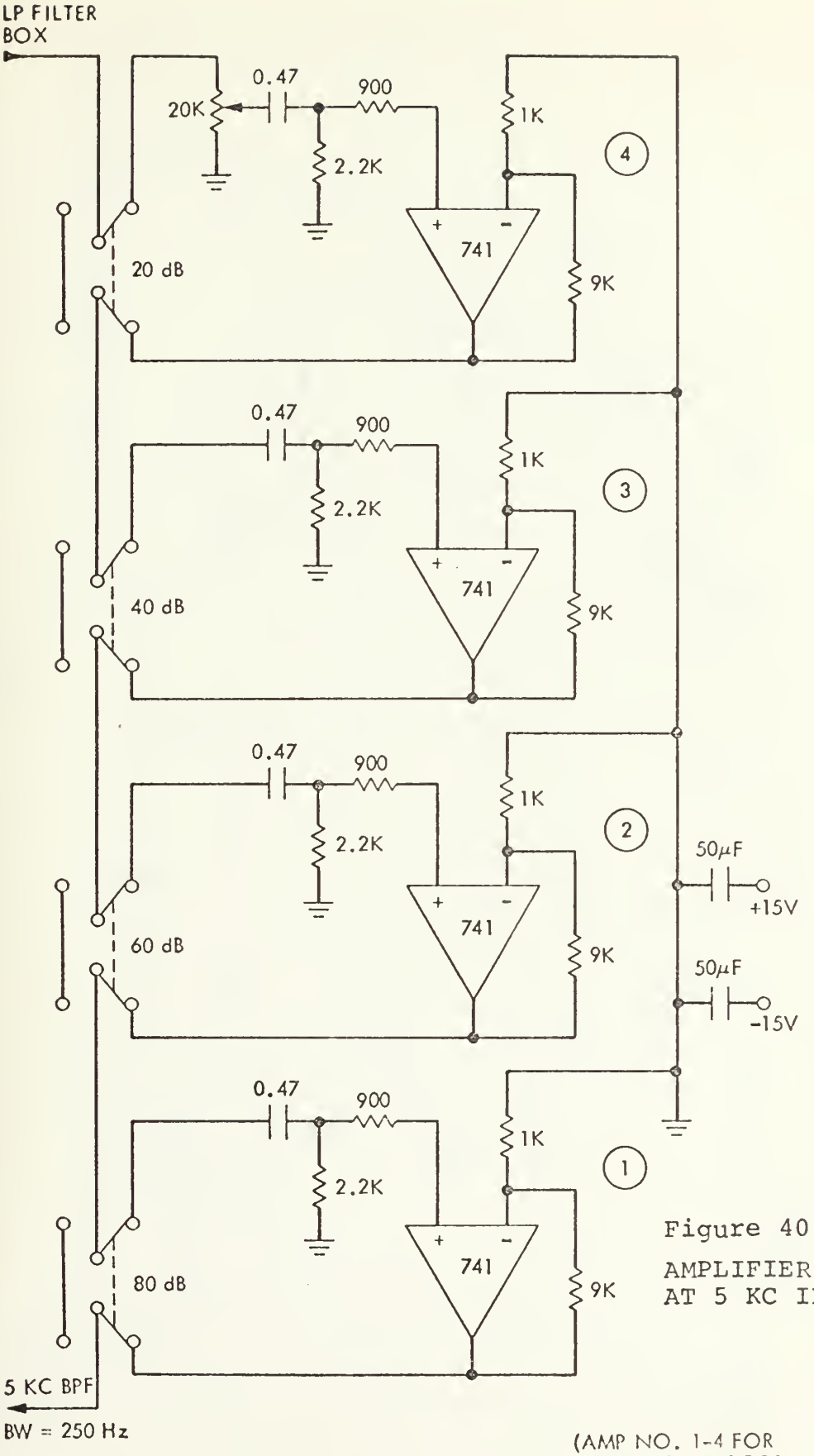

Figure 40

AMPLIFIER STAGES AT 5 KC IF

(AMP NO. 1-4 FOR REFERENCE; 5-8 FOR ERROR CHANNEL)

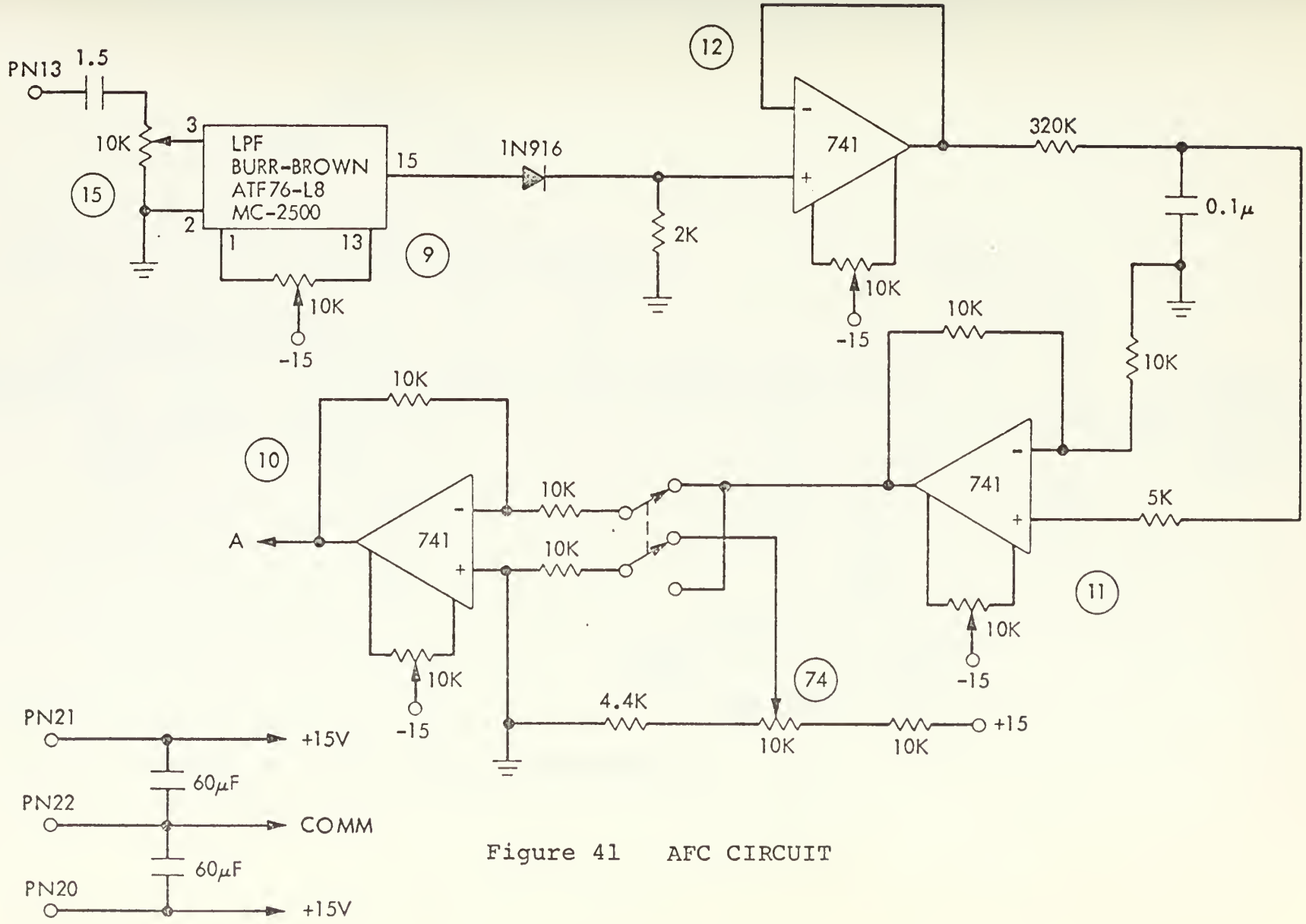

Figure 41 AFC CIRCUIT

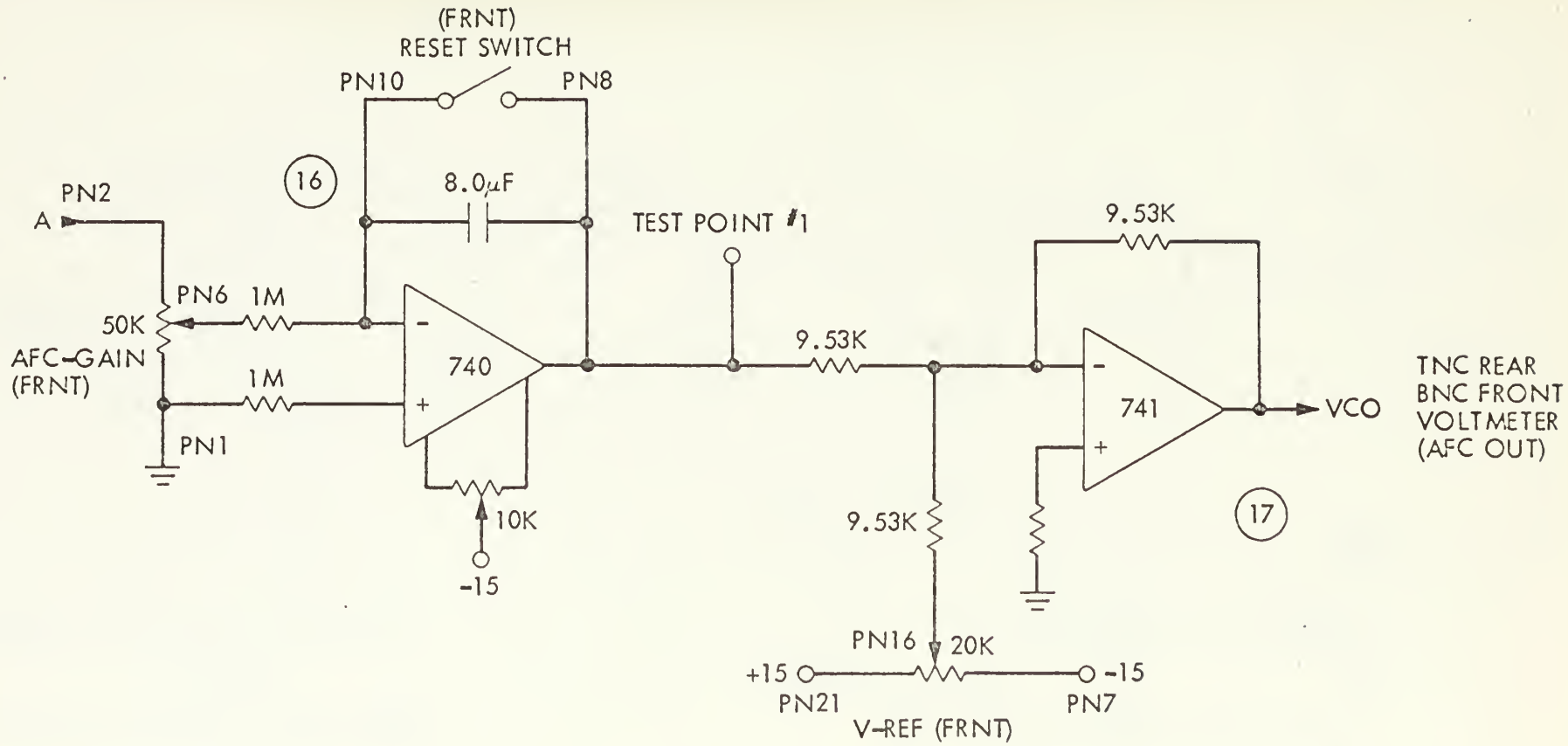

Figure 42 AFC CIRCUIT, CONTINUATION

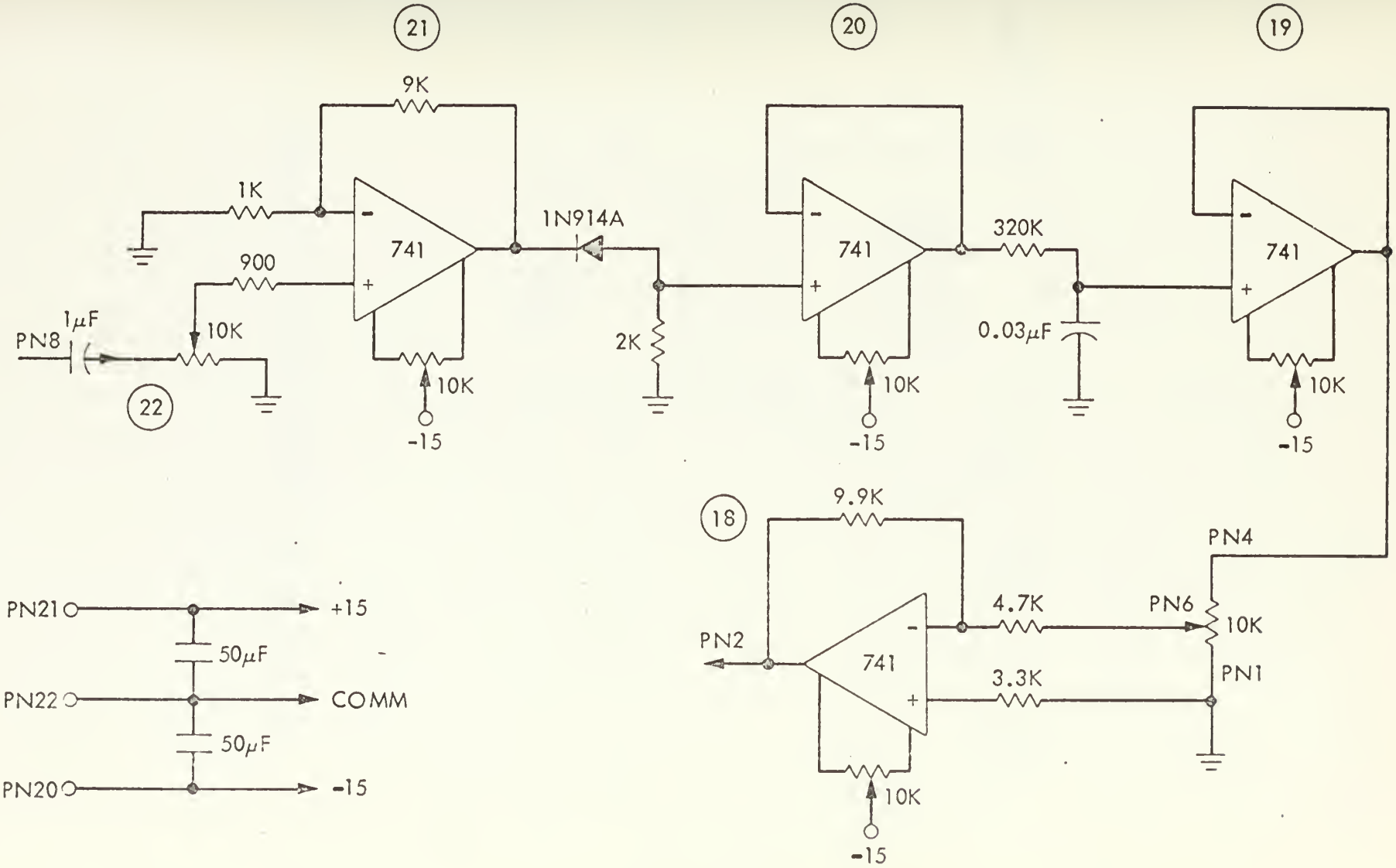

Figure 43 AGC CIRCUIT

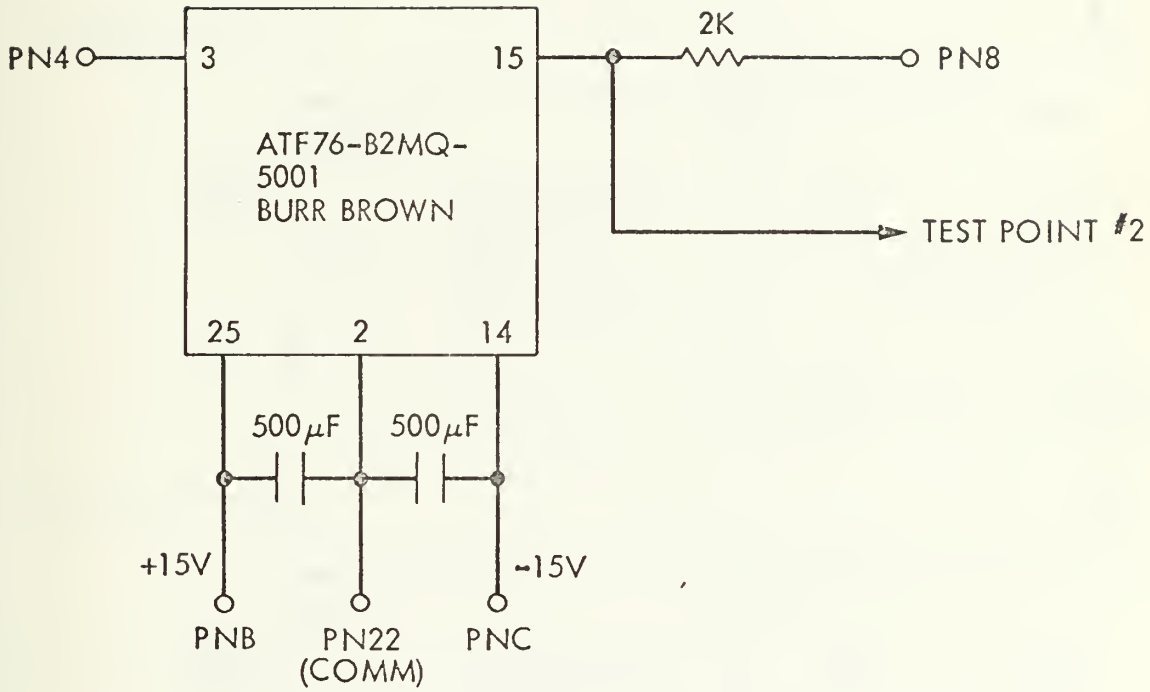

Figure 44 ERROR CHANNEL BPF AT 5 KC IF

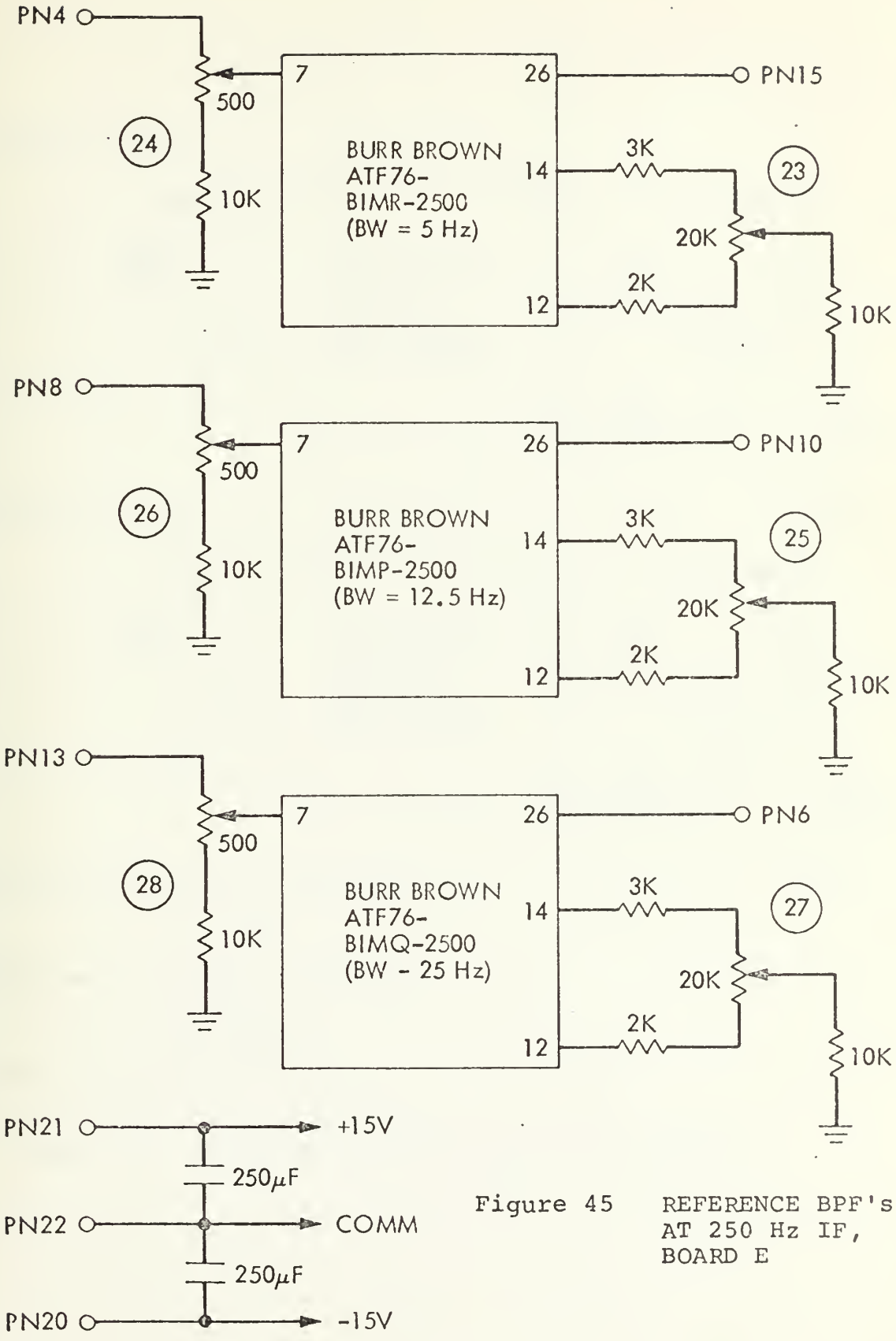

Figure 45 REFERENCE BPF's AT 250 Hz IF, BOARD E

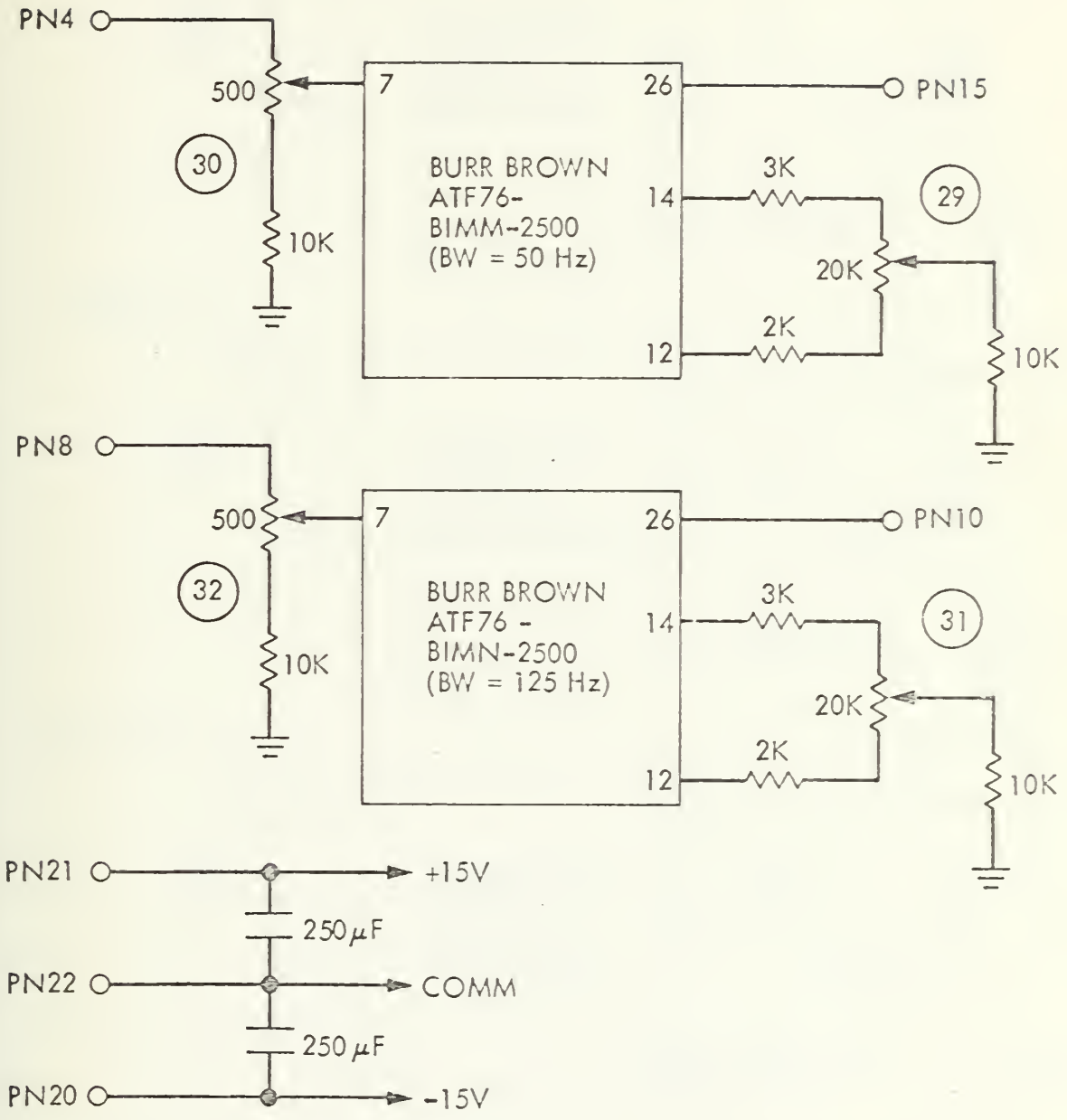

Figure 46 REFERENCE BPF's AT 250 HZ IF, BOARD F

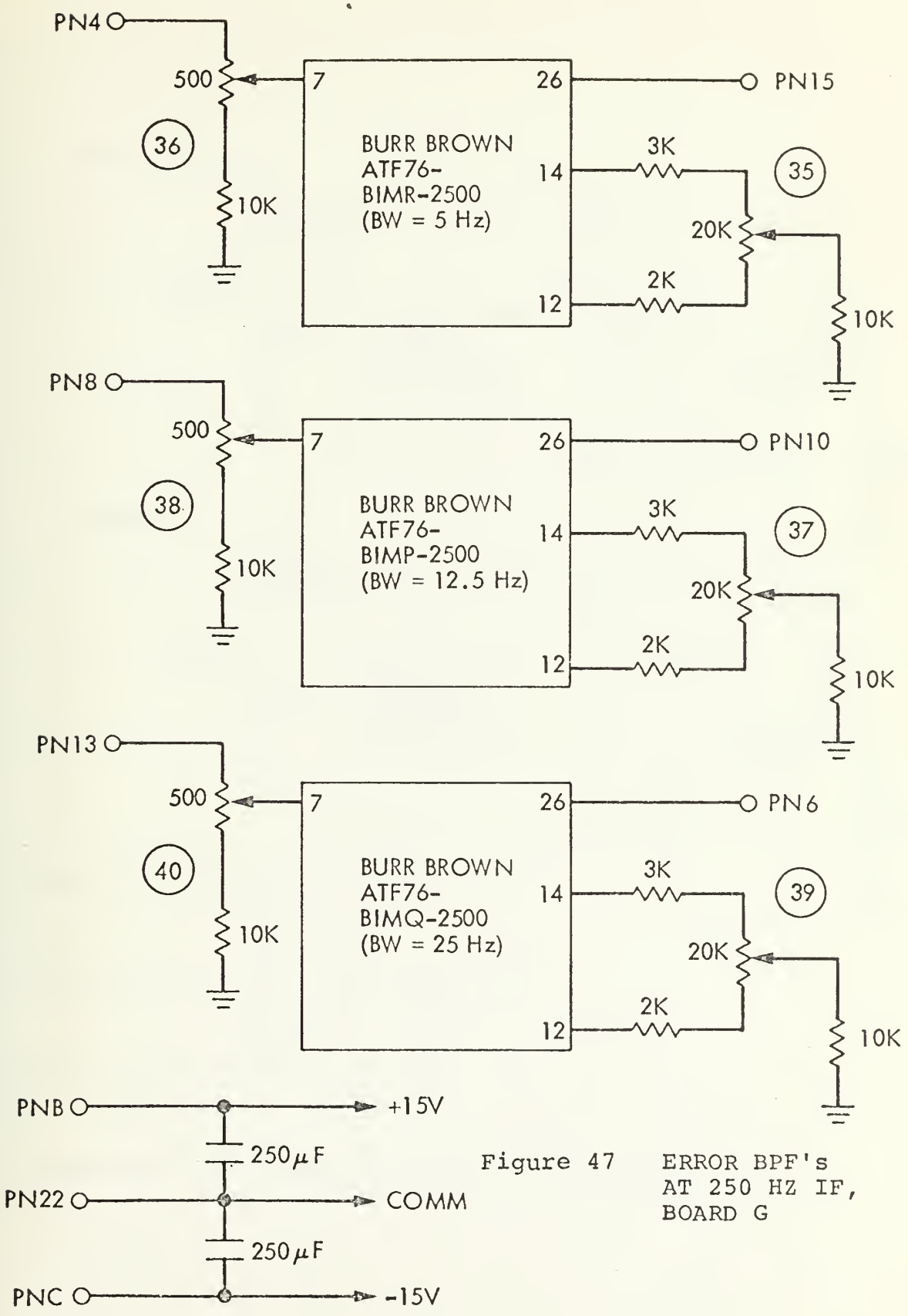

Figure 47 ERROR BPF's AT 250 HZ IF, BOARD G

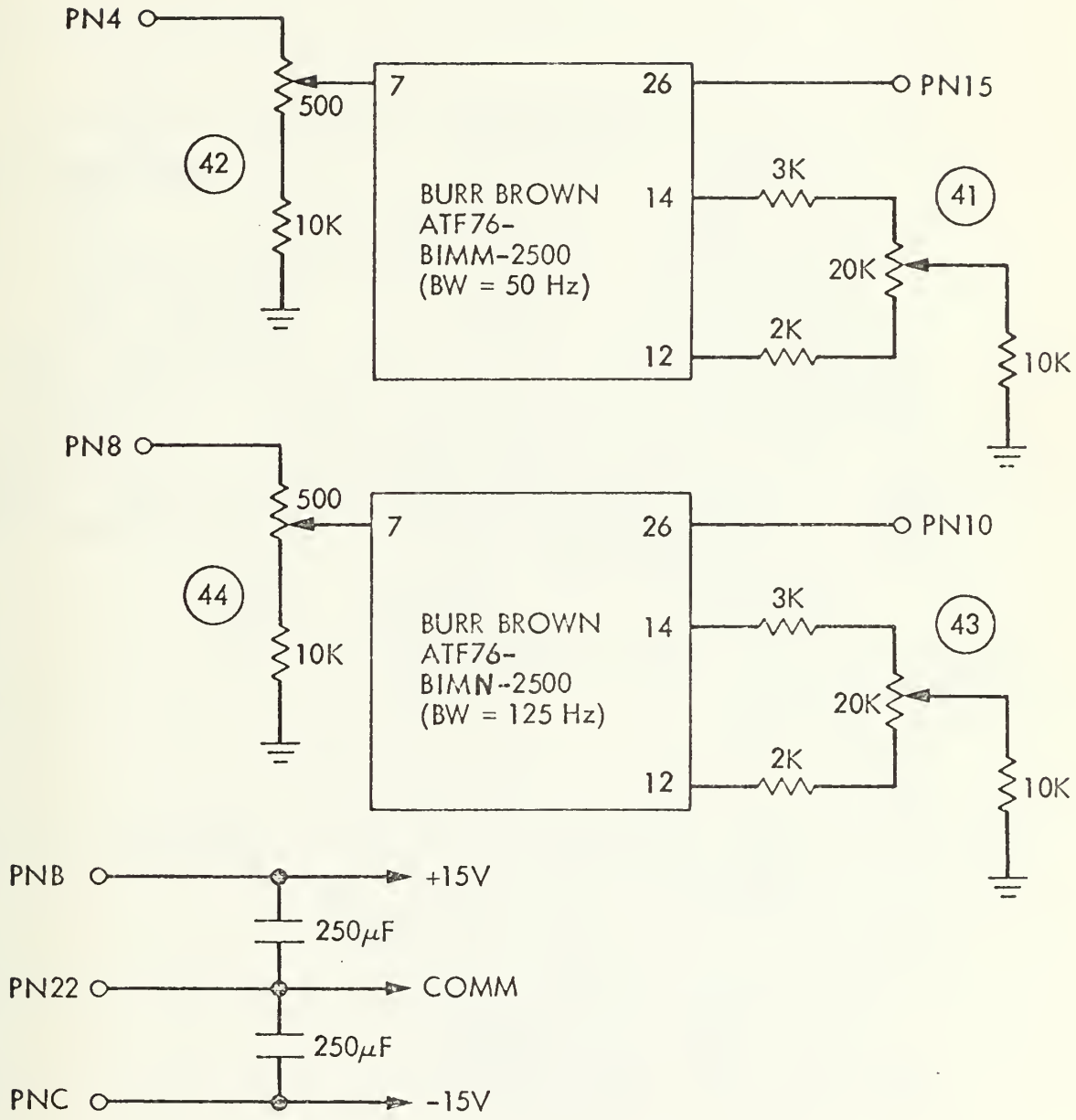

Figure 48 ERROR BPF's AT 250 HZ IF, BOARD H

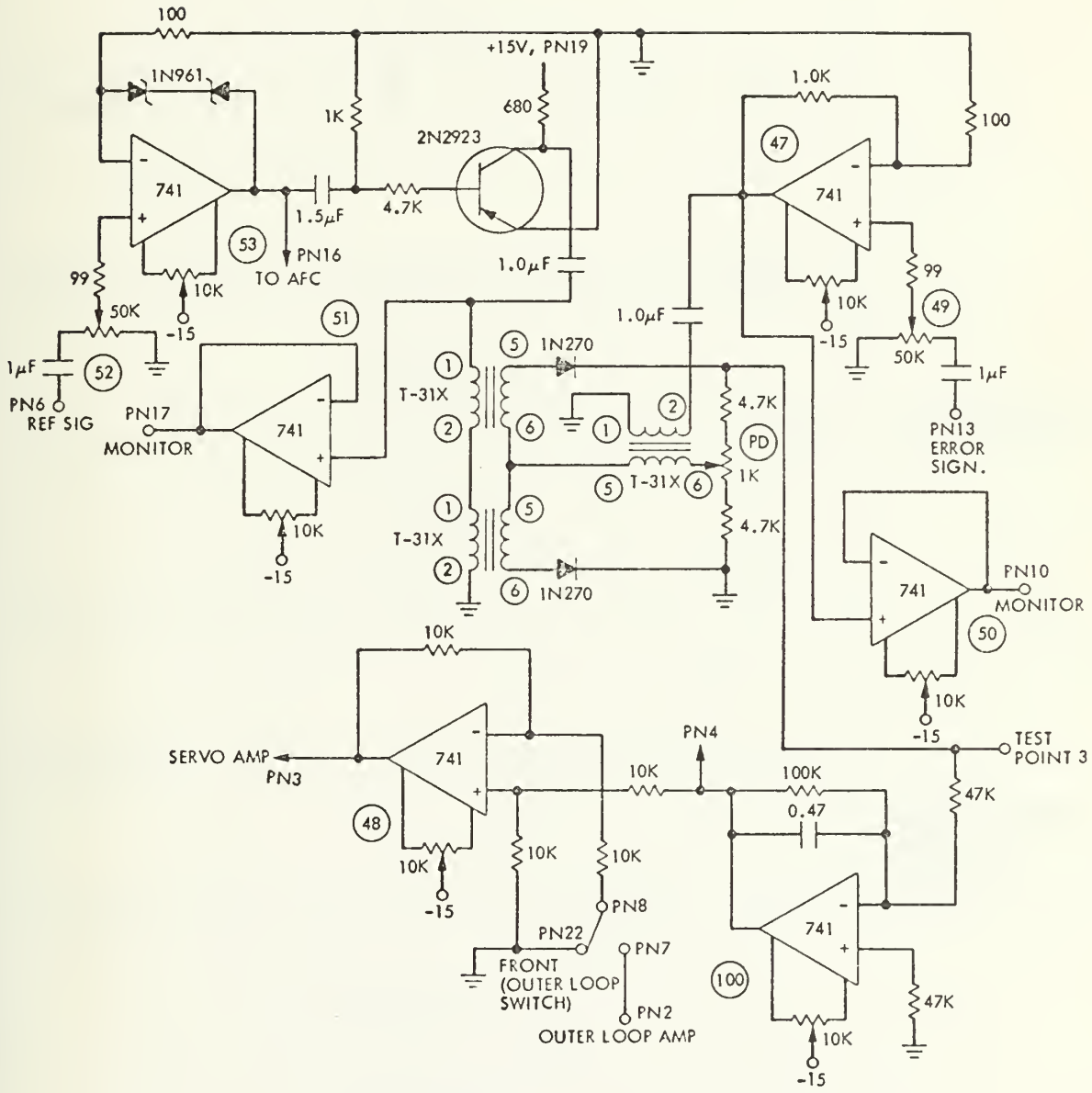

Figure 49 INNER LOOP PHASE DETECTOR CIRCUIT

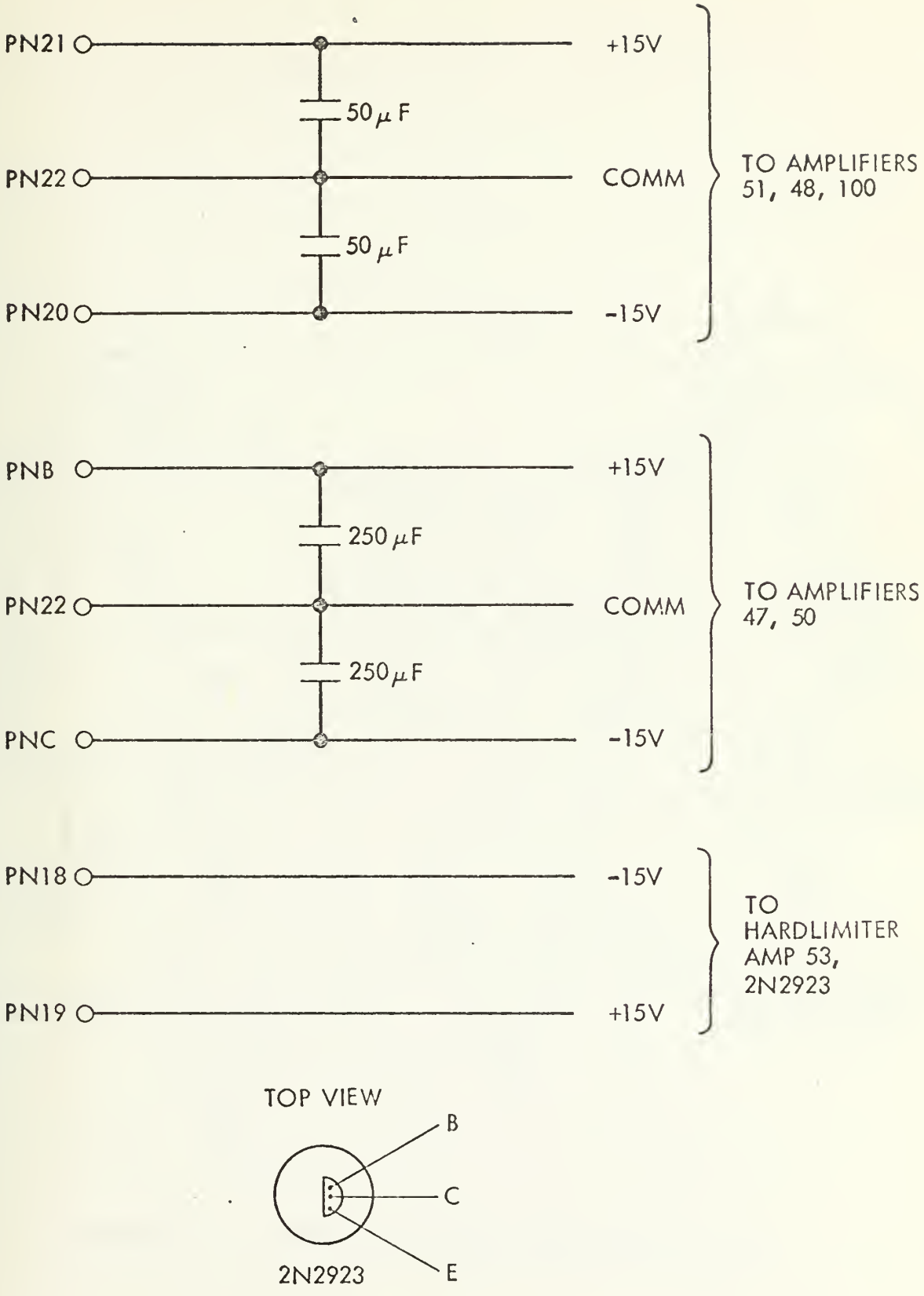

Figure 50 INNER LOOP PHASE DETECTOR CIRCUIT, CONTINUATION

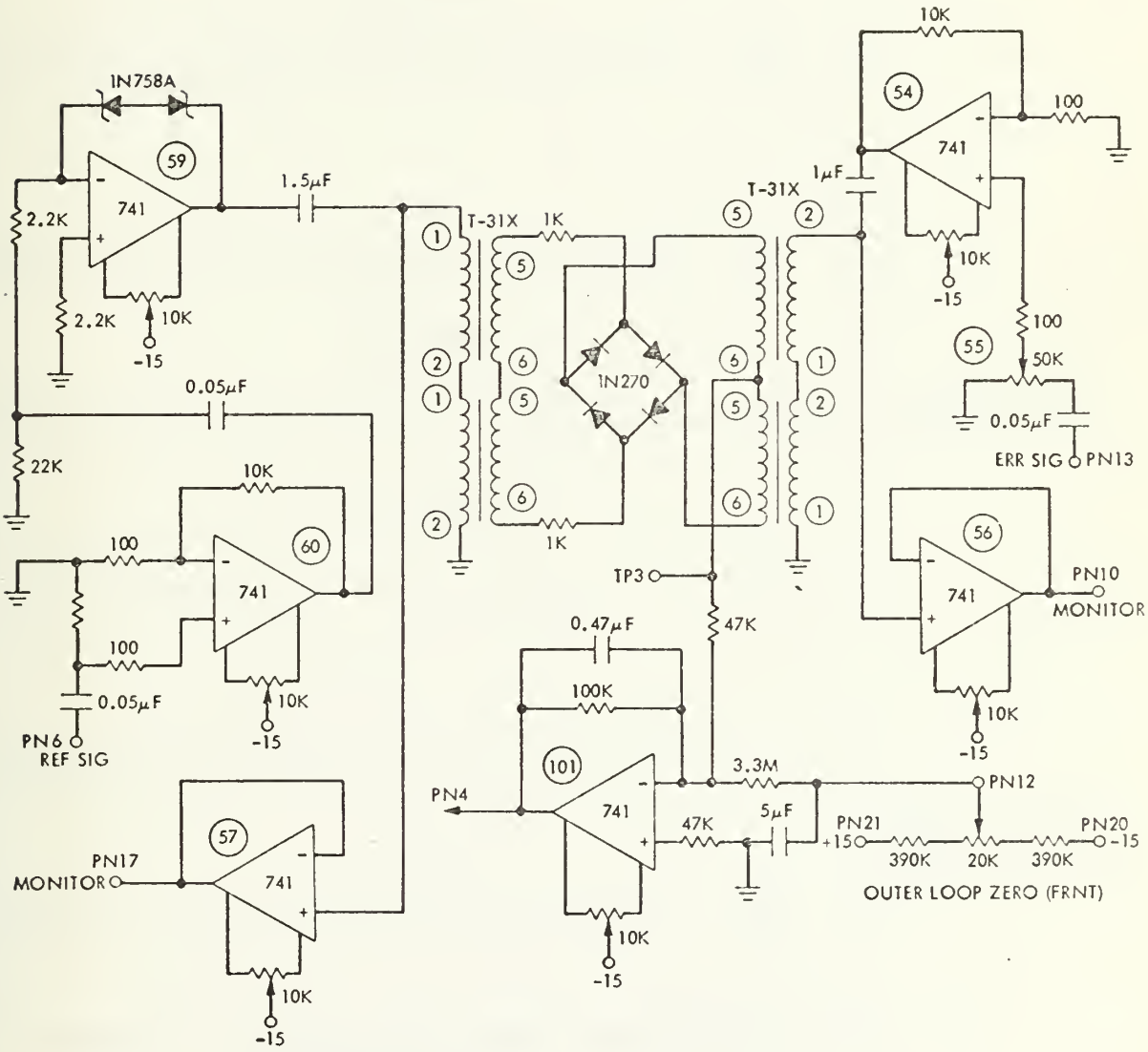

Figure 51 OUTER LOOP PHASE DETECTOR CIRCUIT

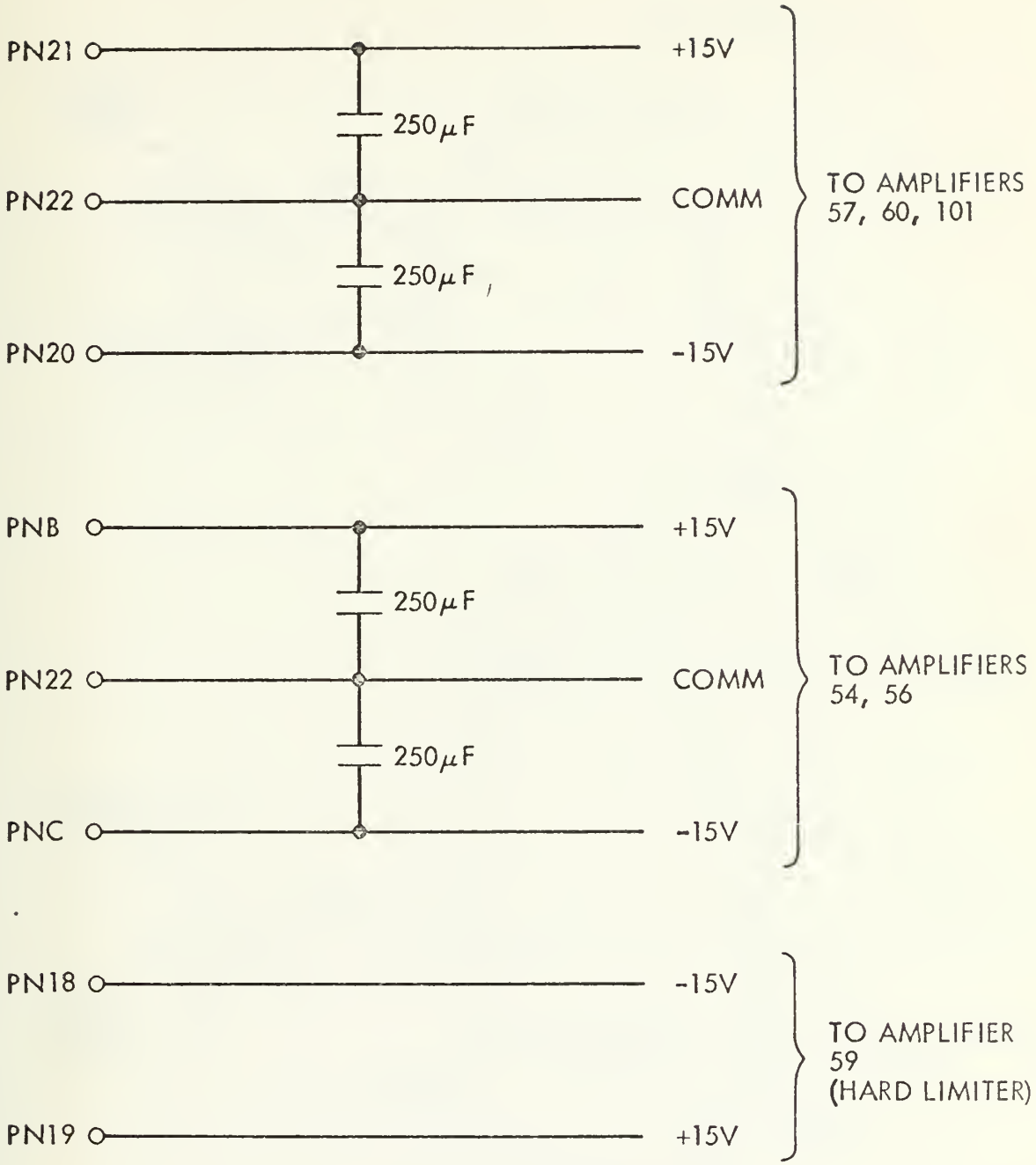

Figure 52 OUTER LOOP PHASE DETECTOR CIRCUIT, CONTINUATION

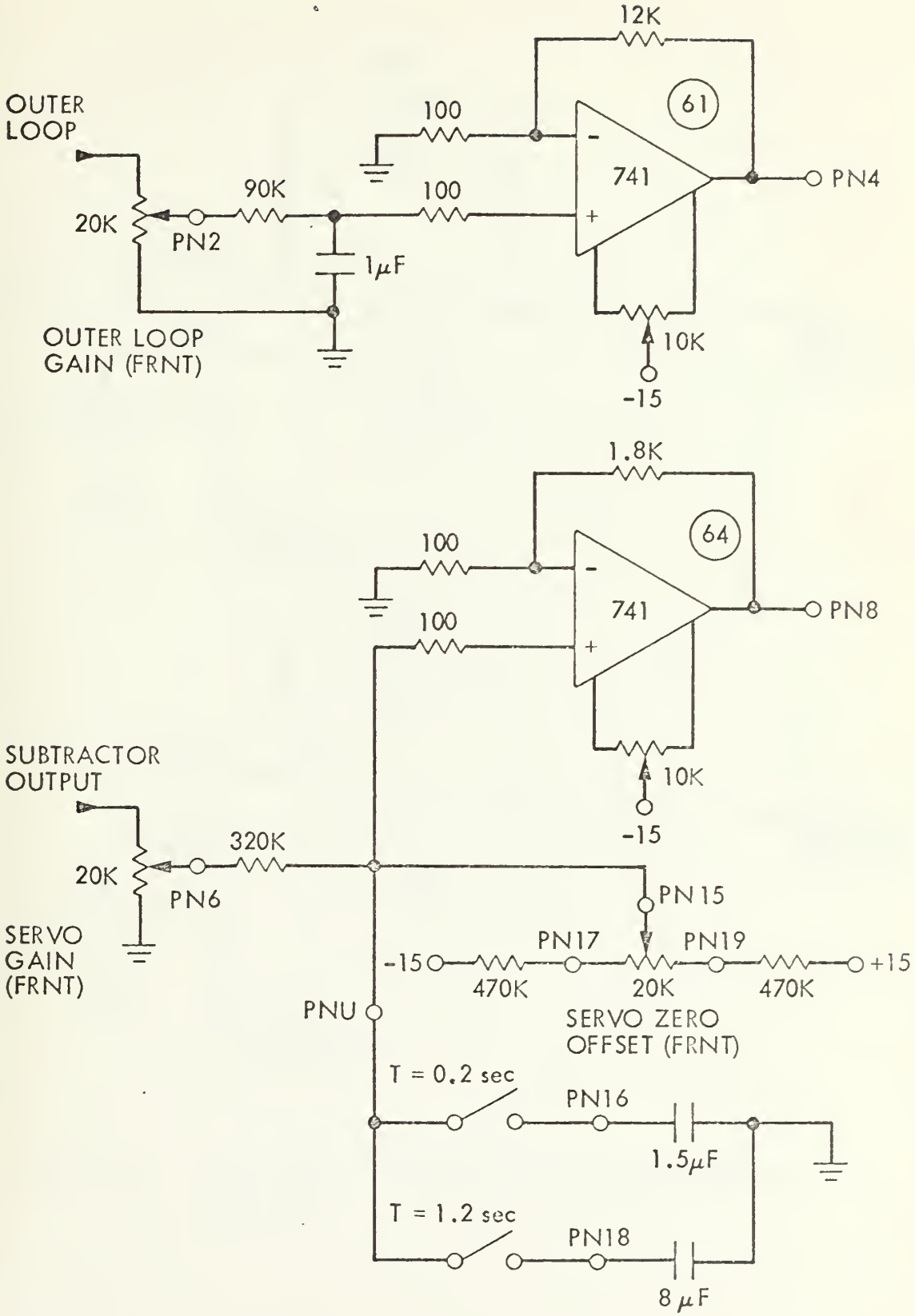

Figure 53 a) OUTER LOOP AMPLIFIER, BOARD L
b) SERVO AMPLIFIER, BOARD L

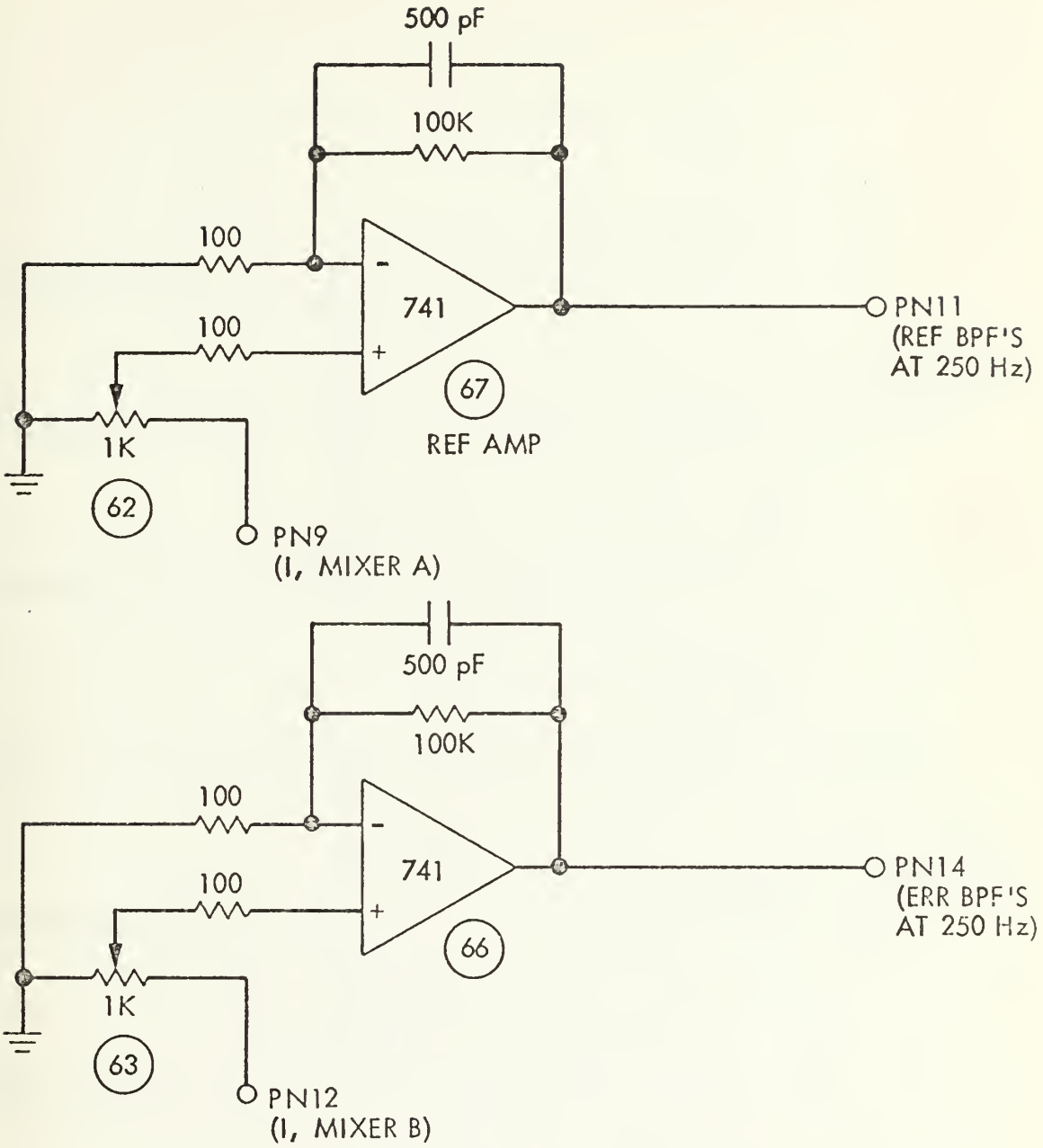

Figure 54 AMPLIFIER IN FRONT OF 250 HZ IF BPF's, BOARD L

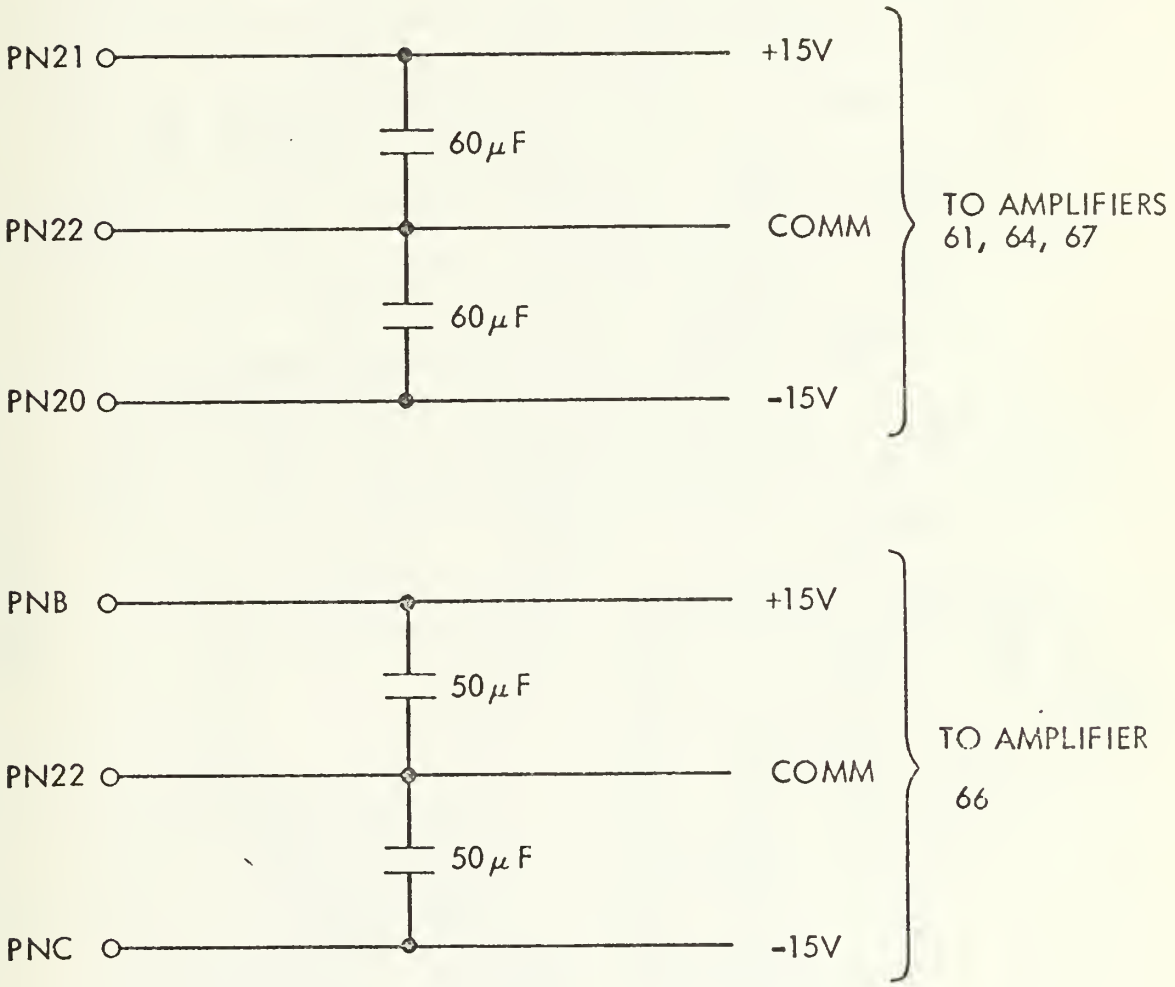

Figure 55 CONTINUATION OF BOARD L

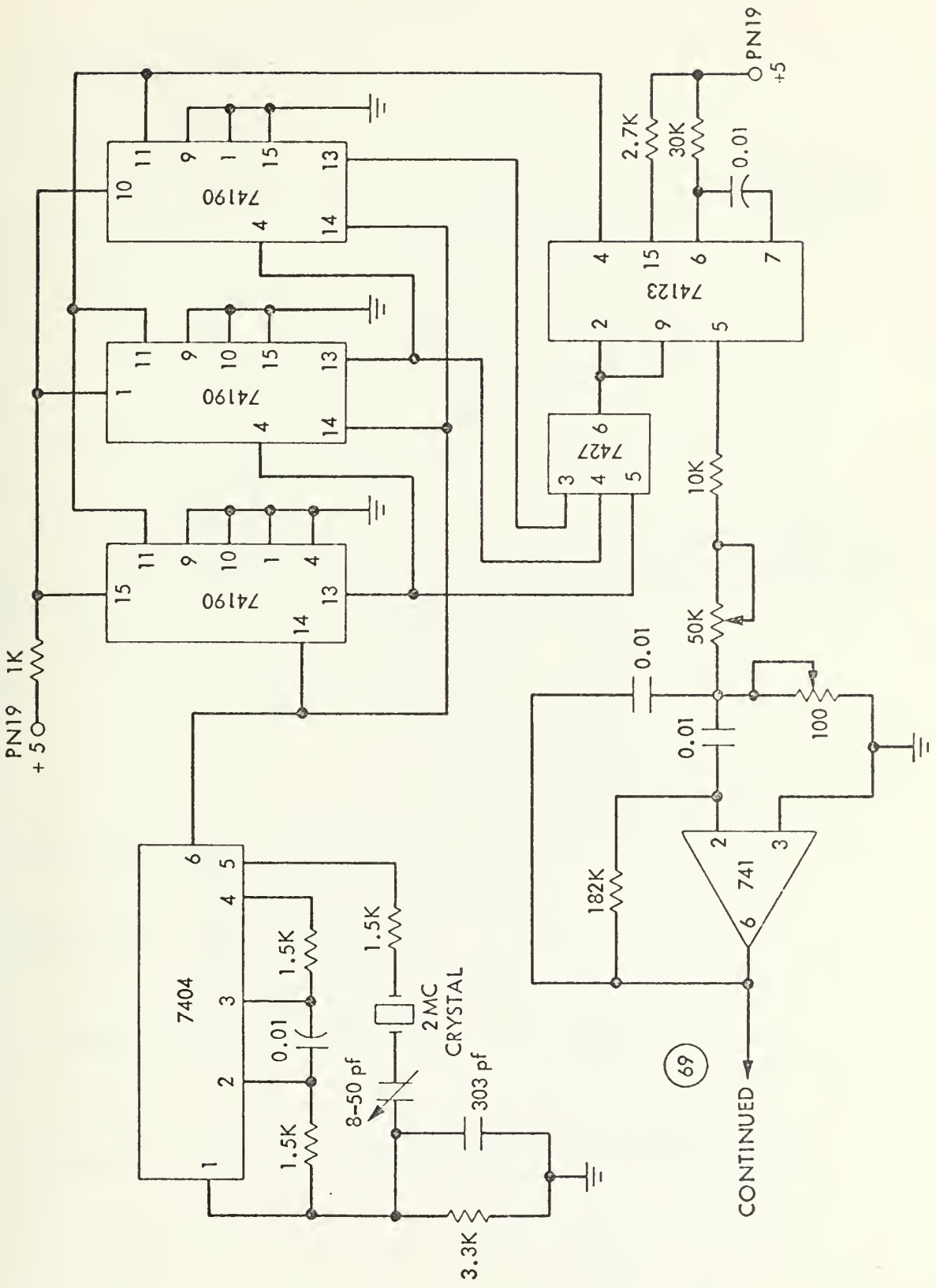

Figure 56 4750 HZ LOCAL OSCILLATOR

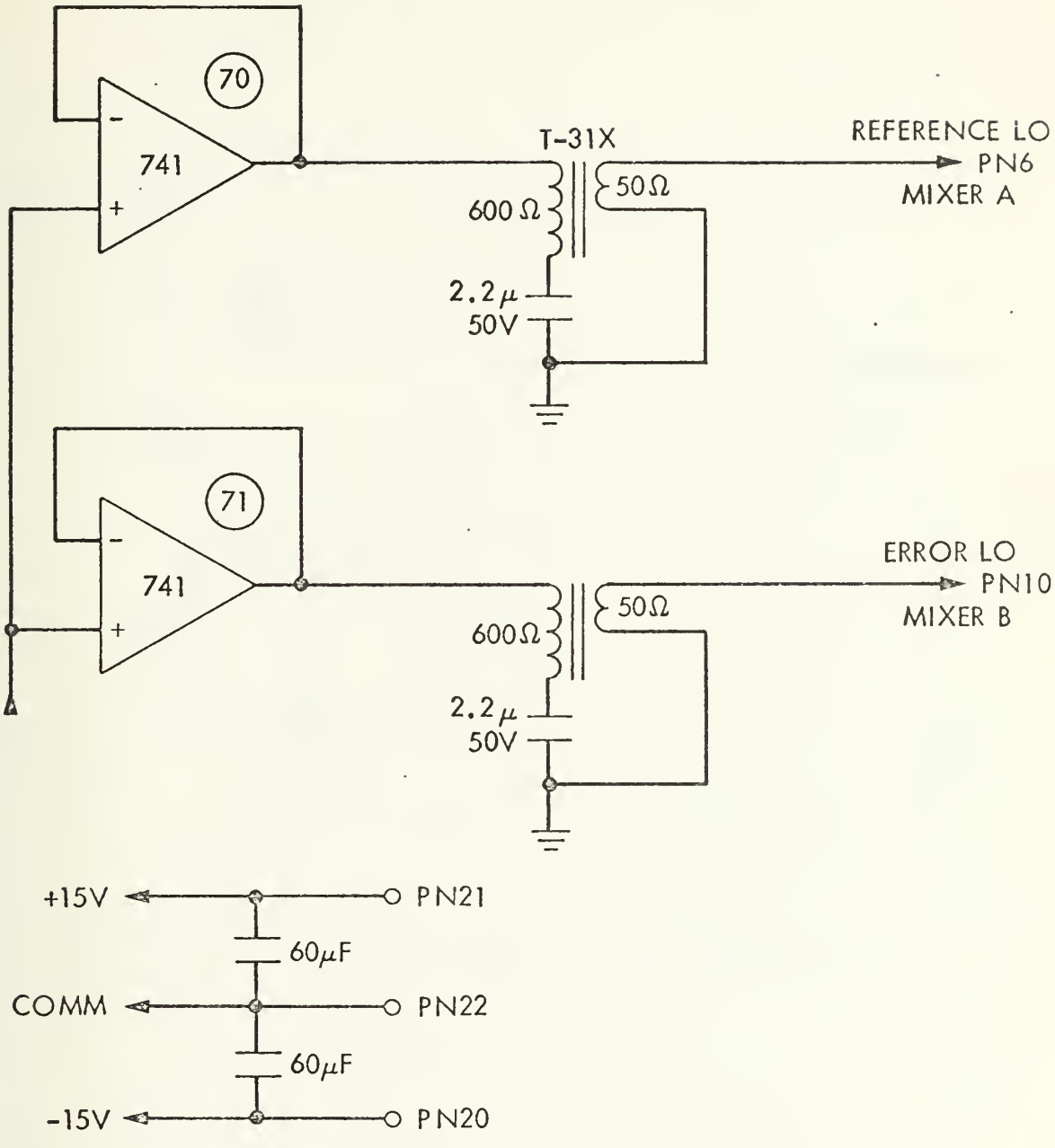

Figure 57 4750 HZ LOCAL OSCILLATOR, CONTINUATION

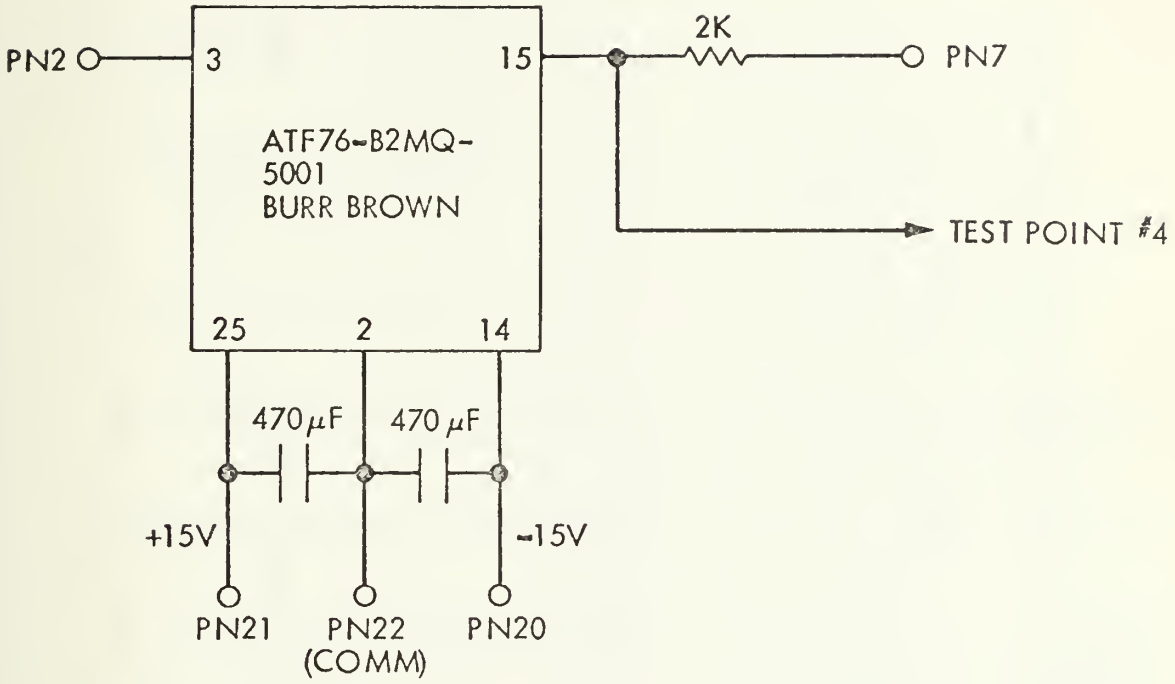

Figure 58 REFERENCE CHANNEL BPF AT 5 KC IF

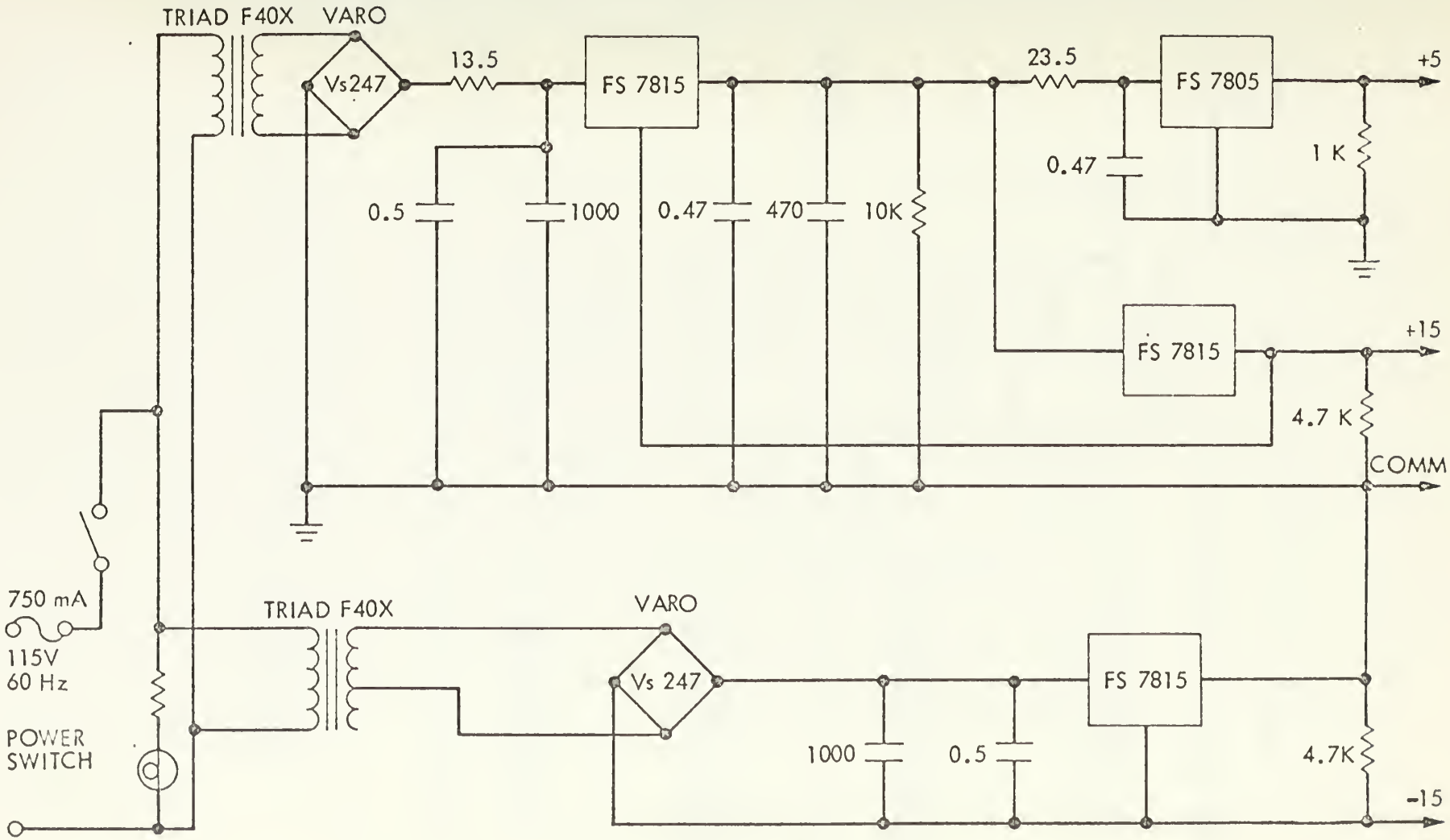

Figure 59 POWER SUPPLY

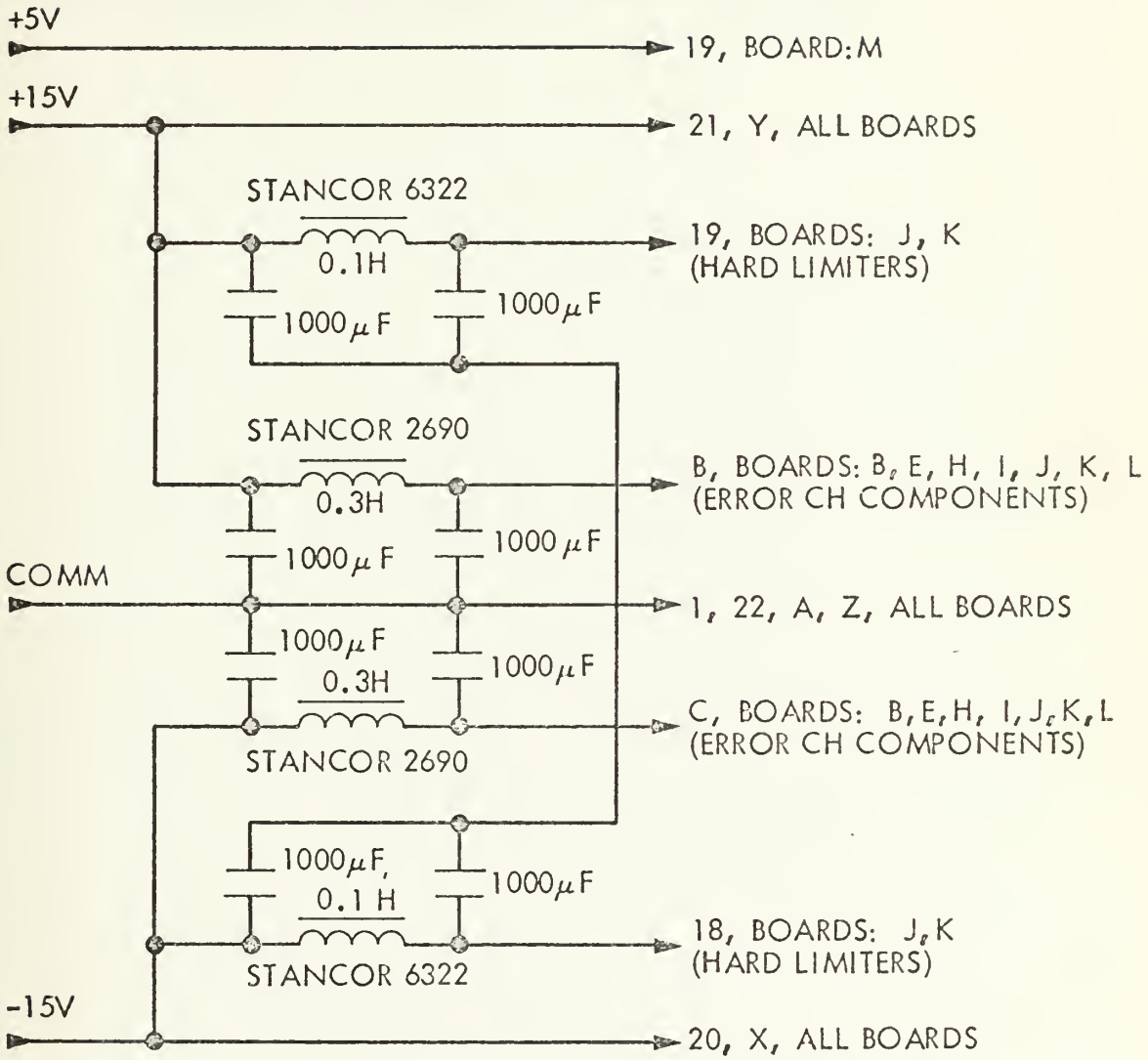

Figure 60 POWER SUPPLY, CONTINUATION

4. CORRELATION POLARIMETER WIRING DIAGRAMS

In the next pages all wiring diagrams as of May 1975 of the Correlation Polarimeter chassis are given.

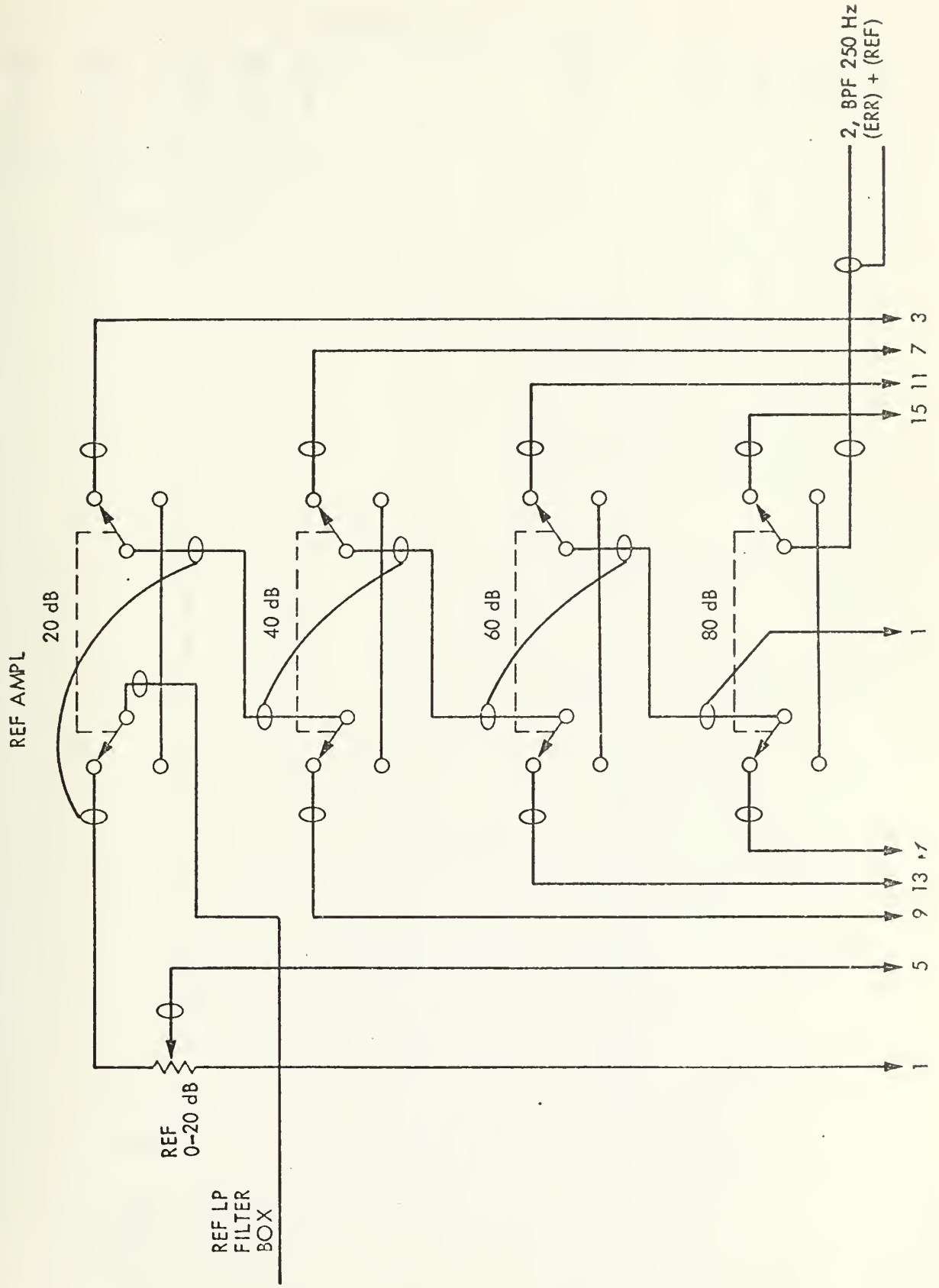

Figure 61 REFERENCE CHANNEL INPUT AMPLIFIER WIRING

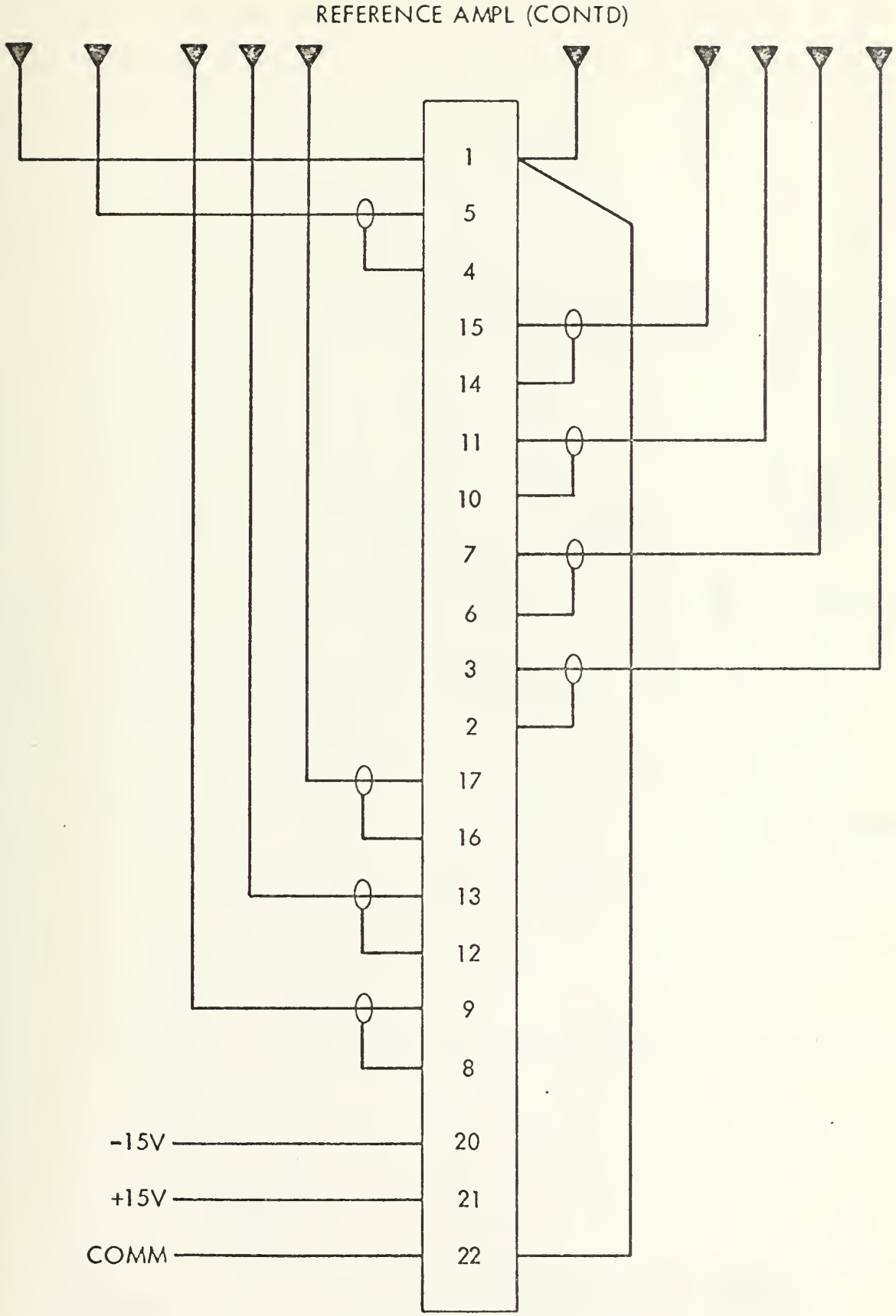

Figure 62 REFERENCE CHANNEL INPUT AMPLIFIER WIRING, CONTINUATION

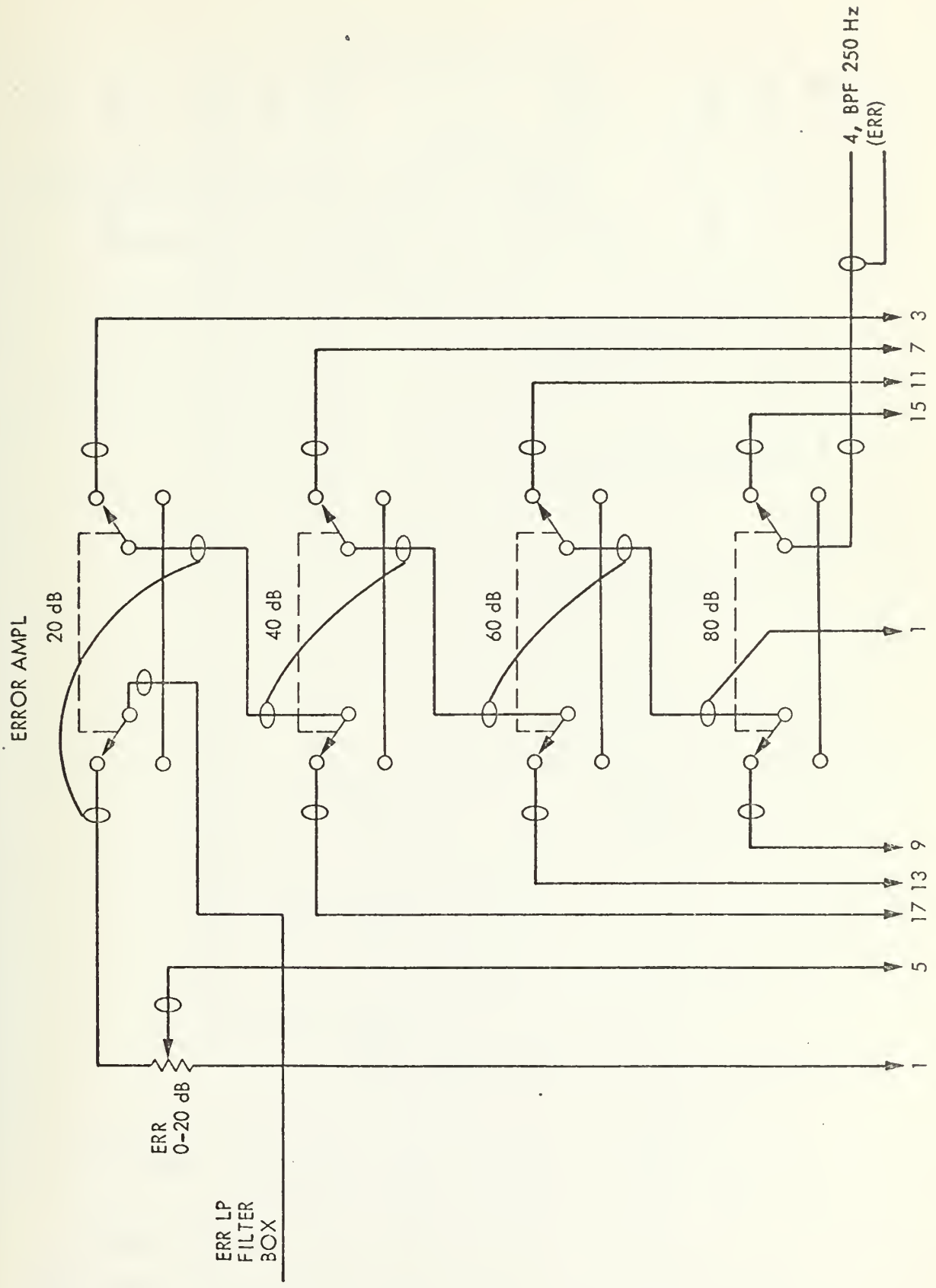

Figure 63 ERROR CHANNEL INPUT AMPLIFIER WIRING

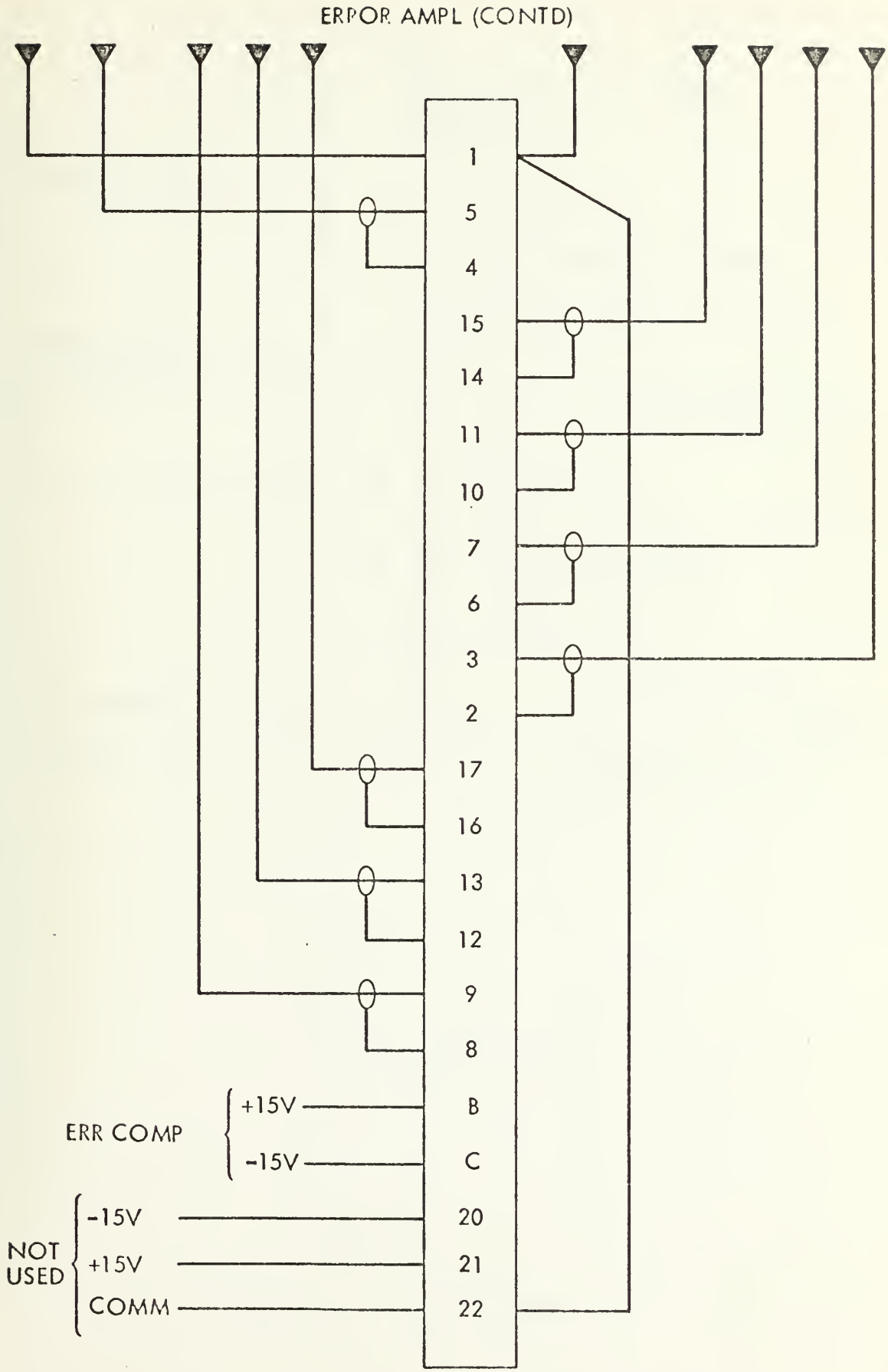

Figure 64 ERROR CHANNEL INPUT AMPLIFIER WIRING, CONTINUATION

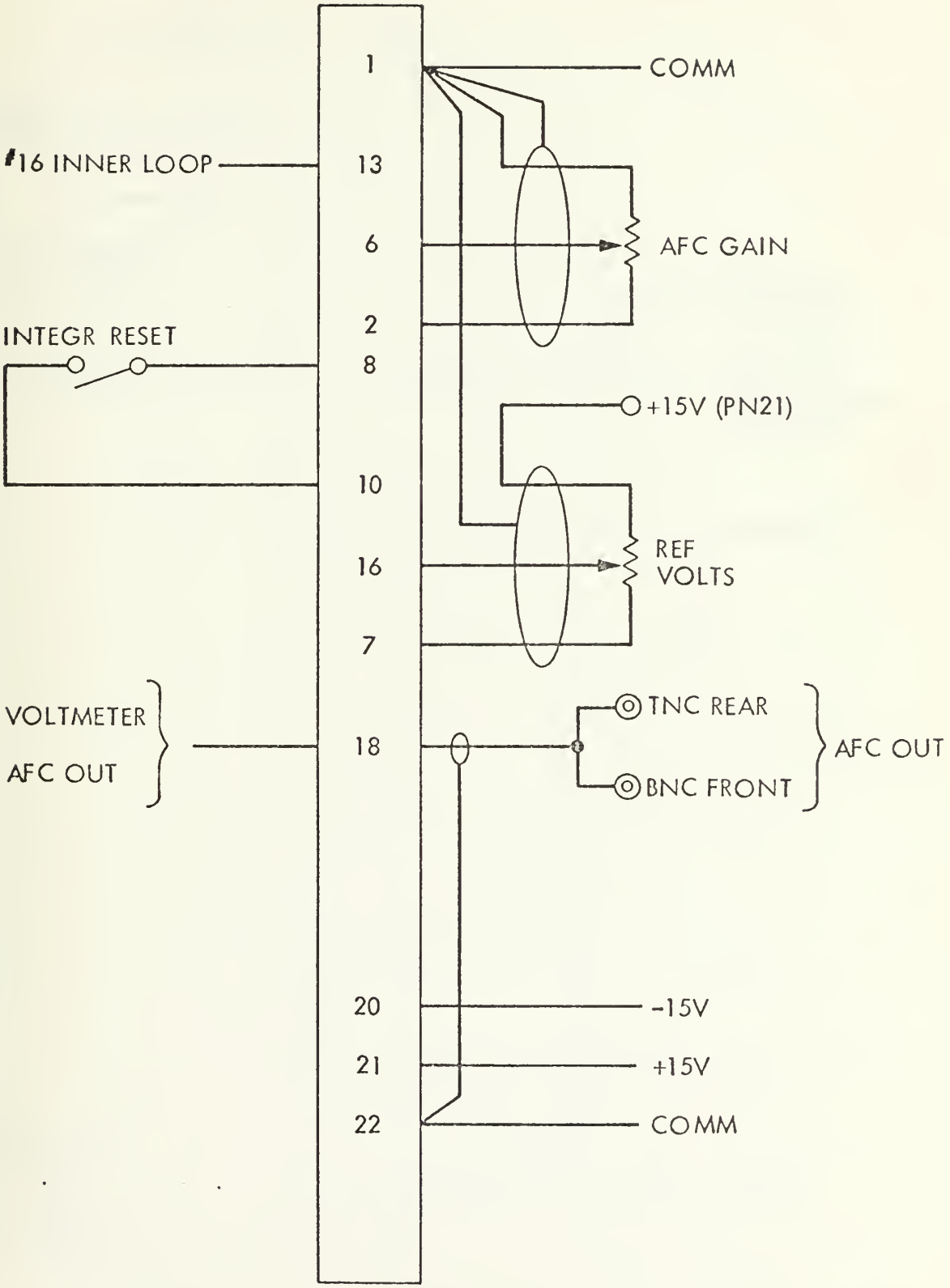

Figure 65 AFC WIRING

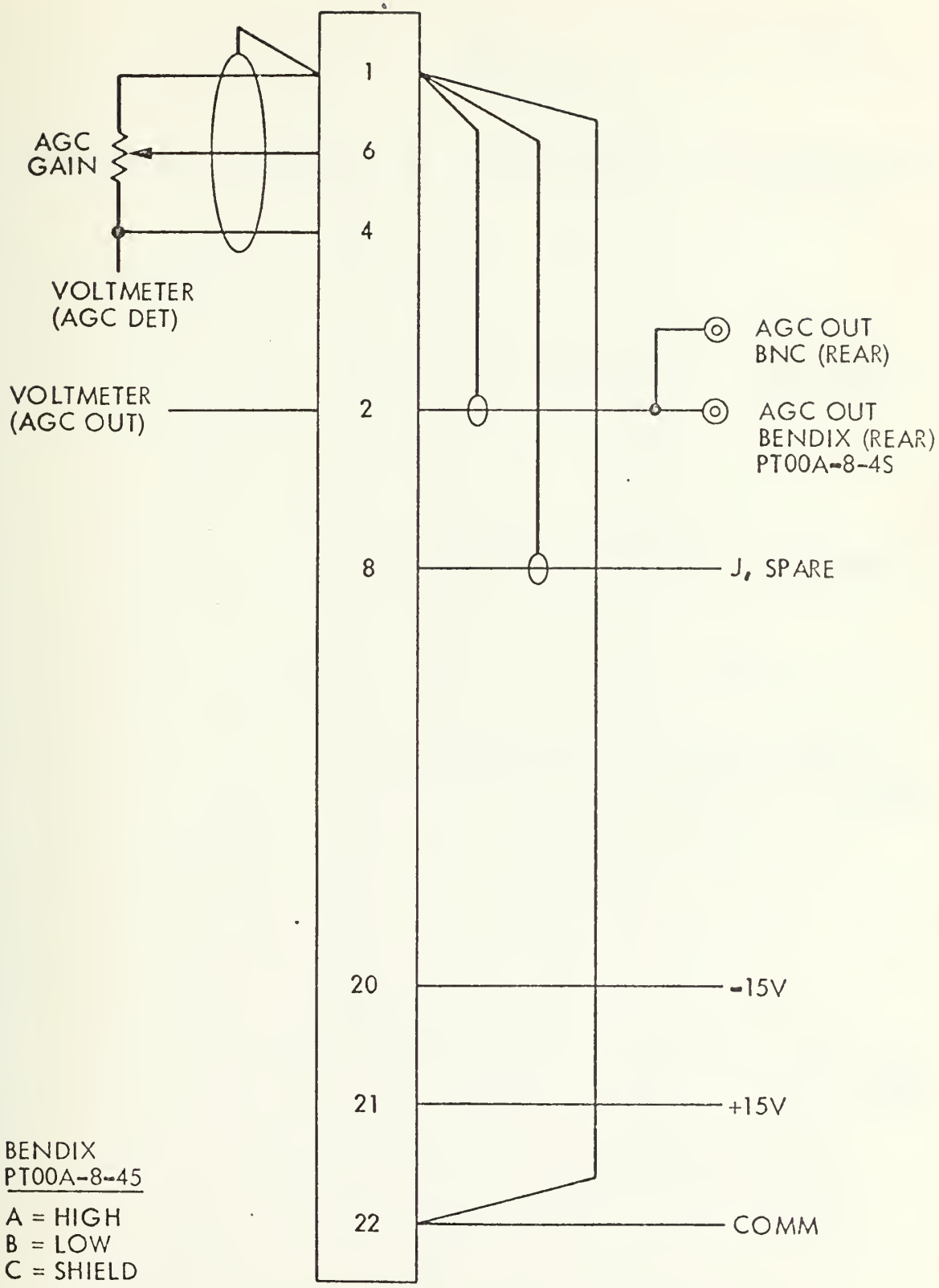

Figure 66 AGC WIRING

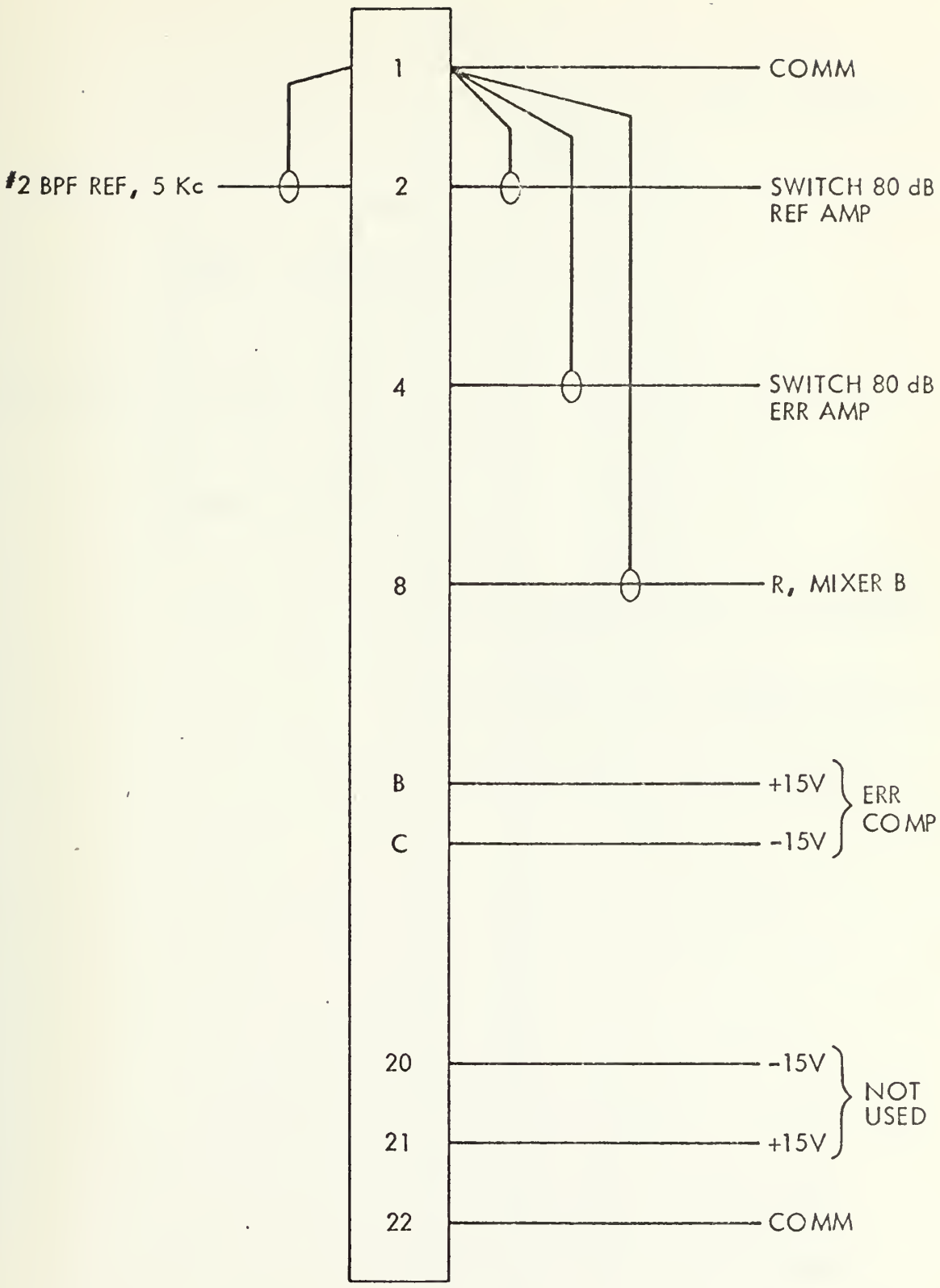

Figure 67 ERROR BPF AT 5 KC IF WIRING

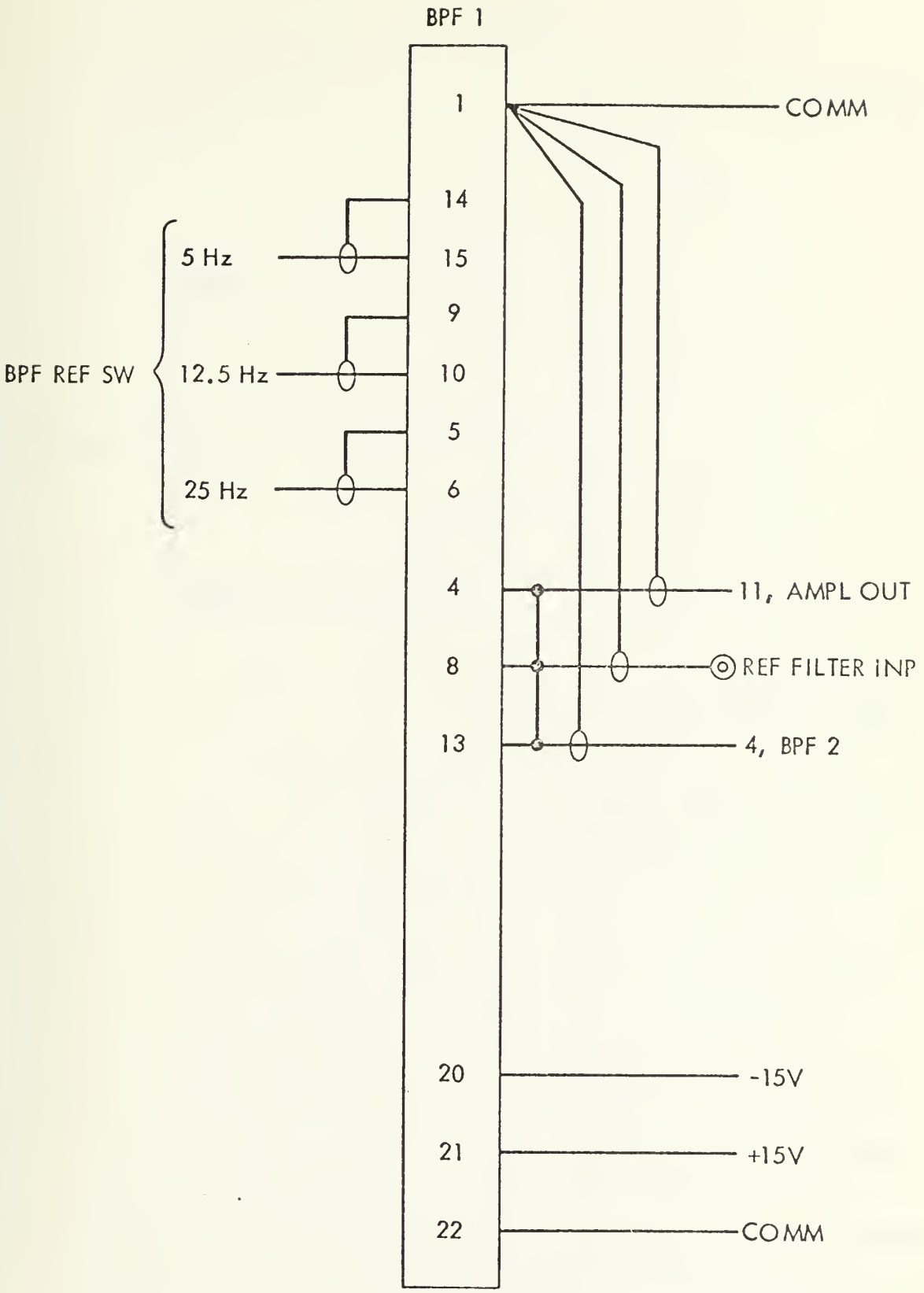

Figure 68 REFERENCE CHANNEL BPF's AT 250 HZ IF 5 TO 25 HZ BW WIRING

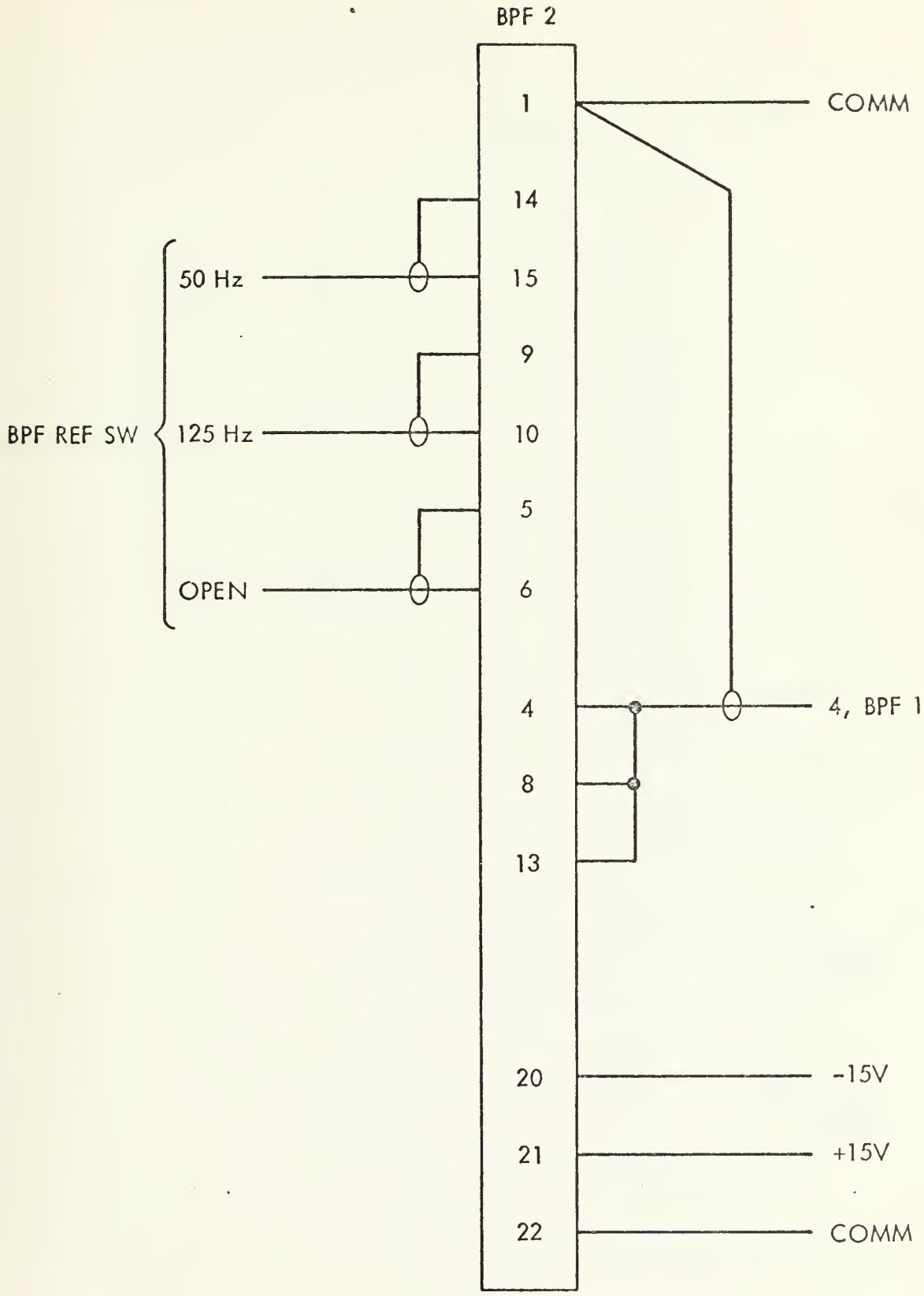

Figure 69 REFERENCE CHANNEL BPF's AT 250 HZ IF 50, 125 HZ BW WIRING

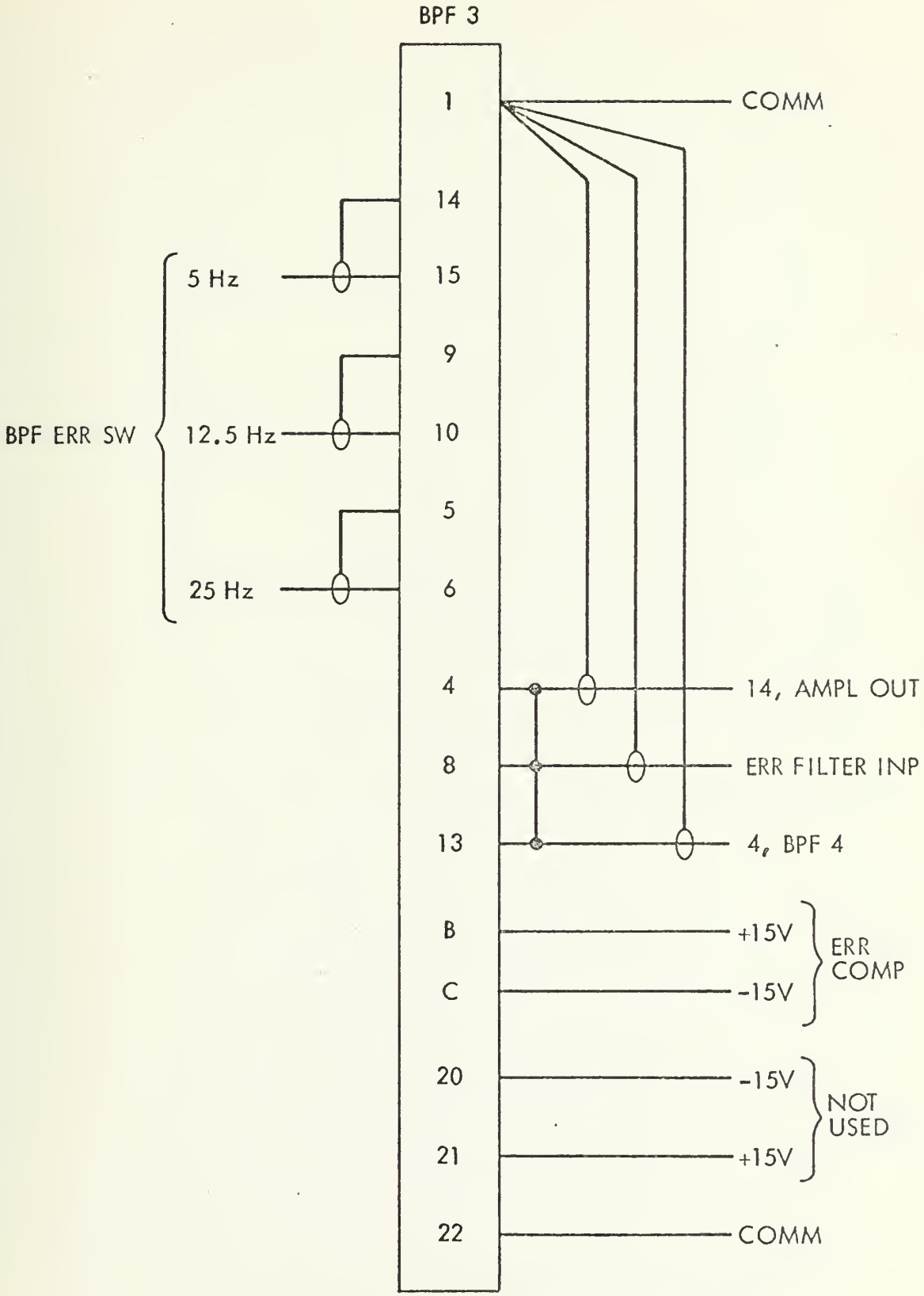

Figure 70 ERROR CHANNEL BPF's AT 250 HZ IF 5 TO 25 HZ BW WIRING

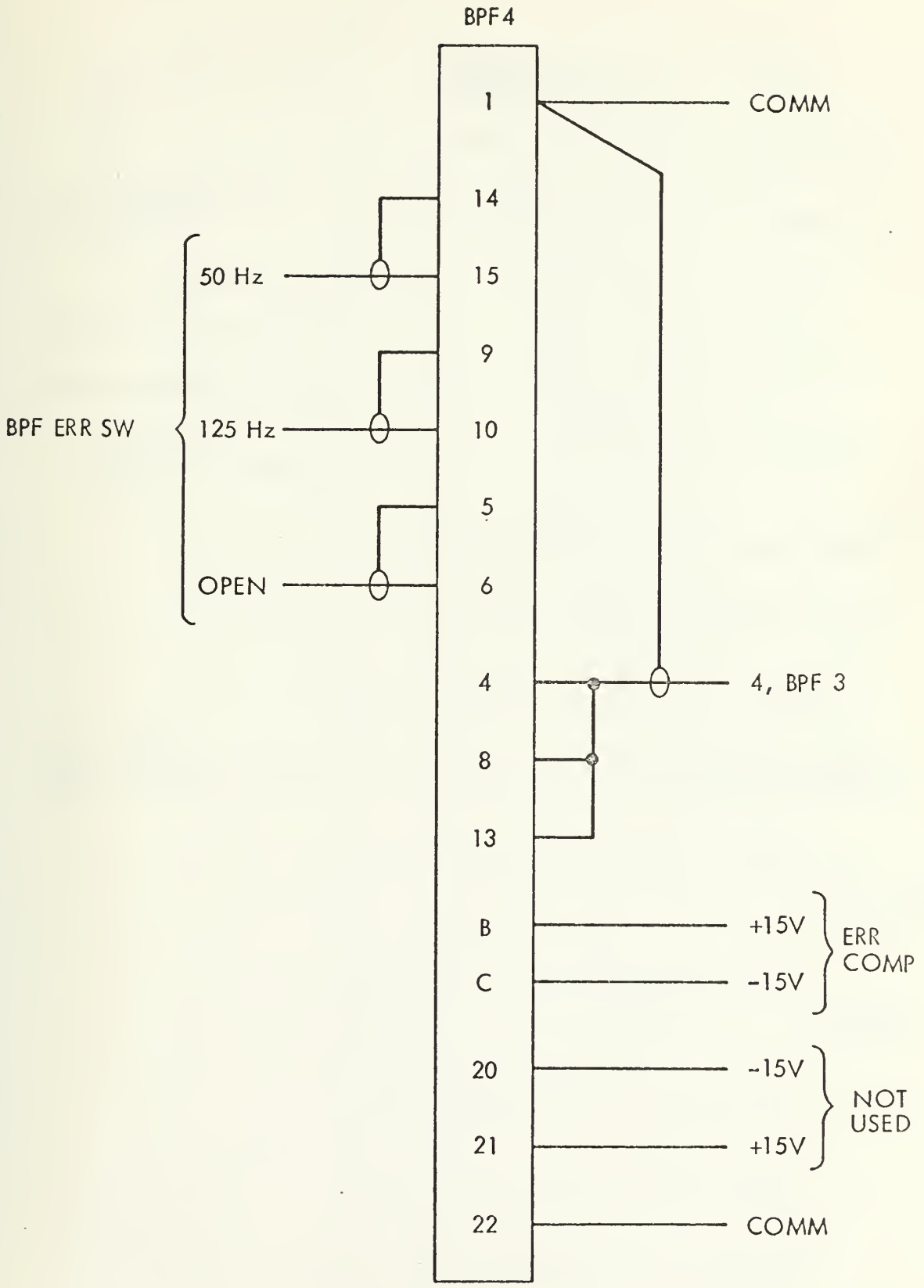

Figure 71 ERROR CHANNEL BPF's AT 250 HZ IF 50, 125 HZ BW WIRING

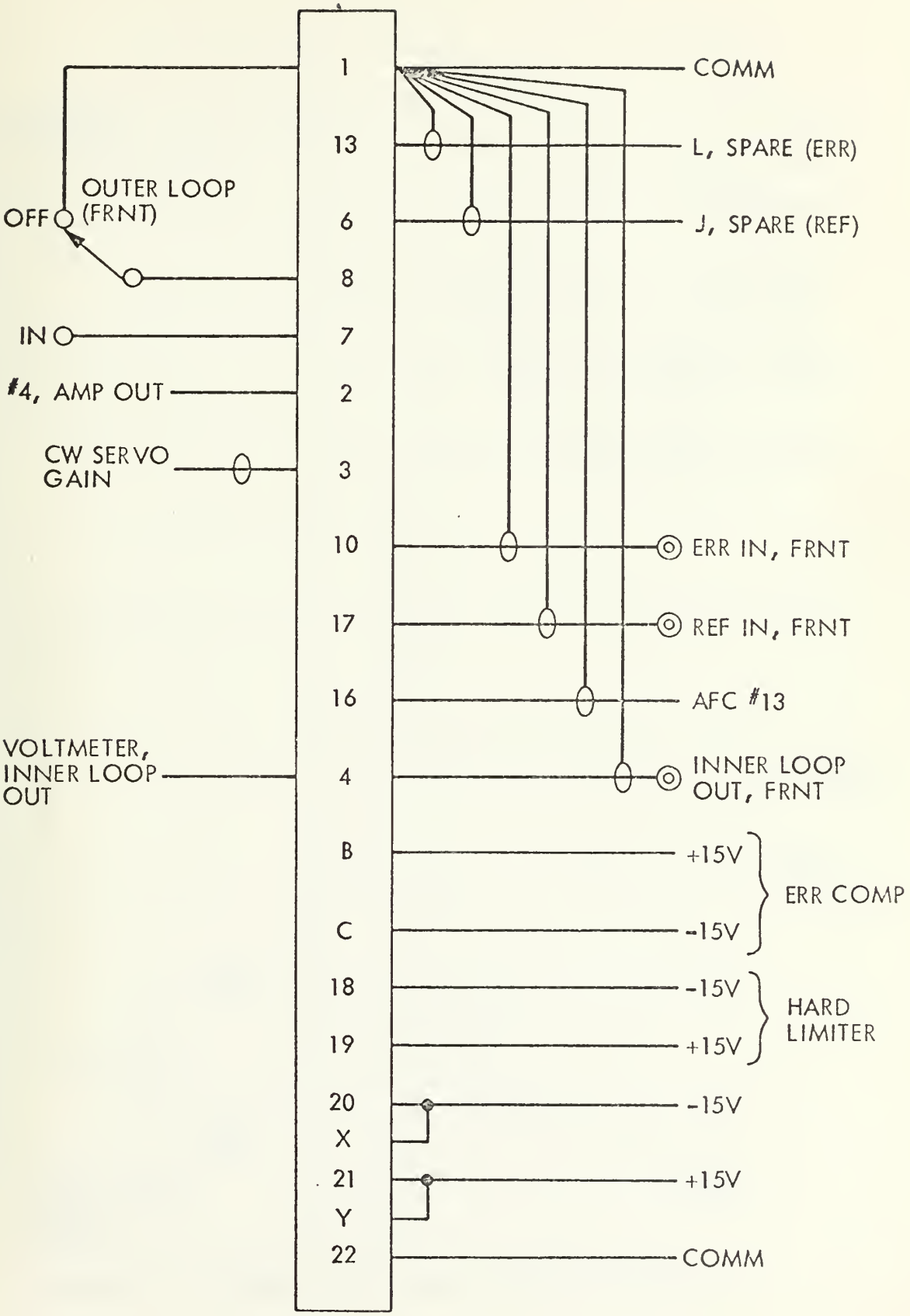

Figure 72 INNER LOOP PHASE DETECTOR WIRING

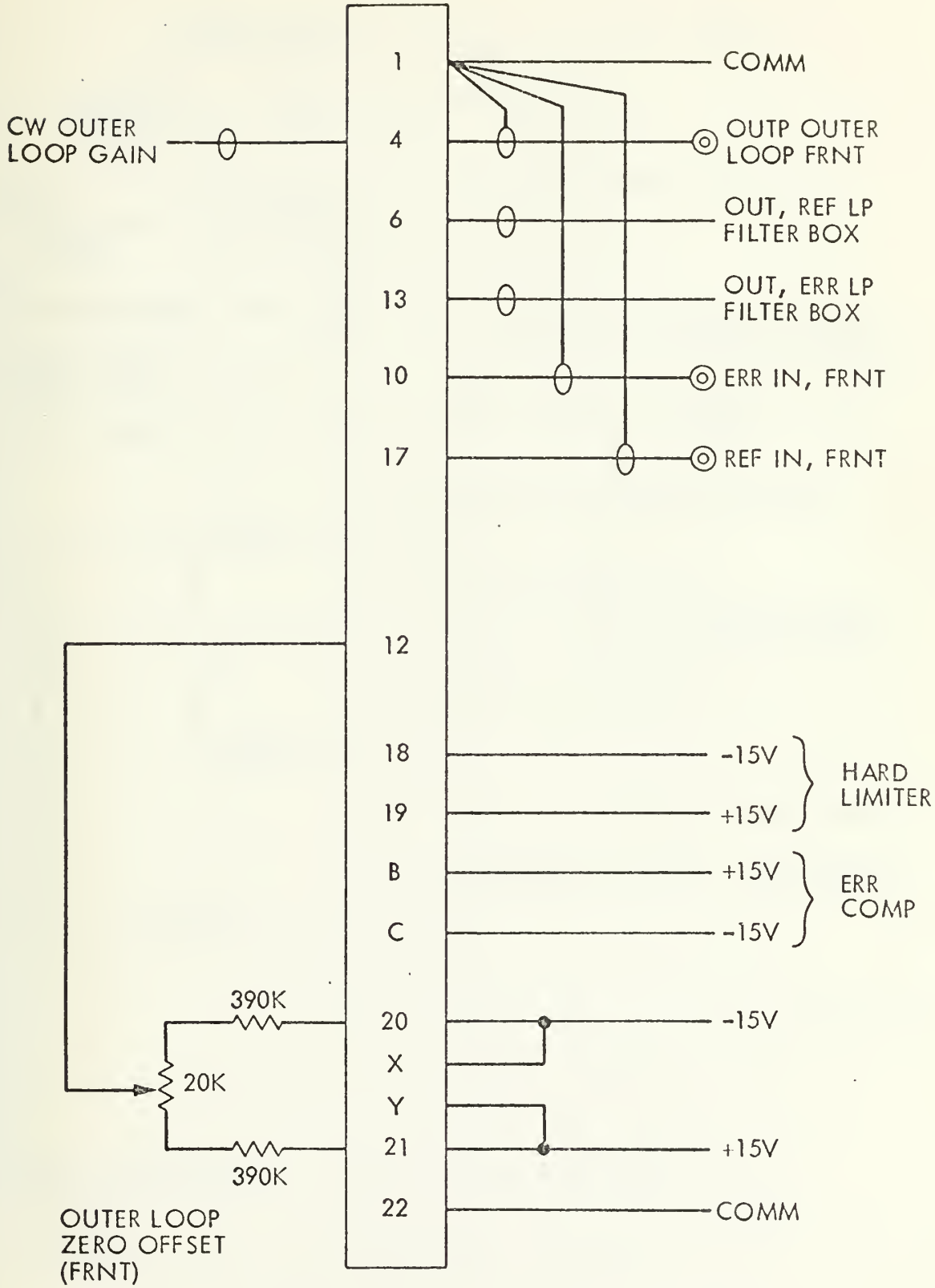

Figure 73 OUTER LOOP PHASE DETECTOR WIRING

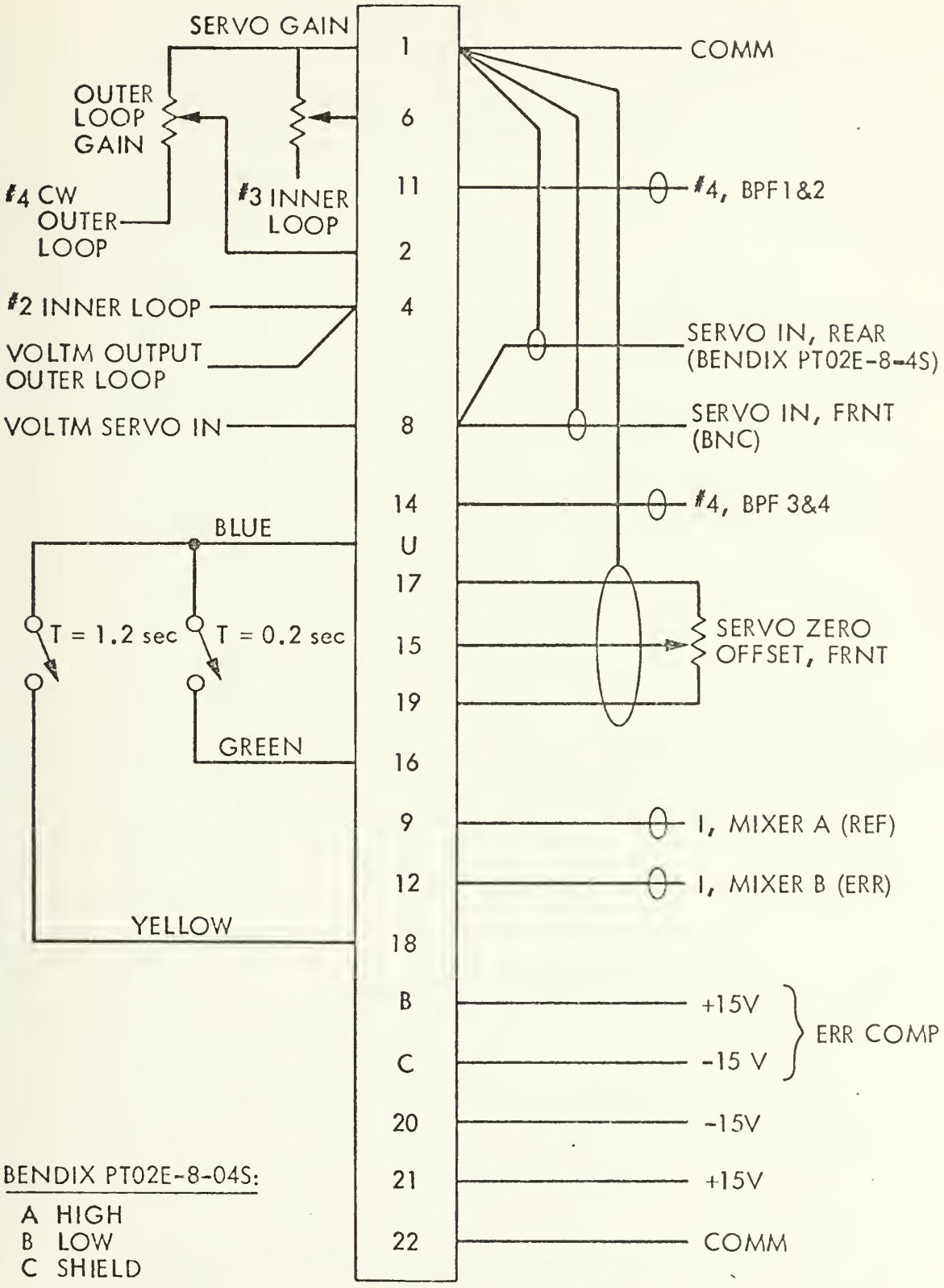

Figure 74 WIRING, BOARD L

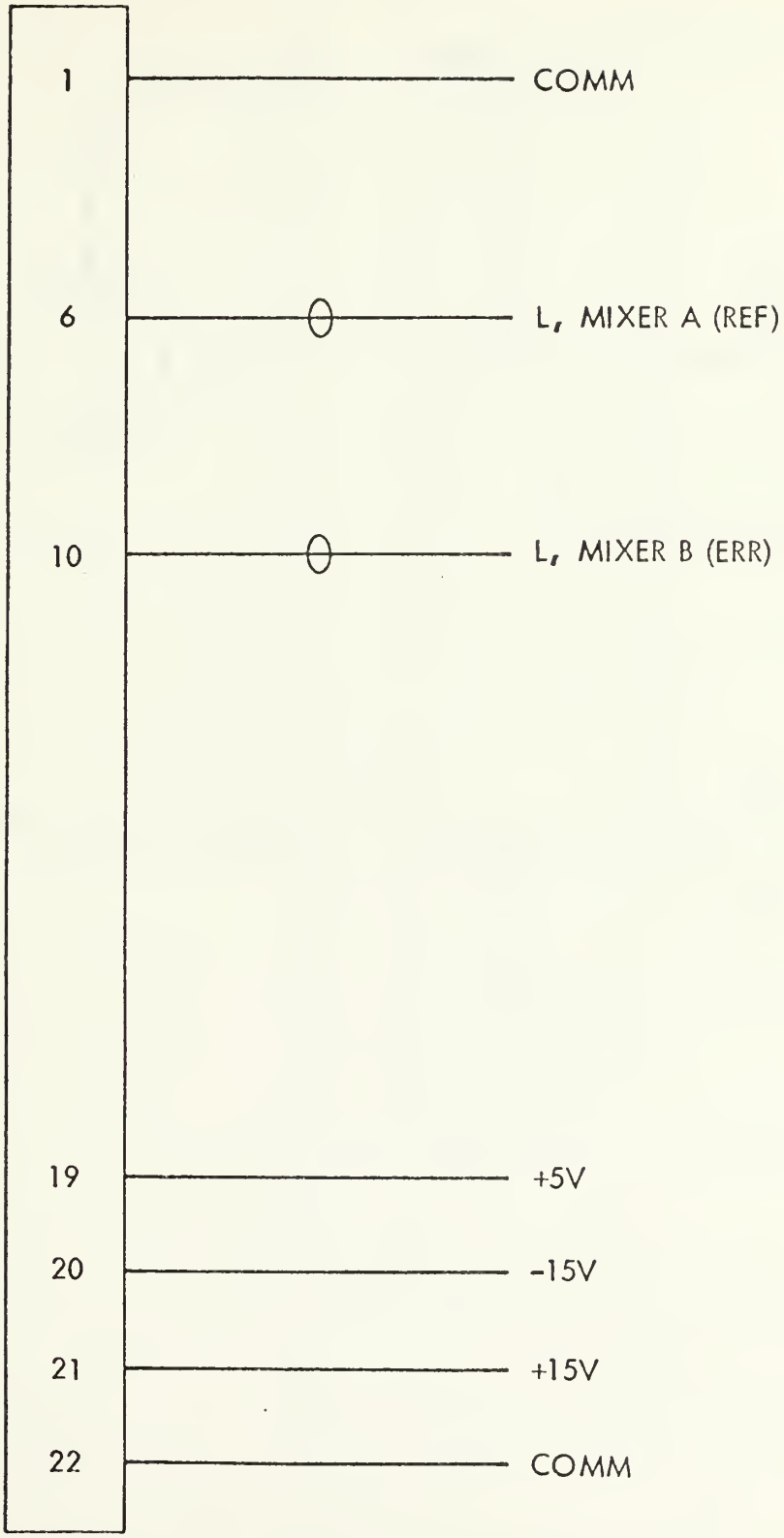

Figure 75 L.O. BOARD WIRING

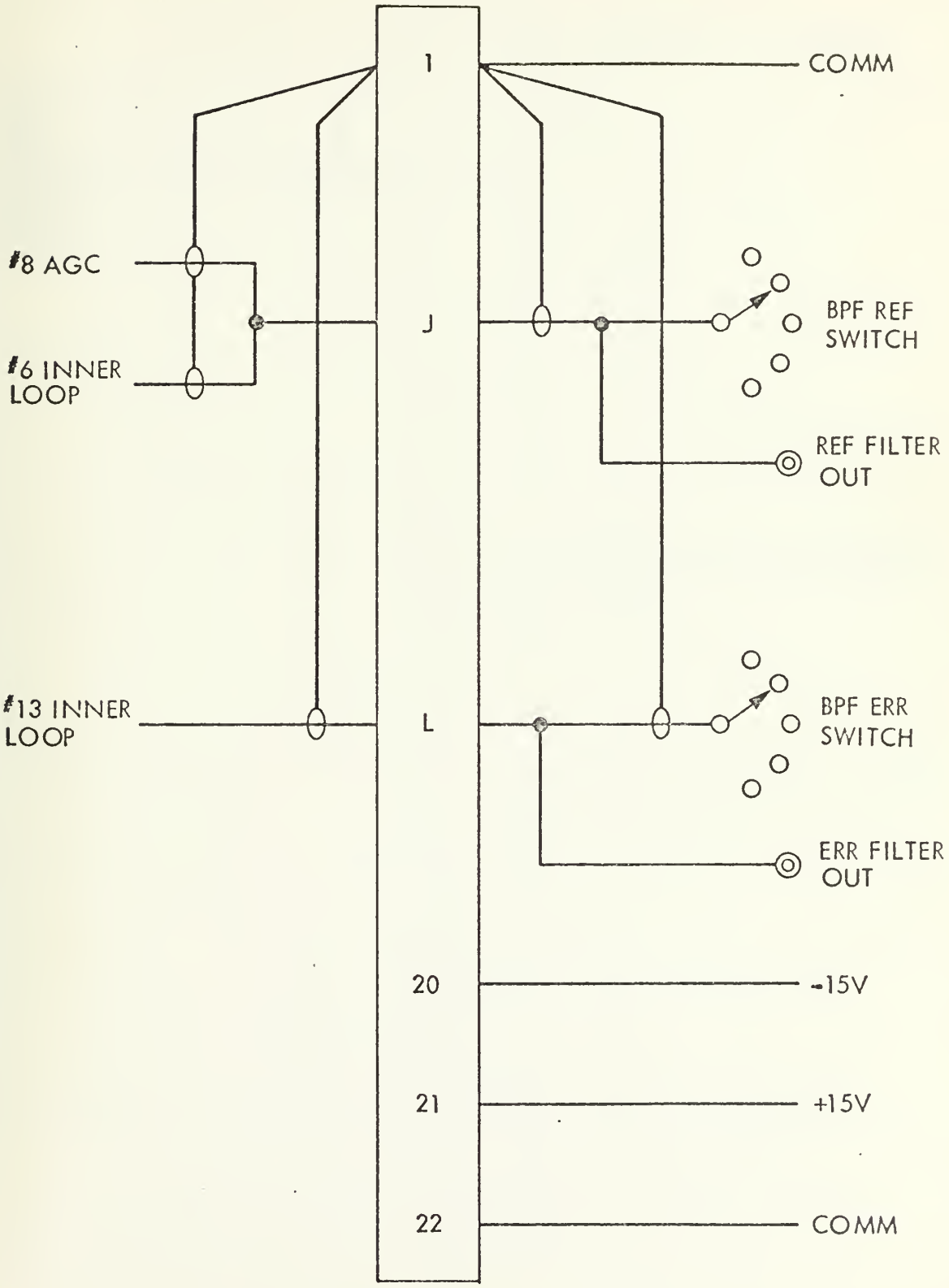

Figure 76 SPARE CONNECTOR WIRING

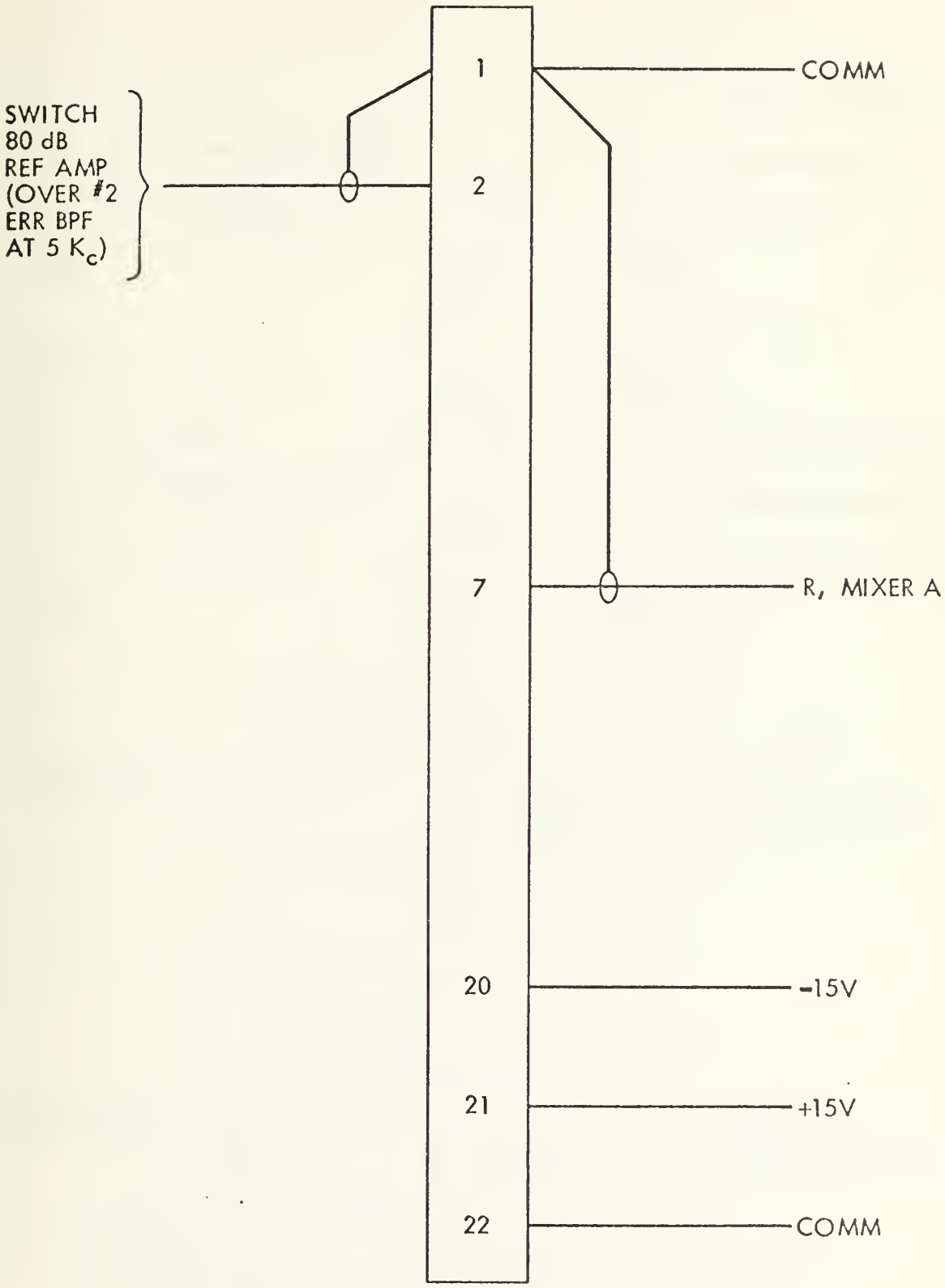

Figure 77 REFERENCE CHANNEL BPF AT 5 KC IF WIRING

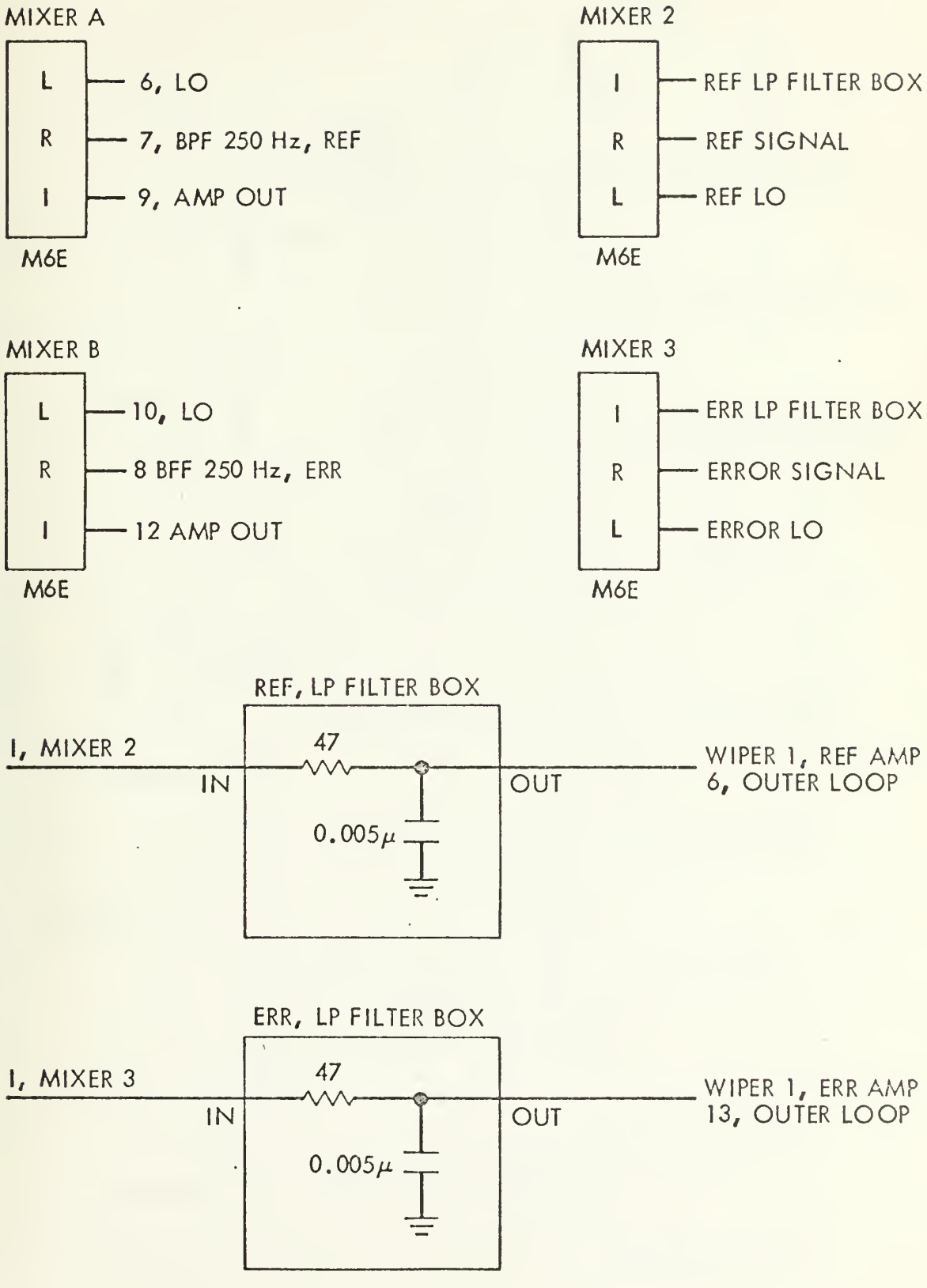

Figure 78 MIXER AND LPF WIRING

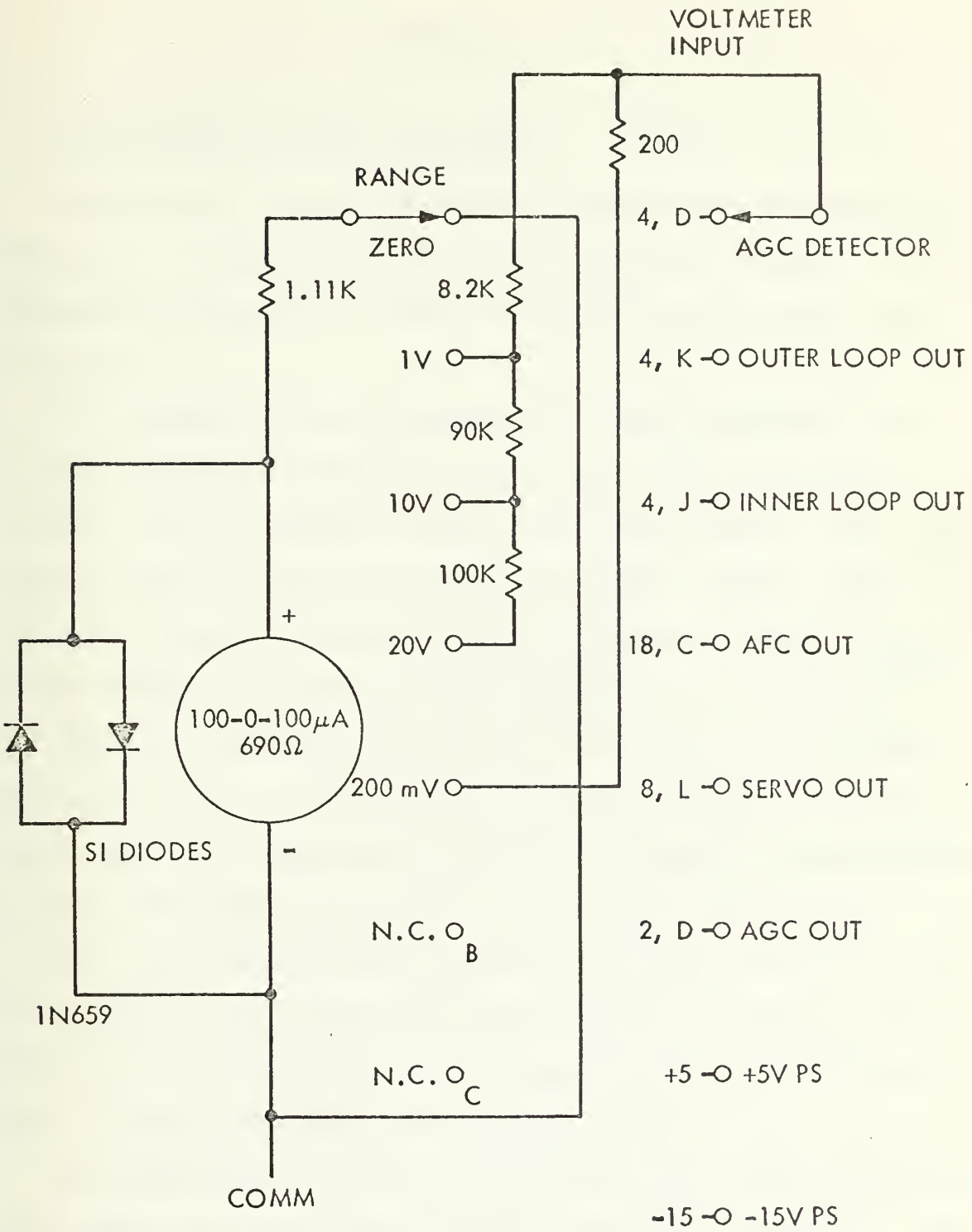

Figure 79 PANEL METER WIRING

APPENDIX B

1. CORRELATION POLARIMETER CHASSIS - SATURATION LEVELS, BANDWIDTHS AND TIME CONSTANTS

Saturation in the correlation polarimeter is determined mainly by the mixers at the front end having a 1 dB compression point of -4 dBm with an equivalent input level of +8 dBm.

The maximum linear sinusoidal voltage out of the 5 KC IF amplifiers was found to be 8.5 V_{rms}. The saturation of the 5 KC IF bandpass filter, the second mixers (A,B) and the amplifier at the 250 Hz IF were lumped together and it was found that the maximum linear voltage out was 7.8 V_{rms} at the output of the amplifiers (adjusted to unity gain).

The 1 dB compression point of the inner loop was found to be at 3 V_{rms} at the input to the phase detector. The outer loop 1 dB compression point was adjusted to be equivalent to the 1 dB compression point of the front end mixers.

The 3 dB points of two stages of the amplifiers at 5 KC IF as used in the operational system were determined to be 300 Hz and 42 KC, clearly wider than the BW of 2 KC at the input to the correlation polarimeter.

The bandwidths of the active filters used in the correlation polarimeter were measured and are tabulated in Table 5. The time constants for the inner as well as outer loop outputs and the servo amplifier were determined to be $\tau = 0.05$ sec.

TABLE 5

Filter Bandwidths in Correlation Polarimeter

Filters at 5 KC IF

	3 DB BW [Hz]	Noise BW [Hz]
Reference Channel Filter	252	277
Error Channel Filter	267	288

Filters at 250 Hz IF

Nominal Filter BW Hz	Reference Channel 3 dB BW [Hz]	Error Channel 3 dB BW [Hz]
5	6.9	7.2
12.5	14.1	14.4
25	25.9	25.6
50	50.8	52.1
125	142.7	144.9

BW of 250 Hz IF Filters in Tandem with 5 KC IF Filters

Filter	3 dB BW [Hz]	Noise BW [Hz]
5	6.7	9.7
12.5	13.5	18.7
25	25.0	32.4
50	44.0	54.0
125	77.5	88.8

Additional filtering for the servo amplifier with time constants of 0.5 and 1.2 sec. is selectable (switches on front panel).

The time constant of the AGC detector circuit was determined to be $\tau = 0.01$ sec.

2. CORRELATION POLARIMETER CHASSIS - TEST SIGNAL AND HIGH NOISE LEVELS

On the basis of the obtained saturation levels, test signal level settings and high noise levels were calculated. The results are given in Figure 80, Figure 81 and Figure 82. It should be noted that the case where the smallest BW at the input to the AGC detector is selected, results in highest noise levels prior to the narrow bandwidth. The AGC loop only acts on a small portion of the total noise reaching the input and therefore does not compress the gain as much as for the case of selection of a wider bandwidth. The calculations for high noise level are therefore based on the selection of the narrowest BW at the 250 Hz IF.

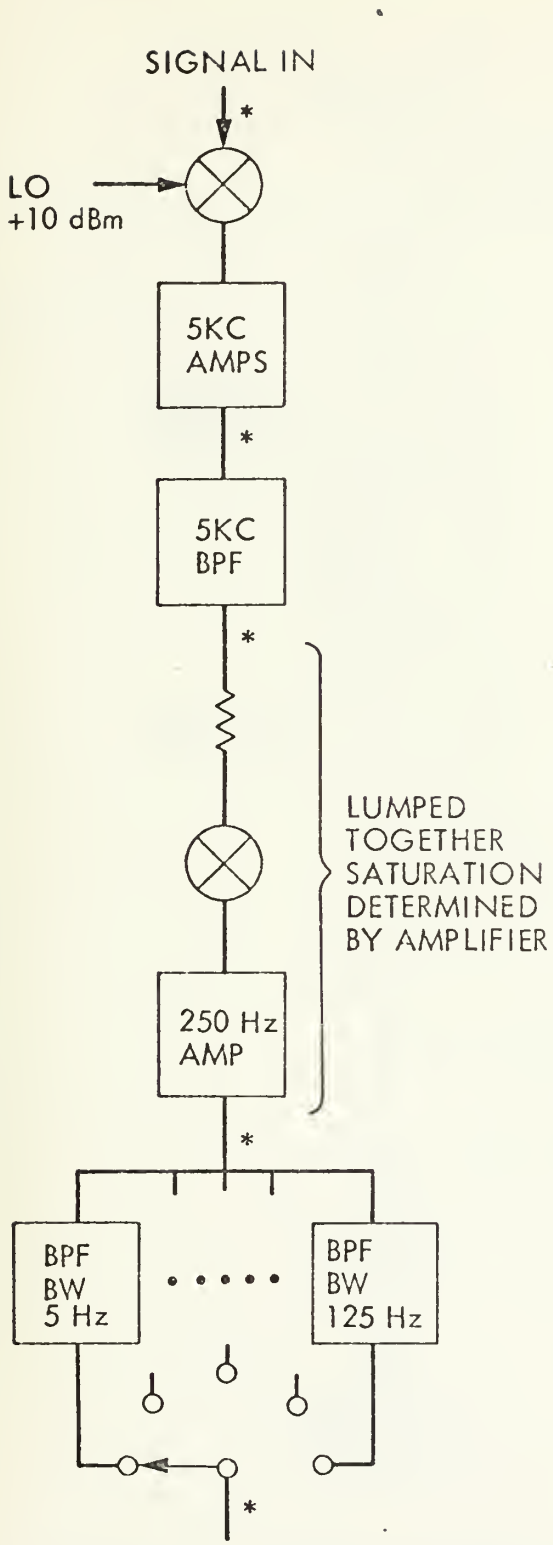

	TEST SIGNAL LEVELS	HIGH NOISE CONDITION
	-28.5 dBm	-3.7 dBm
*		
	0.19 V_{RMS}	3.3 V_{RMS}
*		
	0.19 V_{RMS}	1.19 V_{RMS}
*		
	0.4 V_{RMS}	2.45 V_{RMS}
*		
	0.4 V_{RMS}	0.45 V_{RMS} *

HIGH NOISE CONDITION: AGC DRIVEN BY OUTPUT OF 5 Hz BW FILTER AND NO SIGNAL PRESENT

*1 dB UP DUE TO LINEAR AGC DETECTOR

Figure 80 SIGNAL LEVELS IN CORRELATION POLARIMETER CHASSIS

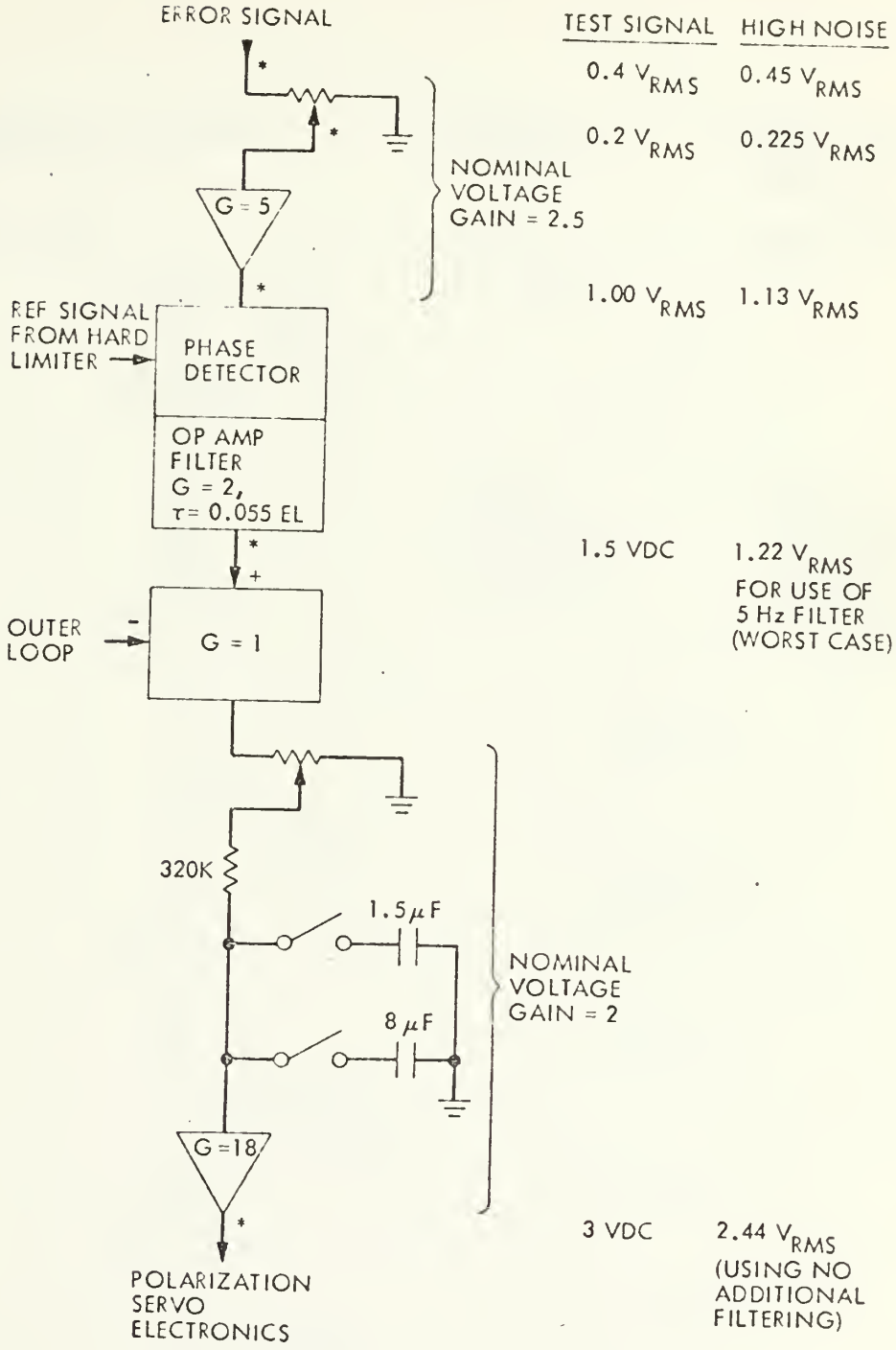

Figure 81 SIGNAL LEVELS IN CORRELATION POLARIMETER CHASSIS, CONTINUATION

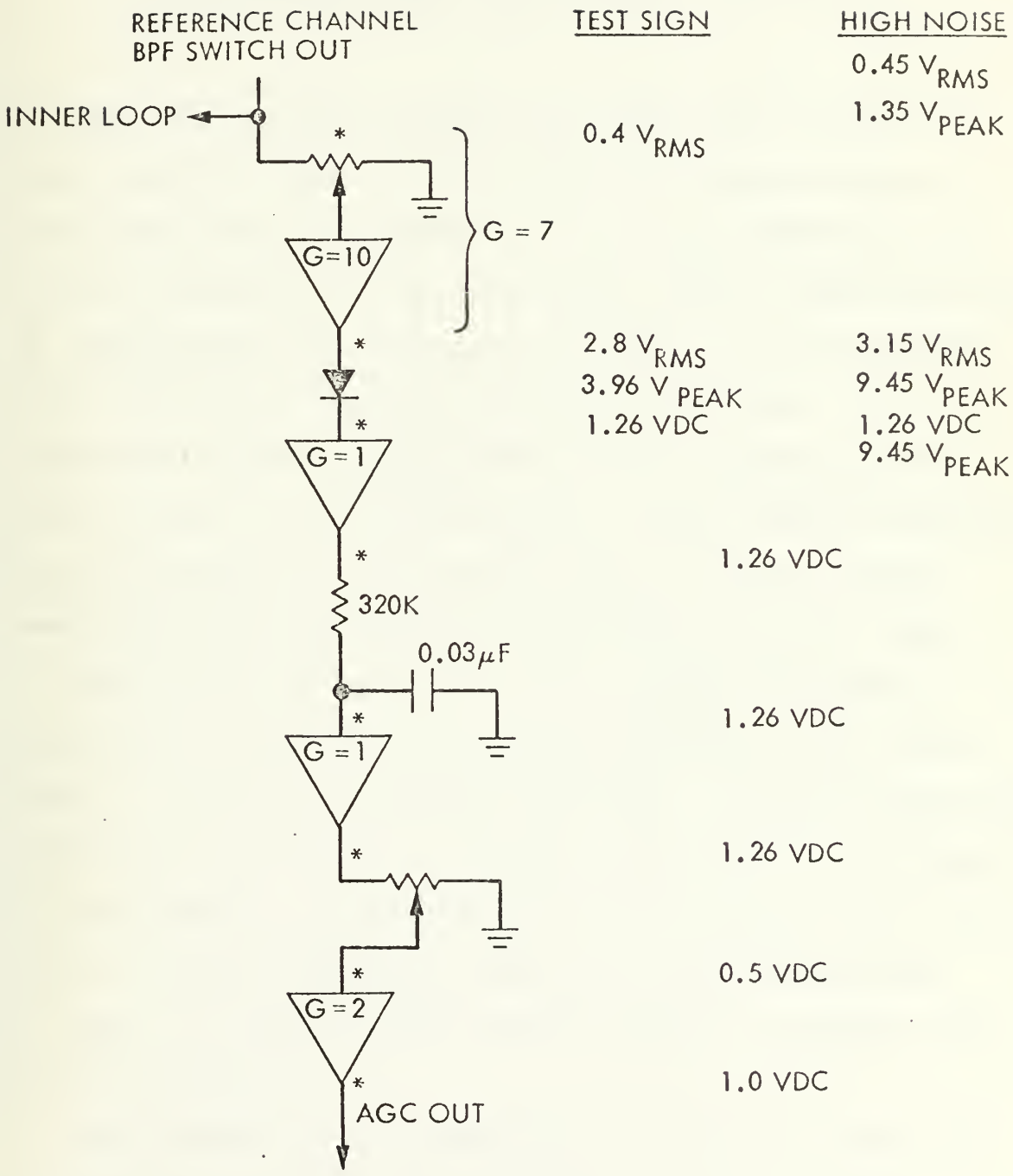

Figure 82 SIGNAL LEVELS IN CORRELATION POLARIMETER CHASSIS AGC CIRCUIT

APPENDIX C

LEVEL CALCULATION FOR RECEIVER 1 BLOCK III AT THE NASA/JPL DEEP SPACE NETWORK MARS STATION

The levels in the receiver for high noise of 1000° K and a received power of -163 dBm were calculated and it was insured that no saturation in AGC mode operation would occur. The basis for the calculation was the specifications as obtained from the Vellum file at JPL. In the schematic block diagrams of the following pages the gains, 1 dB compression points and bandwidths of the components are given as well as the signal levels for the coherent operation. The noise levels for the design point of 1000° K system temperature and theoretical coherent AGC are given also.

The use of the noncoherent AGC of the correlation polarimeter actually will decrease the total power levels since it is acting on signal plus noise. Therefore with the correlation polarimeter the margin before saturation occurs will be greater. If saturation at the 50 MC IF would occur, prior to the AGC controlled amplifier a SNR degradation of about 1 dB (hard limiter effect) would be expected, but this is unlikely.

The documentation has been restricted to the parts of the receivers which are controlled by the AGC action.

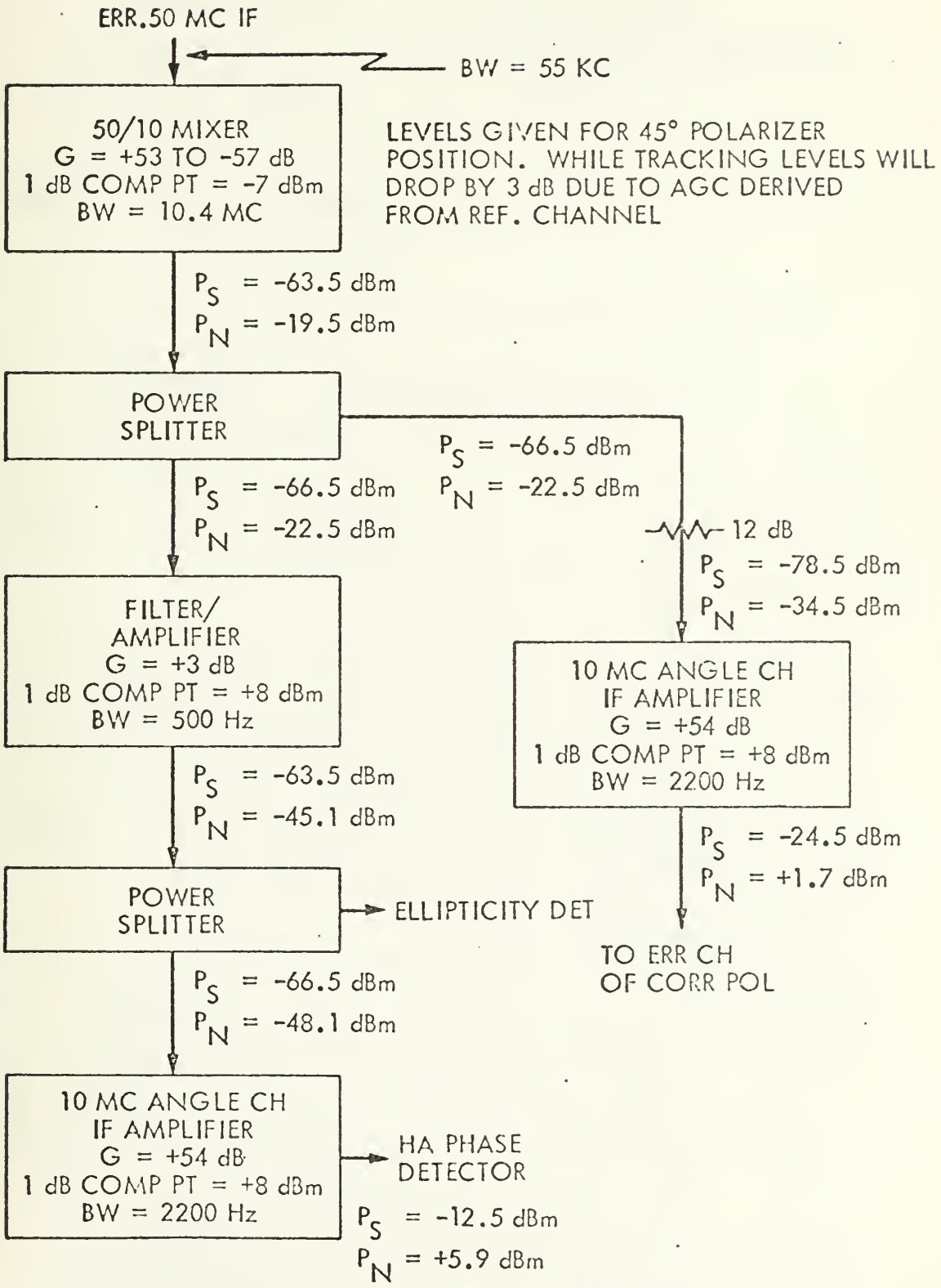

Figure 83 SIGNAL LEVELS IN REFERENCE CHANNEL OF RCVR 1 BLOCK III AT DSS 14

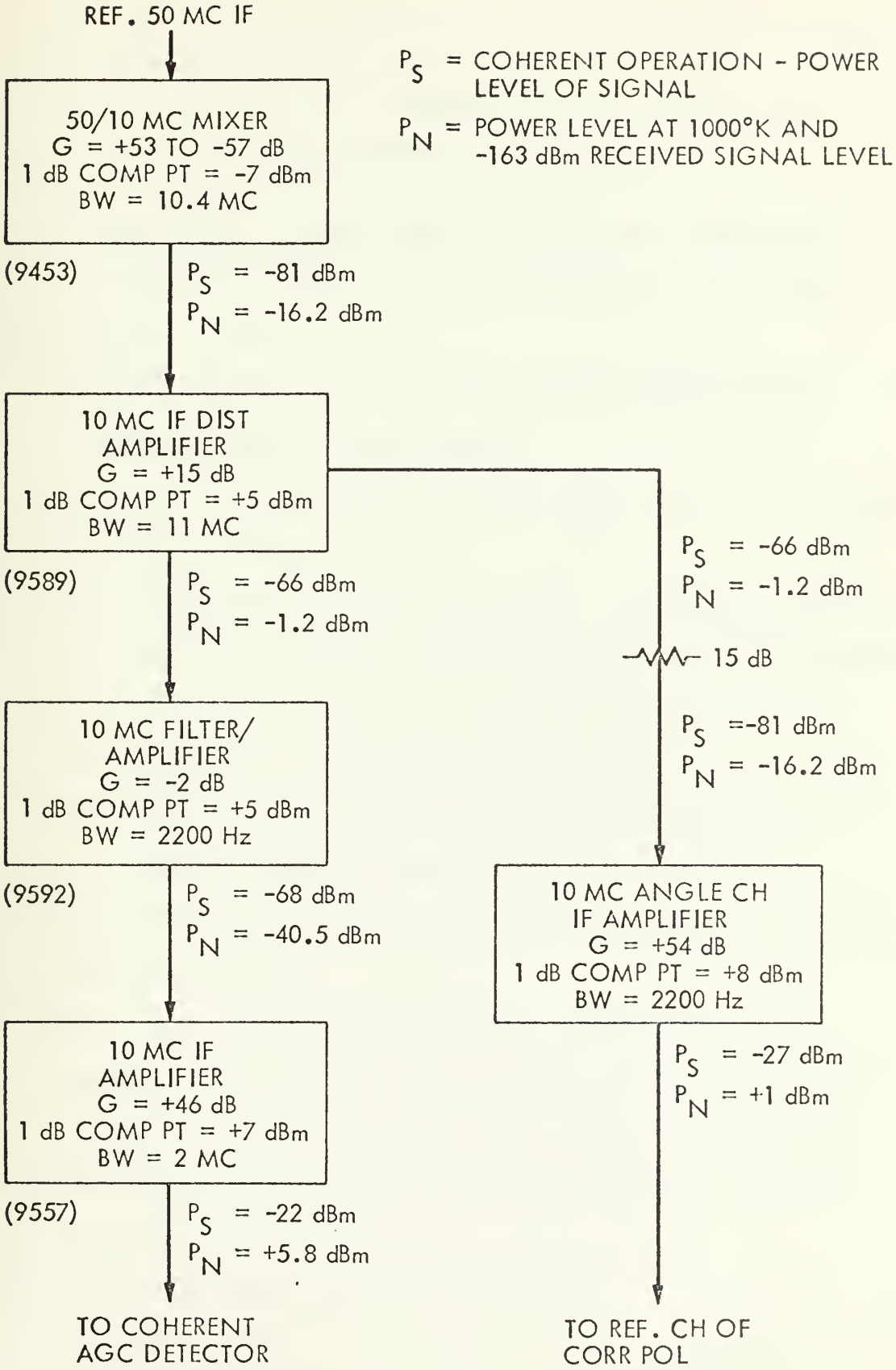

Figure 84 SIGNAL LEVELS IN HOUR ANGLE CHANNEL OF RCVR 1 BLOCK III AT DSS 14

APPENDIX D

CALIBRATION PROCEDURES

1. Correlation Polarimeter Calibration Procedure

If no use of outer loop is required omit steps 9, 17, 21, 22, 23, 24b.

1) Normal RCVR 1 polarization tracking calibration
2) Slew polarizer to 45 degrees
3) On RCVR 2 angle channel panel check with RF voltmeter and note levels.
   A) Phaseshifter (8A 109) output (should be +10 dBm to +11 dBm), (if not, check that HP 5100B synthesizer in RCVR 38 rack is connected in back)
   B) Output-REF ANGLE CHANNEL (8A 116)
   C) Output ERROR ANGLE CHANNEL AMPLIFIER (8A 105)
   (B and C should give -26 dBm to -29 dBm)
4) CP: Flip two upper REF and ERR channel gain switches (20, 40 dB) up
5) CP: Put meter select switch to AGC Detector. Adjust REF channel gain vernier on CP to obtain -1 V on meter (adjusts proper gain of REF channel in CP)
6) Note 50 MC HA channel attenuator setting in RCVR 1, set to Z_o, 70 dB
7) CP: Put METER SELECT TO INNER LOOP
   Reading should be less than ± 5 mV (otherwise have to adjust phase detector inner loop in CP box, POT:PD)

8) CP: Put outer loop switch to OFF

9) CP: meter select switch to outer loop and with outer loop zero vernier, zero meter

10) CP: meter select switch to "servo in", with servo zero vernier adjust meter to zero

11) CP: turn meter range switch to 20 V range.

12) On rack 1946/RCV-6 receiver output meter select hour angle receiver 1. Flip servo switch up on receiver 1 angle channel panel.

13) Set RCVR 1 HA Attenuator to previously (in 6) noted values

14) BORESIGHT Phaseshifter on RCVR 2 ANGLE CHANNEL panel for maximum positive voltage on meter HA receiver out

15) CP: Put meter select switch to INNER loop, adjust ERROR CHANNEL GAIN VERNIER to obtain 1.5 V on meter (proper gain for error channel)

16) CP: Put Meter Select Switch to "Servo in". Adjust Servo Gain to give 3 volts meter reading

17) CP: Put meter select switch to outer loop and adjust outer loop gain to give meter reading according to attached table, (values depending on BW used in inner loop)

18) Set RCVR 1 50 MC HA attenuator to Z_o, 70 dB

19) Flip servo select switch on RCVR 1 HA panel up

20) Select HA on RCVR 1 voltmeter
Reading should be ± 3 mV if not, go to CP out meter switch to SERVO IN and zero with servo zero vernier on CP. Should read ± 3 mV on RCVR 1 HA

21) CP: Put meter select to outer loop and adjust outer loop zero if necessary.

22) CP: Put meter select to servo and switch outer loop switch up to SGN. Meter should stay within ± 3 mV on CP and on HA RCVR 1 voltmeter. If not, switch outer loop switch to GND. Check for servo zero than meter select to outer loop, zero again and repeat procedure in this number.

23) CP: Meter select to outer loop. Outer loop switch to GND

24) Set 50 MC HA attenuator RCVR 1 to noted setting.
a) HA RCVR 1 voltmeter should read + 3 volts
b) CP meter should read values as from attached table according to BW used. (See Appendix D.2.)
If either a) or b) or both don't give specified values go back to 15 and repeat steps if necessary.

25) Select AGC RCVR 1 on RCVR 1 DVM. Note AGC voltage.

26) Select 25 Hz BW on CP and medium AGC BW on receiver 1.

27) RCVR 1 panel: lift up AGC mode switch

28) CP: Put meter select switch to AGC

29) Adjust AGC gain on CP to obtain on RCVR 1 voltmeter same AGC voltage as in 25.

That completes the Correlation Polarimeter calibration.

Note: Insure that for normal receiver operation the servo, AGC mode switches are in normal (down) position and that the VCO/ETO switch is in VCO (down) position.

2. Table 6

REQUIRED GAIN SETTINGS FOR OUTER LOOP IN CORRELATION POLARIMETER

Selected BW INNER LOOP	Meter Reading OUTER LOOP (volts)
5 Hz	0.1
12.5 Hz	0.14
25 Hz	0.18
50 Hz	0.24
125 Hz	0.3

Based on 1.5 V reading at a polarizer angle of 45° for inner loop out and 2.2 KC noise BW of 10 MC IF filter amplifiers in front of correlation polarimeter.

3. Open Loop Receiver Calibration Procedure

1) Antenna at zenith, subreflector on SPD cone

   Attention: No Test Signal required

2) Make sure ETO is operating and connected to X3 in both OLR's.

3) Adjust OLR 1 and OLR 2 MGC voltage to 2.25 volts.

4) Set OLR 1, OLR 2 attenuators to 20 dB (gives about -8 dBm at pedestal, spectrum analysis) for 20° K noise temperature and no signal.

5) Make sure both attenuators on amplifiers in R&D/DSN interface rack in plenum are set to 11 dB (9 dB power attenuators at output to hardlines).

6) a) Calculate in dB

$$\frac{\text{Expected noise temperature}}{20^\circ\ \text{K}} = A\ [\text{dB}]$$

   b) Inquire expected spacecraft signal power Ps in dBm to be received and calculate

$$152 - P_S\ \text{dBm} = B\ [\text{dB}]$$

7) Increase the attenuator settings of OLR 1 and OLR 2 by the larger number of dB obtained in 6).

This completes the OLR calibration.

APPENDIX E

WIRING DIAGRAMS FOR THE CORRELATION POLARIMETER INSTALLATION AT THE NASA/JPL DEEP SPACE NETWORK MARS STATION

In the following figures the wiring diagrams for additional components used with the installation are given. The block diagram of the Correlation Polarimeter with installation indications was already given in Figure 20.

A listing of the cables is given in Table 7.

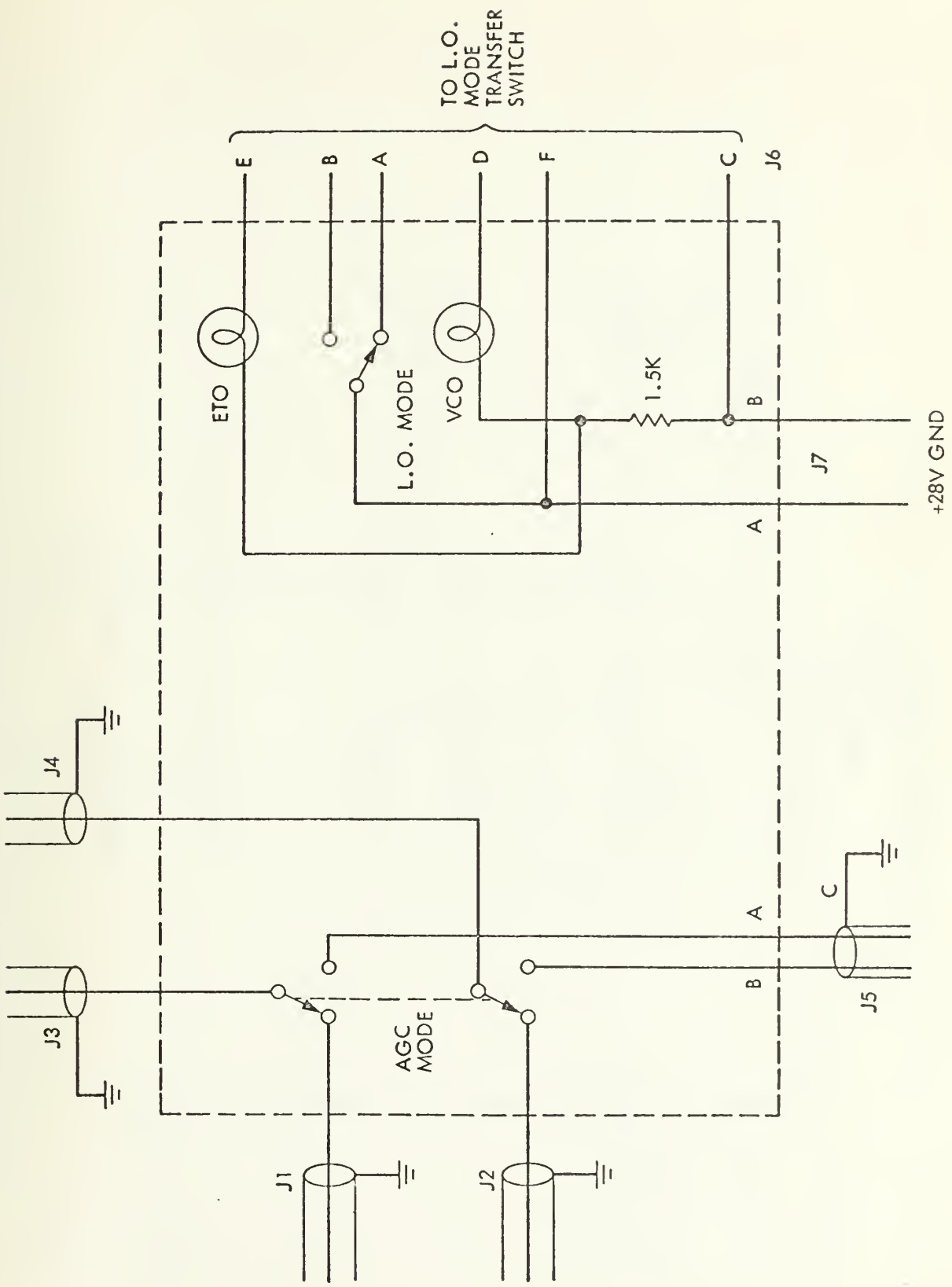

Figure 85 LO/AGC MODE SWITCH WIRING DIAGRAM

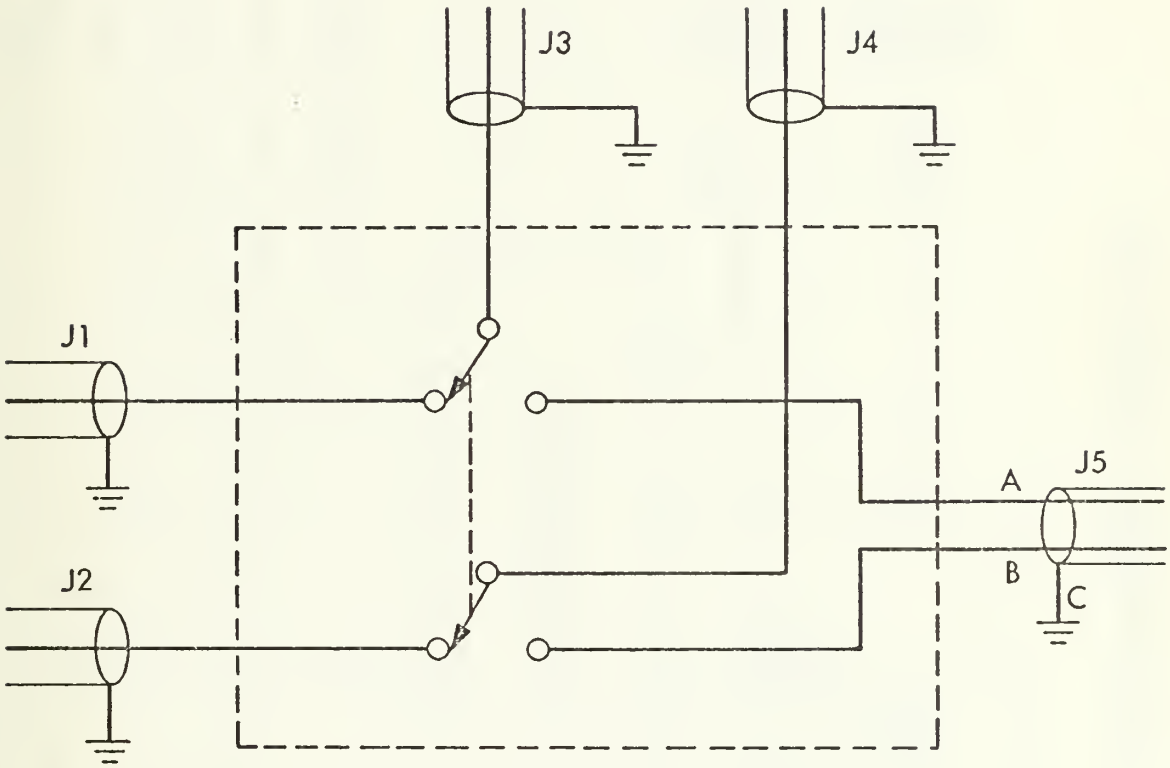

Figure 86 SERVO MODE SWITCH WIRING DIAGRAM

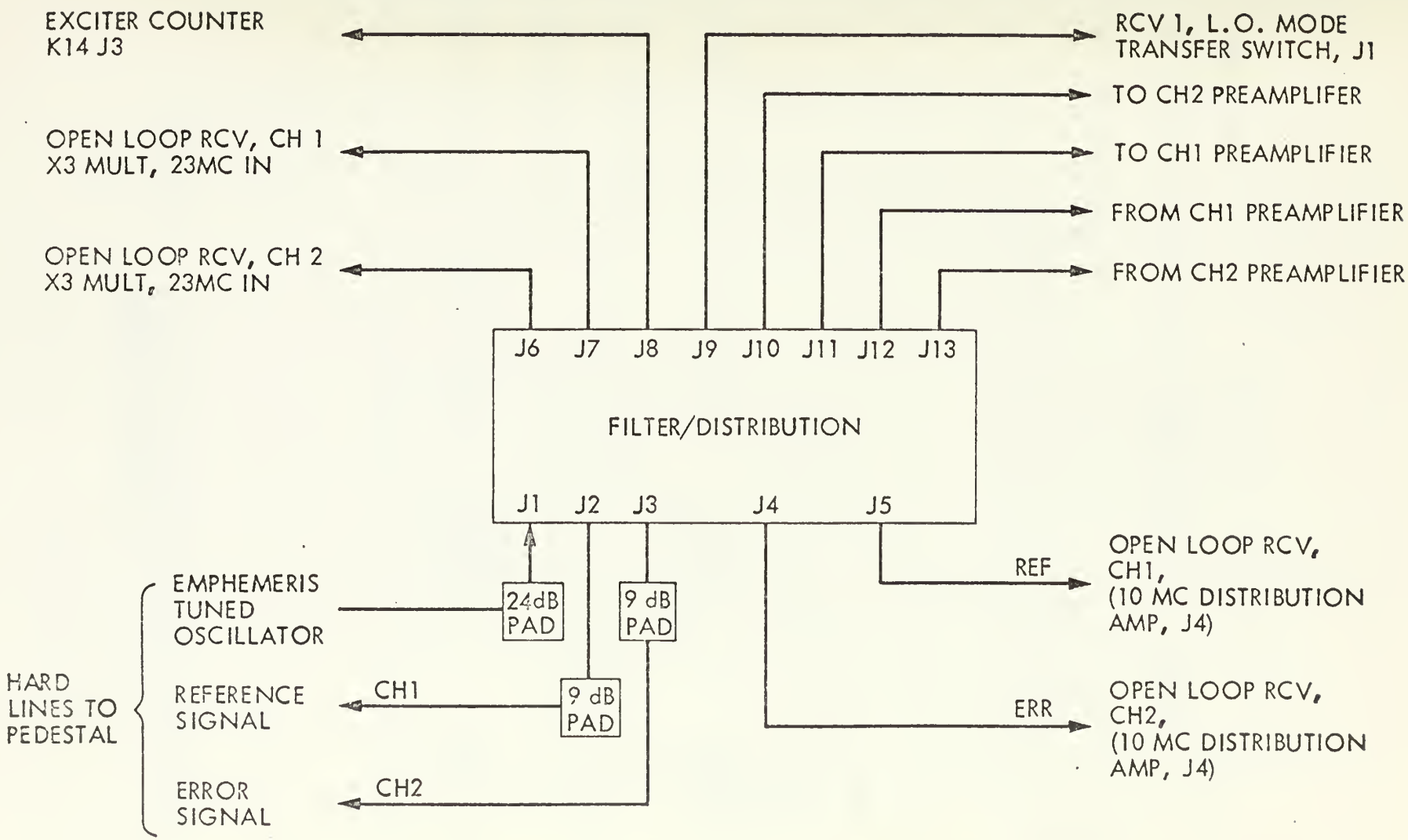

Figure 87 R&D/DSN INTERFACE/DISTRIBUTION CONNECTIONS

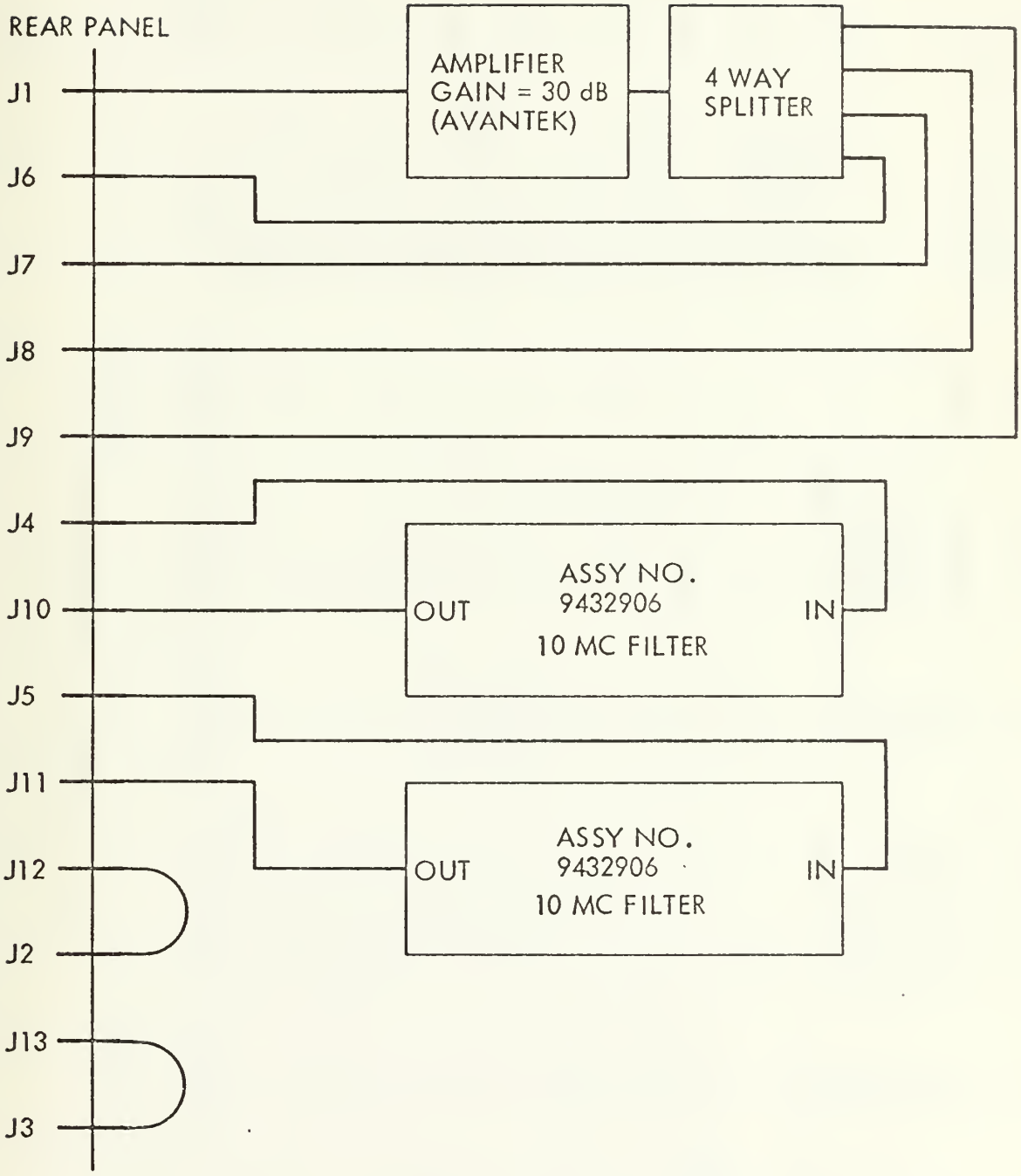

Figure 88 R&D/DSN INTERFACE FILTER/DISTRIBUTION WIRING DIAGRAM

TABLE 7 CORRELATION POLARIMETER CABLE LIST

ONE END				OTHER END				
Unit	Connector	Cable Label	Cable Type	Cable Label	Connector	Unit	Function	Signal Flow
Corr. Pol. (2231/XUWV)	J1	REF SIG CP/J1	Coax	REF SIG	J2	Angle Ch. Amp. (8A116)	Ref. Sig.	←
	J2	ERR SIG CP/J2	Coax	ERR SIG	J2	Angle Ch. Amp. (8A105)	Err. Sig.	←
	J3	REF LO CP/J3	Coax	REF LO	-	Power Div. (near 8A109)	Ref. LO	←
	J4	ERR LO CP/J4	Coax	ERR LO	J2	Ph. Shift. (8A109)	Err. LO	←
	J5	AGC CP/J5	Shielded pair	AGC CP	J5	LO/AGC Switch Box (near 5A405)	AGC	→
	J6	SERVO CP/J6	Shielded pair	SERVO CP	J5	SERVO Switch (5A108)	Servo	→
HP 5100B (1500/RCV-38)	Output	LO COR POL	Coax	LO CP SYNTH	IN	Avantek Ampl. (8A108)	LO	→
Distr. Amp. (5A402)	J6	REF SIG CP	Coax	REF SIG RCV	J1	Angle Ch. Amp. (8A116)	Ref. Sig.	→
Power Divider (feeding 5A103)	Output	ERR SIG CP	Coax	ERR SIG RCV	J1	Angle Ch. Amp. (8A105)	Err. Sig.	→
L.O. MODE TRANSFER SWITCH	J1	ETO	Coax	ETO	J9	Filter/Dist. (R&D Interface Rack-Plenum)	ETO	←
	Multi	TR SW DRIVE	Multi	TR SW DRIVE	J6	LO/AGC Switch Box	VCO/ETO	←
Filter/ Distribution (R&D Interface rack in plenum)	J1	ETO PED	Coax	HARDLINES TO PEDESTAL				←
	J2	REF SIG OUT	Coax					→
	J3	ERR SIG OUT	Coax					→
	J4	ERR SIG OLR 2	Coax	ERR OLR 2	A2J3	OLR Ch. 2 (10 MC Dist. Amp.)	Error Sig.	←
	J5	REF SIG OLR 1	Coax	REF OLR 1	A2J3	OLR Ch. 1 (10 MC Dist. Amp.)	Ref. Sig.	←

TABLE 7 CORRELATION POLARIMETER CABLE LIST - (continuation)

ONE END				OTHER END				
Unit	Connector	Cable Label	Cable Type	Cable Label	Connector	Unit	Function	Signal Flow
Filter/ Distribution (R&D Interface rack in plenum)	J6	OLR 2 LO	Coax	OLR 2 LO	J4	OLR Ch. 2 23 MC IN	LO	→
	J7	OLR 1 LO	Coax	OLR 1 LO	J4	OLR Ch. 2 23 MC IN	LO	→
	J8	ETO FREQ.	Coax	ETO FREQ.	AUX A	Exciter Counter	Freq. Meas.	→
	J9	(see LO MODE Transfer switch above)						
	J10	TO CH 2 AMP	Coax	CH 2 IN	CH 1 & CH 2 Amplifiers			→
	J11	TO CH 1 AMP	Coax	CH 1 IN	(R & D Interface Rack-Plenum)			→
	J12	FM CH 1 AMP	Coax	CH 1 OUT				→
	J13	FM CH 2 AMP	Coax	CH 2 OUT				→
HP 3580A Spectrum Analyzer (2231/XUWV)	Tracking Oscillator Output	TRACK OSC/CP	Coax	COUNTER CORR POL	Feed-through	HP 5300A Counter (2735/XRAK)	Sp. Anal. Calibration	→
J-Box at back of HP3580A	OUT	SPECTRUM RECORDER	Coax	SPECTRUM CP		Strip Chart	Record Spectrum	→

BIBLIOGRAPHY

1. Stelzried, C.T., "A Faraday Rotation Measurement of a 13-cm Signal in the Solar Corona", JPL Technical Report 32-1401, Jet Propulsion Laboratory, California Institute of Technology, Pasadena, California, July 1970.

2. Levy, G.S., Sato, T., Seidel, B.L., Stelzried, C.T., Ohlson, J.E., Rusch, W.V.T.,"Pioneer 6: Measurement of Transient Faraday Rotation Phenomena Observed during Solar Occultation", Science, v. 166, p. 596-598, Oct. 1969.

3. Stelzried, C.T., Levy, G.S., Sato, T., Rusch, W.V.T., Ohlson, J.E., Schatten, K.H., Wilcox, J.M., "The Quasi-Stationary Coronal Magnetic Field and Electron Density as Determined from a Faraday Rotation Experiment", J. Solar Physics, 14 (1970), No. 2, p. 440-456, Oct. 1970, D. Reidel Publishing Company, Dortrecht-Holland.

4. Cannon, A.R., Stelzried, C.T., Ohlson, J.E., Faraday Rotation Observation during the 1970 Pioneer 9 Solar Occultation, Jet Propulsion Laboratory, Pasadena, Technical Report 32-1526, Vol. XVI.

5. Ohlson, J.E., Levy, G.S., Stelzried, C.T., "A Tracking Polarimeter for Measuring Solar and Ionospheric Faraday Rotation of Signals from Deep Space Probes", IEEE Transactions on Instrumentation and Measurement, Vol. IM-23, No. 2, June 1974, pp. 167-177.

6. Goldstein, R.M., "Superior Conjunction of Pioneer 6", Science, v. 166, p. 598-601, Oct. 1969.

7. S-Band Polarization Diverse Cone Assembly, Technical Manual TM 506044, Jet Propulsion Laboratory, California Institute of Technology, Pasadena, California, July 1972.

8. Skolnik, M.I., Introduction to Radar Systems, New York: McGraw-Hill, 1962.

9. Zimmermann, W.R., A Correlation Polarimeter for Deep Space Tracking, Electrical Engineer's Thesis submitted to USN Postgraduate School, Monterey, Sept. 1973.

10. Viterbi, A.J., Principles of Coherent Communication, New York: McGraw-Hill, 1966.

11. Ohlson, J.E., "A Correlation Polarimeter for Noise like Signals", submitted to IEEE Transactions on Aerospace and Electronic Systems.

12. Kraus, J.D., Radio Astronomy, New York: McGraw-Hill, 1966.

13. Steinberg, J.L., Lequeux, J., Radio Astronomy, New York: McGraw-Hill, 1963.

14. Brandt, J.C. and Hodge, P.W., Solar System Astrophysics, McGraw-Hill, New York, 1964.

15. Kundu, M.R., Solar Radio Astronomy, Interscience Publishers, New York, 1965.

16. Block III Ground Equipment S-Band Receiver/Exiter Subsystem, Detailed Specifications for, Jet Propulsion Laboratory, Spec DOR-1276-DTL B, Pasadena, California, June 1970.

17. Davenport, W.B., Root, W.L., Random Signals and Noise McGraw-Hill, New York, 1958.

18. Ohlson, J.E., "Exact Dynamics of Automatic Gain Control", IEEE Transactions on Communications, Vol. COM 22, No. 1, January 1974.

19. Thomas, J.B., An Introduction to Statistical Communication Theory, p. 284, Wiley, 1969, New York.

20. Selby, M.S., Standard Mathematical Tables, The Chemical Rubber Company, Cleveland, Ohio, 1970.

21. Springett, J.C., Simon, M.K., "An Analysis of the Phase Coherent-Incoherent Output of the Bandpass Limiter", IEEE Transactions on Communication Technology, vol. Com. 19, No. 1, February 1971.

22. Gradshteyn, I.S., Ryzhik, I.M., Table of Integrals, Series and Products, Academic Press, New York, 1965.

23. Davenport, W.B., "Signal to Noise Ratios in Band-Pass Limiters", Journal of Applied Physics, v. 24, No. 6, p. 720-727, June 1953.

24. Stix, T.H., The Theory of Plasma Waves, New York: McGraw-Hill, 1962.

25. Papas, C.H., Theory of Electromagnetic Wave Propagation, New York: McGraw-Hill, 1965.

26. Helios - Reprints from Deep Space Progress Reports, TR 32-1526 Vol. II, Jet Propulsion Laboratory, Pasadena, California, 1974.

27. Helios Project - Spacecraft Telecommunication System Presentation at JPL, May 5, 1972, Jet Propulsion Laboratory, Pasadena, 1972.

28. Special Printing Messerschmidt Bolkow Blohm, Raumfahrt-forschung, Heft 4, July, August 1972, Munchen, Germany.

29. White, R.J., "Space-Single Precision Cowell Trajectory Program" JPL, Memorandum No. 33-198, Jet Propulsion Laboratory, Pasadena.

INITIAL DISTRIBUTION LIST

		No. Copies
1.	Defense Documentation Center Cameron Station Alexandria, Virginia 22314	2
2.	Library, Code 0212 Naval Postgraduate School Monterey, California 93940	2
3.	Dokzent Bundeswehr - See 53 Bonn Friedrich Ebert Allee 34 Federal Republic of Germany	1
4.	Marineamt - A 1 - 294 Wilhelmshaven Gökerstraße Federal Republic of Germany	1
5.	Associate Professor John E. Ohlson, Code 52OL Department of Electrical Engineering Naval Postgraduate School Monterey, California 93940	3
6.	G. S. Levy 238 - 737 Jet Propulsion Laboratory Pasadena, California 91103	1
7.	B. Seidel 238 - 737 Jet Propulsion Laboratory Pasadena, California 91103	1
8.	C. T. Stelzried 238 - 737 Jet Propulsion Laboratory Pasadena, California 91103	1
9.	LCDR. Heinz R. Prunsch, FGN 7119 Ernsbach Sindringer Straße 148 c/o Elsa Setz Federal Republic of Germany	2